Engineering and Physical Sciences Research Council

Newcastle University

A Novel Riemann Solver for Modelling Partial Barriers to Flow within 2-D Hydrodynamic Models

James John M^{c}Kenna

Principal-Supervisor: Vassilis Glenis
Co-supervisor: Chris Kilsby

A thesis presented for the degree of
Doctor of Philosophy

Faculty of Science, Agriculture & Engineering
School of Engineering
Newcastle University
United Kingdom

March 2024

A Novel Riemann Solver for Modelling Partial Barriers to Flow within 2-D Hydrodynamic Models

Abstract

Flooding, exacerbated by anthropogenic climate change, is a pervasive natural phenomenon with profound and widespread implications that necessitates effective flood risk management. Within contemporary flood risk management practice, hydrodynamic modelling comprises a key tool, providing a means for producing crucial quantitative evidence upon which informed decisions can be based. The analysis of flood risk, hazards and exposure is predicated by the accurate determination of the hydrodynamic flow characteristics however, there is great potential for complex interactions which necessitates a more holistic approach. There is therefore a desire for the next generation of flood models to not only accurately simulate the flow dynamics but also possess the capability to effectively account for the myriad of associated events.

This thesis therefore presents novel contributions towards the advancement of contemporary hydrodynamic modelling practice via the development of new numerical solutions. Specifically, it addresses limitations in accurately capturing transient flow interactions with partial barriers to flow; within urban environments, obstacles to flow can significantly influence the local flow characteristics and the accurate modelling of the flow interactions is therefore required. This is achieved via the development of two novel Riemann solvers, which enable the flexible and general treatment of partial barriers to flow. The predictive capacity of the solvers is validated via laboratory experiments, demonstrating their capability to resolve numerical fluxes across a range of flow and barrier configurations. The first solver is simple and easy to implement, with a focus on compatibility with existing numerical schemes to enhance the likelihood of implementation and immediate impact. The second solver addresses the limitations of the first, sacrificing simplicity in favour of greater accuracy and complexity.

Furthermore, to account for the desired flexible future requirements of hydrodynamic models, the potential for flood flows to transport scalar quantities is also considered. Flood events have the potential to pollute water bodies and degrade water quality, particularly when the capacity of the sewage system is exceeded. In such events, hazardous substances may be transported within the urban catchment, compounding the associated risk. As a consequence, the advection and diffusion of a well mixed scalar quantity is also considered within the context of partial barriers to flow. The unique validation procedure based upon hydro-optical theory, enables the nonintrusive determination of the fieldwise concentration via the observation of the scattering and absorption of incident light by an injected fluorescent tracer mass. The collected data enables validation of the predictive capacity of the model to model the advection diffusion process through a partial barrier to flow whilst also providing a valuable insight into a otherwise seldom explored phenomena.

It is hoped that the presented advances will contribute positively towards the development of the next generation of flood models and the implementation of effective flood risk management practice.

Acknowledgements

First and foremost, I would like to express my deepest gratitude to my supervisors, Vassilis Glenis and Chris Kilsby. Towards the end of my undergraduate studies, I had grown disillusioned with academia. However, the opportunity to work with Vassilis and Chris on my Master's dissertation reinvigorated me and without their suggestion, I do not believe I would have had the confidence to commit to a PhD.

I would like to thank Vassilis in particular for indulging me in opportunities to challenge myself and for sharing a similar passion for all things Riemann solvers and numerical methods. I have thoroughly enjoyed working together and I look forward to future opportunities to continuing doing so.

I would also like to thank Chris for his wisdom and his kind words in acknowledgement of my progress that helped to keep me motivated. His application and impact based focus has helped to steer me away from overly esoteric pursuits.

Thank you as well to my family for their love and support, especially to my partner Tonicha who has supported me at every step of my journey. Without Tonicha's love, support and companionship my experience would not have been as fulfilling and I will be forever grateful.

Finally, I would also like to express my gratitude to the EPSRC for funding the project.

Contents

List of Figures

List of Tables

Chapter 1

Introduction

1.1 A Brief Overview of Flood Models

Flooding is recognised as one of the most prevalent and devastating natural phenomena, accounting for almost half of all recorded weather-related disasters from 1995-2015, with estimates of the affected population reaching a staggering 2.3 billion people [373]. The economic impact of flooding is vast, reported as $40 billion per annum [148], but the true human cost is much harder to measure, with profound social, cultural and environmental ramifications proving difficult to accurately quantify. Anthropogenic climate change is expected to result in an increased frequency of flood disasters with greater impacts; more flood disasters occurred between $2010-2013$ than in the entirety of the 1980's and losses from global flood events nearly doubled in the 2000's compared with the 1990's [243]. As such, flooding is a key theme throughout the United Nations Sustainable Development Goals [448].

Within Europe, there has been a recent shift from traditional flood protection approaches, focussed on hard engineering solutions aimed at preventing flooding, to a more holistic flood risk management approach, focussed on minimising impacts [157]. In order to effectively manage the risk of flooding, it is first necessary to predict and quantify flood flows and flood models are therefore a vital component of contemporary flood risk management practice, providing the crucial evidence upon which informed decisions can be based. Of particular interest is the modelling of urban areas, since it is expected that 68% of the world's population will reside in cities by 2050 [449], with the modelling of urbanised areas presenting unique challenges [111].

The propagation of flood flows through urban areas is particularly complex due to the density and variety of topographic features. Buildings, bridges, roads, drain inlets and blue-green infrastructure are but a few features common to urban areas which may significantly influence flood flow dynamics. The complicated flow interactions which occur within urban areas are therefore omnipresent and require special attention to ensure physically relevant modelling predictions.

Flood models can be broadly categorised into physically-based models, which simulate the fundamental physical processes, and data-driven models, which use patterns and relationships derived from data. Despite booming research interest in data-driven methods and the promise of high levels of computational efficiency, data-scarcity, particularly where

model training relies heavily on physically-based hydrodynamic simulations [189], primarily restricts the application of data-driven approaches. As a result, modern practices typically utilise physically-based models, benefiting from greater reliability, generalisability and transparency.

For single phase flood flows, ignoring secondary processes such as erosion and deposition of sediment, the fundamental physical processes are inscribed within the Navier-Stokes equations. The Navier-Stokes equations are three-dimensional non-linear partial differential equations describing the motion of viscous fluids. However, due to the computational complexity of solving the Navier-Stokes equations, it is often necessary to impose additional simplifying assumptions. In order to circumvent computational complexities induced by turbulence, the Navier-Stokes equations are averaged in time to obtain the Reynolds-Averaged Navier-Stokes (RANS) equations. The RANS equations describe the properties of the mean flow and the effects of turbulent fluctuations about the mean flow are handled by a suitable turbulence model. Within the field of computational fluid dynamics (CFD), RANS models are commonly used for applications such as aerodynamics, combustion and heat transfer. For applications requiring more advanced turbulence models, direct numerical simulation (DNS) numerically solves the Navier-Stokes equations without any turbulence model, requiring the resolution of the entire range of spatio-temporal scales of turbulence to be resolved. Large eddy simulation (LES) provides a compromise between RANS and DNS by averaging only the smallest length scales. However, RANS, DNS and LES all remain too computationally demanding for applications on large spatial domains that are relevant to flood risk management.

Consequently, modern hydrodynamic flood models typically utilise the shallow water equations (SWEs), which describe the motion of an incompressible, inviscid and shallow fluid, derived from the Navier-Stokes equations under the key assumption of the existence of a small aspect ratio, in which the depth of the flow is negligible with respect to the horizontal scale of motion. Accordingly, the shallow water equations essentially reduce the three-dimensional incompressible system described by the Navier-Stokes equations, into a two-dimensional system that resembles the Euler equations for compressible flow [472]. This simplifies matters considerably, albeit imposing some important limitations [472, 455, 103, 124]:

- The pressure distribution is approximated as hydrostatic.
- The velocity field is independent of the vertical direction and hence horizontal velocities are assumed uniform across the fluid depth, vertical velocities are neglected and vertical accelerations are equal to zero.
- The bottom slope is assumed to be sufficiently small, such that the small-angle approximation is valid ($\sin\theta \approx \theta$, $\cos\theta \approx 1$, $\tan\theta \approx \theta$).
- The bottom stress is specified in a parameterised form, which typically requires uniform or steady flow assumptions to resolve.
- The effects of density stratification, induced by temperature or salinity gradients, is neglected.
- The effects of turbulence are not accounted for in the classical formulation.

The assumption of a small aspect ratio is not unduly limiting as many naturally occurring geophysical flows, including flood flows, are typified by shallow water dynamics.

Historically, further simplifications have been introduced to derive the simple-inertia formulation [44], the diffusive-wave formulation [107] and the kinematic-wave formulation [316] however, such formulations are inferior to the shallow water equations and inadequate for locally accurate hydrodynamic modelling of urban areas [92, 254]. Many modifications that increase the complexity of the shallow water equations have also been proposed within academic literature, to satisfy the requirements of specific applications for which the classical shallow water assumptions are too restrictive (see for example [182, 159, 136, 77]). However, the classical shallow water system remains as the predominant basis for state-of-the-art urban hydrodynamic modelling applications owing to its balanced computational complexity relative to its capacity to adequately capture typical geophysical fluid dynamics.

Despite the relative simplicity of the SWEs, closed-form solutions remain intractable, except for specific simplified cases of limited real-world applicability, due to the highly non-linear character of the equations. Consequently, flood models employ numerical schemes which provide numerical approximations of the exact solution to the system of partial differential equations. For hyperbolic systems of conservation laws, including the SWE, finite volume methods (FVMs) are currently ubiquitous within state-of-the-art high resolution urban hydrodynamic models due to the inherent conservation properties of the method, the ability to approximate discontinuous solutions, the compactness of the numerical stencil, the flexibility to use either structured or unstructured grids and the simplicity of implementation [69]. The fundamental reliance of the FVM on the integral form of the conservation laws and consequently the ability to capture discontinuous solutions is a key feature of modern high resolution shock-capturing schemes, since unsteady urban flood flows are characterised by shock waves and transitions between subcritical and supercritical flow regimes.

The FVM discretises the spatial domain into disjoint control volumes, referred to as cells, within which the conserved variables are typically represented in a piecewise constant manner. For Godunov-type schemes, the approximate solution of a Riemann problem, via an approximate Riemann solver, at each cell interface is required to compute the numerical fluxes and update the conserved variables within the cell at each timestep. A vast library of literature is dedicated to the numerical solution of the Riemann problem, which has widespread applications in the numerical modelling of physical phenomena, and there are many established approximate Riemann solvers such as the Roe solver [381], Harten-Lax-van Leer (HLL) solver [212], Harten-Lax-van Leer-Contact (HLLC) solver [435] and Osher-Solomon solver [151, 346] to name but a few.

A key concept for FVMs applied to systems of hyperbolic conservation laws is that of the *weak solution*. The differential form of the conservation law is invalid in the classical sense for solutions containing shocks and as consequence, the integral or *weak* form of the equations, which are valid for discontinuous regions of flow, are used. A *weak solution* is therefore a solution which satisfies the integral form of the conservation laws. However, *weak solutions* are not necessarily unique and it is necessary to impose additional conditions to ensure that the scheme converges to a unique and physically correct *weak solution*. The additional conditions are referred to as entropy conditions. Crucially, the Lax-Wendroff theorem [259] proves that for a conservative FVM based on the integral conservation law, if the numerical approximation converges to a solution as the grid is refined and the timestep is shortened, then the solution will correspond to a weak solution of the conservation law. Provided the non-linear stability of a scheme can be guaranteed,

such that the scheme does in fact converge to a solution, and that the supplied entropy conditions are satisfied and physically congruent, it can therefore be expected that the numerical scheme will provide an approximation which is physically relevant.

Significant advances in hydrodynamic modelling have been achieved and, in conjunction with advances in high-performance computing (HPC) techniques [92], shallow water models are now able to handle millions of cells, enabling the modelling of flood flows for spatial domains as large as Greater London, at a spatial resolution of $1m$ [231]. The accuracy of hydrodynamic models utilising the two-dimensional SWEs has been established through experimental and analytical validation (see for example [179, 144, 45]). However, due to data-scarcity, validation using field data has primarily been restricted to the validation of flood inundation extents [111]. Experimental validation procedures are typically best suited for ascertaining the suitability and limitations of the governing equations with respect to a specific physical phenomena, whereas field data can be used to evaluate model uncertainty, overall model performance and limitations with regards to real world applications [92].

Within the commerical sectors of the United Kingdom and the United States of America, there exist several industry standard flood models such as ISIS TUFLOW, Flood Modeller Pro, InfoWorks ICM, HEC-RAS, MIKE FLOOD, SWMM and FLO-2D. Despite state-of-the-art research focussing on the development of finite volume schemes to solve the classical shallow water equations, of the referenced models only ISIS TUFLOW, InfoWorks ICM and MIKE FLOOD incorporate such features. Hence, finite difference schemes and simplified models maintain relevance within contemporary industry practice. This is further supported by the recent commercial success of LISFLOOD-FP, which includes several simplified numerical schemes.

It is not uncommon for there to be a gap between academia and industry [388] and for the specific case of flood modelling there are a number of contributing factors including but not limited to:

- The closed-source nature of most commercial software packages coupled with the significant investment required to develop, validate and establish new models.
- The desire for user-friendly graphical user interfaces and the training costs associated with adopting new software.
- Institutional inertia driven by accumulated skill, familiarity and trust in current practices.

It is also important to note the differing aims and incentives which drive industry and academia [8].

Although the adoption of modern numerical methods within the commercial sector has proven slow, the implementation of HPC techniques such as graphics processing unit parallelisation has been more widespread [445, 169, 233, 338]. This is perhaps a consequence of the scarcity of model validation: in lieu of validation data, the limitations of finite difference or schemes utilising simplified equations with respect to finite volume schemes solving the classical shallow water equations are not readily apparent. Whereas the same model running faster is readily apparent with obvious and direct consequences on profitability. Hence, it is imperative for those responsible for furthering the field of urban hydrodynamic modelling to better demonstrate and communicate the limitations of

existing methods to encourage the adoption of modern methods where appropriate.

1.2 Aim and Objectives

It is within the outlined context of contemporary hydrodynamic modelling practice and high resolution, Godunov-type, shock-capturing finite-volume schemes for the solution of the two-dimensional shallow water equations, that this project seeks to study and advance the modelling of partial barriers to flow. Hydraulic structures such as bridges, gates and weirs, alongside a myriad of urban features such as building façades, street furniture and parked vehicles, act as partial barriers to flow, however, a unified approach to modelling such features does not exist, with industry standard models using coarse approximations, empirically based methods or even omitting such features entirely [234, 54, 444, 81, 109, 308, 309]. There is a clear requirement for progress in this regard and therefore the overarching aim of the project can be summarised as:

Aim: *To contribute to advances in contemporary hydrodynamic modelling via the development of improved methods for modelling linear features such as bridges, gates and weirs within two-dimensional flood models.*

This is to be achieved via the following objectives:

Objective 1: To develop and experimentally validate a novel approximate Riemann solver (Solver 1) capable of resolving numerical fluxes across a linear fixed immiscible partial barrier to flow, with a focus upon ease of implementation and compatibility with existing flood models to promote uptake in practice.

Objective 2: To develop and experimentally validate an improved approximate Riemann solver (Solver 2) capable of resolving numerical fluxes across a linear fixed immiscible partial barrier to flow, with a focus upon maximising accuracy.

Objective 3: To develop and experimentally validate the capability to model the transport of well-mixed dissolved scalar quantities through linear fixed immiscible partial barriers to flow for Solver 2.

1.3 Thesis Outline and Research Contributions

Chapter 2 is dedicated to a systematic and comprehensive review of the relevant literature. Firstly, the importance of modelling obstacles within hydrodynamic models is outlined, providing important context and motivation for the proposed research. Next, existing methods for modelling obstacles are explored and the requirement for improved methods for modelling linear features which act as partial barriers to flow is demonstrated. The potential avenues for improvement upon the published methods for the numerical treatment of such features, based on their respective limitations, is thoroughly discussed. This is then followed by a demonstration of the importance of the capability to model the transport of water-soluble pollutants, especially within an urban context. A general review of advances in modelling of the advection and diffusion of well-mixed dissolved solutes is subsequently provided, since the combination of solute transport and shallow water interactions with partial barriers to flow is seldom explored within academic literature relating to hydrodynamic flood modelling. A review of validation practices for hydrodynamic modelling, with a particular focus upon methodologies for experimental

validation of the advection and diffusion of a dissolved solute is also provided. The chapter is finally concluded with a cross-referencing of the identified research gaps with the aim and objectives of the project.

Chapter 3 addresses Objective 1, outlining the development and experimental validation of a simple approximate Riemann solver designed for modelling partial barriers to flow. The presented numerical method represents structures as existing at the interface between neighbouring cells and uses a combination of internal boundary conditions and a different form of the conservation laws in the adjacent cells to resolve numerical fluxes across the interface. Through the use of the two-layer shallow water equations, a vertical discretisation of the numerical flux is obtained to enable modelling of the barrier at the interface. A key aspect is the use of simple assumptions to enable the restoration of depth dependence for the horizontal velocity component normal to the barrier. Validation is provided via experiments conducted within a state-of-the-art research flume, demonstrating the suitability of the solver for modelling a range of flow conditions and barrier configurations. The presented solver provides a simple and easily implemented method for resolving numerical fluxes across any obstacle geometry of negligible width with respect to the scale of the computational cells.

Chapter 4 addresses Objective 2, outlining the subsequent development and experimental validation of a more sophisticated Riemann solver designed to address the primary accuracy limitations of Solver 1. Solver 2 also represents structures as existing at the interface between neighbouring cells and uses a combination of internal boundary conditions and a different form of the conservation laws in the adjacent cells to model obstacles that may act as a partial barrier to flow. Whereas Solver 1 essentially modifies the numerical flux across the interface at which the structure is modelled in accordance with the modified conservation laws, Solver 2 introduces a permanent vertical discretisation of the neighbouring cells. As such, the vertical variation in the velocity profile is more accurately captured, resulting in a more accurate prediction of the flow variables. The permanent vertical discretisation of the neighbouring cells is facilitated through the use of a special form of the multi-layer shallow water equations. Due to the significant numerical challenges posed by conditional hyperbolicity, the presence of non-conservative product terms and the need for the layers to retain alignment with the barrier modelled at the interface, novel numerical approaches are explored. The accuracy of the improved solver is demonstrated via comparisons between the two solvers and the previously established experimental validation dataset.

Chapter 5 details the addition of the capability to model the transport of well-mixed dissolved solutes through partial barriers to flow for Solver 2, addressing Objective 3. This is achieved via the coupling of the shallow water system with the advection-diffusion equations. An extensive and complex experimental validation procedure is detailed involving the conduction of planar concentration analyses (PCAs), in which the scattering and absorption of incident light by an injected dissolved fluorescent tracer mass enables the nonintrusive determination of the fieldwise concentration for the duration of the experiment. Within the relevant literature, the experimental validation of numerical advection-diffusion models is exceedingly rare due to the challenging nature of the required experiments, with the collected validation data providing a unique experimental insight into the relevant physical phenomena. Next, analytical validation of a simple two-dimensional scheme is provided to demonstrate the validity of the wider scheme and the necessity for special numerical treatment of numerical diffusion for first-order upwind schemes. Fi-

nally, preliminary results are compared with the validation data collected from the PCA, demonstrating encouraging results, signalling the requirement for further work.

Chapter 6 concludes the thesis with a brief summary of the main results, which are cross-referenced against the corresponding relevant objectives, followed by a discussion of future research and recommendations.

1.4 Publications

Chapters $3-5$ are written in the format of academic publications. The current status of the publications is as follows:

Chapter 3 has been published as: James Mckenna, Vassilis Glenis, Chris Kilsby, A new Riemann Solver for Modelling Bridges in Flood Flows - Development and Experimental Validation, Applied Mathematics and Computation, Volume 447, 2023, 127870, 10.1016/j.amc.2023.127870.

Chapter 4 is available as a preprint and has been accepted for publication in Computer Methods in Applied Mechanics and Engineering: James Mckenna, Vassilis Glenis, Chris Kilsby, A Local Multi-Layer Approach to Modelling Interactions between Shallow Water Flows and Obstructions, arXiv:2304.10262 [physics.flu-dyn], 10.48550/arXiv.2304.10262.

Chapter 5 is to be submitted for publication, pending successful publication of Chapter 4 and the completion of significant further work to address current limitations.

Chapter 2

Literature Review

2.1 Urban Hydrodynamic Flood Modelling and Flow Obstacles

2.1.1 The Effect of Obstacles on Flood Flows

Urban areas are littered with obstacles to flow at a range of scales, which can significantly influence the local flow characteristics. Obstacles which induce a constriction of the flow produce a backwater effect, where the backwater depth is defined as the maximum increase in upstream depth produced by the flow contraction with respect to the normal water surface profile in absence of a flow contraction. The backwater effect, also referred to as afflux, is of importance to flood modelling and flood risk management since the increase in upstream water depth may be sufficient to induce flooding. For hydraulic engineers, the estimation of afflux is an important tool to ensure minimisation of flood risk in the design of hydraulic structures. In fact, many design codes require bridges to have a low chord elevation which exceeds the maximum water level by a minimum freeboard for a specified design flood [241, 34, 442, 158, 220].

The localised nature of the effect of obstructions has been demonstrated by Cook and Merwade [105], who compared one-dimensional steady-state simulations for two rivers with and without bridges and culverts. They noted that omitting bridges and culverts did not have a relevant impact on the overall inundation extent. However, this does not diminish the importance of modelling such features, as inundation extent is but a single metric by which flood risk can be determined and by omitting such features, the localised flood risk may be significantly misrepresented. This is supported by Ali [16], who identified that the inclusion of hydraulic structures within a hydrodynamic model has an effect on the flood hazard categorisation. Further evidence for the importance of the hydrodynamic modelling of hydraulic structures for the purpose of analysing flood risk is provided by:

- McEnroe [300], who provides guidance for the use of two-dimensional hydrodynamic modelling in the assessment of the downstream impacts of the replacement of a culvert or bridge with a larger hydraulic structure.
- Trueheart et al. [443], who used two-dimensional hydrodynamic modelling to analyse the interdependence of hydraulic structures along a river corridor under tran-

sient flood conditions. Their conclusions identified the value of transient modelling in particular, as synthetic flood simulations may be biased towards capturing the farthest-reaching impacts at the expense of substantial localised impacts.

- Mateo-Lázaro et al. [298], who present a methodology for the evaluation of the potential impact of proposed hydraulic structures through the use of two-dimensional hydrodynamic modelling.
- Wang et al. [479], who demonstrated the potential for backwater induced flooding produced by bridge piers via a case study on the Jialing river in China.
- Hailemariam et al. [208], who analysed the influence of minor hydraulic structures using a combination of one- and two-dimensional flood models, concluding that the effect of the structures on peak flood inundation was limited however, significant differences were observed during the drainage phase of the flood.
- Pappenberger et al. [354], who employed the Generalized Likelihood Uncertainty Estimation (GLUE) to perform a comprehensive analysis of the sensitivity of flood mapping to uncertainties surrounding boundary conditions and the representation of bridges within the model. The findings underscore the localised influence of bridge implementation, emphasising that the magnitude of the upstream and downstream impact was dependent on the choice of method for modelling bridges.
- Costabile et al. [109], who analysed backwater effects for a fluvial case study, with and without the inclusion of bridges within the model. Their conclusions highlighted the importance of two-dimensional modelling, despite the supposed suitability of the case study for one-dimensional modelling, due to the significant two-dimensional nature of the resulting flows.
- Brandimarte and Woldeyes [75], who argue for a transition from traditional deterministic approaches for the hydraulic modelling of backwater effects, to better account for modelling uncertainties. A practical approach to doing so is illustrated via the exploration of a fluvial case study.

There is also an emerging acknowledgement of the requirement to account for the interactions between floating debris and fixed obstacles to flow. Macchione et al. [285], reconstructed hydraulic data from the historic flooding of Crotone in 1996, for which the obstruction and subsequent clearing of bridges proved significant in determining the characteristics of the flood event. Martín-Vide et al. [296], similarly reconstructed a 2019 flash flood that occurred in Catalonia which involved the blockage of multiple bridges. In this case, not only did the blockage of the bridges worsen the inundation extent but the sudden release of a woody jam at a narrow bridge resulted in a catastrophic surge of approximately $1090 m^3 s^{-1}$, directly resulting in two deaths. Fernández-Nóvoa et al. [160], also identified the debris blockage of a bridge bottleneck as playing a key role in the intensification of a historic flood which occurred in Portugal. Furthermore, eyewitness reports identified that the build-up of debris under bridges exacerbated flood flows for an urban flood event which occurred in Carlisle in 2005 [337, 104].

This evidence further underscores the requirement for transient flood modelling, in order to accurately ascertain flood risk, as well as demonstrating the need to not only model obstacles to flow but also the interactions with debris and the effect of varying degrees of clogging or blockage. This requirement has been identified within academic literature by

authors such as Mazzorana et al. [299], who propose a combined stochastic-deterministic approach to modelling flood hazards via the coupling of deterministic hydrodynamic modelling with a stochastic or quasi-deterministic modelling of processes such as clogging by large wood and Gschnitzer et al. [188] who propose structural modifications to bridges to reduce the likelihood of large wood entrapment, with corresponding recommendations for the inclusion of clogging scenarios in hydrodynamic models.

There is therefore a clear requirement for the use of hydrodynamic modelling in the assessment of flood risk relating to hydraulic structures which obstruct flow. This encompasses the design of new infrastructure, the modification of existing infrastructure as well as its removal. In accordance with the shift towards a more holistic flood risk management approach, the concept of river restoration and rewilding of ecosystems has grown in popularity since Gore's seminal text on *The Restoration of Rivers and Streams: Theories and Experiences* [185]. This has been reinforced by policy implementation such as the European Union's Water Framework Directive [431], which marked a clear shift towards a more ecological perspective to river restoration [344] and more recently the United Nations declaration of $2021 - 2030$ as the decade for the restoration of ecosystems [447]. Such projects, of which there are many [100, 413, 65, 421, 484, 467, 336, 407], may be facilitated by the use of hydrodynamic modelling to assess the impact of the removal of man-made fluvial interventions. Similarly, there is a demand for improved modelling techniques to assess the effectiveness of novel small-scale interventions which mimic or complement natural processes such as leaky barriers [263, 262].

Hydraulic structures, namely bridges, have been the primary focus so far, however, houses, buildings and streets, which are perhaps the most predominant obstacles to flow associated with urbanisations, have yet to be discussed. Early investigations into the interactions between buildings and flood flows in relation to hydrodynamic modelling were instigated via the European Union Investigation of Extreme Flood Processes and Uncertainty (EU IMPACT) project including the *Dam-break Flow Experiment: The Isolated Building Test Case* [414, 416], which experimentally investigated a single impervious block subjected to a dam-break flow and the *Model City Flooding Experiment* [15], which used a reduced scale ($1 : 100$) concrete model of the Toce river valley, fitted with a number of concrete blocks to represent buildings. Within the same time period Ishigaki et al. [236], experimentally investigated the propagation of flood flows through urban streets via a $1 : 100$ scale model of Kyoto, which uniquely also included a subsurface network. Soares-Frazão and Zech followed up on the *Dam-break Flow Experiment: The Isolated Building Test Case* with the *Dam-break Flow through an Idealised City* experiment [415], which repeated the previous experiment for a 5×5 layout of impervious blocks.

In isolation, the blocks representing buildings, were demonstrated to significantly influence the flow with the extreme nature of the incident dam-break flows amplifying their effect during the initial phases of the experiment. Observations of the flow demonstrated the presence of a strong initial reflection of the incident flood wave, followed by a separation of the flow and the formation of a series of intersecting shock waves producing re-circulation and wake zones [170]. When multiple blocks are arranged in configurations that are more representative of urban districts, the complexity of the resulting flow intensifies with the model streets conveying flows which are characterised by a complex interaction of wave reflections, re-circulation zones, wake zones and hydraulic jumps [430, 415]. The routing of the flow by the streets within the idealised city block was clearly demonstrated through comparisons between the results for the flow aligned city block and rotated city

block scenarios. Of particular interest, due to the great deal of complexity inherent to the resultant flows, is the effect of crossroad and junction configurations for a variety of flow regimes. These have been experimentally, theoretically and numerically explored by numerous authors; see for example [200, 201, 225, 428, 481, 205, 369, 226, 258, 367, 370, 51, 235, 71, 380, 62, 482, 375, 245, 227] for three branch flows and [335, 313, 312, 379, 314, 168] for four branch flows. In straight streets, flows are typically much simpler, presenting one-dimensional flow characteristics with mean velocities parallel to the building façades [315].

Urban structures have remained the subject of intensive experimental investigations over the last two decades, with Mignot et al. [310], providing a comprehensive review of 45 laboratory experiments relating to: flow through a single street intersection, subsurface-surface flow exchanges, obstacle arrays and quasi-realistic urban districts. More recently, Mignot and collaborators have spearheaded investigations into the effect of small-scale topography and flow exchanges through openings in building façades. Bazin et al. [46] first investigated flows representative of typical floods in dense urban areas through a model of a three branch junction. Using a shallow water model, equipped with a constant eddy viscosity to account for turbulent stresses, the Authors were able to investigate the impact of obstacles and sidewalks typically found in urban areas. Their study demonstrated that obstacles located in the downstream branch of a junction can significantly impact the velocity distribution downstream of the junction, concluding that detailed topography and street furniture should be modelled for situations in which local velocities are of importance.

This research was followed by Mignot et al. [315] who aimed at investigating the error induced by neglecting street furniture such as bus stops, trees and parked cars. Through an investigation of 14 different flows and a range of permutations of 9 obstacles arranged in the crossroad, it was determined that the induced errors were as large as 15% for high Froude numbers. The introduction of the obstacles resulted in complex flow structures such as wakes, re-circulation zones and secondary flows with some obstacles producing notable backwater effects. In Paquier et al. [355], this research was applied to a study of the 1988 flood event at Nîmes, with sewer network flow exchanges and the impact of small-scale obstacles identified as sources of uncertainty requiring sensitivity analyses. This is especially the case where flow transitions occur within a crossroad as it can result in errors as large as 20%. In Bazin et al. [45] strategies for representing the effect of urban obstacles are proposed and comparisons with laboratory data indicated that two-dimensional models, utilising a constant eddy viscosity, are suitable for capturing such flows, provided depths are neither too shallow nor supercritical.

In Liu et al. [278], a physical model was used to perform a detailed analysis of the interactions between flood flows and houses. Of particular interest were comparisons between the flows observed for houses with a locked or unlocked door, which demonstrated the importance of considering buildings as porous, as opposed to perfectly impervious obstacles. Mignot et al. [308] produced further experiments investigating the intrusion of flood flows into buildings. A total of 26 building opening configurations were tested producing 220 flow cases. Investigations showed that, although flow patterns were quite similar to flow over a lateral rectangular weir, empirical equations had mixed success in describing the flow, producing errors in the range of $\pm 100\%$ in some instances. The authors concluded with recommendations that the largest objects, such as bus stops and parked cars, be somehow represented within numerical models due to their influence on

intruding flows, which resulted in $50 - 80\%$ differences in intrusion discharge for high Froude numbers.

Further investigations of the impact of considering urban blocks as porous were performed by Mejia-Morales et al. [304], who determined that flow properties may vary by as much as $12 - 70\%$ in the streets surrounding a porous building block compared with an impervious building block. More recently, Dewals et al. [138] have investigated the suitability of the two-dimensional shallow water equations for modelling flow intrusion into buildings during urban floods. Their work concluded that, despite strong three-dimensional flow characteristics, the two-dimensional shallow water equations provide a sufficient simplified description of the flow interactions.

It is therefore clear that the modelling of urban obstacles is a critical aspect of urban hydrodynamic modelling. However, recent research has called into question traditional modelling practices, which treat buildings as impervious and omit small-scale urban obstacles such as parked vehicles and street furniture. As a result, there is a demand for novel numerical techniques capable of capturing the complex flow dynamics. The successful validation of hydrodynamic models which treat buildings as impervious [501, 230], suggests that flow interactions with structures are predominantly representative of interactions with impervious blocks and that small-scale obstacles primarily produce localised effects. However, although models have been successfully validated against flood inundation extent, model agreement is far from 100% and as a result there is still much progress to be made, with the modelling of flow intrusions and urban furniture providing experimentally backed avenues for future progress. Furthermore, although macro-scale inundation extent is relatively unaffected, the accurate modelling of the effect on the local flow properties is of clear importance for high resolution applications concerning property scale vulnerability and hazard analysis.

Overall, although the scale of a bridge compared to a parked vehicle or a sluice gate compared to a opening in a building façade or a weir compared to a damaged window are clearly very different, there are clear commonalities in the induced localised flow characteristics and a subsequent demand for the capability to model the effect of obstacles to flow at a range of scales within hydrodynamic models.

2.1.2 The Impact of Flood Flows on Obstacles

The effect of obstacles to flow on flood flows and the consequent estimation of flood risk has been extensively covered, however, it is equally, if not more, important to consider the impact of flood flows on the obstacles themselves. This is of course intrinsically linked to the accurate prediction of the associated flow interactions, since knowledge of the flow variables is prerequisite to the derivation of the relevant impacts.

For buildings, exposure is typically estimated via stochastic extrapolations of damages based upon the flow properties in the immediate vicinity of the building [61, 232, 501]. It is therefore crucial that the flow interactions with the structure are accurately captured in order to perform effective exposure analyses. This also highlights the importance of more detailed representations of urban obstacles; as noted by Mignot et al. [304] the large differences in the observed internal and external flow depths for porous building blocks calls into question the typical assumptions used in exposure analyses to estimate flood damages. For people, flood hazard categorisation defined by human body stability criteria

is highly dependent on the accurate determination of the local flow characteristics [277, 240, 5, 486].

Understanding the impact of flooding on hydraulic structures, particularly bridges, has a range of important applications. First and foremost is the hazard of flood induced collapse, which is the subject of intensive research [279, 246, 187, 187, 21, 20, 319, 244, 280, 350, 392] due to the devastating consequences. Indirect flood impacts are much harder to analyse but can cause cascading failures due to the interdependent nature of critical infrastructure such as transport networks [24], of which road and rail bridges are integral components. The collapse of critical urban infrastructure, or less severely a simple loss of function, can also be related to the stability of urban obstacles via compound risk analyses and multi-hazard assessments [318]. Consider for example, previous discussions pertaining to wood debris and the stability of urban obstacles such as parked vehicles [297], which can contribute to compound risks and inter-dependent hazards. In this regard, there is a clear feedback loop between the effects of obstacles on flow and the impact of the flow on the obstacles themselves.

Via integrations with modern technologies such as Building Information Modelling (BIM) [252, 410], there are opportunities to enhance the maintenance and management of structures exposed to flooding risk. Through the development of cutting-edge digital visualisation tools such as digital twins, this can be achieved at a city-scale, with integrated hydrodynamic modelling providing the basis for enhanced visualisation and analysis of urban flooding impacts [41]. Novel visualisation techniques, such as the work of Costabile et al. [113], of this kind are already emerging within academic literature due to the acknowledgement of the limitations of traditional risk communication via flood maps [382, 173, 307, 342, 422, 217]. There are also opportunities to couple agent based modelling and hydrodynamic modelling to develop more robust disaster response planning [128]. Within all these important and much needed applications is the requirement to accurately model flow interactions with obstacles within the hydrodynamic modelling component.

At the network level, Pregnolato et al. [362] recently proposed an interdisciplinary framework for the integrated analysis of bridges. Within the proposed framework, hydrodynamic modelling plays a crucial role by providing initial flood intensity measures used to inform subsequent analyses. The primary novelty of the framework is the combination of hydrodynamic flood modelling, computational fluid dynamics (CFD) analysis and finite element structural analysis with a network analysis of bridges subject to flooding. Such analyses are crucial for the development of climate resilient infrastructure [2]. However, advances in the availability of high quality information on hydraulic structure assets is required, with Pregnolato [361] calling for the development of a national bridge inventory for the UK.

In light of the presented evidence it is unequivocally clear that the modelling of obstacles within urban environments is a crucial capability for modern flood models. Due to the interdependencies between the effects of the obstacles on the flow and the derived impacts upon the obstacles themselves, the accurate modelling of the complex flow interactions is of paramount importance. Having established the importance of modelling such features, it is important to explore the state-of-the-art methods for the numerical treatment of obstacles in order to establish avenues for the advancement of contemporary hydrodynamic modelling practice.

2.2 Modelling Obstacles to Flow

2.2.1 Complexity Limitations and Modelling Requirements

Urban hydrodynamic modelling is notorious for requiring intensive computational processing, especially for high resolution applications at city-scale and beyond. The development and deployment of appropriate flood modelling software must therefore be cognisant of the required scale, resolution, duration and computational complexity of the simulation in relation to the available processing capabilities for the desired application. Maximal capabilities of modern software in this regard have been boosted by advances in HPC, with modern software architectures taking advantage of the parallelisation capabilities of central processing units (CPUs) and graphics processing units (GPUs) via parallel computing platforms like Nvidia's CUDA [92]. This is complemented by the increased availability of vast computational resources through cloud computing platforms such as Microsoft Azure, Amazon Web Services and Google Cloud Platform, which provide cost-effective alternatives to the ownership of high-end computational resources for sporadic or high priority applications [180]. In accordance with the famous aphorism of George Box [73, 72] that '*all models are wrong, but some models are useful*', it is important to consider the appropriate role of one-, two- and three-dimensional modelling within the established paradigm of contemporary flood modelling practice.

In this regard it is clear that three-dimensional CFD analysis is the most appropriate tool for ensuring a *comprehensive* analysis of the complex interactions between flood flows and obstacles. This is exemplified by the presence of three-dimensional flow features for junctions [368, 315, 339, 1, 282] and flows intruding into buildings [138, 278, 304], for which one- or two-dimensional models can only hope to capture adequate simplifications of the resultant flow dynamics [45, 138, 282]. For the modelling of flow interactions with bridges, Munoz and Constantinescu [327] argue, on the basis of comparisons between two-dimensional hydrostatic and three-dimensional non-hydrostatic modelling outputs, that the accurate prediction of the flow hydrodynamics, effects on bed shear stresses and sediment entrainment is only possible for three-dimensional non-hydrostatic codes. Therefore, as proposed in the framework of Pregnolato et al. [362], it is evident that the primary role of three-dimensional CFD analysis, is to enable the detailed analysis of individual or small groups of structures. This is primarily due to the inherent computational complexity of three-dimensional codes, which restricts analyses to smaller scale applications. This is slowly changing due to the aforementioned advances in computing power and the development of particle-based approaches [292] however, three-dimensional flood models incorporating realistic topographies are currently exceedingly rare [429].

For conventional two-dimensional shallow water based hydrodynamic models, the aforementioned advances in HPC have enabled the most sophisticated and efficient numerical models to handle domains containing cells of the order $10^6 - 10^7$ for realistic applications [309, 450, 231]. It is well established within academic literature, that the spatial resolution for urban applications should be reflective of the characteristic length scale of the urban structures to adequately capture urban flow paths and localised flow phenomena [231, 294, 166, 489, 401, 295, 174, 153, 450, 480, 191]. As such, the current primary role of two-dimensional shallow water models is to provide analyses of localised flood hazards and exposure for spatial domains of city or catchment scale. This can be upscaled to national or continental scale analyses, provided adequate topographic information is available [191].

For applications which are only concerned with modelling inundation extent, due to the established localised nature of the effect induced by obstacles to flow, a high degree of spatial accuracy is of lesser importance. In fact, Savage et al. [400] argue that for flood inundation extent predictions, model performance degrades at resolutions coarser than $50m$ and that it is more important to account for uncertainty through probabilistic analyses, than it is to refine the spatial resolution. In this regard, simplified formulations such as the simple-inertia formulation [44], the diffusive-wave formulation [107] and the kinematic-wave formulation [316] may be beneficial, provided the simplifying assumptions are sufficiently satisfied. From this perspective, one may argue that due to the unavoidable aleatory and epistemic uncertainties, two-dimensional shallow water analyses of localised flood hazards are currently inappropriate, as the computational demands obviate statistical approaches, which require repeated simulations. Opinion on this matter will be related to whether one ascribes to the Keynesian philosophy that '*it is better to be roughly right than precisely wrong*'. However, it is evident that two-dimensional shallow water models are the best deterministic tool currently available for investigating spatio-temporally varying property level exposure and flooding hazards and that anthropogenic climate change demands immediate action. Furthermore, it can be argued that the degree to which simplified models, suitable for probabilistic modelling, are '*roughly right*' is simply inadequate for the detailed hazard and exposure analysis. This is supported by Costabile et al. [111] who concluded, following comprehensive analysis of three two-dimensional models of varying complexity, that '*fully-dynamic modeling should be the unavoidable reference tool when the goal of urban flood mapping activity is not limited to the evaluation of the flood-prone areas extent but also involves the local estimation of flood hazard/vulnerability*'.

One-dimensional overland flow modelling has remained popular despite the emergence of two-dimensional shallow water schemes, due to the reduced computational burden and lower data requirements [110], especially within industry practice where there is vast institutional knowledge and experience. In comparison with two-dimensional approaches, the primary limitation for one-dimensional approaches is the inability to capture transverse variations in the flow regime. This is particularly problematic for applications such as modelling compound channels [108] and steep mountain rivers [360]. Although it is possible for one-dimensional models to produce flood inundation extents which are comparable with two-dimensional models, there is a much higher skill involved and two-dimensional modelling may be required as a reference [112, 110]. Due to the inherent challenges of capturing overbank flows, 1D-2D schemes have been developed in which overland flows are modelled by a two-dimensional scheme which is coupled with a one-dimensional scheme describing a supposedly one-dimensional component of the domain, such as a river. However, even for scenarios in which prevailing wisdom would suggest one-dimensional approaches are suitable, there may be significant challenges due to the emergence of two-dimensional flow characteristics [109] or skew features such as bridges [112]. This is a stark contrast to two-dimensional schemes, where these features are almost seamlessly integrated. Therefore, the role of one-dimensional overland flow modelling is somewhat restricted to scenarios in which the application is relatively simple, there is an extreme data scarcity, computational efficiency is of paramount importance or where modellers have developed sufficient skill. For subsurface sewer drainage networks, one-dimensional models remain the state-of-the-art for dual drainage models [143, 198, 309, 383].

One must be careful not to fall foul of the fallacy that the most complex model is always the most appropriate, however, it is clear that there are minimum complexity requirements corresponding to the ability to capture *key* behaviours. Three-dimensional models are able to capture detailed three-dimensional processes which may be important for detailed analyses of individual structures such as buildings or bridges. Two-dimensional models are unable to capture three-dimensional processes but are able to dynamically model shallow water flows with adequate accuracy, enabling detailed property level exposure and hazard analyses for realistic urban topographies. Although fully dynamic two-dimensional models are able to accurately model inundation extents, reduced complexity two-dimensional models, where the assumptions are sufficiently satisfied, or one-dimensional models offer advantages in terms of computational efficiency which enables probabilistic approaches or even real-time forecasting.

Considering the project aim is to:

> **Aim:** *To contribute to advances in contemporary hydrodynamic modelling via the development of improved methods for modelling linear features such as bridges, gates and weirs within two-dimensional flood models.*

and the role of two-dimensional flood models has been identified as providing analyses of flood inundation extent, local flood hazards and local flood vulnerability, it is important to assess existing methods for the numerical treatment of obstacles to flow within this context. Specifically, a fit for purpose numerical treatment of obstacles to flow should not only capture steady-state flow properties but also the transient variations in the local flow characteristics.

2.2.2 Mesh Methods

The simplest and most straightforward methods for implementing obstacles to flow within numerical schemes include the object within the properties of the mesh used to discretise the spatial domain. As a consequence they are referred to here as *mesh methods*, since they act at the scale of the mesh. As part of the aforementioned EU IMPACT project, work package three called upon the research community to submit '*blind*' and '*aware*' numerical modelling runs for the two experimental benchmarks (the isolated building test case and the idealised city test case) [325]. Since the two test cases idealise structures as solid blocks, the focus was therefore on suitable methods for modelling the propagation of flood waves and their interaction with impervious obstacles. It is also important to note that negligible overtopping of the impervious obstacle occurred during the experiments. Furthermore, the assumptions for the shallow water equations are invalidated in the immediate vicinity of the obstacle however, the inability to capture detailed three-dimensional features such as saddle vortices is neither expected or required; the shallow water equations are expected to provide an adequate simplified approximation of the resulting flows.

Eight different modellers from six institutions submitted the results of their test runs for comparison, utilising the following techniques to represent the building:

- Local friction based representation.
- Finite bottom elevation.
- Solid walls.

Based on the comparisons of the submitted results with the validation data, it was concluded that representing the edges of the building with a solid wall boundary condition was the most faithful representation but that all three methods provided comparable accuracy [171, 12]. Despite the fact that the EU IMPACT project concluded two decades ago, there haven't been huge advances in the development of novel techniques for modelling fixed impervious obstacles to flow other than the further development of the sub-grid porosity method, initially proposed by Braschi and Gallatti [76], which is complementary to the local friction based representation. However, a number of subsequent comparative studies have been performed to further ascertain the advantages and disadvantages of each method [405, 424, 404, 412, 79, 230]. As such, discussion of the presented techniques maintains relevance.

Due to a lack of consistency in the nomenclature for the presented methods the most common alternative names for the respective methods are presented below for clarity:

- Local friction based representation: building resistance method, high roughness method.
- Finite bottom elevation: stubby building method, island method, building block method, raised elements.
- Vertical walls: mesh discretisation method, building hole method, mesh-hole method, Cartesian cut cell method, blocked out, hollow buildings.

Local Friction Based Representation

A local friction based representation parameterises the effect of an obstacle on the flow by increasing, locally, the resistance to flow. As highlighted by Vreugdenhil [472], the definition of bottom stress for the two-dimensional shallow water equations is problematic in comparison to the three-dimensional Navier-Stokes equations, since the specification of the bottom stress requires information on the three-dimensional flow structure. Since this is obviously unavailable for the two-dimensional form, the bottom stress is specified in a parameterised form and it is typically resolved in accordance with Manning's equation, where Manning's n is an empirically derived constant which incorporates the combined effect of all sources of resistance within the channel.

As noted by Yu and Lane [489], the resistance to flow is therefore accounted for as a sink in the momentum equations, which does not account for potential blockage effects. The effect of potential blockage effects are important to consider as they reduce the conveyance capacity, inducing contractions and expansions of the flow. This is demonstrated within a three-dimensional context by Lane et al. [256], who show that parameterisation of topographic resistance to flow via the upscaling of roughness heights does not adequately model mass blockage effects. Syme [424] acknowledges that an energy loss coefficient is more physically representative of the expected energy losses induced by contraction and expansion. Although this is also an imperfect solution, as the selection of an appropriate energy loss coefficient is just as fraught as the definition of an appropriate roughness coefficient. Furthermore, classical head loss models that are direct functions of the flow velocity do not admit self-similar solutions for piecewise constant initial boundary value problems and therefore cannot adequately capture the sub-grid losses [196]. As a consequence, local friction based models of topographic obstructions are an unphysical representation of the effect of an obstacle to flow since the entirety of the interaction is captured through a

parameterised resistance to flow.

Despite not providing an explicit physical description of the flow interactions, friction based representations have been shown to accurately capture the effect of urban obstacles on inundation extents in practice. Alcrudo and Mulet [14] reported overall predictions within 25% of observations for the idealised city test case, with Soares-Frazão et al. [170] reporting predictions within 15% of observations for the depth specifically. The predictions based on a local friction representation were seen to be comparative in accuracy to the other, more explicit, methods for modelling obstacles. Schubert and Sanders [404] demonstrated that a local friction representation of buildings enabled an accurate prediction of the flood extent, with localised velocities proving more difficult to predict. Baretta et al. [55], were able to satisfactorily reproduce a real flood event which occurred in Italy using a local friction representation for buildings, despite a lack of detailed information on the geometry of the buildings. Tang and Gallien [426], used USGS National Land Cover Classifications to assign roughness without calibration in the successful validation of inundation extent for an urban coastal flooding event. Similarly, Gallegos et al. [175] used a simple land cover classification to assign a Manning's n to each cell in the successful validation of inundation extent and streamflow predictions for an urban dam-break flood.

The primary value of a local friction based representation is the simplicity of the method: it is easy to implement, it is relatively computationally efficient and it is compatible with almost all solution methods and mesh geometries. In fact, the method is likely optimal and necessary for data scarce regions where detailed building geometry is unattainable [404, 55], as explicit representations are unfeasible in the absence of the required data. However, in such cases, only inundation extents can be reliably discerned. Although calibration of the roughness parameters is recommended, it is likely that this practice will be limited by time constraints and data availability. The Development of Rescue Actions Based on Dam-Break Flood Analysis (RESCDAM) project [286] provides a reference for a rigorous calibration process in which a scale model was constructed and the derived Manning's coefficients were scaled using the Froude model law to eliminate inconsistencies resulting from scaling effects. However, this is clearly impracticable in most cases.

As demonstrated by Teng and Gallien [426] and Gallegos et al. [175], the use of land cover classifications to assign spatially distributed roughness coefficients which are approximately representative can be effective in the absence of any calibration. However, as highlighted by Yu and Lane [489], the upscaling of n to account for topographic resistance to flow based on land cover classification assumes that:

1. Roughness relationships derived from flume experiments can be applied to a two-dimensional mapping of n based solely on land cover classification.
2. The classes are suitably homogeneous such that the primary control on n is the type of land cover and there is no need to calibrate roughness to account for the specific height, density or turbulence characteristics of the obstacle(s).
3. The value of n is determined by the topography and not the spatial discretisation.

As such, a sensitivity analysis or a probabilistic approach would be recommended to account for the significant uncertainty. Although, if the mesh is sufficiently coarse, then the sensitivity to n is expected to be significantly reduced [489]. Schubert and Sanders [404] also report a reduced sensitivity to n for a fine resolution model, which they speculate

is due to well defined preferential flow paths. Perhaps future advances in algorithms for automatic parameter calibration [177] may provide a convenient solution to this issue in the near future.

The primary challenge in implementing the method in practice can therefore be summarised as the selection of an appropriate roughness since there isn't an apparent physical basis upon which an a priori determination can be obtained. This is further complicated by the, usually parabolic, dependence of friction formulae upon the depth-averaged flow velocity which potentially results in inconsistent behaviour across a range of flows. The effect of increasing values of the friction coefficient are presented in Alcrudo [14] via comparisons between the numerical results and the gauge point measurements for the idealised city test case. Since the buildings were idealised by impervious blocks in this case, $n \geq 0.25$ was found to be consistent with observations for the tested flow rate. Values of $n > 0.5$ proved quasi-indistinguishable with significant oscillations in the numerical predictions of the depth induced by the physically unrealistic values of n. Similar tests were performed by Syme [424], who numerically investigated the effect of an increasing Manning's n on the flow characteristics in the vicinity of a single obstacle. At a value of $n = 0.05$ there was very little difference in the flow properties outside and inside the footprint of the obstacle. For values of $n \geq 1$, there was an almost total blockage of the flow within the footprint of the obstacle.

The ability to manipulate the value of the friction coefficient to enable a range of behaviours from negligible resistance, to complete obstruction, is potentially valuable, since it provides the necessary flexibility required to handle any potential obstacle. This is demonstrated by Neal et al. [337], who successfully calibrated n for a channel containing a debris blocked bridge. However, it is worth mentioning once again that in such cases only the macro-scale properties of the flow can be considered relevant and a local assessment of the flow characteristics is essentially meaningless. When considering buildings in particular, there is often much debate as to the extent to which flow intrudes into buildings and the subsequent storage effect that is induced [230, 424, 412, 79]. As demonstrated via aforementioned experimental work, localised intrusion of flows into buildings may play an important role in determining the local flow characteristics within urban areas. However, the mechanisms that enable the ingress of water within a building are poorly understood and highly uncertain, considering for example, ingress enabled by the destruction of windows or doors. The extent to which local friction based representations can accurately capture this behaviour in a detailed manner is unlikely, as the unphysical foundations of the method result in a significant averaging of the resultant flow characteristics. This is supported by the investigations of Schubert and Sanders [404] who acknowledged that the method was unable to capture building scale variability in the velocity field. However, the efficiency of the method, particularly on coarse grids, potentially facilitates probabilistic studies of the effect of flow intrusions into buildings on the overall inundation extent.

Numerically, the presence of very large friction coefficients can induce some instability however, common semi-implicit [49, 80, 95, 134, 274, 454] treatments or implicit treatments [14, 12, 488] of the bed friction source term should be sufficient to ensure stability. Explicit treatments [451] may experience numerical oscillations for high roughness coefficients and the presence of stiff resistance terms may result in an inefficient restriction of the timestep. It may also be necessary to implement a limiter to ensure that as the water depth approaches zero, which may be common in areas of very high friction, unphysical changes to the flow direction and negative flow depths are prevented. However, mod-

ern numerical schemes which are equipped to handle the numerical challenges of wet-dry interfaces will already be sufficient to handle these features [80].

Of note, and seldom discussed in the literature regarding the local friction representation, is the benefit of a well-balanced discretisation of the bed friction source term in regions where the friction source term is dominant. A suitable well-balanced discretisation of the bed friction term is presented by Cea and Vázquez-Cendón [94]. As discussed by the Authors, the requirement for a well-balanced treatment of the bed slope is widely acknowledged, since inadequate numerical discretisation of the bathymetry with respect to the discretisation of the convective flux results in an inability to preserve equilibrium states for variable bottom topographies. However, the requirement for a well-balanced treatment of the bed friction is rarely discussed, as it is only in the somewhat rare case in which the bed friction and the bed slope are leading terms in the momentum conservation equations, as opposed to the inertial and hydrostatic pressure forces, that the discretisation of the bed friction has a significant implication on the numerical result. In such cases, the proposed upwind discretisation of the friction source term provides superior accuracy and stability in comparison with a classical centred semi-implicit discretisation.

Overall the local friction based representation of obstacles to flow can be summarised as an effective but flawed method. It is most effective when implemented on coarser meshes for applications concerned only with the flood inundation extent. The implementation is incredibly simple and the method is computationally efficient although, these advantages are somewhat offset by the steep calibration requirements, especially without the use of semi-automatic or automatic processes for assigning roughness coefficients. Furthermore, local friction based representations are insufficient for resolving the detailed topological structure of the flow and are therefore unsuitable for high resolution hazard and vulnerability analyses.

Sub-grid Porosity

A class of shallow water equations referred to as the porous shallow water equations (PSWEs) have been derived and developed for modelling obstructed flows. The PSWEs use the concept of porosity to enable shallow water models to account for the sub-grid mass blockage effect induced by urban topography, directly addressing one of the primary limitations of the friction based approach. The concept was first presented within the context of urban hydrodynamic modelling in the seminal works of Braschi and Gallatti [76] and Defina [131, 130], with Hervouet et al. [218] presenting the first realistic application.

Porosity may be defined in volumetric terms as the fraction of a control volume occupied by voids, or alternatively, by considering a slice or plane through a porous media, with the fraction of the plane occupied by voids representing the areal porosity [47]. When the porosity concept is applied to an urban environment, the urban area is modelled as a porous media, within which the potential flow paths, defined by the space between urban obstacles, represent voids through which flood flows are conveyed and stored. As identified by Sanders et al. [396], the distinction between volumetric and areal porosity is promising since areal porosity is inherently anisotropic, which is an important feature considering the inhomogeneity of preferential flow paths within urban topographies.

Within the relevant literature the established PSWE formalisms are as follows:

- Single Porosity (SP) model.
- Integral Porosity (IP) model.
- Dual Integral Porosity (DIP) model.
- Binary Single Porosity (BSP) model.

The SP model was first proposed by Guinot and Soares-Frazão [197], utilising a differential form of the PSWEs and considering only the volumetric porosity. The IP model was independently and concurrently proposed by Sanders et al. [396], utilising an integral formulation and considering both volumetric and areal porosity. The DIP model, proposed by Guinot et al. [196], built upon the IP model by dividing the flow variables into domain variables and boundary variables and by developing improved momentum dissipation and drag models. Most recently, Varra et al. [459] proposed the BSP model which is derived from the SP model by constraining the porosity to the value of one in a void and zero inside an obstacle. A number of variations and alternative formulations have also been developed such as the depth-dependent IP model derived by Özgen et al. [353], a SP model derived by Velickovic [465], the multiple porosity model derived by Guinot [194] and a differential form of the IP model derived by Guinot and Delenne [195]. PSWEs have therefore been the subject of much research over the last two decades, with promising developments aplenty.

A key feature of the presented models is the choice between the differential and integral form of the equations and the corresponding assumption of the existence of a representative elementary volume (REV). An REV is essentially a volume within a porous medium where the properties governing flow can be assumed to be sufficiently uniform, enabling the application of continuum mechanics principles and the derivation of differential equations to describe flow behaviour at a macroscopic level [47]. A consequence of assuming the existence of an REV, which may not be guaranteed or even identifiable in a realistic urban area, is that it mandates an isotropic porosity and requires differentiability of the porosity and the flow variables.

Guinot [194] demonstrated via numerical experiments that an REV, which is approximately one or two orders of magnitude larger than the distance between buildings, can be defined for urban environments with periodic geometry. However, as pointed out by Varra et al. [459], urban environments are typically fractal, not of periodic geometry, so it is still unclear whether an REV can be defined for realistic urban configurations. Furthermore, real urban environments are filled with an assortment of small scale obstacles such as bus stops and parked cars, which are typically not considered when attempting to define an REV.

In the pursuit of anisotropic porosity whilst maintaining validity for transient flows, Sanders et al. [396] therefore chose to formulate the IP model using an integral formulation. Furthermore, Sanders et al. [396] identified that the differential SP model can be obtained from the integral IP model by assuming the existence of an REV, thus demonstrating that the SP model implicitly assumes the existence of a REV, explaining the isotropy of the model.

In Varra et al. [459], it is shown that the BSP model corresponds to a SWE model with an obstacle directly incorporated into the governing equations. The direct introduction of the obstacles within the BSP model is achieved via an internal free-slip (vertical wall)

boundary condition, which results in the generation of non-conservative products accounting for the interaction between the fluid and the solid boundaries. Since the formulation of the BSP model refrains from averaging any processes or variables, the assumption of a REV is crucially not required. Furthermore, it is shown that the integral formulation of the IP model corresponds to the integration in space of the SWE with free-slip boundary conditions and the integration in space of the BSP model. Hence, the IP model, BSP model and shallow water model equipped with free-slip wall boundary conditions are consistent and, most importantly, a differential form of the PSWEs is derived independent of the assumption of an REV. This demonstrates that in fact, all integral formulations of the equations cast as finite volume numerical schemes are equivalent to BSP finite volume schemes and as a result, the SP Riemann problem is the fundamental component upon which all porosity schemes should be built. The work of Varra et al. [459] therefore provided a crucial advance in the formalism of PSWE numerical schemes, providing an important theoretical basis to explain the unexpected performance of differential forms, despite prior consensus verdict that only integral formulations of the PSWEs were meaningful due to REV assumptions.

The initial SP model proposed by Guinot and Soares-Frazão [197] was simplistic and fully isotropic, accounting only for the storage effect of buildings without fully accounting for their effect on the flow paths. As a consequence, two momentum sinks are necessary to overcome the limitations of the model: a classical skin-friction term relating to the bed shear and a head loss term designed to replicate the effect of multiple wave reflections and changes in the flow regime through the porous media [197, 387]. Testing of the SP model was presented by Soares-Frazão et al. [387], which demonstrated the capacity of the model to reproduce the mean flow characteristics of the model city test case at a comparable level of accuracy to that of a refined classical shallow water model. The SP model therefore provides a significant computational advantage over refined classical shallow water models since a much coarser mesh can be utilised, however, this does come at the cost of a loss of local accuracy. In comparison to friction based approaches, the method provides similar accuracy without the need for calibration since the parameters can be explicitly derived from the geometrical properties of the urban area. However, it is important to note that the explicit calculation of the parameters was not presented and instead, a spatially uniform and isotropic porosity was assigned, which corresponded well to the idealised test case due to the artificial homogeneity of the urban layout.

Through analysis of the eigenstructure of the SP model, Lhomme [270] determined that the wave propagation speeds of the SP model are identical to the wave propagation speeds of the shallow water model. The SP model also inherits the favourable hyperbolicity and rotational invariance properties of the SWEs and the SP Riemann problem can conveniently be solved using standard approximate Riemann solvers for the SWEs [95]. Lhomme further identified the requirement for a division between the domain based porosity, to account for storage effects, and a boundary based connectivity porosity, to account for the conveyance effect, to improve the SP model but found no way to derive the connective porosity from the urban geometry.

With the introduction of the IP model, Sanders et al. [396] achieved this and overcame the primary limitations of the SP model by taking advantage of the anisotropy of areal porosity, defined at the boundary of a cell, to introduce a local description of the connectivity at each cell interface. This was importantly accompanied by deterministic methods for calculating the areal and volumetric porosity based on the underlying urban topog-

raphy. Specifically, the calculation of the porosity parameters is achieved by sampling the terrain data within the cell and along the interface to determine the ratio of samples which strike an obstacle. For realistic applications, this may require additional detailed surveying since smaller gaps between structures may not be correctly detected using aerial scanning techniques such as LIDAR [176]. Directionality is also introduced to the drag model via a frontal area term. However, this is somewhat problematic to calculate, as the frontal area is dependent on the flow direction which is not known a priori in realistic scenarios. Consequently, realistic applications may require an iterative solution procedure or alternatively, the drag can be calibrated using a refined shallow water model [196].

Unfortunately, the mechanisms through which the anisotropy is introduced result in high mesh sensitivity and mesh dependence [194, 193, 404]. Guinot [193] provides guidance on suitable meshing strategies however, this realistically precludes the use of Cartesian structured grids and is of questionable practicability even for unstructured meshes when considering complex urban configurations. Nonetheless, the IP model validated well against the model city test case [405], where comparisons between the SP model and IP model illustrated negligible differences in predictive skill. However, it should be noted that the homogeneity of the artificial urban geometry fails to provide an adequately anisotropic and inhomogeneous environment suitable for showcasing the comparative advantages of the IP model. Schubert and Sanders [404] further demonstrated the computational efficiency and accuracy of the IP model when compared with local friction based approaches, finite bottom elevations and vertical wall implementations for a realistic urban flood event. The Authors also presented a convenient, simplified method for calculating the frontal area, which performed comparably with the flow based definition.

Through derivation of a differential form of the IP model, Guinot and Delenne [195] performed an analysis of the eigenvalues for the system. The eigenvalues were found to be equal to the SWE eigenvalues multiplied by the ratio of the porosities, which is intuitively more consistent with reality than the wave propagation speeds for the SP model. However, the system permits supposedly unphysical behaviour as it does not preclude the existence of a conveyance porosity greater than the storage porosity, resulting in a wave propagation which is faster than the SWEs, despite the presence of obstacles. The inaccuracy of the wave propagation speeds for the IP model was confirmed via numerical experiments, which demonstrated that the IP models underestimates the wave propagation speed [353]. Özgen [353] also questioned the validity of the assumption of a smooth free surface when modelling very shallow flow. Ultimately, the model lacks the capacity to account for sub-grid topographic variations which are wholly contained within the cell, due to the interfacial definition of the areal porosity. This was identified by Guinot [193], who identified the requirement for an approach that better reflects the connectivity properties of the cell as a whole, as opposed to the presented approach which only defines connectivity at the interfaces. Özgen [353] also addressed the implicit assumption that the obstacles are not fully submerged by introducing a depth-dependent anisotropic porosity formulation of the IP model.

Through the derivation of the DIP model, Guinot et al. [196] provided further advancements with the promise of greater anisotropy and the preservation of self-similar solutions via a more congruent momentum dissipation mechanism. As identified by Guinot and Soares-Frazão [197] a major challenge for sub-grid porosity approaches is introducing an appropriate mechanism to capture the sub-grid momentum dissipation effects that occur. The necessity of additional momentum dissipation mechanisms was clarified via numerical

experiments conducted by Guinot [194], involving frictionless shallow water propagation through an idealised urban street network with piecewise constant initial data. The experiments demonstrated that a lack of adequate momentum dissipation results in severe errors, especially for positive waves which raise water levels.

As explained by Valiani and Caleffi [453], the classical shallow water equations include only two dissipation mechanisms:

1. Friction: the mean velocity multiplied by the bed shear is proportional to the mechanical power dissipated per unit width, per unit weight of the liquid.

2. Hydraulic jumps: analogous to the inviscid shock for compressible fluids, resulting in a dissipation of specific energy.

Although real open channel flows also experience localised dissipation due to geometric discontinuities in the bed or the channel, as is the case under consideration here, this is not included in the classical formulation and must be added to the momentum and/or energy balance if the localised head losses are significant. This was achieved for the SP model via the introduction of a Borda-type formula [43] which expressed head losses over the cell as proportional to the square of the depth-averaged velocity. For the numerical experiments presented by Guinot [194], it is therefore clear that without the inclusion of friction or additional momentum dissipation and in the absence of capturing the effects of sub-grid hydraulic jumps, the model has no mechanisms for adequate momentum dissipation and the large errors are to be expected.

However, it is not sufficient to just implement any dissipation mechanism; Guinot et al. [196] also identified that the implementation of classical head loss models is incompatible with the production of self-similar solutions for piecewise constant initial boundary value problems and is therefore insufficient for modelling the localised dissipation produced by sub-grid bores. Furthermore, the calibration of building drag models also cannot correctly account for the localised dissipation produced by sub-grid bores. This raises an important point that, although calibration may improve results, it is not a substitute for adequate process representation. Consequently, the improved momentum dissipation mechanism implemented by Guinot et al. [196], acts upon the momentum fluxes, rather than acting as a momentum sink, with directionality being accounted for via the second-order tensor form. The drag model is also improved by introducing a depth-dependence and the capacity to capture anisotropic effects via a tensor-based description. The new form of the drag model also significantly simplifies the calculation of the frontal area, presenting an improvement over the previous implementation.

The numerical tests conducted for a positive wave, negative wave and dam-break flow entering an idealised frictionless urban street network demonstrate the advantages of the improved DIP model compared to the IP model in reference to a refined classical shallow water model [196]. For the positive wave test case, in which momentum dissipation is a key feature, the DIP model with a calibrated momentum dissipation approximated the refined shallow water model solution whereas, the IP model underestimated the propagation speed, which cannot be corrected via calibration of the building drag as this would only slow the wave further. For the negative wave test, which is not characterised by localised momentum losses due to sub-grid bores, the DIP model was found to inaccurately replicate the spreading of the wave produced by the shallow water model, despite capturing the average propagation speed. Since the negative wave scenario is not characterised

by transient momentum dissipation, calibration of the momentum dissipation tensor is ineffectual. In contrast, the IP model was found to significantly underestimate the wave propagation speed, which once more cannot be accounted for by calibration. For the dam-break flow case, comparisons were also presented with the SP model and the results demonstrated that the IP and SP models both performed poorly in comparison with the DIP model, which captured all aspects of the refined shallow water model solution except the steepness of the wave front.

The comparative suitability of the models when applied to a field-scale realistic application was also demonstrated via numerical investigations of a levee-break induced flood of a small neighbourhood in West Sacramento [196]. The tests involved comparisons of coarse grid implementations of the IP and DIP models, both using the improved momentum dissipation model, with respect to a fine grid implementation of a classical shallow water model, utilising the vertical wall method, for a steady-state and transient analysis. For the steady-state case, the DIP model was shown to exhibit slight improvements over the IP model however, both models predominantly failed to accurately capture the preferential flow paths, exhibiting a directional bias in the diagonal direction. For the transient case, the DIP model presented a greater prediction of the overall flood inundation extent and average flow characteristics than the SP and IP models with respect to the refined shallow water model. However, the unusual optimal values of the calibrated momentum dissipation coefficients, which were highly anisotropic despite the relative isotropy of the neighbourhood geometry, hinted at underlying model deficiencies.

The suspected deficiency of the DIP model is confirmed by the rigorous analysis of the SP Riemann problem performed by Cozzolino and collaborators. Of particular interest is the solution of the SP Riemann problem at a porosity discontinuity [123, 459, 460, 457], which may physically occur at the boundaries between urban zones of different density. The solution of the SP Riemann problem at a porosity discontinuity coincides with the solution of the shallow water Riemann problem where there is a discontinuity in the width [118, 452, 461], which in turn is analogous to the solution of the shallow water Riemann problem with a bottom step [348, 13, 121, 211, 453].

Specifically, where the porosity is discontinuous, the non-conservative products, which represent the force per unit width exerted on the flow by the sub-grid obstacles, prevent the definition of weak solutions in accordance with classical theory based upon the notion of distributions [268]. More precisely, a non-conservative product represents the product of a Heaviside step and a Dirac delta, which is not well-defined due to ambiguity in absence of further information [343]. The analytical theory of Dal Maso et al. [127] enables the definition of weak solutions by means of a family of paths connecting the left and right states. Whereby the choice of path represents supplementary information, based upon physically congruent considerations, necessary to overcome the non-uniqueness of the solution and define a suitable generalised Rankine-Hugoniot condition.

As discussed by Cozzolino et al. [123], Guinot and Soares-Frazão assumed that the porosity discontinuity is equivalent to a channel discontinuity where the flow exerts a hydrostatic thrust on the solid walls and this porosity discontinuity definition has been adopted by successive Authors who implemented differential PSWE models [167, 194, 466, 164]. Cozzolino et al. [123] demonstrate that this definition is unphysical, as it permits an increase in energy through the jump at a porosity discontinuity. Furthermore, Varra et al. [459] demonstrate that the lack of capacity for existing Riemann solvers to capture moving

shocks results in a systematic underestimation of the dissipated energy, explaining why other porous shallow water models required empirical transient momentum-dissipation coefficients. The rigorous analysis of the SP and BSP models also demonstrates that alternative differential formulations are physically inconsistent as they violate the principle of Galilean invariance by failing to adequately account for the influence of porosity variations on the wave propagation. Further exploration of the SP Riemann problem is presented by the works of Varra et al. [460, 457], whereby the disambiguation of multiplicity of solutions for the PSWE is accomplished and an approximate Riemann solver, based upon a modification of the generalised hydrostatic reconstruction method proposed by Castro et al. [88], is presented.

Overall, the DIP model, which provides improved performance compared with the IP model, has been shown to provide a good prediction of inundation extents and a satisfactory approximation of the flow field produced by a refined shallow water model, whilst utilising a much coarser grid resolution. Overall however, the approach is unsuitable for applications concerned with flood hazard or vulnerability analysis due to the lacking local accuracy. The efficiency of the model is therefore the most attractive feature, potentially facilitating applications or approaches which require multiple model runs. However, this is balanced by the requirement to first run a refined shallow water model in order to calibrate the empirical momentum dissipation coefficients. Furthermore, the mesh dependence and mesh sensitivity which plagues the integral forms of the equations and the somewhat unrealistic meshing requirements are serious barriers to implementation for realistic field-scale applications. The presented field-scale application was relatively small, including only a single relatively homogeneous neighbourhood, and it remains to be seen whether a similar accuracy can be achieved for city-scale applications, especially due to the identified issues relating to the overall inability of the model to capture the anisotropy of the flow.

The development of a suitable scheme based on the differential SP model is therefore attractive, especially in light of the advances provided by Cozzolino et al. [123] and Varra et al. [460, 457] on the solution of the SP Riemann problem. Not only does the SP model not require the assumption of the existence of a REV but the ability to capture moving shocks within the SP Riemann problem precludes the necessity to calibrate empirical momentum dissipation coefficients. However, as of yet, a field-scale application has not been presented. Such an application would be required to confirm that the advances in the solution of the SP Riemann problem suffice to solve the inability of the DIP model to capture the anisotropy of the flow. The differential SP model implemented in the PARFLOOD 2D model, as presented by Ferrari et al. [164, 165, 163, 162], provides an insight into the potential accuracy of the SP model. Despite a number of numerical flaws in the scheme:

- The conservation laws are written in a non-conservative form to enable convenient well-balancing of the scheme for at rest states. However, the non-conservative form of the equations means that the scheme is only valid for weak shocks [438], with the scheme converging to incorrect solutions in the presence of strong shocks [224];
- As proven by Cozzolino et al. [123], the definition of the porosity discontinuity utilised by the scheme is unphysical and the model violates the principle of Galilean invariance by failing to adequately account for the influence of porosity variations on the wave propagation. The scheme also does not adequately account for the

presence of non-unique solutions for specific initial conditions;

- The use of a path conservative scheme [356] for the treatment of the non-conservative products means that the scheme is expected to produce errors which are proportional to the strength of the porosity discontinuity [3]. Specifically, path conservative scheme generate a convergence error source term which is a locally bounded error, provided that the total variation remains uniformly bounded [90];

the application of the scheme for the model city test case demonstrated a level of accuracy comparable to a refined shallow water model. Hence, it should be expected that a correction of these numerical flaws can only suffice to improve the presented results. However, an application to a field-scale urban environment is still required to determine the extent to which porosity models can be used for flood hazard and vulnerability analyses. Ultimately, such schemes can only be expected to produce an approximation of a refined shallow water model and it remains to be seen whether the approximation is of high enough quality to enable flood hazard and vulnerability analyses.

It is also important to note that the solution of the SP Riemann poses a significant numerical challenge due to the presence of non-conservative product terms and the related numerical flaws identified for the numerical scheme implemented by Ferrari et al. [163, 162] are not easily resolved. As has been mentioned, the analytical theory developed by Dal Maso et al. [127] may be used to define weak solution by means of a suitable family of paths. Via the framework of path-conservative methods introduced by Parés [356] numerical schemes for the solution of non-conservative systems can be designed, as utilised by Ferrari et al. [163, 162]. However, as displayed by Abgrall and Karni [3], even if the the correct path definition is known, such schemes will not in general converge to the assumed path and different path-conservative schemes based on the same path definition may converge to different solutions. Ultimately, viscous terms that arise due to truncation errors dominate the computation regardless of the choice of path and whilst the same can be seen to occur for conservative schemes, convergence to the physically relevant weak solution is not predicated upon convergence to a specific path [3].

This is further complicated for shallow water systems as there is no *obvious* path definition based upon the underlying physics, as demonstrated by the referenced developments on the correct choice of path for the analogous porous shallow water system. Furthermore, Castro et al. [90], determined that such schemes generate a *convergence error* source term which is a locally bounded error, provided that the total variation remains uniformly bounded. This means that the error measure may not be negligible along shock trajectories in practice, which is supported by the computations performed by Abgrall and Karni [3], who demonstrate relative errors which are proportional to the strength of a discontinuity. In the absence of further advances in the design of numerical schemes which guarantee convergence to the physically relevant weak solution for non-conservative hyperbolic systems, some authors have sought writings of the conservation laws which eliminate [418, 70, 59] or minimise [253] such terms in physically justifiable ways. In this case, that is not possible and therefore the design of suitable numerical schemes will remain problematic until further advances are realised.

Whilst the models efficiency on coarser grids can certainly be leveraged to facilitate more computationally efficient simulations there is also potential, in absence of REV assumptions, to apply a SP scheme at a refined resolution in an attempt to capture an approximation of the influence of decimetric topographic variations. In such cases, the accuracy

of the topographic data would likely be a limiting factor but it presents an interesting and promising opportunity that warrants further exploration. Considering the compelling experimental evidence provided by Mignot and collaborators on the importance of small-scale urban topographies and the potential for intruding flows in determining localised flow characteristics, there would have to be significant advances in the collection and availability of the required data to model such effects using a SP model. For example, current information sources and deterministic methods for estimating porosity are incompatible with the assumption that buildings themselves are porous.

Finite Bottom Elevations

The finite bottom elevation method for modelling obstructions to flow, locally elevates the bed topography to model the effect of an obstacle to flow. It is therefore an explicit representation of an impervious obstacle of fixed and finite height, however, the spatial accuracy of the representation is highly dependent on the mesh resolution and the order of spatial accuracy provided by the numerical scheme. Since the method locally elevates nodes within the mesh, a slope is generated between the elevated node and it's neighbours, with the angle of the slope dependent upon the mesh spacing and the difference in elevation. As shown by Haider [206], this can cause problems when the obstacle is intended to have vertical sides and the mesh is insufficiently refined with regards to the spacing between obstacles.

Issues of this nature were overcome by Schubert et al. [405] through the use of a piecewise linear terrain model and a sophisticated unstructured mesh with localised refinement. It is therefore important to highlight that the use of finite bottom elevations is highly unsuitable for representing obstacles to flow on coarse meshes; the use of finite bottom elevations will provide a crude representation of obstacles, which can result in the blockage of preferential flow paths [337, 405, 206, 207]. This corresponds with the established wisdom that high resolution modelling of urban areas requires a mesh resolution that is reflective of the characteristic length scale of the urban structures [231, 294, 166, 489, 401, 295, 174, 153, 450, 480, 191]. Although, this may be further clarified to state that the mesh resolution should be reflective of the characteristic length scale of the *gaps* between urban structures if possible [404]. However, this is a much more stringent and potentially unrealistic target.

Hence, although the method is relatively easy to implement and it is compatible with any type of computational mesh, it benefits greatly from local mesh refinement around obstacles. Unstructured meshes are attractive in this regard as they offer greater flexibility when generating a mesh which conforms to complex urban topographies. However, care should be taken when selecting between unstructured and structured mesh generation. For example, formal mathematical proofs on the order of convergence of discretisation errors for unstructured meshes are yet to be obtained [69]. Typically, when methods are formally referred to as being first order or second order accurate in regard to the order of spatial accuracy, this indicates that the scheme exhibits a first or second order truncation error on uniform Cartesian grids. It is not yet known whether the same order of spatial accuracy is achieved for unstructured grids and there is reason to doubt that it is the case as Bouche et al. [69] have shown that, in general, the truncation error for unstructured grids *does not* tend to zero as the mesh is refined. Other studies have demonstrated that the convergence of truncation errors can only be achieved on meshes with a certain degree of geometric regularity and that this does not necessarily imply a degradation of

discretisation-error convergence, nor does it contradict the Lax theorem [142]. As such, this topic remains the subject of debate and research.

Importantly, this does not mean that unstructured meshes cannot be used for high resolution hydrodynamic modelling, as shown by Schubert et al. [405] and Schubert and Sanders [404], however, modellers should be aware of the respective advantages and limitations of potential mesh geometries. Overall it it challenging to quantify the quality of a mesh regardless of the mesh geometry or geometric regularity [417], however, it can certainly be said that irregular unstructured mesh generation is much more complex than regular structured mesh generation, with a greater potential for deficient features that unfavourably effect convergence rates and accuracy with the risk of numerical divergence [490].

Concerning the steep slopes that may be generated, strictly speaking, the shallow water approximation, in which the fluid depth is evaluated along the vertical direction as an approximation of the bottom normal, is only valid for small slope angles of smaller than $\approx 6°$ or $1:10$ [103]. For scenarios where the slope exceeds this limitation, vertical acceleration can no longer be considered negligible and the pressure deviates from a hydrostatic profile. A class of shallow water equations referred to as the steep-slope shallow water equations (SSSWE) [290] have been derived, whereby a change in coordinate system removes the small angle limitation. Maranzoni and Tomirotti [291] numerically explored the difference in results for a dam-break problem against a steep slope, which is representative of the idealised behaviour of an incident wave upon a structure modelled using a finite bottom elevation, albeit at a much finer mesh resolution. The results show that the SSSWE model provides an improvement upon the classical SWE model but that both models are unable to capture detailed behaviour such as the emergence of a backwash bore or plunging bore. It is therefore sensible to take the pragmatic approach of Alcrudo [12] and accept that the SWEs can only provide a simplification of the interactions, especially since the steep slopes are often an unintended artefact of the spatial discretisation and not a property of the actual obstacle being modelled.

Ignoring the theoretical challenges, the steep slopes may also result in numerical challenges. Firstly, steep slopes may induce strong source term forcing which can be problematic for schemes utilising an explicit time integration. Secondly, provided the obstacle is not overtopped, the method introduces a wet-dry front which may be a source of instability for less sophisticated schemes as previously discussed (see Section 2.2.2). Issues relating to steep gradients can be overcome by using robust numerical techniques such as a fully implicit time integration [12], special local numerical treatment or by reducing the elevation of the obstacle. A specific local treatment that checks for steep slopes and a depth of flow smaller than the obstacle and sets the source terms and mass flux to zero with the momentum flux equal only to the hydrostatic pressure contribution, as proposed by Alcrudo [12], is equivalent to a solid wall implementation in which the normal velocity component is set to zero. This appears to be a suboptimal solution since it is more straightforward to implement the equivalent solid wall boundary condition, which will also ensure a perfectly vertical representation of the obstacle façade, without the need for any unnecessary conditional logic. The only advantage of the proposed local treatment would be the capacity to model the overtopping of the obstacle, which is not possible for a straightforward reflective boundary condition implementation. The stubby building method is the term given to the option of reducing the elevation for taller obstacles (primarily buildings), whereby the maximum elevation increase is restricted to $30cm$ [230,

179], eliminating any potential instabilities. The choice to restrict elevations to a maximum increase of $30cm$ is intended to represent the threshold height at which water is able to intrude into a building. This is clearly a vast oversimplification and as shown by Iliadis et al. [230] the method performs poorly in practice due to unrealistic flow paths through building footprints.

For more realistic implementations that use elevations appropriate to the obstacle being modelled, on sufficiently refined grids, the method is shown to perform well, provided the obstacle being modelling can assumed to be impervious. As for a local friction based representation, Alcrudo and Mulet [14] report predictions to be within 25% of observations for the idealised city test case. Soares-Frazão showed that the method predominantly overestimated depths however, depth prediction remained within 15% of observations at a maximum, with most predictions within 10% of observations. Schubert et al. [405] also demonstrated the potential accuracy of the method, which was shown to perform well for refined meshes and poorly for coarse meshes. However, the study lacked validation data so conclusions are based on comparisons with other methods and convergence rates. Schubert and Sanders [404] also demonstrated the accuracy of the method for realistic field-scale applications on high resolution meshes with local refinement, reproducing inundation extents and stream flow measurements to within 10%.

The method can theoretically support the modelling of the overtopping of obstacles, providing valuable flexibility in terms of the potential obstacles and flow conditions that can be modelled. However, the accuracy of the method for overtopped obstacles is relatively unexplored since it is primarily used to model buildings, which when modelled realistically, are rarely overtopped. The comparison study performed by Iliadis et al. [230] involved the overtopping of building footprints modelled using a stubby building approach which validated poorly, even where significant flow intrusion was recorded. However, the poor performance of the method in this case can be attributed to the poor representation of the physical behaviour and little can be ascertained as to the skill of the method in accurately modelling the overtopping of obstacles. Haider et al. [207] suggest that the modelling of a row of cars, via a local elevation raise of $1.25m$ produced results that were more representative of the expected behaviour however, no detailed comparison with validation data is provided and it is unclear if the cars were overtopped. From a theoretical standpoint, it is clear that the finite bottom elevation approach can only provide an approximation of flows over sharp geometric discontinuities such as bottom steps or weirs, even within the constraints of a shallow water approximation, due to the assumption of a continuously variable bottom topography. For the accurate modelling of sharp geometric discontinuities special numerical treatment is required [453, 348, 211, 121, 58, 13]. When considering flows which overtop obstacles it is also important to consider whether the assumption that the obstacle remains stable is valid. Models such as HEC-RAS and Tuflow have added the capability to remove obstacles to flow to simulate their destruction and this is possible to replicate using a finite bottom elevation representation by resetting the elevation. Although logical conditions can be imposed to determine when structural collapse may occur based on approximate forces derived from the local flow, the highly uncertain nature of the process based on the available information suggests either detailed local three-dimensional CFD analysis or probabilistic two-dimensional approaches are required.

Overall, the finite bottom elevation approach to modelled obstruction to flow can be described as a satisfactory method for modelling fixed, impervious obstacles on sufficiently

refined meshes. The potential to model the overtopping of obstacles provides some flexibility but the accuracy and limitations of the method in such scenarios is relatively unexplored. Due to the requirement for a sufficiently refined mesh, the method requires efficient numerical schemes and adequate processing capabilities, with features such as local mesh refinement, unstructured mesh generation and local time stepping proving useful. Ideally, meshes should be able to accurately discern the gaps between obstacles to ensure that preferential flow paths are adequately captured.

Vertical Walls

The vertical wall method models obstructions to flow via the introduction of reflective boundary conditions along the edges which delineate the perimeter of the obstacle. In contrast with the finite bottom elevation method, modelling obstacles with vertical walls produces a perfectly vertical boundary. An efficient implementation removes the cells contained within the footprint of the obstacle from the computational domain [179, 230, 404, 405]. The effectiveness of the method is enhanced when the removed cells are retained as a buildings layer, enabling processes such as roof drainage, flow intrusion and blue-green infrastructure to be modelled where required [179]. Furthermore, the removal of the cells from the obstacle footprint prevents the generation of unnecessary wet-dry fronts.

A solid reflective boundary condition can be implemented as [438, 437, 268]:

$$\left.\begin{aligned} h^n_{\text{ext}} &= h^n_{\text{int}} \\ u^n_{\text{ext}} &= -u^n_{\text{int}} \end{aligned}\right\} \tag{2.1}$$

whereby h is the depth of flow, u is the velocity component normal to the interface, the superscript n refers to the time level, the subscript int refers to the properties of the *internal* cell and the subscript ext refers to the properties of the *external* ghost cell. This reflective boundary condition ensures that the fluid does not penetrate the boundary, producing a normal velocity and mass flux equal to zero at the interface. The symmetry of the variables across the interface results in a stationary contact discontinuity at the interface, meaning any jump in the tangential velocity across the interface will propagate with zero normal velocity. This corresponds to a free-slip boundary condition, in which the fluid is able to freely move in the transverse direction, unimpeded by the wall.

In reality, when a viscous fluid flows over a solid surface, a no-slip condition is induced, in which friction reduces the transverse velocity at the wall to zero and energy is lost through viscous dissipation [377]. However, since the shallow water equations are inviscid, it is not possible to impose a no-slip condition. As the SWEs are inviscid hyperbolic equations, they model the vanishing viscosity limit ($\epsilon \to 0$) and therefore the thickness of the boundary layer which emerges at the wall can also be assumed to be of vanishing width for large Reynolds numbers [268]. However, even where this assumption is valid, large-scale turbulence may still be induced, for example, at the corners of obstacles if flow separation occurs. As prior explained, shallow water models are not expected to capture this behaviour, nor is it realistic to expect that meshes could be sufficiently refined to capture the boundary layer if a suitable turbulence model was implemented [405] but it does point to some of the limitations of the method.

A more rigid implementation of a reflective boundary, which corresponds to the local numerical treatment suggested by Alcrudo (see Section 2.2.2), involves setting the value

of the velocity equal to zero in both cells:

$$\begin{cases} h^n_{\text{ext}} = h^n_{\text{int}} \\ u^n_{\text{ext}} = 0\,, u^n_{\text{int}} = 0 \end{cases} \tag{2.2}$$

This is generally over-restrictive in comparison with (2.1), although it is mostly consistent; the resulting free-slip condition has a mass flux and normal velocity identically equal to zero. However, by artificially setting the normal velocity to zero, the resultant Riemann problem at the interface is decoupled from the conserved variables for the *internal* cell. As a consequence, the momentum flux through the interface, which represents a momentum sink for the shallow water system, is always equal to the hydrostatic pressure exerted by the neighbouring shallow water column. For (2.1), provided the normal velocity within the neighbouring cell is non-zero, the momentum flux is larger and equal to a hydrostatic pressure component plus a convective component. As a consequence, an incident surge of water will typically reach a greater depth, with a higher momentum upon crashing against the boundary for (2.2) compared with (2.1).

It is also worth pointing out that despite producing similar outcomes, since both methods act as impervious barriers to flow, there are clear differences in the numerics for the finite bottom elevation method and the vertical wall method. As such, Alcrudo [12] claims that the vertical wall method of modelling fixed impervious obstacles to flow is the most theoretically robust since it is most consistent with the shallow water assumptions with greater topological accuracy for sheer-sided obstacles.

Although the solid wall method refers to the implementation of reflective boundary conditions, the method is potentially flexible since each interface corresponds to an initial value boundary problem across which an *internal boundary condition* can be applied. For example it is also possible to implement a moving solid reflective boundary [438, 437, 268]:

$$\begin{cases} h^n_{\text{ext}} = h^n_{\text{int}} \\ u^n_{\text{ext}} = -u^n_{\text{int}} + 2u_{\text{wall}} \end{cases} \tag{2.3}$$

where the additional variable u_{wall} denotes the velocity at which the fixed boundary is moving. For, a more rigorous treatment of moving boundaries including the interaction of waves with a lateral piston or the evolution of the contact line between a floating object and the water readers are referred to the work of Iguchi and Lannes [229], who present a general framework for the solution of one-dimensional initial value boundary problems. That said, moving boundaries are rare within urban hydrodynamic contexts. *Internal boundary conditions* are to be explored in detail within Section 2.2.3 and consequently the focus here will be on solid wall implementations.

As for the finite bottom elevation method, this method of modelling obstructions requires a sufficiently refined mesh that is at least reflective of the characteristic length of the structures and ideally sufficiently refined to resolve the gaps between structures. This is necessary to ensure preferential flow paths are adequately captured. Schubert et al. [405] demonstrated that the use of local mesh refinement can maintain a consistent representation of obstacle shapes with mesh coarsening however, Schubert and Sanders [404] noted that coarsening of the mesh substantially altered localised velocities. Due to the removal of cells from the computational domain, the efficiency of the method is comparatively superior. Schubert et al. [405] reported a 30% increase in runtime efficiency

compared to the finite bottom elevation method for a $1m$ mesh. A comparative 28% decrease in total runtime was also reported by Iliadis et al. [230], who point out that runtime savings compared to methods which erroneously enable intruding flows are likely to be even greater. This is because preventing flows from intruding into structures results in a concentration of the flow and although this may result in a greater restriction upon the timestep during peak flows, peak flows will dissipate faster providing overall savings. Of course such savings are only justified where it is correct to assume that the structures are impervious.

In practice the vertical wall method has been widely implemented and validated. Costabile and collaborators [109, 112] have demonstrated the suitability of the vertical wall method for modelling bridge piers. The successful validation of CityCAT against the idealised city test case [179], a real flood which occurred in Newcastle upon-Tyne [230] and for a real flood which occurred in London [231] demonstrates the suitability of the method for modelling structures within urban environments. This is further verified by the work of Schubert and Sanders [404] and Schubert et al. [405] among others.

Overall the vertical wall method for modelling obstructions to flow provides accuracy that is comparable with the finite bottom elevation for fine mesh resolutions at a lesser computational cost. As for the finite bottom elevation method it is unsuitable for use on coarse meshes and similar considerations must be made on the suitability of the preferred mesh geometry and regularity. Considering only the implementation of reflective boundary conditions, the method is relatively inflexible and unable to capture overtopping flows or flows under obstacles such as gates. However, for fixed impervious objects, ignoring the inability to resolve turbulence, which is a limitation of the model and not the method, the method provides the optimal theoretical consistency and accuracy when considering the limitations of the shallow water model.

2.2.3 Internal Boundary Conditions

As has been briefly mentioned, and explored to a small extent already via the solution of the SP Riemann problem at a porosity discontinuity, obstacles to flow may be modelled via the solution of a one-dimensional initial value boundary problem. Since this corresponds to the solution of a modified one-dimensional Riemann problem at an interface, the resultant numerical fluxes are also inherently one-dimensional. As a consequence, internal boundary conditions neglect the streamwise width of the obstacle, assuming that the feature lies within the infinitesimal width of the cell interface, and therefore cannot account for transverse effects or a reduction in storage capacity. However, the method offers advantages in that it enables the approximation of sub-grid effects, particularly for linear features which are of negligible width with respect to the geometry of a cell. Considering for example a fence or a wall, the resolution required to explicitly model a linear obstacle using the outlined mesh methods is extreme, whereas representation as an internal boundary condition at a cell interface is a much more natural and efficient representation.

A large number of internal boundary conditions have been presented within the literature for the modelling of a range of obstacles including:

- Lateral contractions and expansions.
- Sluice gates.

- Weirs.
- Bridges.
- Check dams.

A key feature of internal boundary conditions is the flexibility to explicitly model flow around, under, over and through a partial barrier to flow. For the outlined mesh methods, explicit modelling is restricted to flow around, and in some cases over, obstacles, although the validity of the methods for overtopping flows is questionable. Internal boundary conditions therefore provide a unique opportunity to model flow under and/or over obstacles. Furthermore, internal boundary conditions may be complemented by local implementations of modified conservation laws to locally overcome limitations of the shallow water equations. The implementation of modified conservation laws across the entirety of the computational domain is primarily restricted by computational efficiency requirements however, local implementation offers an efficient method for supplying additional complexity only where it is most required.

Lateral Flow Contractions and Expansions

The first internal boundary condition to be analysed is that of lateral contractions and expansions of the flow. As explored previously, geometric transitions in the channel geometry induce a backwater effect and can also result in the dissipation of momentum via bores and hydraulic jumps. For a sufficiently refined mesh, it has been shown that the effects of lateral contractions and expansions of flow produced by impervious obstacles can be accurately captured using vertical walls to model the obstacles, as shown by Costabile and collaborators [109, 112] when modelling the effect of bridge piers for example.

Unlike the sub-grid porosity method, the implementation of an internal boundary condition to model such features does not account for the reduction in storage capacity produced by the presence of obstacles, accounting only for the reduction in conveyance capacity across the interface. Hence, where features that induce a contraction and/or expansion of the flow can be considered of negligible width with respect to the geometry of the mesh, the difference in storage volume can also be considered to be negligible and implementation as a internal boundary condition is permissible. In such cases, the use of internal boundary conditions may present an opportunity for greater computational efficiency via a reduction in mesh resolution; Varra et al. [458] demonstrated a 40% reduction in normalised CPU time when modelling a bridge pier with an internal boundary condition.

The simplest method of implementing the outlined internal boundary condition is to modify the flux in accordance with an empirically derived flow relation. This method is presented in Zhao et al. [498], whereby the mass flux is calculated as equal to the unit discharge provided by an appropriate empirical discharge formula and the momentum flux is consequently reformulated in terms of the calculated unit discharge. This guarantees that the mass and momentum flux is consistent with the selected empirical discharge formula however, it also invariably requires an assumption of steady-state, gradually varied flow conditions corresponding to an instantaneous equilibrium between the upstream and downstream flow and it is therefore invalid for rapid transients. As briefly outlined by Pepe et al. [359] this method of implementing internal boundary conditions may also result in numerical instabilities for less robust schemes; when using static formulas, it is

implicitly assumed that the outer left and right states are sufficiently close to the inner states within the structure of the Riemann problem, where this is not the case, with sharp gradients to be expected for rapid transients, a lack of numerical convergence may occur.

Finite volume schemes for the solution of hyperbolic systems of conservation laws, such as the SWEs, overcome the smoothness assumptions associated with gradually varied flow required for the differential form of the equations by leveraging the integral (weak) form of the equations, seeking convergence to physically relevant weak solutions [269, 268, 438, 437, 124]. Therefore, it is possible to capture the effect of rapid transients through the solution of the Riemann problem whereby shocks, governed by Rankine-Hugoniot conditions, connect gradually varied regions of flow. As a consequence, the study of geometric discontinuities as a special class of standing discontinuities within the Riemann problem, which connect the upstream and downstream flow conditions, has gained popularity due to the capability to capture transient flows through channel discontinuities [118].

As explained by Valiani and Caleffi [452], when considering a geometric discontinuity at a cell interface, the effect can be modelled via the augmentation of the classical conservative form of the equations with a new variable representing the nature of the geometric discontinuity. In the case of a discontinuity in the channel width, the introduced variable is the channel width and represents the difference between the total discharge and the unit discharge. The newly introduced geometric variable experiences a stationary discontinuity (at the interface), producing the aforementioned stationary contact wave within the structure of the Riemann problem. The presence of stationary wave enriches the structure of the Riemann problem, introducing inner states, connected to the outer left and right states via elementary waves (shocks and rarefactions). Via the classical and additional generalised Riemann invariants, the conservation properties for the problem are defined, which for the case of a lateral change in width is the conservation of total discharge and specific energy.

As such there are parallel advancements in the development of the Riemann problem in which a width variation occurs. In the first case, and most applicable to the use of internal boundary conditions within two-dimensional shallow water equations, is the modelling of a localised contractions and expansions as shown in Figure 2.1 (**b**) and (**c**). In the second case, is a width variation in a channel as shown in Figure 2.1 (**a**). This corresponds directly to the modelling of variable channel widths in one-dimensional models using the Saint-Venant equations or to the modelling of porosity discontinuities when using PSWE models.

Considering first the case of localised obstructions, Cozzolino et al. [118] investigated the dam-break problem (null initial velocity). The presented method consists of connecting the left and right states through a standing discontinuity, situated at $x = 0$ corresponding to the geometric discontinuity, via the elementary waves permitted by the shallow water equations. Due to the presence of non-conservative product terms a suitable regularisation is required according to the theory of Dal Maso et al. [127] to define a suitable generalised Rankine-Hugoniot condition. The presented solution therefore accounts for composite wave configurations across a non-monotonic width variation, with proofs provided for the existence and uniqueness of the corresponding solutions. When compared with the solutions provided by a refined two-dimensional shallow water model for four

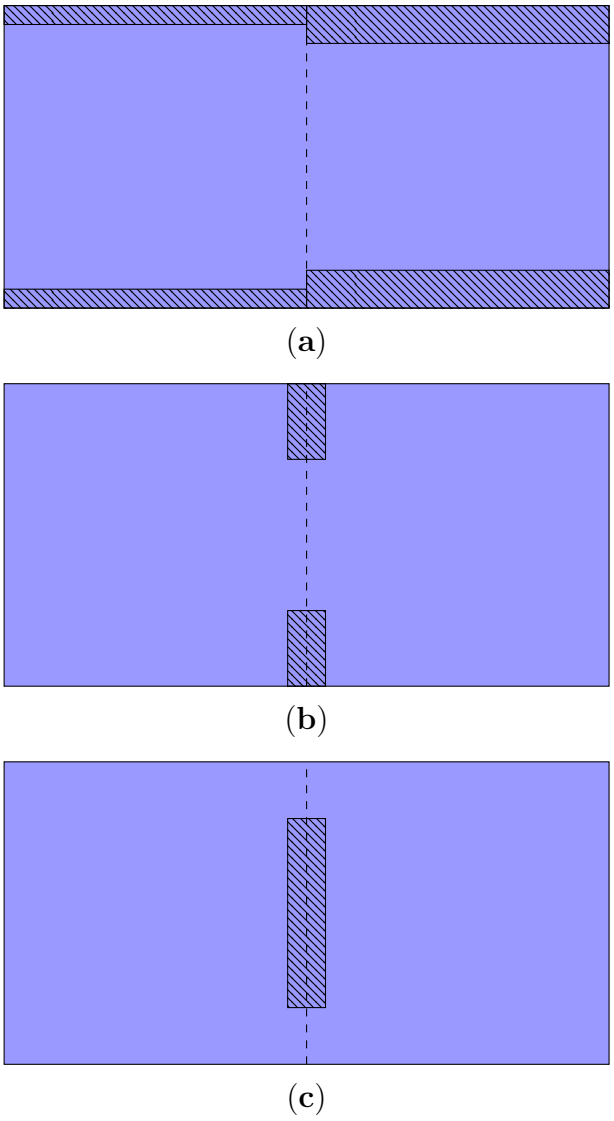

Figure 2.1: (a) illustrates a plan view of a width variation. (b) illustrates a plan view of a localised constriction of the flow by obstacles which impinge on the interface. (c) illustrates the expansion and contraction of the flow due to an obstacle contained within the interface.

dam-break configurations corresponding to the four potential wave configurations, the provided solutions demonstrated a high level of agreement away from the position of the initial discontinuity at $x = 0$, with satisfactory agreement in close proximity to $x = 0$. Comparisons with experimental results provided by Townson and Al-Salihi [441], show good agreement overall with the potential for further improvement: a hydraulic jump which emerges downstream of the discontinuity is incorrectly modelled as being of infinitesimal length whereas the physical solution results in a hydraulic jump of finite length. This can theoretically be captured via the definition of a generalised Rankine-Hugoniot condition that is consistent with experimental observations however, this is not explored within the publication.

Pepe et al. [359] extended the method to account for non-zero initial velocities enabling the application of the method to more realistic scenarios. Due to the potential for geometric transitions to induce head loss, a brief exploration of the case of non-negligible

head losses is also provided. This involves a more accurate definition of the standing wave which must be inferred from laboratory experiments. Comparisons with the results for refined two-dimensional shallow water simulations demonstrate that the proposed method is accurate, although as expected, the one-dimensional Riemann problem is unable to capture transverse variations in the flow that are produced by the two-dimensional scheme. The solution procedure, which is derived from a graphical construction of the exact solution of the Riemann problem, can be easily implemented as an iterative solver. Even if the iterative solver is somewhat inefficient compared to a standard approximate Riemann solver, the localised implementation of internal boundary conditions and the potential for a reduced mesh resolution can contribute to an overall increase in computational efficiency [458].

However, when applied in a two-dimensional context to model a bridge pier some of the limitations of the method can be observed. A numerical test case presented by Varra et al. [458] involves a frictionless horizontal rectangular channel which is $1465m$ in length and $43.48m$ in width. A bridge pier of length $35m$ and width $10m$ is located in the channel centre, $765m$ downstream. The bridge pier results in a local 33% reduction of the cross-section. A refined shallow water model is produced by using the vertical wall approach to model the bridge pier using a triangular mesh with cell interfaces ranging from $5m$ in width at the channel ends to $2m$ in width at the bridge pier. The internal boundary condition is implemented as a straight line through the centre of the bridge pier with a reduced mesh resolution where interfaces are of uniform width equal to $5m$. Both meshes are shown in Figure 2.2 for clarity.

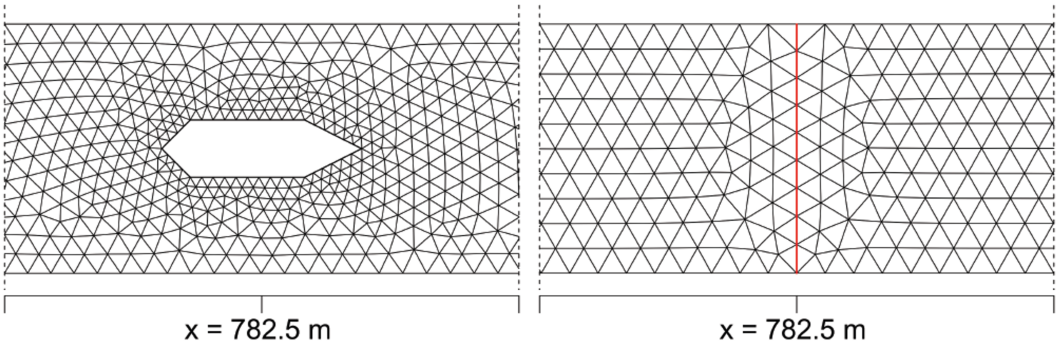

Figure 2.2: Representation of the bridge pier using the vertical wall methodology, with removal of the internal cells and representation of the bridge pier using the exact solution of the Riemann problem with a non-monotonic local width discontinuity as per Pepe et al. [359]. Diagrams adapted from Varra et al. [458].

Comparisons between the two methods of representing the bridge pier demonstrate that the internal boundary condition approach is able to adequately capture the macro-scale behaviour of the flow, with local accuracy increasing further from the pier. However, the one-dimensional nature of the method results in a smoothing of the transverse variations in the flow which are clearly present for the refined model, which exhibits a bow shock upstream of the bridge pier and a complex system of transverse waves reflecting on the lateral channel walls downstream of the pier [458].

The presented use case is clearly designed to demonstrate the effectiveness of the method

in enabling a computationally efficient representation of the main flow characteristics, boasting normalised CPU time savings of 0.73 when compared to the higher resolution mesh. Considering the fact that the approximate area of the bridge pier is $\approx 350m^2$, which is roughly equivalent to the area of 30 cells, there is a significant underestimation of the reduction in storage produced by the pier. Furthermore, the pier cannot be assumed to be of negligible width with respect to the geometry of the mesh elements and it is therefore surprising that the method was as effective as it was. However, the results are clearly inferior to the refined shallow water model and as such, where a refined mesh can be used, the vertical wall representation is clearly superior for high resolution flood hazard and vulnerability applications. Where the method can present superior accuracy compared to the vertical wall method for flood hazard and vulnerability applications, is for the modelling of highly linear features which are genuinely of negligible width with respect to the flow and cannot be easily resolved using a refined mesh, such as walls or fences. Or alternatively, the presented internal boundary condition may be used along the edges of buildings to capture the effects of intruding flows or the presence of small gaps between buildings which are otherwise unfeasible to include within the mesh.

Considering next the case of channels with variable width, as shown in Figure 2.1 (**a**), resembling the classical the Stoker dam-break problem [420] or the flow through a porosity discontinuity for the PSWEs. The relevant Riemann problem was first studied by Ostapenko [349, 347] and in his first work on the topic [349], he considered a dam-break flow through a contraction in the channel width for a rectangular frictionless channel. Taking inspiration from similar problems encountered in gas dynamics, a solution was found under the assumption of the conservation of total head and discharge through the width discontinuity. In his second publication on the topic, Ostapenko [347], expanded the scope to consider more general monotonic variations in the width (contraction and expansion), determining that the assumption of head and discharge invariance across the discontinuity does not permit the existence of a solution for certain initial conditions. Kovyrkina and Ostapenko [250] then addressed this by considering cases with non-zero head loss. This was achieved via the introduction of a parameter, $\sigma \in (0, 1]$ where $\sigma = 1$ represents a conservation of total energy, which enables specification of the proportion of energy lost across the geometric discontinuity. The Authors demonstrated that the value of the energy loss parameter may be suitably determined based on two-dimensional numerical experiments, whereby a relationship between the parameter and the ratio of the upstream and downstream channel widths can be derived. Further experiments performed by Degtyarev et al. [133] demonstrated that the provided solutions compare well with the results of physical experiments. However, Cozzolino et al. [123] later demonstrated that the standing wave definition used by Ostapenko [347] was defective.

As discussed in Section 2.2.2, Cozzolino et al. [123, 120] examined the same problem within the context of the SP Riemann problem. A solution to the problem was achieved via the inclusion of a stationary wave corresponding to the porosity discontinuity, which is identical to a width discontinuity, with proofs of existence and uniqueness of the solutions also provided. Cozzolino et al. [120] then considered the potential multiplicity of solutions for the SP Riemann problem including a dry state. It is shown that a solution always exists but that for specific initial conditions, corresponding to an impinging supercritical flow, disambiguation of the non-unique solutions based on physical principles is required. The Authors consider the numerical phenomena to be connected to the physical hydraulic hysteresis phenomena [470], providing a potential avenue for the identification of the

physically relevant solutions.

In comparison with the previous standing wave definitions proposed by Ostapenko [347, 349, 250], the regularisation proposed by Cozzolino et al. [123] guarantees consistency between standing waves with energy invariance and standing waves with energy loss. Whereas, Kovyrkina and Ostapenko [250] added a physically unspecified parameter to account for cases in which head loss is non-zero, essentially resorting to numerical experiments to overcome the bifurcation of solutions, the standing wave definition provided by Cozzolino et al. [123] specifies the energy loss mechanism, as opposed to parameterising it, meaning there is no need for disambiguation criteria.

Valiani and Caleffi [452] further contributed to the solution of the dam-break problem in a rectangular channel with different upstream and downstream widths, producing the same solutions as presented by Cozzolino et al. [123]. The work of Valiani and Caleffi [452] differentiates itself via the presented approach to the problem, in which the role of the width is extracted via the generation of a third equation describing its time invariance. This enables a simplification of the analytical treatment, and the derivation of analytical limit curves for classifying the solution regions in the (r_b, r_h) plane, where r_b is the downstream to upstream width ratio and r_h is the downstream to upstream depth ratio. Despite the differences in approach of Cozzolino et al. [123] and Valiani and Caleffi [452] the derived solutions are in agreement. In fact, the standing wave definition proposed by Cozzolino et al., is automatically recovered from the generalised Riemann invariants derived by Valiani and Caleffi.

The numerical scheme presented by Valiani and Caleffi [452] utilises a generalised path-conservative [356] Osher-type Riemann solver, specifically the second-order Dumbser-Osher-Toro solver [146] presented by Leibinger et al. [266], due to the presence of non-conservative product terms. Despite the potential for errors across strong discontinuities [3], the numerical results present a strong agreement with the derived exact solutions. The Authors argue, as in Cozzolino et al. [123] for the use of a non-linear path, inspired by the structure of the generalised Riemann invariants, as the classic linear path performs poorly across large amplitude contact waves where significant errors related to a lack of conservation of energy at the width discontinuity emerge.

Again, it is worth noting that whilst the choice of path should absolutely be chosen based upon physically relevant considerations, the correct choice of path, assuming one is identifiable, does not guarantee convergence to the correct solution across strong discontinuities when using a path-conservative scheme [3]. Despite this, the differing path conservative methods presented by Cozzolino et al., which uses a modified generalised hydrostatic reconstruction method [88], and Valiani and Caleffi [452], which is based upon the the second-order Dumbser-Osher-Toro solver [146] presented by Leibinger et al. [266], provide accurate results. Unfortunately, the design of suitable numerical schemes for non-conservative systems is an open and challenging area of research and despite the flaws associated with path-conservative schemes, there are currently no suitable alternatives. Whilst some schemes may seek to overcome the numerical challenges related to the presence of non-conservative products by eliminating [418, 70, 59] or minimising [253] them, that is not possible in this case.

In Varra et al. [461], the results of Cozzolino et al. [123] and Valiani and Caleffi [452] are generalised. The multiplicity of the solutions is discussed with reference to the theory and experimental observations of hydraulic hysteresis, with the identification of the physically

relevant solution remaining somewhat ambiguous; in the case of hydraulic hysteresis, the flow can be changed by altering the boundary conditions or by disturbing the flow which is incompatible with the numerical representation due to the limitations of the Riemann problem. It is speculated that using a higher dimensional scheme can elucidate the relevant solution however, the implemented scheme is found to tend towards an alternate solution. Furthermore, the study reveals an inadequacy of the numerical scheme, based upon the generalised hydrostatic reconstruction method proposed by Castro et al [88], in capturing a hydraulic jump at a channel expansion.

The study of the Riemann problem across a geometric discontinuity representing a width or porosity jump is concluded in the works of Varra et al. [460, 457]. In Varra et al. [460, 457] a two-dimensional shallow water scheme is used to identify the physically relevant solution, as previously proposed, and a modification of the numerical scheme is also presented to ensure convergence to the identified solution. The identified solution, which consists of a backwards moving shock, is consistent with the solution identified for similar problems.

Unlike for the case of localised obstructions, the case of a width discontinuity is of lesser relevance to two-dimensional models based upon the SWEs. For the PSWEs, as discussed in Section 2.2.2, it is integral to the development of more sophisticated and accurate sub-grid porosity models. The presented solutions are relevant to one-dimensional Saint-Venant schemes or coupled 1D-2D schemes, although such schemes are typically inferior to fully dynamic two-dimensional models due to the ambiguity in the coupling methods between the one-dimensional and two-dimensional domains [108]. More generally however, the techniques used to overcome the numerical challenges associated with modelling obstacles to flow as geometric discontinuities within the Riemann problem are important to consider in the design of schemes for other types of obstacles.

Modelling Gates

The modelling of gate-type structures, that is obstacles which permit the passage of flow underneath their form, is unique in comparison with the capabilities of the methods considered thus far. Whilst local friction representations may be calibrated to model the overall effect of a gate type structure, the unphysical nature of the method renders it incapable of enabling analysis of localised flow characteristics. Furthermore, it should generally be considered, as previously outlined, that calibration is insufficient to overcome an inadequacy in process representation.

The finite bottom elevation and vertical wall representations of obstacles are clearly insufficient to model the passage of flow underneath obstacles since in both cases obstacles are considered to be impervious and of infinite or finite height. Whilst a refined mesh using a vertical wall representation can offer a potentially more precise representation for obstacles that entirely block flow through their footprint, this approach falls short when dealing with obstacles acting as gates, meaning an internal boundary condition representation is uniquely placed to model such features.

Classical porosity methods are also unable to capture gate-type structures since porosity is estimated from aerial imagery, assigning a binary value corresponding to an impervious obstacle or lack thereof. Depth-dependent porosity models have the potential to introduce a unique internal boundary condition by modifying the conveyance porosity at an interface in accordance with the gate opening. However, the division between the storage porosity

and conveyance porosity only occurs for integral formulations, which suffer from mesh sensitivity and mesh dependency issues and the definition of an accurate depth-dependent porosity would also require a modification of current deterministic porosity assignment algorithms. Furthermore, this would also be unsuitable for high resolution modelling of gates, since it would be approximated as an equivalent lateral contraction.

Therefore, a dedicated internal boundary condition for the purpose of modelling the passage of flow beneath linear fixed barriers to flow provides a unique opportunity to introduce the capability to model gate-type structures within two-dimensional shallow water models. Once more, the assumption of negligible width of the obstacle with respect to the geometry of the mesh must apply to minimise errors related to the lack of capacity to account for the reduction in storage capacity induced by the structure. However, the linear nature of gate-like features aligns well with these assumptions.

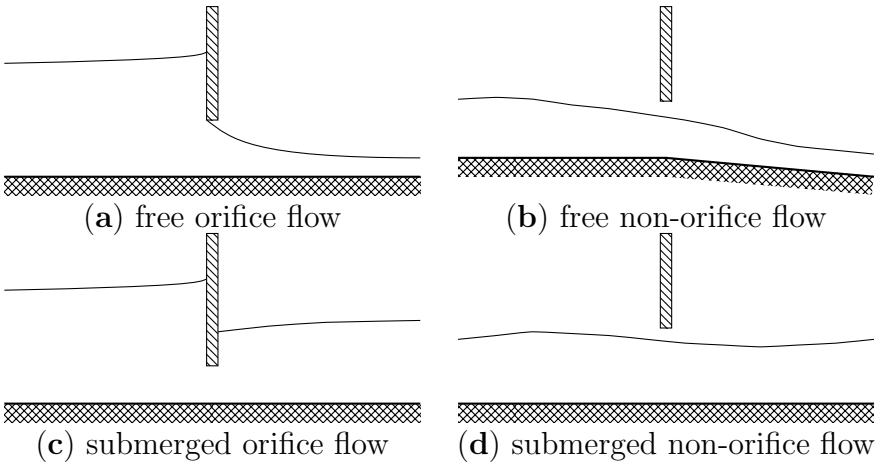

Figure 2.3: Depiction of the four potential flow regimes at a gate structure in accordance with classical hydraulic theory. Flow is directed from left to right.

As for localised contractions and expansions, a weak coupling of the conservation laws can be achieved via the method of Zhao et al. [498], whereby the mass and momentum fluxes are adjusted in accordance with the unit discharge calculated via appropriate empirical discharge formula. Morales-Hernández et al. [322] proposed an internal boundary condition based on this principle, using logical conditions to alter the empirical discharge relation based upon the relationship between the neighbouring left and right flow depths and the gate opening. Specifically, four potential flow configurations were considered:

1. When the upstream and downstream free-surface elevations do not exceed the elevation of the gate lip, non-orifice flow conditions are assumed and the gate interface is treated as a transmissive boundary.

2. When the gate is closed, the gate interface is treated as a free-slip reflective boundary.

3. When the upstream free-surface elevation exceeds the elevation of the gate lip, and the downstream free-surface elevation is exceeded by the elevation of the lip, the discharge across the gate interface is assumed to occur under free orifice flow conditions.

4. When both the upstream and downstream free-surface elevations exceed the eleva-

tion of the gate lip, the discharge across the gate interface is assumed to occur under submerged orifice flow conditions.

Hence, this method simplifies the determination of the flow regime (Figure 2.3) by neglecting the role of the *vena contracta* in determining the transition between free and submerged orifice flow [276, 203, 366, 215]. Moreover, capturing the transition between orifice and non-orifice regimes is also non-trivial as shown by Alminagorta and Merkley [17], who compared the use of an empirical equation, the traditional submerged non-orifice equation the specific-energy equation for open-channel flow to define the limit between the regimes. Within the transition region, defined by a lower limit corresponding to the the point at which the upstream free-surface reaches the gate lip and an upper limit corresponding to the completion of a hydraulic seal, empirical equations are typically of lower accuracy [17].

Comparisons with derived exact solutions, involving the time dependent opening and closing of two gates, demonstrate the effectiveness of the internal boundary condition. However, upon closer examination of the scenario for which the exact solutions are derived,

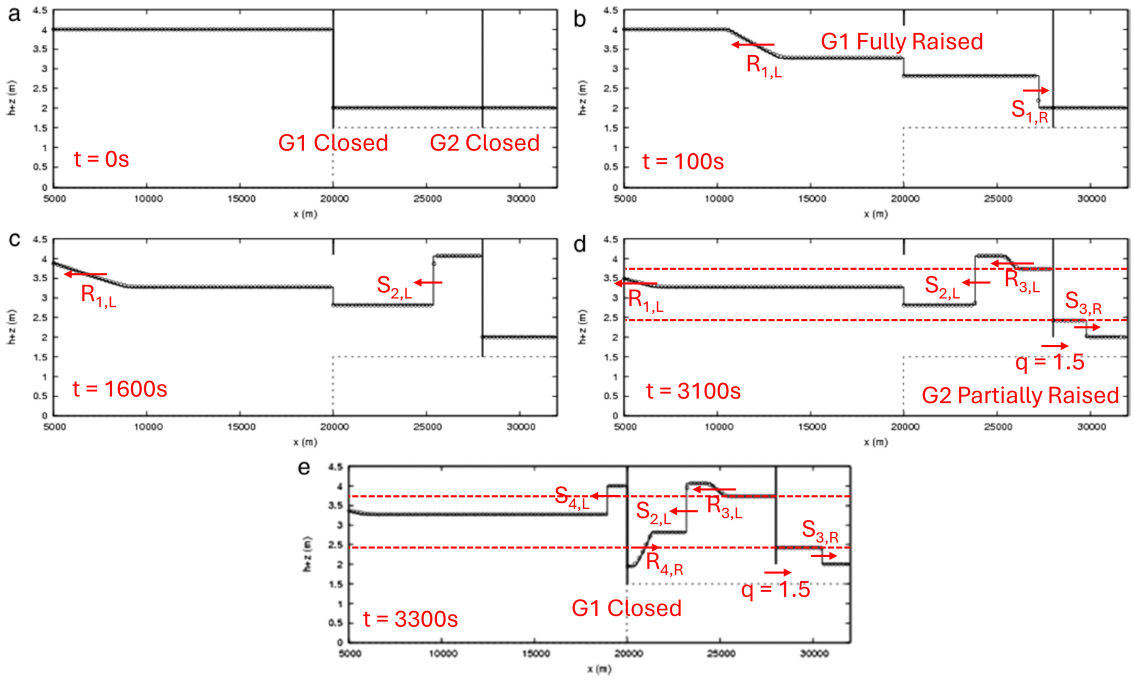

Figure 2.4: Annotation (red) of the elevation plots for the comparisons between the exact solution (solid line) and numerical solution (circles) provided in Morales-Hernández et al. [322].

it becomes apparent that the scenario does not adequately test the suitability of the proposed internal boundary condition for unsteady flow conditions. Referring to the annotated diagram provided in Figure 2.4:

(a) Shows the initial conditions at $t = 0s$. A bed discontinuity occurs at $x = 20000$, with closed gates $G1$ and $G2$ situated at $x = 20000$ and $x = 28000$, respectively.

(b) Shows the solution at $t = 100s$ where the first gate, $G1$, is instantaneously raised. This action initiates a dam-break problem, generating a leftward-moving rarefaction,

$R_{1,L}$, and a rightward-moving shock, $S_{1,R}$, separated by a stationary contact wave at $x = 20000$ above the bed discontinuity.

(c) Shows the solution at $t = 1600s$ following reflection of the rightward-moving shock, now labelled as $S_{2,L}$, against the fully closed second gate $G2$.

(d) Shows the solution at $3100s$, $500s$ following the initial opening of $G2$. The opening of $G2$ is controlled such that the discharge is maintained at a constant rate of $1.5m^2s^{-1}$. The opening of the gate produces another dam-break problem with a leftward-moving rarefaction, $R_{3,L}$, and a rightward-moving shock, $S_{3,R}$.

(e) Shows the solution at $3300s$, $200s$ after panel (d), following instantaneous closure of $G2$, which initiates another dam-break problem with a leftward-moving shock, $S_{4,L}$, and a rightward-moving rarefaction, $R_{4,R}$.

As such, the following properties are verified: (i) The internal boundary condition correctly functions as a transmissive boundary when fully open (ii) The internal boundary condition correctly functions as a reflective boundary when closed (iii) Under locally steady submerged flow conditions, the internal boundary condition accurately replicates the derived exact solution.

(i) and (ii) are to be expected, since transmissive and reflective boundary conditions are established boundary conditions which aren't unique to the modelling of gates. For case (iii), the artificially controlled raising of the gate to maintain an exact flow rate of $1.5m^2s^{-1}$, for which one must presume some circular logic has been implemented via the use of the same submerged discharge formulae to calculate the required opening of the gate, ensures that steady flow conditions are maintained in the proximity of the partially raised gate, as evidenced in panels (d) and (e) via the horizontal dashed lines. Typically the empirical discharge relations used in such methods assume steady or gradually varied flow and therefore optimal conditions have been established in the test, which are often not present during the propagation of rapid transients. Whilst it is understandable that the scenario has been designed in such a way to facilitate obtaining exact solutions by means of preserving the self similarity of the solutions, important requirements for unsteady applications such as the transition between flow regimes, an impinging hydraulic bore and rapid variations in the discharge remain untested.

The presented field-scale study of a historical flooding event in the Ebro River Basin demonstrates the capability of the internal boundary condition in contributing towards the replication of the historical flooding extents. However, the role of the gate in determining the flood extents is shown to be limited due to the extreme nature of the studied storm and therefore the overall suitability of the internal boundary condition remains somewhat inconclusive. Furthermore, comparisons with flood inundation extents reveal little in regards to the appropriateness of the internal boundary condition for modelling rapid transients, where the effects may be concentrated locally in space and time.

Further validation of the internal boundary condition is provided by Lacasta et al. [255] involving proportional-integral-derivative (PID) control of a series of gates along an irrigation channel located in Pina de Ebro, Zaragoza, replicating the measured flow conditions over a period of 120 hours. The presented results demonstrate that the model was able to accurately capture the water depth at each of the gates, when using a PID algorithm which adjusts the gate opening in accordance with the measured upstream water level. This is a valuable development for practical applications involving irrigation channels

where there is either upstream water depth measurements available or known gate operation criteria that can be integrated into a PID algorithm. However, when considering more generally obstacles which act as a partial barrier to flow in a gate like manner, PID control is not applicable; the PID algorithm can be considered in this case as an ad-hoc calibration method for the discharge through the internal gate boundary conditions. PID algorithms may also experience a short lag period as the algorithm attempts to converge to the new setpoint, which may be problematic for highly transient flows.

Jaafar and Merkley [237] present a more detailed method that couples the shallow water equations with equations for free and submerged orifice and non-orifice flow regimes via characteristic equations. In contrast with the method presented by Morales-Hernández et al. [322], empirical equations are used for non-orifice flow regimes, as opposed to the use of the unaltered shallow water fluxes, and a more sophisticated determination of the flow regime is utilised. This does introduce some uncertainty, with the potential for calibration, via the introduction of a parameter, $C_0 \in [0.8, 0.99]$, which controls the threshold between orifice and non-orifice flow, as determined by Alminagorta and Merkley [17]. Although, compared with the method of Morales-Hernández et al. [322], this is equivalent to the determination of the energy loss coefficients introduced into their chosen form of the discharge formulae. The presented test cases demonstrate that the method is able to accurately capture the transition between the four potential flow regimes. The main drawback of the method is the potentially high computational cost of the solution method, requiring the iterative solution of a higher order non-linear polynomial, for which existence of a solution is not guaranteed [122, 119, 150].

Cozzolino et al. [122], contributed to the derivation of internal boundary conditions for the modelling of gate-type structures by analysing the solution of the dam-break Riemann problem for a partially lifted gate. The presented solution procedure utilises gate equations based upon the classical Energy-Momentum (EM) formulation [216], assuming a constant contraction coefficient that does not depend on the relative opening of the gate and is based only on the initial state of a transient. Whilst the Authors' acknowledge, with reference to experimental and theoretical studies, that for steady state conditions the relative opening of the gate does in fact influence the value of the contraction coefficient for both real and ideal fluids, if it is considered to *only* depend on the relative opening then the self-similar nature of exact Riemann solutions implies a time invariant contraction coefficient for the derived analytical solutions.

The use of the classical EM gate equations is also somewhat problematic as the equations are unable to adequately capture the transition between free and submerged flow conditions, whereby partial submergence is attained. This manifests itself within the chosen gate equations as a sharp drop in the predicted discharge at the limit between free and submerged flow conditions. As a consequence, it is not possible to derive an analytical solution for some initial conditions. In spite of this finding, numerical schemes produce seemingly sensible results within the sub-domain for which no solution exists, undermining confidence in previous approaches to the problem.

Considering the special case of an initial dry bed, Cozzolino et al. [122] demonstrate the existence of multiple solutions. To overcome this, a disambiguation criteria based upon the principle of maximising discharge is selected. Although there is some uncertainty in this assumption, it is supported by referenced experimental studies and has been applied successfully in a similar scenario to characterise the geometry of a submerged jet. The

analytical solutions are presented as an aid to assist the development and verification of future numerical schemes however, it should be noted that there are ambiguities relating to the underlying assumptions that must be considered although, they are handled transparently and in great detail by the Authors.

Results produced by a first-order finite volume numerical scheme based upon the third-order Spectral Volume scheme of Cozzolino et al. [116], which primarily differs from that of Morales-Hernández et al. [322] via the use of more sophisticated criteria to determine the flow regime, demonstrate convergence to the derived analytical solutions. Interestingly, the coarse mesh results highlight the implicit assumption that by applying the steady state empirical discharge relations in the presented manner, an instantaneous equilibrium is assumed between the upstream and downstream flow variables. In reality there is a short lag time before hydraulic conditions are equilibrated by the numerical scheme, in which the adaption time is dependent on the speed at which information travels which is of course proportional to the dimensions of the mesh. This result shows that so called '*equilibrium approaches*' may lose accuracy as a consequence of insufficient mesh resolution in the presence of rapid transients.

Following the work of Cozzolino et al. [122], a study conducted by Lazzarin et al. [260] aimed to verify the physically relevant solution for dam-break flows across a partially raised gate and to study the stability of free orifices flow at large gate openings. The conclusions of the study were twofold; (i) the correction disambiguation criteria is the *minimisation*, not maximisation, of discharge across the gate (ii) for large gate openings the dependence of contraction and discharge coefficients on the relative gate opening has a significant influence on the stability of orifice flow.

Consequently, these findings were addressed by Cozzolino et al. [119], via the derivation of improved analytical solutions and a corresponding new approximate Riemann solver. The improved approach replaces the classical EM gate equations for determining submerged flow, due to the presence of the aforementioned discharge gap, with an improved expression provided by Bijankhan et al. [64]. Furthermore, an improved method for calculating a variable contraction coefficient, that accounts for the continuous dependence of the contraction coefficient on the flow variables, is introduced, based on an experimental formulation provided by Defina and Susin [132].

The identified issues relating to the assumption of instantaneous equilibrium are overcome through a relaxation of the gate equations, referred to as the '*non-equilibrium approach*' by the Authors. The novel form of the equations seeks to reduce the error produced by equilibrium formulations by relaxing the requirement for discharge invariance through the gate. Moreover, an improved disambiguation criteria is introduced based on the continuous dependence of the solution on the initial conditions, which contradicts the criteria determined by Lazzarin et al. [260] within a very small region, corresponding to a gate opening to initial depth ratio of between 0.491 and 0.495. However, the incongruency can be physically justified by considering the role of friction within the laboratory experiments, which is neglected in the derivation of the analytical solutions.

The results produced by a simple numerical scheme demonstrate the superiority of the *non-equilibrium approach* in replicating the derived analytical solutions and the dam-break experiments performed by Lazzarin et al. [260]. Overall, the work of Cozzolino et al. [119] represents a significant advance in terms of the development of a suitable internal boundary condition for the modelling of gate type structures within hydrodynamic models.

Other than the validation of the interactions resulting from an approaching supercritical bore it is hard to identify where the method is lacking and it appears that only incremental improvements may be achieved via improved discharge relations. The largest conceivable improvement would be to somehow remove any reliance on empirical discharge formulae however, such an approach is challenging to envisage. The relative simplicity and ease of implementation, especially when compared to methods which necessitate the use of non-conservative numerical schemes, is a clear advantage.

Modelling Weirs

When considering the modelling of weir-type structures or more generally just the overtopping of obstacles to flow, the topic has already been discussed briefly within Section 2.2.2, in relation to the suitability of the finite bottom elevation method. Unlike an internal boundary condition, modelling an obstacle with the finite bottom elevation will account for the storage reduction induced by the obstacle, which will be of importance if the size of the obstacle is sufficient. However, without special treatment, the assumption of a continuously varying bed slope will result in representation errors for objects with sharp façades. Furthermore, the SWE are not strictly valid across steep slopes so the validity of overtopping flows in the presence of slope gradients that exceed $\approx 6^\circ$ or $1:10$, is questionable. Whilst the use of the SSWE is a possible solution, it appears an unnecessary solution when the slopes are likely an unwanted aspect which degrades the quality of the representation.

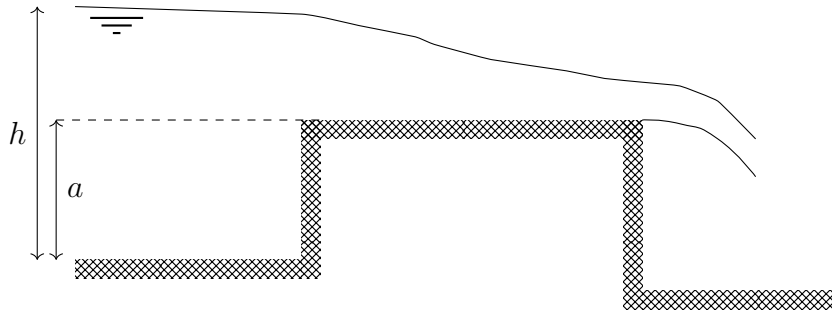

Figure 2.5: Conceptualisation of a non-submerged broad crested weir as a bed discontinuity. h is the depth of the approaching flow and a is the height of the weir, above which critical flow conditions are attained at the crest.

An alternative solution, as proposed by Cozzolino et al. [115, 117], is to interpret the solution of a the Riemann problem across a bed step as equivalent to a broad-crested weir, as shown in Figure 2.5. The solution procedure leans on existing theory for the treatment of shallow water equations with bottom steps, which is analogous to a channel width discontinuities, belonging to the more general class of Riemann problems containing geometric discontinuities. For the case of a broad-crested weir, it is assumed that energy conservation is enforced across the bed discontinuity and that critical depth conditions are attained atop the weir crest. Due to the presence of non-conservative product terms, corresponding to the geometric discontinuity, the theory of Dal Maso et al. [127] must be used to select an appropriate family of paths such that weak solutions can be obtained via the definition of a generalised Rankine-Hugoniot condition.

Cozzolino et al. [115] defined two families of paths and demonstrates that the multiplicity of solutions is independent of the choice of multiple paths due to resonance effects pro-

duced by the superposition of characteristics from different characteristic fields. Following implementation of a simple numerical scheme, the capability of the proposed solution procedure is demonstrated via comparisons with exact solutions for simple but challenging scenarios, where the right boundary condition is defined as a broad crested weir with a right dry state. However, the lack of experimental validation fails to verify that the path definitions result in convergence to the physically congruent weak solution.

This was later addressed in a following publication by Cozzolino et al. [117]. A third path definition is introduced and criteria for the disambiguation of solutions are presented on the basis of a physical interpretation of the problem and the results of relevant laboratory experiments. A more comprehensive analysis of the proposed solution is presented via comparisons with derived analytical solutions and the results of laboratory experiments, with a naive implementation of the weir boundary condition, which is only rigorously valid for steady subcritical approaching flow, providing a benchmark reference.

The results demonstrate the general suitability of the boundary condition for modelling transient flow interactions across a broad crested weir and the capacity to produce physically relevant unique solutions for all potential initial conditions consistent with the presented disambiguation criteria. Comparisons with the naive approach demonstrate that the methods converge to the same solution when the assumptions for the naive approach are satisfied however, the proposed approach demonstrates a greater level of accuracy on coarser grids due to a superior capability to capture transient variations. This corroborates with the observations of Cozzolino et al. [119] for internal gate boundary conditions, where the naive approach is referred to as an equilibrium approach and the time required for such a scheme to drive the neighbouring states to equilibrium is dictated by the speed at which information travels through the computational grid, which is proportional to the mesh spacing. For the case of approaching supercritical flow that remains supercritical over the weir crest only the proposed solution is able to correctly capture the behaviour.

An alternative approach, which forgoes the use of a non-conservative scheme based upon the solution of a Riemann problem containing a geometric discontinuity in favour of coupling the weir equations with the SWEs via nodal conditions [67] is provided by Guerra et al. [190]. Although the proposed scheme has the benefit of being conservative, the method is only valid for subcritical approach flows, diminishing the flexibility of the method in comparison with that of Cozzolino et al. [115, 117]. As a consequence the potential multiplicity of solutions is not considered. Furthermore, only validation by expert falsification is presented, with no comparisons to other schemes, analytical solutions or experiment results given. In the regions for which the approach is valid, the method of Guerra et al. [190] appears consistent with that of Cozzolino et al. [115, 117].

The solution procedure presented by Cozzolino et al. [115, 117] therefore presents a satisfactory method for the treatment of non-submerged broad-crested weirs. As demonstrated by the accurate reproduction of the analytical solutions and experimental results, the proposed boundary condition is suitable for modelling a one-dimensional domain which is bounded by a non-submerged broad-crested weir. However, the general applicability of the method for the modelling of obstacles which may be overtopped and/or act as weirs, is perhaps questionable as the assumption of a dry state atop the bed step is better suited to an external boundary condition. At a minimum, the method would require modification to ensure the existence and uniqueness of solutions for submerged conditions for

more general deployment of the method within two-dimensional models as an internal boundary condition. The fact that the modelling of the obstacle as a bed step accounts for the reduction of storage capacity is potentially positive, providing greater accuracy for obstacles of non-negligible width however, it is detrimental for the modelling of highly linear features.

The non-conservative nature of the scheme, as for all schemes concerned with the numerical solution of Riemann problems involving geometric discontinuities presents a numerical challenge. The nodal coupling approach used by Guerra et al. [190] therefore warrants further exploration to see if a suitable conservative alternative can be derived, provided a solution to overcome the ill-posed initial conditions can be found. A relaxation of the weir equations, as per Cozzolino et al. [119] for internal gate boundary conditions, would likely be required to overcome the issues related to equilibrium approaches.This would also require experimental and analytical validation of the method which is currently lacking.

Modelling Combined Weir and Gate Flow

While the ability to model gate and weir flows separately and individually is crucial, there are instances where it becomes necessary to simulate the combined flow induced by simultaneous gate and weir flows. An exemplary scenario is an overtopped bridge deck, where the passage of flow is permitted both beneath its low chord and above its deck. However, such scenarios are also ubiquitous at smaller scales in urban environments when considering the localised impacts of intruding flows and street furniture. Furthermore, in the design of weirs as a mechanism for flow control or measurement, gate or orifice openings are often introduced to improve hydraulic performance and remove sediment [389, 393, 391]. Since the presented methods for modelling gate and weir flows individually are not suitable for combined gate and weir flows, a dedicated method is required.

Whereas the hydraulic theory regarding the discharge relations across gates and weirs is well developed, with well established empirical discharge relations available in classical literature, the corresponding theory for combined gate and weir flow is comparatively less developed. As explained by Salehi and Azimi [389], combined gate and weir discharge cannot be determined by a simple superposition of weir and gate discharges due to interactions between the flows and as a consequence, the derivation of suitable discharge relations is the subject of recent research [389, 393, 464, 391, 172, 390].

There is therefore potential for development of a nodal coupling approach, as implemented by Cozzolino et al. [119] for partially lifted gates, however, no such method has been developed as of yet and it should be expected that further experimentation will be required to disambiguate the likely non-unique solutions for certain initial conditions, particularly incipient dry states. Within the wider field, physically based approaches, such as the work of Salehi et al. [391], have been successful in replicating combined weir and gate flows within CFD packages.

One of the few established methods for modelling combined weir and gate flow is the internal boundary condition proposed by Dazzi et al. [129]. The proposed internal boundary condition uses the method of Zhao et al. [498], with a similar implementation to that of Morales-Hernández et al. [322], adapted to consider gate and weir flow. The main difference in comparison with the method of Morales-Hernández et al. [322], other than the inclusion of weir equations, is the use of gate formulae to tentatively determine the depth

at the *vena contracta* and the corresponding conjugate depth to determine the transition between submerged and free flow conditions, similar to the approach of Cozzolino et al. [122].

The combined weir and gate flow is modelled simplistically as a superposition of gate flow and weir flow, neglecting the interaction between the flows, which contradicts experimental observations and theory [389, 393, 464]. Furthermore, the method sacrifices accuracy in favour of efficiency, utilising a non-conservative form of the equations to ensure well-balancing and treating the upstream and downstream of the internal boundary conditions in a quasi-one-dimensional manner. The latter, corresponds to an assumption that the neighbouring flow is perfectly perpendicular to the interface and may result in unphysical directionality, especially for skew features. The method therefore represents a simple equilibrium method which is easily implemented and computationally efficient but unsuitable for rapid transients and limited to applications in which local accuracy is of lesser importance.

The only established alternative method capable of handling simultaneous gate and weir flow is the method presented by Ratia et al. [371]. The proposed method is presented as an alternative to modelling bridges with a refined mesh and vertical wall boundaries, implementing a computationally efficient modified Borda-Carnot equation to account for the losses induced by contraction and expansion of flow through a hydraulic structure, enabling the modelling of all potential flow regimes. Whilst this method is effective in capturing the macro-scale effects induced by the presence of the structure, it is unable to sufficiently capture near-field flow effects including potential downstream supercritical flows.

It can be speculated that a combination of a refined mesh, vertical walls and the novel head loss term may be used to produce greater accuracy than a simple refined mesh with vertical wall representation however, the use of the head loss term can require impractical calibration to produce effective results [96]. Following a review of the introduction of Borda-like head loss terms within porosity models in Section 2.2.2, this is an unsurprising result. Furthermore, the recent work of Goudiaby and Kreiss [186] on the existence of solutions for the coupling of shallow water and Borda-Carnot equations with Riemann data has demonstrated a lack of existence of solutions for certain initial conditions. Hence, it should be considered that a method based on static equations such as the Borda-Carnot equations are likely inadequate for unsteady applications.

Therefore, in contrast to the prior discussed features, there is significant progress to be made in the modelling of partial barriers to flow which permit combined gate and weir flow, with no existing method providing a suitable solution. Moreover, the development of an internal boundary condition which can adequately model gate flow, weir flow and combined gate and weir flow presents a unique opportunity to develop a flexible and general solver for linear features which act as partial barriers to flow within urban hydrodynamic models.

However, when considering the development of a flexible and general solver for partial barriers to flow, it is worth considering the potential for pressurisation resulting from the vertical confinement of flow induced by a structure. The classical SWEs assume a hydrostatic pressure distribution and therefore modification of the conservation laws is required to relax this constraint and account for the effects of vertical confinement. As demonstrated by Munoz and Constantinescu [327], adequately accounting for non-hydrostatic

effects is required for analyses of bridges subjected to extreme flood flows. Although two-dimensional shallow water models are to be considered inadequate for detailed analyses of individual structures, the effect of pressurisation on the local flow characteristics is important to consider when the streamwise width of a structure cannot be negligible with respect to the mesh geometry. Consider for example, large bridge structures or underground river reaches within urban areas.

One of the simplest methods to account for the vertical confinement of flow is the use of the Preissmann slot concept [363] as proposed by Cunge and Wegner [125]. This has been incorporated within a shallow water model for the purpose of modelling structures by Maranzoni and Mignosa [289]. However, the Preissmann slot concept suffers from some severe limitations that reduce its effectiveness and practicality as discussed by Vasconcelos et al. [462] and Malekpour and Karney [287]:

1. The introduction of the hypothetical slot may introduce an additional fictitious storage capacity, which may also adversely impact the prediction of advancing waves.

2. When pressurisation occurs, the width of the slot should be selected to reproduce a physically representative wave celerity for transient pressure waves. However, accurate sizing of the slot width may result in an impractical reduction of the time step for acoustic wavespeeds on the order of hundreds of meters per second.

3. When there are mixed flow regimes or regime transitions and the wave celerity is very large, diffusive numerical schemes introduce excessive numerical diffusion within free-surface portions of the flow.

4. Post shock oscillations may occur behind bores which induce pressurisation.

Moreover, the proposed method is unable to handle overtopping of the structure, suitable only for free-surface or pressurised flow which passes underneath a structure.

Cea et al. [96] propose an alternative method that also addresses the vertical confinement of flow induced by structures with fewer practical and theoretical challenges. This method modifies the shallow water equations in accordance with an adapted two-component pressure approach [463]. In this case, the roof inducing the vertical confinement of the flow is considered to be elastic, with the elasticity controlled by a stiffness constant which also determines the pressurised wave celerity, just as the slot width does for Preissmann slot based methods. As for Preissmann slot based methods, in practice, a compromise must be found between numerical stability and accuracy for cases involving heavily pressurised conditions [93]. The main benefit of the two-component pressure approach in comparison with the Preissmann slot concept is therefore the fact that only the stiffness constant requires calibration for the two-component pressure approach whereas, the calibration of two slots must be performed for Preissmann based approaches. When the two-component pressure approach of Cea et al. [96] was applied to the modelling of bridge structures the method was found to be comparable to that of Ratia et al. [371], in that it was unable to accurately capture nearfield flows patterns, with the benefit of not requiring excessive and impractical calibration. However, the method is unfortunately incompatible with the modelling of the overtopping of structures.

The congested shallow water model derived by Godlewski et al. [182] enables the introduction of a static or dynamic roof which constrains the water surface. However, implementing the congestion constraint across the entirety of the computational domain

is unnecessary and likely unfeasible from a computational efficiency perspective due to the complicated numerical requirements of the proposed relaxation scheme. Furthermore, a localised implementation restricted only to the cells which contain a structure is unlikely to be feasible due to compatibility issues with standard solution methods applied to classical shallow water models; for the congested shallow water model, classical Godunov solvers are too dissipative and impose too much restriction on the timestep [137, 192]. As for the other non-hydrostatic models that have been considered, the method is incompatible with the modelling of overtopped structures.

It is possible to incorporate the effects of vertical confinement within an initial value boundary problem as demonstrated by Iguchi and Lannes [229], who considered the problem of a floating body. However, coupling strategies typically require the assumption of smooth flow to enable a transmission condition to be defined at the coupling surface which is not suitable for hydrodynamic modelling applications concerned with unsteady and transient flows [182]. A further example of such an approach is provided by the work of Bosi et al. [68], who presented a depth-integrated boussinesq model for modelling non-linear wave-body interaction, suited for modelling floating bodies in marine applications.

Therefore, whilst the satisfactory numerical treatment of pressurised flows is highly desirable to adequately account for the effect of vertical confinement of flow by structures, it is not possible, or likely required due to the localised nature of the effects, for structures modelled as internal boundary conditions. Although methods exist for the suitable treatment of non-hydrostatic pressures for structures that aren't of negligible streamwise width, the challenge of representing overtopping flows remains open. The modelling of disjoint layers of flow within mono-layer or multi-layer shallow water models is challenging and perhaps best left to detailed three-dimensional analyses of individual structures provided suitable two-dimensional approximations can be derived.

2.2.4 Summary

Following a review of the available numerical methods for modelling obstacles to flow within two-dimensional hydrodynamic models it is clear that there is a gap in modelling capabilities for combined gate and weir flow. For solid obstacles which are considered to be completely impervious, the vertical wall method with a sufficiently refined mesh presents an optimal method of representation. The main challenge is in designing a suitably conformal mesh and managing the computational burden produced by the required mesh refinement. Where obstacles are sufficiently small such that adequate mesh refinement is unfeasible, the internal boundary condition proposed by Pepe et al. [359] provides a suitable solution for capturing sub-grid contractions and expansions of flow. However, the non-conservative nature of the method poses some numerical challenges.

The use of an optimised differential porosity model presents an intriguing alternative to classical shallow water based models. However, it remains to be seen whether such models are simply a computationally efficient method for determining macroscale flow characteristics or whether they can be implemented on a sufficiently refined mesh to provide results which are accurate enough to enable local flood hazard and vulnerability analyses. There are however, some limitations with the method in terms of accurately modelling features such as weirs and gates, particularly for differential forms. Furthermore, the non-conservative nature of the resulting schemes presents numerical challenges,

especially since strong porosity discontinuities should be expected within realistic urban environments.

For obstacles of significant streamwise width with respect to the mesh that permit the passage of flow through their footprint but are not overtopped, local implementation of a suitable non-hydrostatic model may be considered to account for pressurisation. However, issues relating to the numerical treatment of highly pressurised flows requires further attention. For linear features which act as gates, the internal boundary condition proposed by Cozzolino et al. [119] is capable of modelling transient flow variations, distinguishing the physically relevant and unique solutions.

Obstacles which act as weirs are perhaps more challenging. The method of Guerra et al. [190] is simple and easy to implement but it is only well-posed for subcritical approaching flows when the weir is unsubmerged. There is also a lack of validation which must be overcome. The method of Cozzolino et al. [115, 117] is well-posed and extensively validated for transient flows however, the non-conservative nature of the scheme is a potential barrier to implementation.

In contrast to the method of Guerra et al., the method of Cozzolino et al. acts at the scale of the mesh, treating the obstacle as a bed step, atop which there is an assumed dry state. This may be a benefit for representing obstacles which are not of negligible streamwise width however, under such circumstances the underlying assumptions are somewhat questionable. Indeed, the assumption of a dry state atop the bed step suggests that the method is more suited to implementation at external domain boundaries, where it can easily be ensured that an external ghost cell maintains a dry state despite flow over the weir.

It is therefore unclear as to how the method could be adapted for use as an internal boundary condition and the mesh scale nature of the method may prove problematic for linear features. Without a special numerical treatment, as soon as there is flow across the bed step, the assumption that the state atop the crest is dry and that critical flow conditions are attained will be violated. Since the more general problem of shallow water flow across a bed step has been extensively researched [348, 13, 121, 211, 453], it could be possible to use this as a method for representing mesh scale obstacles which may be overtopped. However, the validity of such an approach has yet to be explored in practice. Therefore, further work is required to:

1. Determine what obstacles to flow can be approximated as behaving like weirs when overtopped and whether modelling urban obstacles of non-negligible width as bed steps, or even finite bottom elevations, is viable.

2. To extend, if possible, the validity of the method of Guerra et al. [190] to all potential flow regimes, including the adequate disambiguation of non-unique solutions.

3. To investigate modification of the method of Cozzolino et al. [115, 117] to enable implementation as an internal boundary condition, where obstacles may be approximated as acting like unsubmerged broad-crested weirs.

When considering the modelling of partial barriers to flow which may permit the simultaneous passage of flow under and over their form, there is a lack of suitable options for high resolution modelling in the presence of transient flows. The proposed research objectives:

Objective 1: To develop and experimentally validate a novel approximate Riemann solver (Solver 1) capable of resolving numerical fluxes across a linear fixed immiscible partial barrier to flow, with a focus upon ease of implementation and compatibility with existing flood models to promote uptake in practice.

Objective 2: To develop and experimentally validate an improved approximate Riemann solver (Solver 2) capable of resolving numerical fluxes across a linear fixed immiscible partial barrier to flow, with a focus upon maximising accuracy.

therefore address this gap within the research directly. As detailed in Section 2.1.1, the accurate modelling of obstacles to flow is crucial for accurately predicting the local flow characteristics and subsequently in Section 2.1.2 it was shown that in order to accurately characterise local flood hazards and vulnerabilities, it is necessary to accurately predict the local flow characteristics. There is therefore a mutual feedback mechanism between the accurate representation of obstacles to flow and the characterisation of the associated flood risk and hazards. The lacking capacity to model partial barriers to flow which enable simultaneous gate and weir flow is therefore a restriction upon the ability to accurately analyse localised flood risk and flood hazards and the outlined objectives seek to address this directly.

The experimental validation of the solvers is intended to ensure the physical relevance of the solutions and provide a mechanism for understanding the limitations of the method. Furthermore, the publishing of the associated validation datasets will aid the development and validation of other relevant solvers. The contrast between the two proposed solvers in terms of complexity and accuracy is designed to provide flexibility. It is hard to forecast the computational cost and accuracy of the proposed solvers and therefore by aiming to provide flexibility in terms of accuracy and computational complexity it is intended that the likelihood of uptake and implementation is maximised. It is certainly possible that both solvers will prove viable solutions depending on the desired application.

2.3 Urban Hydrodynamic Flood and Water Quality Modelling

When reviewing recent advances in the experimental data and validation supporting the development of hydrodynamic modelling, Mignot et al. [310] emphasised that the forthcoming generation of urban flood models should be multifaceted; urban flood models should not only accurately simulate the hydrodynamic characteristics of the flow, they should also possess the capability to effectively account for the myriad of '*associated events*'. Among the various *associated events*, it is crucial to consider the capability to account for hazards related to the contamination of water by pollutants or pathogens. This capability is important from a practical perspective and an intuitive addition from a mathematical perspective. Furthermore, the capacity to model advection, diffusion, and, if necessary, reaction of passive scalar quantities is not limited to hazards alone. Such capabilities also find relevance in fertigation applications [83] and the environmental study of fluvial ecosystems [474].

The addition of advection-diffusion(-reaction) equations to the two-dimensional SWEs is relatively straightforward under the classical assumptions that the quantity is well-mixed in the vertical direction and that the quantity is passively advected with the fluid, negli-

gibly influencing the dynamics of the flow for sufficiently small concentrations [438]. It is straightforward to add as many unique species equations as desired, albeit at an increasing computational cost. When considering the eigenstructure of the coupled system, the advection-diffusion equations are entirely analogous to the tangential component of the velocity and hence coupling with the two-dimensional shallow water equations is numerically simple, although some additional computational burden is introduced especially when considering the source terms relating to the diffusion and reaction of the quantity. Since, it is assumed that the quantity transported by the flow does not effect the flow dynamics it is also possible to implement a decoupled treatment of the transport problem.

2.3.1 Flood Hazards and Water Quality

Since the turn of the millennium, there has been a growing emphasis on water quality policy implementation. This is highlighted by initiatives such as the European Union Water Framework Directive [431], United States Clean Water Act [106], Australian National Water Quality Management Strategy [33] which is supported by frameworks such as the European Water Initiative [156] and the United Nations Sustainable Development Goals [448]. With regards to water quality, sources of pollution are typically divided into point and non-point sources.

A point source refers to the collection and discharge of pollutants from a single, identifiable source. Examples of point sources include sites such as sewage treatment plants, factories and oil refineries or accidental emissions and spillages from incidents such as road traffic accidents, spillages and the exceedance of sewerage capacity. Discharges from these sources include heavy metals, pathogens, nutrients, oxygen-depleting substances and toxic chemicals [238].

A non-point source is diffuse in its origins and cannot be easily attributes to a single source. Typically, non-point sources of pollutants are mobilised by rainfall runoff, which is exacerbated by the increase in impervious surfaces brought about by urbanisation [288, 181]. Pollutant concentrations are typically higher following dry periods and during the start of a rainfall event due to a phenomena referred to as the '*first flush*' [60]. The *first flush* phenomena occurs when high concentrations of pollutants accumulate on impervious surfaces during dry periods and are subsequently rapidly dispersed by a rainfall event. Examples of non-point sources include excess fertilisers, herbicides and insecticides, oil, grease, sediment, salt, bacteria and nutrients [238]. This form of pollution has become a predominant contributor to the degradation of water quality, leading to the concept of priority pollutants of storm waters [469]. However, there is great complexity involved in modelling, controlling and monitoring of diffuse pollution sources due to inherent uncertainties that are involved.

In some cases an additional category is introduced, referred to as internal pollution. Internal pollution refers to the pollution emitted by water bodies due to the degradation of floating matter such as litter, aquatic plants and algae and via the release of contaminants from sediment [214]. Sewage discharges into water bodies are a major contributor to internal pollution sources, as they may lead to the formation of a thick black and odorous sediment layer which release pollutants and degrades the water quality [214, 473, 99, 409]. Other contributors to internal pollution include agricultural and aquacultural backwaters and industrial wastewaters [214].

The hazards associated with contaminated water are numerous and varied:

Human Health: Human exposure and ingestion of waterborne pollutants can severely impact health, potentially disrupting endocrine formation [139], increasing cancer risk [326], and causing microbiological illnesses and infectious diseases [9]. In particular, the spread of epidemics has been shown to be correlated with flooding events [372, 293]. Since a significant number of human diseases are linked directly to unsafe drinking water and inadequate sanitation, the pollution of drinking water source areas is particularly hazardous [397].

Environmental Degradation: Pollution of water bodies can lead to severe eutrophication and the death of aquatic ecosystems [214]. Furthermore, this may result in the occurrence of odorous black water agglomerates which emit odorous gasses [473]. More generally, the pollution of water bodies results in a reduction of biological diversity and a loss of ecological integrity for freshwater ecosystems [26]. There are also feedback mechanisms effecting related economic activities and human health, with Bickford et al. [63] identifying non-carcinogenic risks due to the ingestion of fish in contaminated waterbodies.

Economic Losses: Decontamination of polluted water bodies and the treatment of water for the purposes of drinking is costly and time consuming [223]. Furthermore, flooding induced damages may be exacerbated by flood water which is contaminated by hazardous pollutants [384]. The contamination and subsequent closure of swimming and bathing areas also induces economic losses [9].

Preventative action and swift emergency response, where prevention fails or is absent, is therefore required to manage the associated risks and minimise harm.

2.3.2 Field-Scale Applications

As evidenced, water quality has been the focus of global policymakers. For practitioners concerned with water quality, hydrodynamic models, capable of modelling water quality, are an important tool. The following sections are therefore dedicated to exploring the existing role of hydrodynamic models within academic literature relating to the transport of scalar quantities.

Source Identification

Disastrous point source emissions are fortunately rare. However, they are also hard to predict, with the potential for widespread hazards. An extreme example is the Fukushima nuclear accident which occurred in March 2011, resulting in the widespread dispersion of radionuclides [446]. Smaller scale point source emissions are of increasing frequency in developed urban areas due to ageing drainage and sewage infrastructure which is increasingly unable to cope with demand. This demand is only expected to worsen due to increasing urbanisation and anthropogenic climate change [28]. In the United Kingdom it is estimated that two-thirds of urban flooding is a result of the exceedance of urban drainage system capacity [406] and Thames Water were fined £6million for releasing raw sewage into surface waters due to a lack of sewerage capacity [152].

Under the acceptance that prevention is not always possible, there has been much research interest in methods for source identification. Following detection of pollution, a reliable

and accurate estimation of the time, source location and source intensity of a point source following an accidental or intentional discharge is an important process. Once the source is identified optimal remediation strategies can be executed and the responsible parties may be fined and/or charged for remediation costs via powers granted by environmental policy.

The required unknown information regarding the point source may be retrieved via solution of an inverse transport model. The inverse transport model considers the backwards in time evolution from the measurement(s) to the unknown source. However, the inverse transport problem is ill-posed as per the well-posedness criteria of Hadamard [204]; whilst the existence criteria is satisfied, the problem is under-determined, due to the limited data availability, and the problem is also unstable, since small errors in the measured data may produce large errors in the solution, or more precisely, there is a lack of continuous dependence of the outputs on the the input data [42]. Further complexity is introduced by inherent epistemic and aleatory uncertainties in the model and data. This is then amplified further if multiple point sources coexist.

Solution procedures can be categorised into three groups: (i) simulation-optimisation methods [281, 475, 267, 495, 36, 35] (ii) probabilistic and geostatistical methods [478, 477, 476, 487, 497, 494, 126, 202, 213, 496] (iii) mathematical models [351, 317, 272, 284, 22, 210, 209], which are compared in Table 2.1. A thorough review of contemporary inverse modelling of contaminant transport for pollution source identification in surface and groundwaters can be found in Moghaddam et al. [42]. In each case a direct model, that is the forward in time physically based modelling of the pollutant transport as would be solved in a hydrodynamic model, is used in combination with an inverse model, as shown in Figure 2.6.

Method	Advantages	Disadvantages
Simulation-optimisation	Simple	Non-unique solution & high computational cost
Probabilistic and geostatistical	Requires fewer simulations, accounts for uncertainty	Limited number of identifiable pollutant sources
Mathematical	Computationally efficient, unique results	Complex

Table 2.1: Simple comparison of inverse methods for solving the inverse transport problem [42, 18].

Surface water source identification is a nascent field compared to groundwater studies, which originated approximately four decades ago [18, 478]. Surface water approaches have tended to use simplified forward models, limiting their effectiveness. Amiri et al. [18] therefore proposed a general framework for integrating established hydrodynamic modelling software with pollutant transport capabilities into inverse modelling contexts. Recent advancements, such as the novel remote sensing based inversion technique proposed by Luo et al. [283] demonstrate that the growing integration of more sophisticated

forward models is already manifesting in positive research developments and applications. However, despite the outlined potential for point source emission during urban flooding events, applications involving point source identification following urban flooding involving sewerage exceedance are not apparent. There is therefore scope for future research with regards to urban applications as the fields of source identification and hydrodynamic modelling continue to mature.

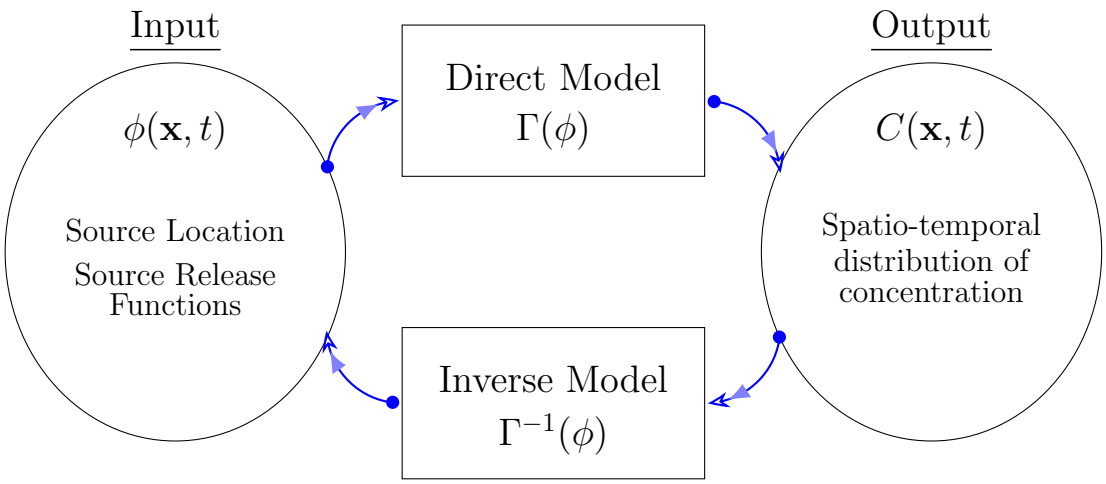

Figure 2.6: The relationship between a direct and inverse model of pollutant transport for point source identification, adapted from Moghaddam et al. [42]. $\phi(\mathbf{x}, t)$ denotes the source term which includes all of the pollution sources. $C(\mathbf{x}, t)$ denotes the spatio-temporal distribution of the pollution concentration in the solution domain.

Real-time Forecasting

The real-time forecasting and subsequent prediction of pollution events is critical for ensuring sufficient lead time to implement protective measures and, where necessary, proactive remediation strategies [394]. Sämann et al. [395, 394] proposed a Lagrangian transport model coupled with a dual-drainage model to develop a computationally efficient method for real-time forecasting of potential point source pollution emissions originating from surcharged sewers. Optimisation of computational efficiency is necessary for real-time forecasting applications to ensure a timely forecast process. Consequently, the authors investigated potential simplifications of the hydrodynamic component of the model. However, the research concluded that no meaningful simplification of the hydrodynamic processes could be recommended [395]. This is primarily because accurately predicting the transport dynamics demands high spatio-temporal resolution of the flow patterns, especially for abrupt changes.

Similarly, Kim et al. [247] developed a forecasting system to prevent contamination of drinking water resources following chemical accidents. The proposed model coupled the Storm Water Management Model (SWMM) [306], for modelling the subsurface domain, with a three-dimensional environmental fluid dynamics model [10], for modelling the surface domain. The capability of the model is assessed through the analysis of hypothetical scenarios, and although the results appear sensible, it is concluded that the model is insufficiently efficient for timely responses to accidents. Consequently, the authors propose the use of data-driven surrogate models, as presented in other relevant fields, to enable timely forecasts.

The work of Jin et al. [239] demonstrates the potential of data-driven models for real-time early warning systems. The Authors implemented a genetic algorithm to select optimal initial parameters for a neural network, and a back propagation network is used for fine-tuning the connection architectures within the neural network. The use of an artificial neural network is desirable since a sliding window prediction pattern can be implemented to overcome a lack of long-term time series data records. The model therefore analyses the inherent variations in the time series data for water quality parameters collected by automatic sensors placed within a river. Through a field-scale application investigating a railway bridge monitoring site of the Ashi river in the Songhua River Basin located in China, the Authors demonstrate the capability of the model to identify water quality anomalies.

This archetype of a model is ideal when paired with the point source identification methods presented in Section 2.3.2. While the real-time early warning system presented by Jin et al. [239] can successfully identify anomalous water quality readings observed within a receiving water body, that information alone is insufficient to enable effective action. The use of sophisticated hydrodynamic models within a source identification model may present issues in terms of the time required to set up and run the model in a timely manner. However, with the aforementioned advances in high-power computing, parallelization, and the availability of cloud computing platforms [323], it is suggested that where the identified pollution justifies the required resources, timely simulations can be performed.

The use of data-driven models for the flow routing component is highly desirable albeit unfeasible under current circumstances. Ultimately, data-driven methods require high-quality data to make predictions and flood modelling has a severe dearth of available data, which is a significant barrier to the validation of physically based models, never-mind the training of data-driven models. The consequent reliance on physically based hydrodynamic simulations for model training [189] is clearly a challenge in this regard, especially due to the rate at which urban environments change and develop.

Pollution Accidents and Multi-Hazard Modelling

Explorations of potential point source emissions resulting from an accident, or alternatively flood-induced pollution, may be facilitated by hydrodynamic water quality models. Through such studies effective preventative measures may be identified. The quantification and implementation of point source discharges, especially those originating from hypothetical accidents, is relatively simple in comparison to the quantification and implementation of non-point sources. However, non-point sources of pollution may be the predominant contributors of pollution [469] and therefore necessary to include despite the associated challenges. Overall, the mechanisms through which flood induced discharges occur, the subsequent impacts and the identification of diffuse sources of pollution are challenges which require further attention.

An illustrative investigative study into potential accidental point source discharge is provided by Zavattero et al. [492], who utilised two-dimensional hydrodynamic models to explore the potential consequences of an accidental pollution spill in the River Var. The study investigates scenarios such as pollution resulting from a truck accident on one of the four intersecting road bridges or via an industrial discharge. While the presented results demonstrate the capability of hydrodynamic models in simulating both conservative and non-conservative pollutants transported through the river, comparisons between the

tested models (Mike 21, Mike 21 FM, and Telemac2D) reveals a lack of consistency in the respective results. Unfortunately, due to a lack of validation data it is not possible to discern the accuracy of the models. The different results produced by the different models for the same scenario demonstrates the sensitivity of the advection diffusion process to the numerical treatment, highlighting the importance of sophisticated and validated numerical schemes to ensure physically relevant predictions. Similar studies examining potential impact of point source discharges on drinking water sources in China have been conducted by Sang et al. [397], Ding et al. [141], and Zhai et al. [493]. However, as with the work of Zavattero et al. [492], much work remains to be done in terms of accounting for sources of uncertainty and validating model results.

The degree of uncertainty involved in modelling flood-induced pollution events is underscored by Stuyt et al. [423]. The Authors thoroughly investigated the potential for flood-induced pollution via a model study of a wide dike breach impacting a study area in the western Netherlands. Stuyt et al. [423] aimed to investigate the potential for flood induced failure of objects resulting in the discharge of hazardous chemicals following a detailed and exhaustive data collection process. However, the Authors discovered that even when attempting to introduce simplified failure criteria based on local depth and velocity, expert judgment had to be exercised due to a lack of supporting evidence. Merz et al. [305] go so far as to question whether it is feasible to predict the release and transport of pollutants in such scenarios. It is certainly the case that even if suitable parameterisations of release conditions can be obtained through experimental studies, a high degree of uncertainty will persist.

The data collection requirements for diffuse sources are also immense and likely impractical in most scenarios for most practitioners. Nevertheless, it is revealed that seemingly less relevant objects, such as cars, when grouped, release substantial and damaging quantities of toxic materials into floodwaters, whereas more obvious dangers, such as chemical plants, were only problematic under extreme flood flows. This suggests that for the multi-hazard modelling of environmental damage induced by flooding, diffuse sources should be accounted for. To assist this, inventories of relevant substances which are made accessible to those involved in environmental modelling endeavours would be of great benefit. Furthermore, a lack of validation remains a limiting factor, as once again, this study was unable to verify either the numerical results or the failure assumptions.

A similarly detailed study was performed by Mark et al. [293], who analysed the link between urban flooding and health risks. Reiner et al. [372] identified a correlation between El Niño flooding and cholera epidemics in Dhaka, Bangladesh, which Mark et al. [293] investigated further. Specifically, the Authors employed a hydrodynamic water quality model to examine the transport of *V. cholerae* originating from drainage exceedance induced by flooding. Although uncertainties were accounted for via Monte Carlo simulation, this case study once more highlights the lack of process understanding prevalent within the field of environmental flood modelling: in this case, the absence of supporting evidence to derive dose-response relations hindered the Authors ability to directly link the transport process to health hazards. Ahmed et al. [9] also identify challenges in determining the concentration of pathogens within flood flows, which Mark et al. [293] were able to overcome by taking aseptic samples. Such studies are referred to as quantitative microbial risk assessments (QMRA) and the use of hydrodynamic water quality models is currently limited. Addison-Atkinson et al. [6] identified the absence of a methodological framework to enable the application of hydrodynamic modelling for conducting QMRAs

as limiting effectiveness and progress. Brouwer et al. [78] also identify opportunities for the integration of hydrodynamic modelling to reduce uncertainty in exposure estimations resulting in more precise risk quantification.

There is therefore scope for the increasing integration and application of hydrodynamic water models in the determination of risks and evaluation of hazards associated with flood induced pollution events. Whilst there are clearly limitations that need addressing with regards to data, validation and the physical understanding of associated physical processes, it is important to remember that in all applications the accurate prediction of the hydrodynamic properties of the flow is a fundamental prerequisite. Therefore such applications are also supported by numerical advancements for the solution of the governing equations.

Ecological Modelling

Understanding and modelling of the transport processes is also crucial to the management of the ecology, especially in receiving water bodies. Consider for example the work of Shen et al., [408] on fish habitats for dammed rivers. High dams often cause total dissolved gas supersaturation downstream, negatively impacting fish populations by increasing the incidence of gas bubble disease and mortality. However, downstream areas experience lower total dissolved gas saturation due to gradual gas exchange and long retention times, creating a temporary refuge for fish during dam discharge. Via study of the total dissolved gas at the confluence of the Zumuzu River and its tributary, the Mozigou River, the Authors utilised a two-dimensional hydrodynamic model to identify engineering measures for the expansion of the suitable shelter area. Following introduction of the proposed engineering measures, the low total dissolved gas saturation zone was observed to be increased by a factor of 30, significantly improving fish habitat quality along the river.

Wang et al. [474] studied the effect of hydrodynamic characteristics on the benthic diatom biomass within natural streams. Benthic algae play a pivotal role in nutrient cycling, serving as primary producers and food sources for various aquatic organisms. These algae not only regulate chemicals such as heavy metals but also provide habitat and stability within riverine environments. Furthermore, their sensitivity to pollutants and abiotic factors renders them valuable bioindicators of aquatic ecosystem health. Although in this case, the Authors only studied the effect of shear stress and the hydrodynamic characteristics on benthic diatom biomass, the introduction of advection diffusion equations would have enabled the further study of the relationship to nutrient and pollutant transport. This is also relevant to the topic of river restoration, with the removal of hydraulic structures altering flow characteristics and subsequent transport processes which are important to consider from an ecological perspective.

Pyo et al. [365] demonstrated that the use of hyperspectral imagery to define initial conditions can support the prediction of algal blooms. Harmful algal blooms can cause major damage to aquatic ecosystems by degrading water quality and therefore predicting the spatio-temporal characteristics of a bloom can facilitate proactive mitigation strategies. Pyo et al. [365] used the three-dimensional environmental fluid dynamics code developed by the South Korean National Institute of Environment Research, known as EFDC-NIER, to study the Chlorophyll-a concentrations in the Nakdong River, South Korea.

The use of three-dimensional codes for fluvial studies is common, as evidenced by the review of ecological hydrodynamic models by Anagnostou et al. [19]. The use of three-

dimensional models for fluvial applications makes sense as the computational domain is commonly larger and less complex than for urban applications. Furthermore, the use of a three-dimensional code provides a more explicit and accurate representation of complex three-dimensional flow features such as secondary currents and turbulent mixing processes and enables a more accurate representation of obstacles to flow such as the weirs modelled by Pyo et al. along the Nakdong River. However, the higher computational efficiency of two-dimensional models may provide a means to produce real-time forecasting or probabilistic explorations of the potential for algal blooms.

When considering eutrophication processes in particular, Anagnostou et al. [19] identified that most models do not adequately account for secondary processes. For example metal reactions, zooplankton dynamics, denitrification, sediment diagenesis, organic matter recycling. This highlights the complexity involved and the requirement for further development of models to account for complex interactions when performing detailed analyses. Particularly within the development of hydrodynamic models, the reaction component of the advection-diffusion-reaction equations is seldom considered but may be critical for certain applications.

2.3.3 State-of-the-Art Models, Validation and Numerical Challenges

It is clear from the wide-ranging applications presented in Section 2.3.2 that there is a requirement for hydrodynamic water quality models capable of modelling the advection and diffusion of scalar quantities. The current state-of-the-art hydrodynamic models with water quality capabilities are dual drainage models with efficient GPU implementations [161, 97, 184, 242, 147, 398]. However, it is evident that there is still much progress to be made.

In most cases the reaction process, which is an important consideration for non-conservative tracers, is very rarely considered when presenting numerical schemes or hydrodynamic water quality models. Within the outlined applications, the use of advection-diffusion-reaction equations is clearly beneficial where non-conservative pollutants are under consideration and much more emphasis needs to be placed upon understanding and implementing reaction processes. The most progressive model in this regard is the Water Quality Analysis Simulation Program model (WASP) [485] which is capable of handling up to 10 depth-averaged transportation equations with 20 inbuilt conversion processes.

There is also much progress to be made with regards to the validation of hydrodynamic water quality models. When analysing publications which present numerical developments for the modelling of transport process the vast majority present only numerical tests [440, 333, 334, 101, 84] or limited analytical validation [456, 439, 340, 331, 330, 273, 271, 257, 249, 199, 135, 94, 83, 53, 52, 48, 40, 30] with very few presenting experimental or field validation [178, 332, 321, 85]. In general most of the analytical validation is performed via comparisons with analytical solutions for simple advection diffusion scenarios. The work of Morales-Hernández et al. [321] is unique in that the numerical results are validated against an observed time varying concentration field obtained via laser induced fluorescence. However, even in this exemplary case, the overall modelling scenario is relatively simple and much more work is to be done to have confidence in the application of hydrodynamic water quality models within complex urban environments. The current state of validation for advection diffusion processes is unsurprising considering that the

validation of hydrodynamic flood models, which is comparatively simpler to achieve, is generally limited to flood inundation extents and/or localised depths; amongst the 10 best documented urban flood events only seven contain data suitable for validating flow, which is restricted to watermark data [285].

Whilst field-scale validation data is often considered the most valuable form of validation data for field-scale models [228], the expense, uncertainty and practical challenges involved with field-scale observations of transport processes, especially within urban areas, suggests that the pursuit of field-scale validation data for advection-diffusion-reaction processes is currently unrealistic. Physical models, such as the scale model of the Severn estuary presented by Osei-Twumasi et al. [345], present a more convenient alternative however, there are challenges involved with the production of erroneous predictions due to the difficulty scaling the dispersion and diffusion processes. The work of Osei-Twumasi et al. [345] encountered such issues however, the obtained results still agreed well with field studies and other studies reported in literature relating to tidal dynamics and water quality in the estuary. As of yet, no such physical model has been produced and studied for water quality considerations in urban environments.

Mignot et al. [310] reviewed experimental modelling of urban flooding and identified that there is a lack of experimental data associated with the transport of pollutants in urban environments. As such the Authors recommend that '*future experimental research aims at getting more quantitative insights into these associated processes closely intertwined with flow behaviour during urban flooding*'. A recent example of this is the work of Rubinato et al. [385] on the flow exchanges, energy losses and pollutant transport in a surcharging manhole. For the solute transport component of the study conducted by Rubinato et al. [385] Cyclops-7F™ fluorometers were used to measure the concentration of a fluorescent tracer dye passing through the manhole. Whilst this represents progress, there is still much work to be done.

The cost-effective PCA technique presented by Arques et al. [23] therefore provides a comprehensive and accessible tool for detailed analysis of advection diffusion processes. The proposed method is built upon the PCA technique initially devised by Rummel et al. [386], which leverages established hydro-optical theory [25, 82, 248] to enable the nonintrusive determination of the observed concentration field. Although the method is potentially challenging to implement, as the analysis of the optical response of the tracer and the are non-trivial, the accessibility is important in facilitating experimental studies of advection diffusion processes. The method is however restricted only to advection diffusion processes and not advection-diffusion-reaction processes as the tracer must be conservative.

2.3.4 Numerical Diffusion and Boundedness

A numerical scheme used to approximate a system of partial differential equations, such as the SWEs, does not provide an exact solution. The local truncation error can therefore be determined by assessing how well the approximate solution provided by the numerical scheme, agrees with the exact solution of the differential equation. Since the numerical scheme provides an inexact approximation of the desired system of partial differential equations, it is possible to define a differential equation that the numerical scheme more accurately approximates, which is referred to as the modified equation for the numerical scheme. The classical study of the modified equation, as presented in standard text-

books [268, 437], enables prediction of the qualitative behaviour of a numerical scheme. Through this study it can be seen that qualitative behaviour of first order schemes is diffusive, resulting in a smearing of the solution over time. This type of behaviour is particularly problematic for advection-diffusion schemes, especially for long duration simulations.

The capability for numerical schemes to preserve the peak concentration and the shape of an initial concentration is therefore a desirable property which is tested analytically via long duration numerical tests involving pure advection. Due to the diffusive nature of first order upwind schemes, such schemes are typically unsuitable in this regard, producing increasingly smeared concentration profiles with a corresponding reduction in peak concentrations over the duration of the simulation [199, 331, 321, 330].

The qualitative behaviour of second order schemes is dispersive, which results in a train of oscillations following a discontinuity in contrast with the diffusive behaviour of first order schemes. However, extension of a scheme to second order spatial accuracy to remedy issues relating to excessive numerical diffusion is not necessarily straightforward; for second order schemes utilising flux or slope limiters, the choice of limiter has a strong influence on the quality of the results [53, 83].

Furthermore, Murillo et al. [331] demonstrated that there are fundamental numerical challenges for second order upwind schemes applied to advection diffusion problems which cannot be overcome. Precisely, Murillo et al. [331] proved that it is not possible to obtain second order spatial accuracy for both the conserved variables and the solute concentration for upwind schemes. This is due to the fact that the concentration of a transported quantity is a primitive variable, derived from the flow depth and the mass of the quantity, which are conserved variables. As a consequence, the concentration is independent of the eigenstructure of the system and therefore the monotonicity properties of the numerical scheme apply only to the mass of the quantity and not the concentration.

This means that it is also non-trivial to ensure bounded values of concentration. When a conserved cell variable is updated, a conservative numerical scheme ensures that the updated value of the conserved variable is bounded by the neighbouring minimum and maximum values. Due to the outlined issues regarding solute concentrations, this condition must be explicitly enforced. A solution to this problem is introduced via a conservative redistribution of the updating contributions in [333], with further discussion and implementation being explored in [330, 331, 332, 83] for conservative upwind schemes utilising Roe approximate Riemann solvers [381]. In this regard, the treatment of wet/dry fronts also requires special numerical consideration [332, 40, 48].

The minimisation of numerical diffusion and oscillations can also be achieved via the implementation of higher order accuracy schemes. This is demonstrated by Cai et al. [84], who implemented a fourth order central weighted essentially non-oscillatory reconstruction with an adaptive semi-discrete central upwind scheme. The proposed scheme can achieve an arbitrary order of spatial accuracy in the absence of source terms. However, the second order discretisation of the source terms presented by the Authors proves to be of high-resolution and non-oscillatory. It should be noted however, that Cai et al. only consider the case of pure advection with no diffusion.

It is also possible to eliminate errors relating to both numerical diffusion and oscillations by implementing a non-diffusive decoupled method for the advection diffusion process.

However, caution is advised when considering decoupled implementations for conservative upwind schemes. Historically, decoupled treatment of the advection of the transport process has presented a popular solution since it enables the implementation of simple and computationally efficient schemes, under the assumption that the transported quantity has negligible influence on the flow dynamics for sufficiently low concentrations. However, Burguete et al. [83] showed that a decoupled discretisation of the solute transport results in significant numerical challenges that require special corrections [334]. This supported by the results presented by Bai and Jin [40], which exhibit the same numerical issues outlined by Burguete et al.

Suitable non-diffusive decoupled methods include the use of a hybrid finite-volume-particle method approach as presented by Chertock et al. [101] and Touma and Saleh [440]. In the proposed scheme, the solution of the shallow water system is achieved via a central-upwind scheme and the subsequent advection of the solute is achieved using a particle method. As demonstrated by Sämann et al. [395, 394], Lagrangian transport models provide a suitable alternative to traditional Eulerian approaches due to their non-diffusive nature. In the particular case of a central-upwind scheme, without the decoupled treatment of the transport problem, the scheme is unable to sufficiently resolve the contact wave across which the concentration of a quantity is discontinuous. However, non-dissipative filters are required to remove numerical oscillations which increases the computational cost of the scheme. It should also be noted that both of the referenced methods do not consider the diffusion of a scalar quantity, presenting only the pure advection problem.

When considering the detrimental effects of numerical diffusion it is also important to consider the potential for geometrically irregular meshes to exacerbate local numerical diffusion. For finite volume methods solving advection-diffusion problems, it is common to present a flexible implementation on irregular unstructured grids [30, 53, 249, 271, 456, 321, 199, 94] in order to provide greater meshing flexibility for complex geometries. For explicit schemes, satisfaction of the Courant-Friedrichs-Lewy (CFL) condition [114] is necessary but not sufficient to ensure stability. Within a computational domain the satisfaction of the CFL condition is ensured at each time level by considering the maximum propagation speeds present within the domain. The local truncation error and consequently the modified equation are also functions of the Courant number and therefore the local Courant number has an influence on the local behaviour of the numerical scheme. Therefore, where meshes exhibit a high degree of geometric irregularity, when the smaller cells dominate the time step, slower moving or stagnant flow in larger cells may experience excessive numerical diffusion due to a low local Courant number [301], which is proportional to the wave propagation speed and time step and inversely proportional to the cell size. Adaptive mesh refinement [56], as implemented by Benkhaldoun [53], and local time-stepping [427, 251] are solutions to this problem where flexible meshing is desired however, efficient implementation is complex. Adaptive mesh refinement and local time-stepping can also provide significant improvements in computational efficiency.

2.3.5 Problem Specific Numerical Treatments

Most Authors, when presenting numerical schemes for the solution of advection diffusion equations, operate under the assumption of dominant advection, justifying the treatment of the advection diffusion equations as hyperbolic. However, the advection-diffusion(-reaction) equations are in fact parabolic in nature. Considering the applications presented

in Section 2.3.2, the assumption of pure advection is almost ubiquitously appropriate however, there may be niché cases in which the flexibility to consider diffusion dominant processes is desired. A suitable numerical treatment of the problem to enable the rigorous application of numerical methods for hyperbolic conservation laws is therefore proposed by Montecinos and Toro [320]. The Authors address the parabolic character of the equations by using Cattaneo's relaxation approach [91] to reformulate the system into a hyperbolic system with stiff sources. In Vanzo et al. [456], this technique can be seen to produce a scheme with a favourable stability range, producing robust second order accurate approximations.

If hydrodynamic models are to be applied to applications involving rainfall runoff, which are relevant to water quality studies in urban areas due to the aforementioned first flush phenomena, Cea and Vázquez-Cendón [94] demonstrated that a well-balanced discretisation of the friction source terms is required. The requirement for a well-balanced treatment of the bed slope is widely acknowledged and the satisfaction of the C-property is required for any proposed numerical scheme. However, for cases where the bed friction and the bed slope are the leading terms in the momentum conservation equations, as opposed to the internal and hydrostatic pressure forces in typical scenarios, the discretisation of the bed friction has a significant influence on the numerical approximation. In such cases, the proposed upwind discretisation of the friction source term provides superior accuracy and stability in comparison with a classical centred semi-implicit discretisation.

When considering applications involving meandering channels, Caleffi and Valiani [85] demonstrated the importance of adequately capturing the effects of spiral motion. Spiral motion, which may also be referred to as secondary currents, is a three-dimensional effect induced by the imbalance of centripetal and pressure forces. The effect causes a divergence between the fluid parcels near the free surface, which are driven towards the outer bank, and fluid parcels near the bed, which are driven towards the inner bank. The net effect of this phenomena is a redistribution of the longitudinal velocity and solutes [145, 98] which is important to capture in order to produce physically relevant approximations for channels with high curvature. The scheme proposed by Caleffi and Valiani [85], based upon the mathematical model of Begnudelli et al. [50], includes an exhaustive treatment of the bottom shear, momentum dispersion, scalar dispersion and turbulent diffusion terms which is atypical of common advection diffusion models.

2.3.6 Diffusion Source Terms

As identified by Mignot et al. [311], there is a lack of scientific consensus within published works regarding the formulation of the depth-averaged advection-diffusion equations and the determination of the corresponding coefficients of the dispersion-diffusion tensor. The lack of consistency in this regard can also be seen in the number of schemes discussed in this Section 2.3.3 which neglect the diffusion process entirely. Schemes which also consider the reaction process are seldom found.

For an advection diffusion equation, the diffusion process is implemented via source terms related to the components of a dispersion-diffusion tensor for the depth-averaged mixture. Although the diffusion process is three-dimensional in the nearfield, the depth-averaged nature of the shallow water equations and two-dimensionality of contemporary models requires simplification of the three-dimensional description.

Ignoring the issues associated with the improper formulation of the advection-diffusion equations, the determination of the diffusivity tensor presents a significant practical challenge. As shown by Mignot et al. [311], the diffusivity tensor accounts for a variety of processes and it is therefore imperative that appropriate values are assigned. Within his seminal paper Elder [149] empirically estimated the values of the diffusivity tensor for fully developed boundary layer flows in straight channels. However, the evaluation of the tensor is highly dependent on the application since the diffusivity tensor is used to parameterise the effects of molecular diffusion, turbulent diffusion and diffusion induced by secondary currents which are dependent on the specificities of the application.

Although there is a wealth of publications dedicated to the estimation of the longitudinal dispersion coefficients [7, 27, 37, 39, 38, 341] there is a lack of a coherent approach. As proposed by Mignot et al. [311], the implementation of a consistent and transparent process in which the evaluation of the components of the diffusivity tensor are justified and validated would certainly be of great assistance in future applications.

Once the components of the diffusivity tensor are determined it is also important to consider the suitable discretisation of the source terms. Implicit treatment of the diffusion source terms results in no further restriction of the timestep with respect to the hydrodynamic component albeit requiring a potentially expensive iterative solution. The alternative is to use an explicit treatment which is computationally simpler but imposes a greater restriction on the timestep. Techniques which expand the region of stability, such as [329], are therefore also valuable tools. Similarly, the sub step explicit resolution of the diffusion terms introduced by Morales-Hernández [321] prevents reduction of the time step for the hydrodynamic component, enabling a more efficient computation for explicit treatments.

2.3.7 Summary

The presented literature demonstrates the requirement for hydrodynamic modelling for applications concerning water quality. In particular, hazards induced by point source emissions of pollution present a significant threat to human health and the environment. The predictive study of potential pollution discharges or the retroactive study of accidental or intentional discharges provides a basis for identifying optimal preventative measures and remediation strategies.

Via the introduction of advection-diffusion equations, under the assumption of dominant advection, well-mixed quantities are assumed to be passively advected by the flow field resolved by a hydrodynamic model. The accurate determination of the flow characteristics is therefore a prerequisite for the modelling of transport processes. If the accurate representation of obstacles to flow is required for the accurate determination of the local flow characteristics, as has been evidenced in Section 2.1.1, it therefore follows that this is a minimum requirement for the modelling of the advection and diffusion of scalar quantities. Hence, objective 3 seeks to enhance the accuracy of models in the presence of partial barriers to flow:

Objective 3: To add and experimentally validate the capability to model the transport of well-mixed dissolved solutes through linear fixed immiscible partial barriers to flow for Solver 2.

The validation of the solver via means of laboratory experiments aids not only in the

verification of the predictive capacity of the solver but also in addressing, in a small way, the lacking data and process understanding which is required to support the development of urban flood and water quality models. The choice to only implement this capability for Solver 2 is related to the absolute requirement to accurately resolve the flow as a prerequisite for the modelling of the transport process. The required solution procedure must also address or be compatible with the identified numerical challenges and corresponding solutions in Section 2.3.3.

Chapter 3

A New Riemann Solver for Modelling Partial Barriers in Flood Flows - Development and Experimental Validation

Flows in rivers can be strongly affected by obstacles to flow or artificial structures such as bridges, weirs and dams. This is especially true during floods, where significant backwater effects or diversion of flow out of bank can result. However, within contemporary industry practice, linear features such as bridges are often modelled using coarse approximations, empirically based methods or are omitted entirely. Presented within this paper is a novel Riemann solver which is capable of modelling the influence of such features within hydrodynamic flood models using finite volume schemes to solve the shallow water equations. The solution procedure represents structures at the interface between neighbouring cells and uses a combination of internal boundary conditions and a different form of the conservation laws in the adjacent cells to resolve numerical fluxes across the interface. Since the procedure only applies to the cells adjacent to the interface at which a structure is being modelled, the method is therefore potentially compatible with existing hydrodynamic models. Comparisons with validation data collected from a state of the art research flume demonstrate that the solver is suitable for modelling a range of flow conditions and structure configurations such as bridges and gates.

This chapter has been published as: James Mckenna, Vassilis Glenis, Chris Kilsby, A new Riemann Solver for Modelling Bridges in Flood Flows - Development and Experimental Validation, Applied Mathematics and Computation, Volume 447, 2023, 127870, 10.1016/j.amc.2023.127870.

3.1 Introduction

Hydrodynamic models are a vital component of contemporary flood risk management practice, providing evidence to inform future investment and risk assessment. It follows that the accurate modelling of hydrodynamic phenomena is fundamental to effective flood risk management since the quantification and analysis of risk is dependent on modelling results. Channel structures, such as bridges, weirs and gates can act as partial barriers to flow, significantly influencing the local flow characteristics [479, 105, 109]. Yet, despite the established importance of accurately capturing hydrodynamic phenomena, methods for modelling linear features which act as partial barriers in two-dimensional computational domains are relatively under-developed. Methods for modelling such interactions within three-dimensional simulations exist [261], however, the complex meshing requirements and the inherent computational expense prohibits their use on spatial domains relevant to flood risk management. Moreover, within contemporary industry practice such features are often modelled using coarse approximations, empirically based methods or by omitting such features entirely [234, 54, 444, 81]. There is no unified approach to modelling linear features within horizontal two-dimensional hydrodynamic models, with available methods including:

- Modelling as finite bottom elevations.
- Local friction-based representation.
- Modelling as 'holes' within the mesh.
- Modelling via internal boundary conditions.
- Modelling as source terms within the numerical scheme.
- Modification of the conservation laws.

However, each method has its respective limitations. A study conducted by Alcrudo [11] demonstrated significant challenges related to modelling obstructions with local friction-based representations. This was primarily due to the impracticality of selecting an appropriate Manning's roughness coefficient. The use of finite bottom elevations was also found to be problematic due to numerical instabilities for some numerical schemes. Both methods are coarse, unphysical approximations, making them unsuitable for high resolution modelling of hydrodynamic interactions with hydraulic structures. Modelling features as 'holes 'within the mesh, commonly referred to as the mesh discretisation method, is also unsuitable for generalised treatment of linear features since the method is incompatible with partial barriers to flow. This is due to the fact that once a feature is modelled as a hole within the mesh, the feature is no longer part of the computational domain, disrupting the exchange of conserved variables (depth and momentum for the shallow water equations) across the feature.

More sophisticated approaches include the work of Maranzoni et al. [289], who locally modified the conservation laws by introducing a fictitious vertical slot to the ceiling of the cells representing a linear feature. This enables the transition between free surface and pressurised flow to be captured via the Preissmann slot concept [363]. However, this also means that the method suffers from the well documented limitations of the Preissmann slot concept as discussed by Vasconcelos, Wright and Roe [462] and Malekpour and Karney [287], which the authors also acknowledge in their work. Furthermore, the method requires further work in order to be suitable for generalised treatment of linear features, as it can only currently simulate pressurisation without overtopping.

Morales-Hernàndez et al. [322], Ratia et al. [371] and Dazzi et al. [129] have all proposed implementations of internal boundary conditions to model hydraulic structures. The proposed methods calculate the unit discharge across hydraulic structures by selecting appropriate rating curves or discharge formulae dependent on the inundation depth calculated from the adjacent cells or at the interface. Morales-Hernàndez et al. [322] and Dazzi et al. [129] both present similar methods with the PARFLOOD model presented by Dazzi et al. promising the most general applicability. However, the reliance on stage-discharge relationships under certain circumstances, sensitivity to the selection of uncertain discharge coefficients and the potential to induce directionality for skew features are conceivable flaws. Furthermore, as shown by Hou and Le Floch [224], use of non-conservative schemes can result in convergence to incorrect solutions.

The head loss source term introduced by Ratia et al. [371] accounts for the losses induced by contraction and expansion of flow through a hydraulic structure. Whilst this method is effective in capturing the macroscale effects induced by the presence of the structure, it is unable to sufficiently capture near-field flow effects including potential downstream supercritical flows. It is therefore clear that more progress is required towards the development of a solver capable of accurately resolving fluxes across general partial barriers to flow, within two-dimensional finite volume schemes, for the purpose of flood modelling. Consequently, the purpose of this paper is to build upon some of these methods, presenting a novel method capable of generalised treatment of partial barriers to flow. The method is intended to be compatible with existing flood models utilising Finite Volume (FV) schemes to solve the shallow water equations.

3.2 Mathematical Model

The proposed method utilises internal boundary conditions in addition to using a different form of the conservation laws in the adjacent cells. As a result, hydraulic structures are idealised as existing at the interface and modelled as a partially reflective boundary between the adjacent cells. Consequently the interfaces within the computational domain can be divided into structure interfaces, employing the novel solution procedure to resolve numerical fluxes, and non-structure interfaces, employing a standard solution procedure to resolve numerical fluxes.

For the non-structure interfaces and the corresponding adjacent cells, a one-dimensional (1D) FV scheme is used to solve the 1D Shallow Water Equations (1D-SWE) given as:

$$\mathbf{U}_t + \mathbf{F}(\mathbf{U})_x = \mathbf{S}(\mathbf{U}) \tag{3.1}$$

Where $\mathbf{U}$ is the vector of conserved variables, $\mathbf{F}(\mathbf{U})$ is the vector of fluxes and $\mathbf{S}(\mathbf{U})$ is a vector of sources comprising of $\mathbf{S}_0$, the bed slope source term and $\mathbf{S}_f$, the bed friction source term. These terms are given as follows:

$$\mathbf{U} = \begin{bmatrix} h \\ hu \end{bmatrix} \quad , \quad \mathbf{F} = \begin{bmatrix} hu \\ hu^2 + \frac{1}{2}gh^2 \end{bmatrix} \quad , \quad \mathbf{S}_0 = \begin{bmatrix} 0 \\ -gh\frac{\partial z}{\partial x} \end{bmatrix} \quad , \quad \mathbf{S}_f = \begin{bmatrix} 0 \\ -\tau_f \end{bmatrix} \tag{3.2}$$

Whereby h denotes the depth of flow, z is the elevation of the bed, u denotes the velocity component in the x direction, g is the acceleration due to gravity and τ_f is the shear stress

due to friction in accordance with Manning's equation:

$$\tau_f = C_f u|u| = \frac{gn^2}{\sqrt[3]{h}} u|u|$$

where C_f is the Manning's bed friction coefficient and n is Manning's roughness coefficient. For the structure interfaces and corresponding adjacent cells, a 1D FV scheme is used to solve the two layer 1D-SWE as derived by Spinewine et al. [418]:

$$\mathbf{U}_t + \mathbf{F}(\mathbf{U})_x = \mathbf{S}(\mathbf{U}) \tag{3.3}$$

$$\mathbf{U} = \begin{bmatrix} h_2 \\ h_2 u_2 \\ h_1 \\ h_1 u_1 \end{bmatrix} \tag{3.4}$$

$$\mathbf{F} = \begin{bmatrix} h_2 u_2 \\ \frac{(h_2 u_2)^2}{h_2} + \frac{1}{2} g h_2^2 \\ h_1 u_1 \\ \frac{(h_1 u_1)^2}{h_1} + \frac{1}{2} g h_1^2 + \chi g h_2 h_1 \end{bmatrix} = \begin{bmatrix} q_2 \\ \sigma_2 \\ q_1 \\ \sigma_1 \end{bmatrix} \tag{3.5}$$

$$\mathbf{S} = \begin{bmatrix} 0 \\ \frac{R_{12}}{\rho_2} \\ 0 \\ -\frac{\chi R_{12}}{\rho_2} + R_1 - \tau_f \end{bmatrix} = \begin{bmatrix} 0 \\ -g h_2 \frac{\partial z_1}{\partial x} \\ 0 \\ \chi g h_2 \frac{\partial z_1}{\partial x} - g(\chi h_2 + h_1) \frac{\partial z_0}{\partial x} - \tau_f \end{bmatrix} \tag{3.6}$$

Where the subscript 2 refers to the upper layer and subscript 1 refers to the lower layer of a two layer shallow water model. R_{12} is the reaction force exerted by the lower layer onto the upper layer, R_1 is the reaction of the bed onto the bottom layer and ρ_k is the density of the fluid in layer k. Both sets of equations are discretised using the same first order accurate, explicit FV scheme whereby the conserved variables are updated in accordance with equation (3.7).

$$\mathbf{U}_i^{n+1} = \mathbf{U}_i^n - \frac{\Delta t}{\Delta x} \left[\mathbf{F}_{i+\frac{1}{2}} - \mathbf{F}_{i-\frac{1}{2}} \right] + \Delta t \mathbf{S} \left(\mathbf{U}_i^n \right) \tag{3.7}$$

Where the subscript i represents the ith cell, the superscript n represents the nth time level and Δx and Δt represent the cell size and time step respectively. Although a 1D scheme is implemented in this case, implementation as a 2D scheme requires no fundamental changes to the method.

3.2.1 Numerical Flux Computation

Harten-Lax-van Leer (HLL) approximate Riemann solvers [212] are used to resolve inter-cell numerical fluxes for the entire computational domain, however, other approximate Riemann solvers may be used to resolve numerical fluxes across non-structure interfaces. A novel solution procedure is proposed for resolving numerical fluxes across structure interfaces using a newly developed HLL approximate Riemann solver.

The fundamental concept behind the proposed method is the assumption that the motion of the fluid can be treated as primarily horizontal in nature, which is a necessary condition required for application of the shallow water equations. Consequently, the structure

cells can be divided into horizontal layers corresponding to the structure idealised at the interface. By dividing the layers in such a way, component fluxes can be resolved for each layer. Through summation of the component fluxes at an interface, it is then possible to determine a flux for the left and right sides of the structure interface. The partially reflective nature of the boundary is captured by implementing appropriate boundary conditions for the individual layers as well as discretising the cell average properties of the respective left and right states (see Figure 3.1). Based on the boundary condition applied to the layer at the interface the layers are designated as either '*open*', corresponding to a transmissive boundary condition at the interface, or '*closed*', corresponding to a reflective boundary condition at the interface. Structure interfaces require a left and right flux, as opposed to a single flux for non-structure interfaces, due to the fact that the left and right states for closed layers are considered to be discontinuous. Fluxes for submerged layers are calculated using (3.8).

$$\mathbf{F}_k^{(S)} = \begin{bmatrix} h_k u_k \\ \frac{(h_k u_k)^2}{h_k} + \frac{1}{2} g h_k^2 + \chi g h_u h_k \end{bmatrix} = \begin{bmatrix} q_k \\ \sigma_k \end{bmatrix} \tag{3.8}$$

Where the subscript k represents the kth layer and h_u represents the sum of the layer depths above the submerged layer. Since the layers are the same density the $\chi = \frac{\rho_1}{\rho_2}$ term is always equal to one. Fluxes for free-surface layers (the upper most layer of a structure cell) are calculated using (3.9).

$$\mathbf{F}_k^{(FS)} = \begin{bmatrix} h_k u_k \\ \frac{(h_k u_k)^2}{h_k} + \frac{1}{2} g h_k^2 \end{bmatrix} = \begin{bmatrix} q_k \\ \sigma_k \end{bmatrix} \tag{3.9}$$

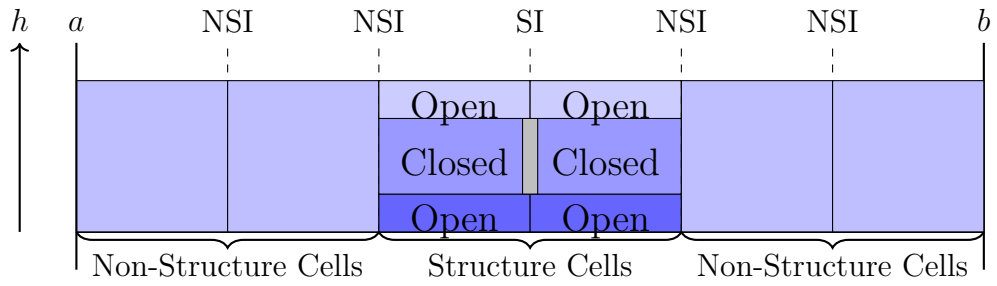

Figure 3.1: A simple computational domain $[a, b]$ illustrating the designation of structure and non-structure cells as well as open and closed layers for the structure cells. Non-structure interfaces are denoted using the abbreviation NSI and structure interfaces are denoted using the abbreviation SI. The split layer properties of the structure cells are only required for computing intercell fluxes across structure interfaces; a non-structure interface that is adjacent to a structure cells treats the structure cell as a non-structure cell utilising the cell-average properties.

3.2.2 Solution Procedure

At each timestep the adjacent cells are divided into horizontal layers corresponding to the base and cover of the idealised structure at the interface, as demonstrated in Figure 3.2. This corresponds with the prior outlined assumption that the direction of flow is primarily

parallel to the bed. Whilst there is undoubtedly a vertical exchange in momentum between the horizontal layers at such an interface, it is impractical to model such effects within a one-dimensional or two-dimensional scheme.

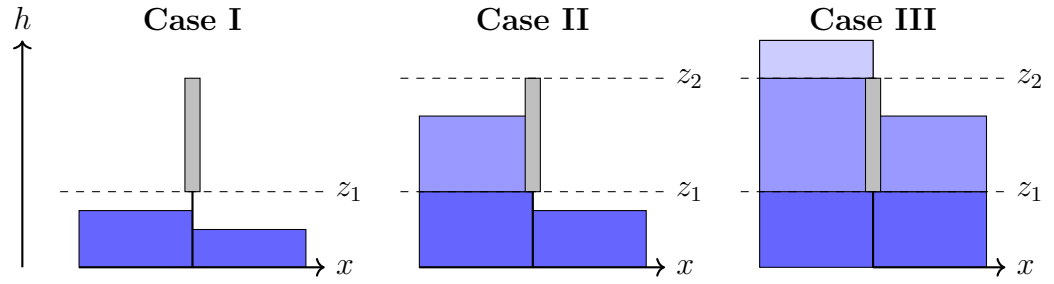

Figure 3.2: Definition of layers for cells adjacent to a structure interface. z_1 and z_2 represent the elevation of the base and cover of the structure.

The next step is to assign velocity to the layers. This is achieved by using the following assumptions:

- $hu = \sum_1^n h_n u_n$ where h is the cell average depth, u is the cell average velocity and h_n and u_n are the depth and velocity of the nth layer.
- The fluid velocity is exactly equal to zero at the interface/structure for a closed layer.
- The fluid velocity in closed layers is much smaller than the fluid velocity in open layers, provided the flow isn't stationary.

The first assumption equates to the conservation of momentum for the cell following layer velocity assignment, which is a necessary requirement. The second and third assumptions are used to justify assignment of zero velocity to the closed layers. In reality, this results in an underestimation of the fluid velocity for closed layers, which is expected to be small but non-zero, and a subsequent overestimation of the fluid velocity for the open layers. However, this only impacts the computation of the numerical fluxes for the open layers since solution of the Riemann problem for closed layers is dependent on the assumed zero velocity at the interface, which is valid provided the structure is motionless. Furthermore, a more sophisticated discretisation of the layer velocities would likely improve the method, however, this simplified approach has been found to be satisfactory in capturing the approximate vertical velocity profile. Using these assumptions, the velocity for each layer can be determined as shown in Figure 3.3. Another simplistic velocity assignment approach that can be considered is to assume that the velocity in each of the layers is equal to the cell average velocity. However, this approach was found to produce a significantly underestimated momentum flux as a result of underestimating the flow velocity, especially for the base layer.

Once the layers and their respective properties are defined the next step is to calculate fluxes layer by layer. As shown by Spinewine et al. [418], due to the lack of coupling between the layers in (3.5), the flow variables in the upper layer are constant across the waves of the bottom layer for the solution of the homogeneous conservation law. This principle can be used to apply the two-layer equations to an n-layer system by taking the lower layer to be the layer in question and the upper layer to be the combined layers of

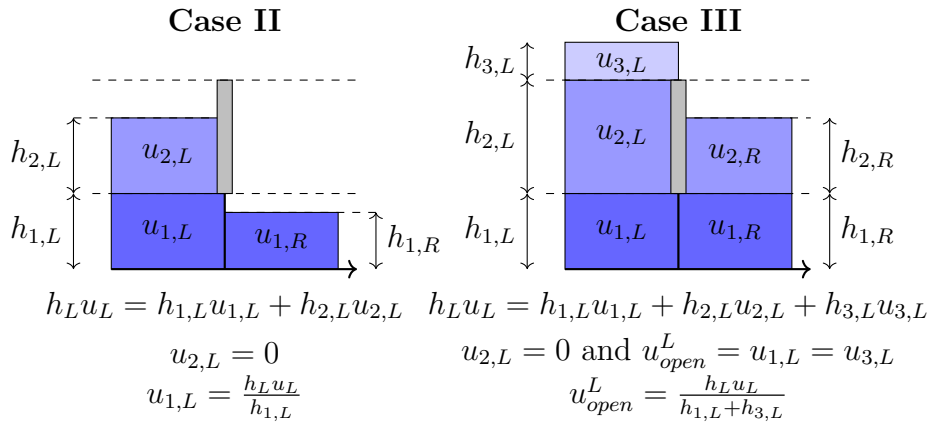

Figure 3.3: Velocity assignment with example calculations shown below. h_L = the depth of the non-split left cell, u_L = the cell average velocity, $h_{n,L}$ = the depth of the nth split layer, $u_{n,L}$ = the velocity of the nth split layer.

flow above.

For the closed layers, since the left and right states are separated by a reflective boundary, two fluxes, as opposed to a single flux for the open layers, are to be calculated corresponding to the solution of two Riemann problems involving the left/right layer state and a reflective boundary condition. Once the component fluxes have been calculated for each layer a flux for the left side of the interface can be calculated by summing the left side fluxes for the closed layers with the fluxes for the open layers and a flux for the right side of the interface can be calculated by summing the right side fluxes for the closed layers with the fluxes for the open layers. Updating of the conserved variables is conducted on a cell average basis using these fluxes, meaning that redefinition of the layers and redistribution of the layer properties must be conducted at each timestep based on the updated cell average properties.

The outlined procedure, which is summarised in the pseudocode contained within Algorithm 1, can be demonstrated by considering the scenarios presented in Cases I-III. Case I is a trivial case, requiring no special treatment in comparison to the non-structure cells since there is only one open layer containing depth of flow for both left and right states. Case II is more complex, requiring the resolution of two fluxes via the solution of two Riemann problems: a flux for the base layer and a flux for the left side of the structure. As illustrated in Figure 3.4, the solutions to the Riemann problems constructed at the left and right side of the interface for a closed layer always produce a depth flux of zero and a momentum flux equal to the pressure force exerted by the layer of water on the wall (assuming a hydrostatic pressure distribution), which is equal to $1/2gh^2_{2,L}$ for Case II.

Case III introduces further complexity, requiring the resolution of four fluxes via the solution of four Riemann problems: a flux for the base layer, a flux for the left side of the structure interface, a flux for the right side of the structure interface and a flux for the uppermost layer. The Riemann problem constructed for the uppermost layer includes a dry right bed as there is no depth of flow in this layer for the right state. As a consequence, the wave pattern and corresponding wavespeeds displayed in Figure 3.5 are utilised. An alternative approach is to model these types of layers as free outfalls,

Algorithm 1 Structure cell flux computation algorithm. Subscript k refers to the kth layer under consideration. Subscript u refers to the depth of water above the kth layer.

for *each open layer* **do**

calculate wavespeeds **if** *wet cells* **then**

$$S_L = u_{open,L} - a_{k,L}q_{k,L} \quad , \quad S_R = u_{open,R} + a_{k,R}q_{k,R} \tag{1}$$

$$a_k = \sqrt{(h_k + h_u)g}$$

$$q_k = \begin{cases} \sqrt{\frac{1}{2}\left[\frac{(h_*+h_k)h_*}{h_k^2}\right]} \text{ if } h_* > h_k \\ 1 \text{ if } h_* \leq h_k \end{cases}$$

$$h_* = \frac{1}{2}(h_{k,L} + h_{k,R}) + \frac{1}{4}\frac{(u_{k,R} - u_{k,L})(h_{k,L} + h_{k,R})}{(a_{k,L} + a_{k,R})}$$

else if *left dry cell* **then**

$$S_L = u_{open,R} - 2a_{k,R} \quad , \quad S_R = u_{open,R} + a_{k,R} \tag{2}$$

else

right dry cell;

$$S_L = u_{open,L} - a_{k,L} \quad , \quad S_R = u_{open,L} + 2a_{k,L} \tag{3}$$

calculate layer flux

$$\mathbf{F}_k = \begin{bmatrix} h_k u_k \\ \frac{(h_k u_k)^2}{h_k} + \frac{1}{2}gh_k^2 + \chi g h_u h_k \end{bmatrix} \tag{4}$$

$$\mathbf{F}_{layer} = \begin{cases} \mathbf{F}_{k,L} \text{ if } S_L > 0 \\ \mathbf{F}^{hll} = \frac{S_R\mathbf{F}_{k,L} - S_L\mathbf{F}_{k,R} + S_R S_L(\mathbf{U}_R - \mathbf{U}_L)}{S_R - S_L} \text{ if } S_L \leq 0 \leq S_R \\ \mathbf{F}_{k,R} \text{ if } S_R < 0 \end{cases} \tag{5}$$

end for

for *each closed layer* **do**

for *the left side* **do**

introduce fictitious ghost cell for right state (equal depth and equal and opposite velocity) calculate wavespeeds using (1) calculate layer flux using (4)&(5)

end for

for *the right side* **do**

introduce fictitious ghost cell for left state (equal depth and equal and opposite velocity) calculate wavespeeds using (1) calculate layer flux using (4)&(5)

end for

end for

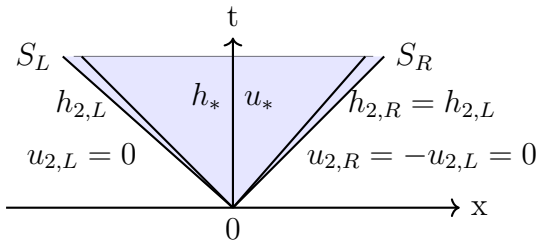

$$\mathbf{F}_{2,k}^{(FS)} = \begin{bmatrix} h_{2,k}u_{2,k} \\ \frac{(h_{2,k}u_{2,k})^2}{h_{2,k}} + \frac{1}{2}gh_{2,k}^2 \end{bmatrix}$$

Figure 3.4: Structure of the general solution of the Riemann problem for the closed layer in the left cell for Case II. The right state is a fictitious ghost cell used to impose a reflective boundary condition at the left face on the structure interface. A reflective boundary condition is imposed via the introduction of a state with equal depth and equal and opposite velocity.

imposing a critical depth condition in the left or right state which contains no depth of flow. Figure 3.6 illustrates the process used to update the conserved variables for

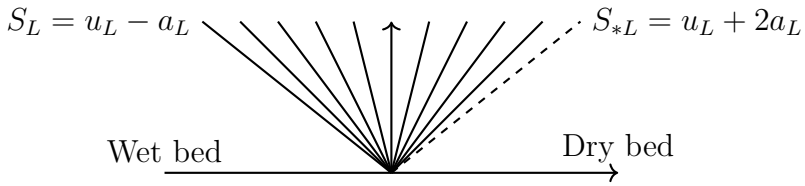

Figure 3.5: Wave pattern for the one-dimensional case with a right dry bed. $a_k = \sqrt{gh_k}$.

the structure cells following summation of the component fluxes. $\mathbf{F}^{(-)}$, the flux for the left side of the interface, is determined by summing the component fluxes for the open layers with the component fluxes for the closed layers on the left side of the interface. Likewise, $\mathbf{F}^{(+)}$, the flux for the right side of the interface, is determined by summing the component fluxes for the open layers with the component fluxes for the closed layers on the right side of the interface. In the case that $\mathbf{F}^{(-)} \neq \mathbf{F}^{(+)}$, which occurs when the left and right states are not in equilibrium, there is a loss of momentum from the shallow water system at each timestep equal to $\Delta t/\Delta x(\mathbf{F}^{(+)} - \mathbf{F}^{(-)})$, which is equal to the resultant hydrostatic pressure force exerted on the structure multiplied by the ratio of the timestep to the cell size. The resultant hydrostatic pressure force is valuable for applications concerned with determining the structural failure of hydraulic structures due to fluid-structure interactions.

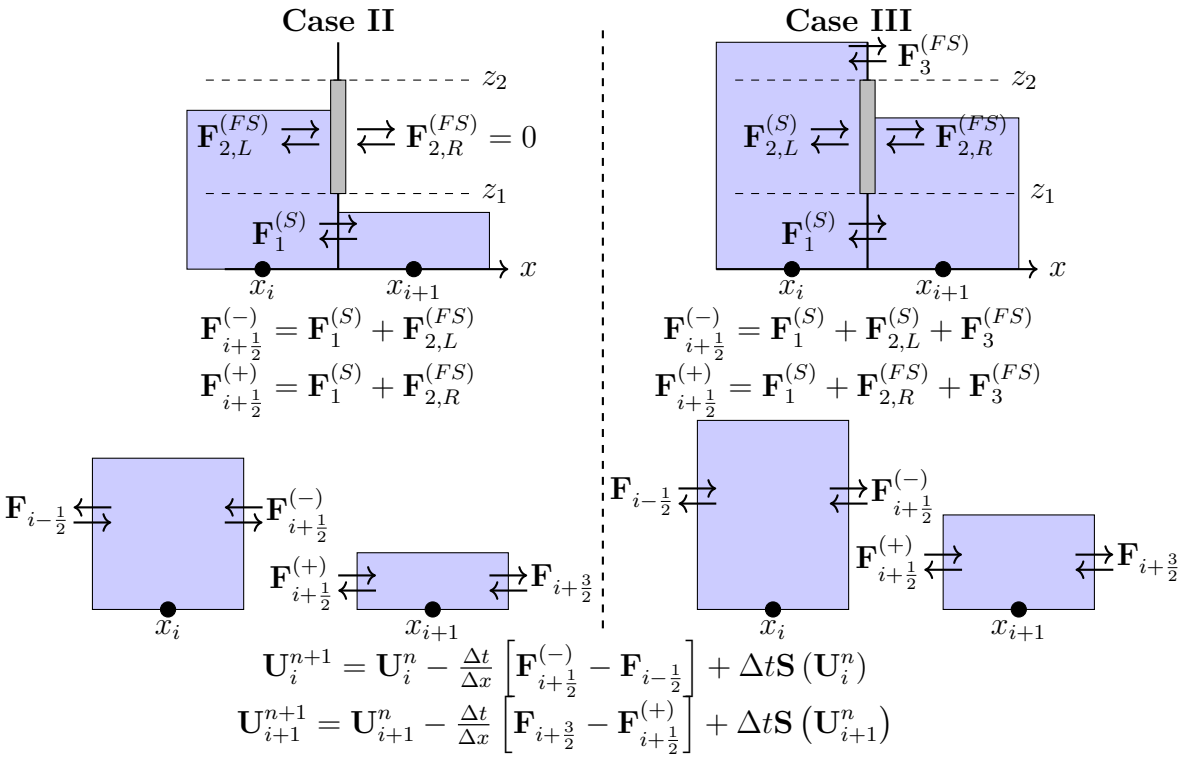

Figure 3.6: Updating of the left and right structure cells following summation of the component fluxes at the structure interface.

3.3 Model Validation

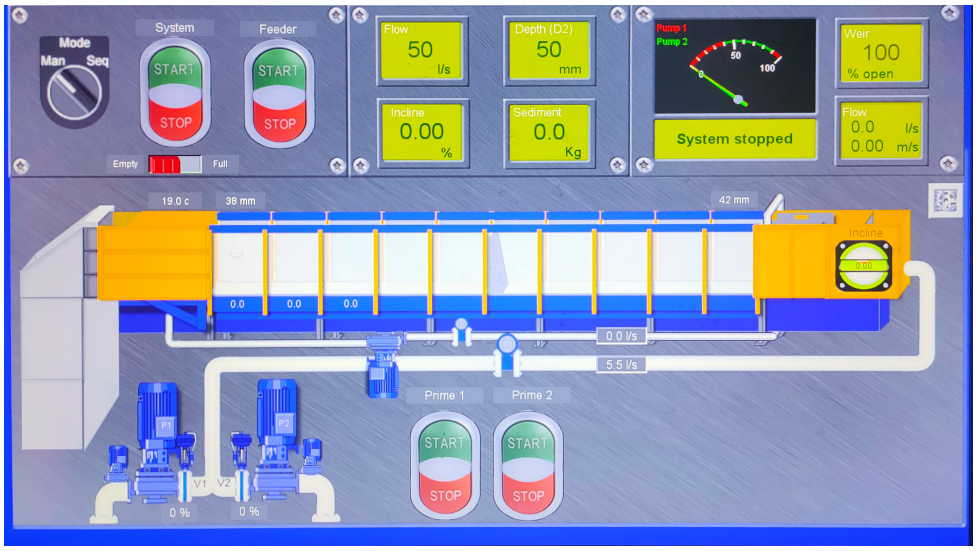

Figure 3.7: Control panel for the S100 Research Flume, including a schematic of the flume. Two pumps are used to draw water from the sump, supplying a constant flow rate to the upstream (right) end of the flume. The flow rate is measured using an electromagnetic flow meter.

In order to validate the method outlined in the previous section, numerical results are compared to steady state measurements taken from experiments conducted in Newcastle University's Armfield S100 Research Flume. As shown in Figure 3.7, the S100 Research

Flume is a $12.5m$ long, $1m$ wide, $0.8m$ deep flume capable of producing flow rates up to $400ls^{-1}$. At $5m$ downstream, grooves in the walls of the flume enable barriers to be slotted into the cross-section enabling their effect to be studied. A series of tests were conducted in the flume using a range of flows and barrier geometries. In order to simplify the numerical scheme the flume was set to zero tilt for all tests. The basic test conditions are outlined in Table 3.1. The full validation dataset is available as supplementary material for potential future use by other researchers.

Validation Test Cases				
Test Case	q (ls^{-1})	z_1 (mm)	z_2 (mm)	Description
Test 1	130	116	316	Flow under barrier.
Test 2	130	122	322	Flow under barrier.
Test 3	35	32	232	Flow under barrier.
Test 4	130	32	232	Overtopped barrier.
Test 5	24	32	232	Flow under barrier.
Test 6	20	32	232	Flow under barrier.
Test 7	275	116	316	Overtopped barrier.
Test 8	175	116	316	Overtopped barrier.
Test 9	177	105	405	Overtopped barrier.
Test 10	150	105	405	Flow under barrier.
Test 11	225	24	324	Overtopped barrier.
Test 12	19	24	324	Flow under barrier.

Table 3.1: Validation test conditions. q is the flow rate, z_1 is the elevation of the base of the barrier above the flume bed and z_2 is the elevation of the cover of the barrier.

3.3.1 Numerical Setup

All numerical tests were conducted on a $12.5m$ 1D spatial domain, discretised into a structured grid comprised of $0.01m$ cells ($\Delta x = 0.01m$). In order to ensure satisfaction of the Courant-Friedrichs-Lewy condition a Courant number of $C = (0.95\Delta x)/(S^n_{max})$ was used to determine a stable timestep, where S^n_{max} is the maximum absolute wave speed at time level n. Since the bed slope is set to 0% this has the intended effect of simplifying the source terms, only requiring the friction source term to be resolved, facilitating clearer analysis of the novel solution procedure. For real cases involving variable bed topography, a well-balanced treatment of the bed slope source term can be achieved via the hydrostatic reconstruction method [31] or via upwinding of the source terms [57]. The friction source term is resolved using a splitting method presented by Liang and Marche [274]:

$$q^{n+1} = q^n - \Delta t S^n_c = q^n - \Delta t \left(\frac{\tau_f}{1 + \Delta t \frac{\partial \tau_f}{\partial q}} \right)^n = q^n - \Delta t \left(\frac{C_f u|u|}{1 + \frac{2\Delta t C_f |q|}{h^2}} \right)^n$$

The following simple limiter is also implemented to ensure stability in regions where the water depth approaches zero:

$$S^n_c = \frac{q^n}{\Delta t} \text{ if } |\Delta t S^n_c| > |q^n| \tag{3.10}$$

A Manning's n of 0.012 is assumed for all test cases.

Upstream Boundary Condition

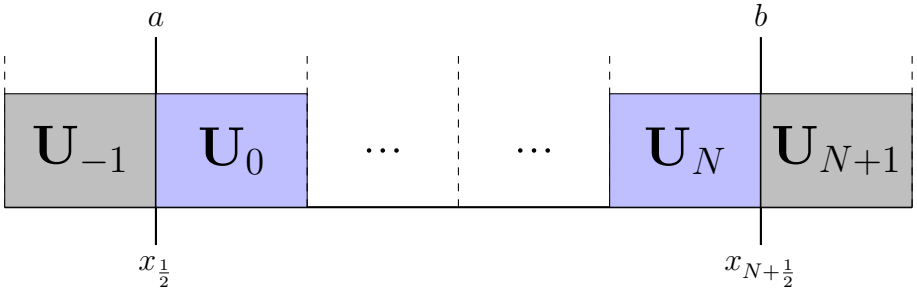

Figure 3.8: Computational domain $[a, b]$, with exterior ghost cells for specifying boundary conditions.

An upstream inflow boundary condition is implemented to ensure a constant flow rate is maintained through the upstream boundary, replicating the pump system used by the S100 flume. This is achieved using exterior ghost cells as shown in Figure 3.8; consider the left boundary $\mathbf{U}_{-1} = \mathbf{U}_L$ (ghost cell) and $\mathbf{U}_0 = \mathbf{U}_R$. Using the Riemann invariant:

$$u_L - 2a_L = u_R - 2a_R$$

and substituting:

$$\begin{aligned} Q_{in} &= h_L u_L \\ u_L &= \frac{Q_{in}}{h_L} \\ a_k &= \sqrt{g h_k} \end{aligned}$$

gives:

$$\frac{Q_{in}}{h_L} - 2\sqrt{g h_L} = u_R - 2\sqrt{g h_R}$$

Which can be rearranged to give the following function:

$$\begin{aligned} \frac{Q_{in}}{h_L} - 2\sqrt{g h_L} - u_R + 2\sqrt{g h_R} &= 0 \\ \frac{Q_{in}}{h_L} + 2\sqrt{g}(\sqrt{h_R} - \sqrt{h_L}) - u_R &= 0 \end{aligned}$$

Let:

$$\begin{aligned} f(h_L, h_R, u_R) &= \frac{Q_{in}}{h_L} + 2\sqrt{g}(\sqrt{h_R} - \sqrt{h_L}) - u_R \\ \frac{d}{dh_L} f(h_L, h_R, u_R) &= -\frac{Q_{in}}{h_L^2} - \frac{\sqrt{g}}{\sqrt{h_L}} \end{aligned}$$

A suitable numerical method such as the Newton-Raphson method can then be used to determine h_L, using an initial guess of $h_0 = h_R$:

$$x_{n+1} = x_n - \frac{f(x_n)}{f'(x_n)}$$

Finally u_L may be determined using:

$$u_L = \frac{Q_{in}}{h_L}$$

providing the initial conditions for use in the Riemann solver at the upstream boundary. Use of the Riemann invariants, as described above, requires that the wave connecting the states at the boundary is a rarefaction wave. This is due to the fact that Riemann invariants are only perfectly invariant across simple waves (the two connected states lie on the same integral curve). The two states connected by a shock wave do not lie on the same integral curve and instead are connected by a Hugoniot locus. Therefore should a shock wave occur at the boundary, which may physically occur when the velocity in the first cell is opposite in direction to the inflow, the outlined method is no longer valid and other conditions must be imposed. However, for the outlined test cases this does not occur so the method is suitable.

Downstream Boundary Condition

At the downstream end of the S100 flume is a sloped free-outfall as shown in Figure 3.6. In order to approximate the behaviour of the flow at this boundary a critical depth boundary condition is imposed. This is achieved by using the following initial conditions at the downstream boundary (Figure 3.9):

$$\mathbf{U}_N^n = \begin{bmatrix} h_N^n \\ h_N^n u_N^n \end{bmatrix} \ , \ \mathbf{U}_{N+1}^n = \begin{bmatrix} h_{N+1} = \left(\frac{\left(h_N^n u_N^n\right)^2}{g} \right)^{\frac{1}{3}} \\ h_{N+1}^n u_{N+1}^n = h_N^n u_N^n \end{bmatrix} \tag{3.11}$$

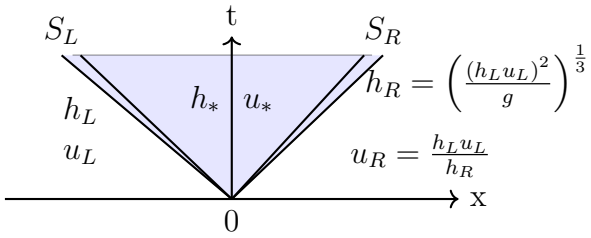

Figure 3.9: Structure of the general solution of the Riemann problem for the downstream boundary with a critical depth condition.

3.3.2 Results

The test cases can be categorised into two primary flow conditions:

1. Flow moving underneath a barrier, which is analogous to flow moving under a gate.
2. Flow which completely inundates the barrier, analogous to an overtopped bridge structure.

Through comparison between the numerical predictions and experimental data for a selection of these test cases, the suitability of the solver for these flow conditions can be determined.

Flow Under a Gate

Figures 3.10 and 4.16 demonstrate that the solver adequately captures the behaviour induced by flow moving underneath a gate-type structure for a range of flows and barrier geometries. It can be seen that for Test Case 10, shown in Figure 3.10a, that the solver contributed to the accurate prediction of flow depths upstream and downstream of the barrier, with a slight overestimation of the velocity and subsequent slight underestimation of the depth downstream of the barrier. Figure 3.10b shows that the percentage error in the depth predictions rises from 0.6% at the left boundary to 23.5% at the right boundary. This corresponds to a small absolute error ranging between 2mm-29mm. Considering the shallow depth of flow downstream of the barrier and the uncertainty in the experimental measurements this is an acceptable result. The discharge is accurately simulated across the domain except for within the cell which immediately precedes the structure. This occurs as a result of the aforementioned $\Delta t/\Delta x(\mathbf{F}^{(+)} - \mathbf{F}^{(-)})$ term. As noted by Dazzi et al. [129], this is a common feature for schemes attempting to model partial barriers to flow such as Ratia et al. [371], Maranzoni and Mignosa [289] and Zhao et al. [498].

For Test Case 2, shown in Figure 3.11, there is a larger, albeit still acceptable, underestimation of the depth upstream of the barrier. Downstream of the barrier, the depth prediction is more accurate, only minimally deviating from the measured data. Figure 3.11b shows that the percentage error in the depth predictions for Test Case 2 are comparable with those for Test Case 10, ranging between $4 - 28\%$, albeit with greater but not unreasonable absolute errors upstream of the barrier. As for Case 2, there is also an underestimation of the flow rate in the cell immediately preceding the barrier, with the discharge being precisely simulated elsewhere within the domain. For both of the presented test cases, it is likely that the errors are as a consequence of a difference in the approximated and real vertical velocity profile at the barrier.

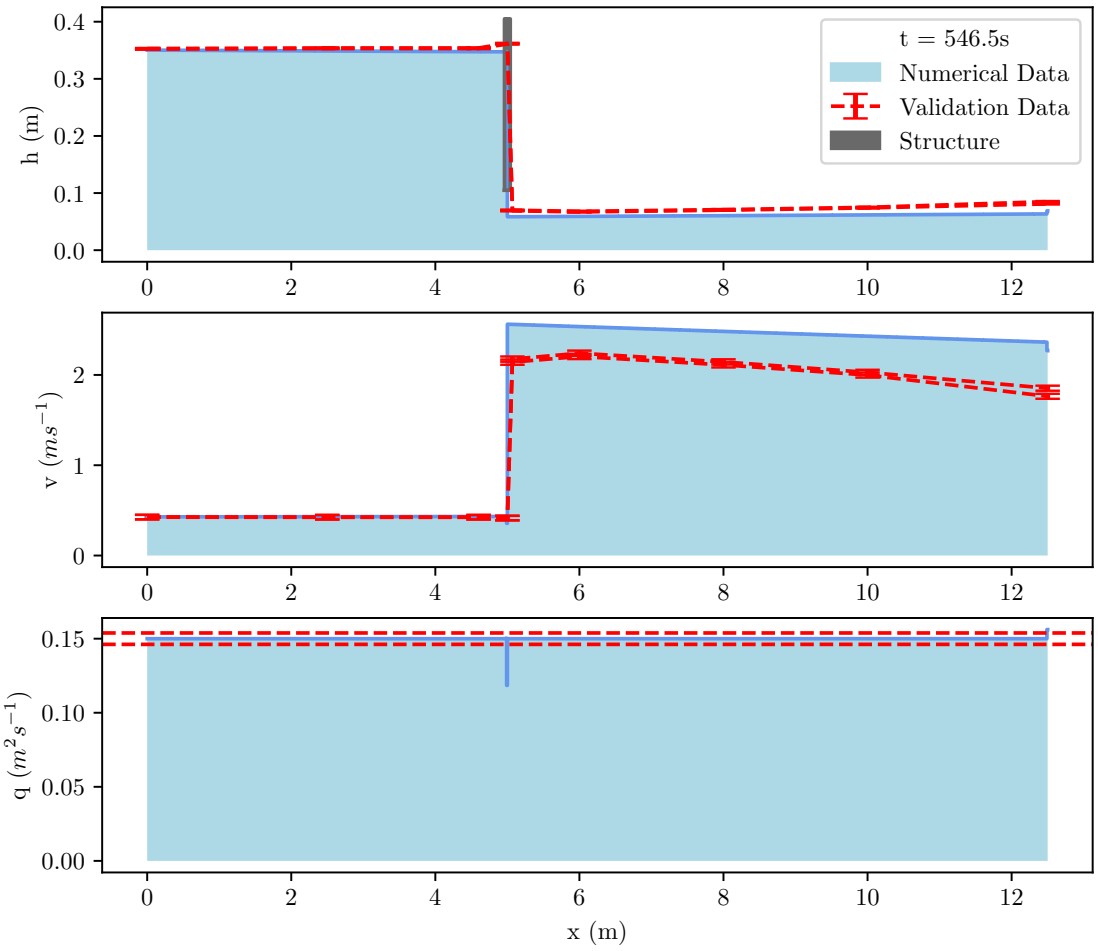

(a)

		x-Position									
		0.00m	2.50m	4.60m	5.00m	5.07m	6.00m	8.00m	10.00m	12.50m	
Average Depth (m)		0.3525	0.3535	0.3535	0.3615	0.0695	0.0675	0.0705	0.0745	0.0830	Experimental Data
Average Velocity (m/s)		0.4255	0.4243	0.4243	0.4149	2.1583	2.2222	2.1277	2.0134	1.8072	
Average Discharge (m^2/s)		0.1500	0.1500	0.1500	0.1500	0.1500	0.1500	0.1500	0.1500	0.1500	
Depth (m)		0.3503	0.3487	0.3474	0.3330	0.0586	0.0592	0.0604	0.0617	0.0635	Simulated Data
Velocity (m/s)		0.4282	0.4301	0.4317	0.3557	2.5601	2.5354	2.4823	2.4292	2.3629	
Discharge (m^2/s)		0.1500	0.1500	0.1500	0.1185	0.1500	0.1500	0.1500	0.1500	0.1500	
Depth (m)	Absolute Error	-0.0022	-0.0048	-0.0061	-0.0285	-0.0109	-0.0083	-0.0101	-0.0128	-0.0195	Error
	Percentage Error	0.6%	1.3%	1.7%	7.9%	15.7%	12.4%	14.3%	17.1%	23.5%	
Velocity (m/s)	Absolute Error	0.0027	0.0058	0.0074	-0.0592	0.4018	0.3132	0.3546	0.4158	0.5556	
	Percentage Error	0.6%	1.4%	1.7%	14.3%	18.6%	14.1%	16.7%	20.7%	30.7%	
Discharge (m^2/s)	Absolute Error	0.0000	0.0000	0.0000	-0.0315	0.0000	0.0000	0.0000	0.0000	0.0000	
	Percentage Error	0.0%	0.0%	0.0%	21.0%	0.0%	0.0%	0.0%	0.0%	0.0%	

(b)

Figure 3.10: Comparison between numerical and experimental results for test case 10. Details of the numerical setup can be found in Section 3.3.1.

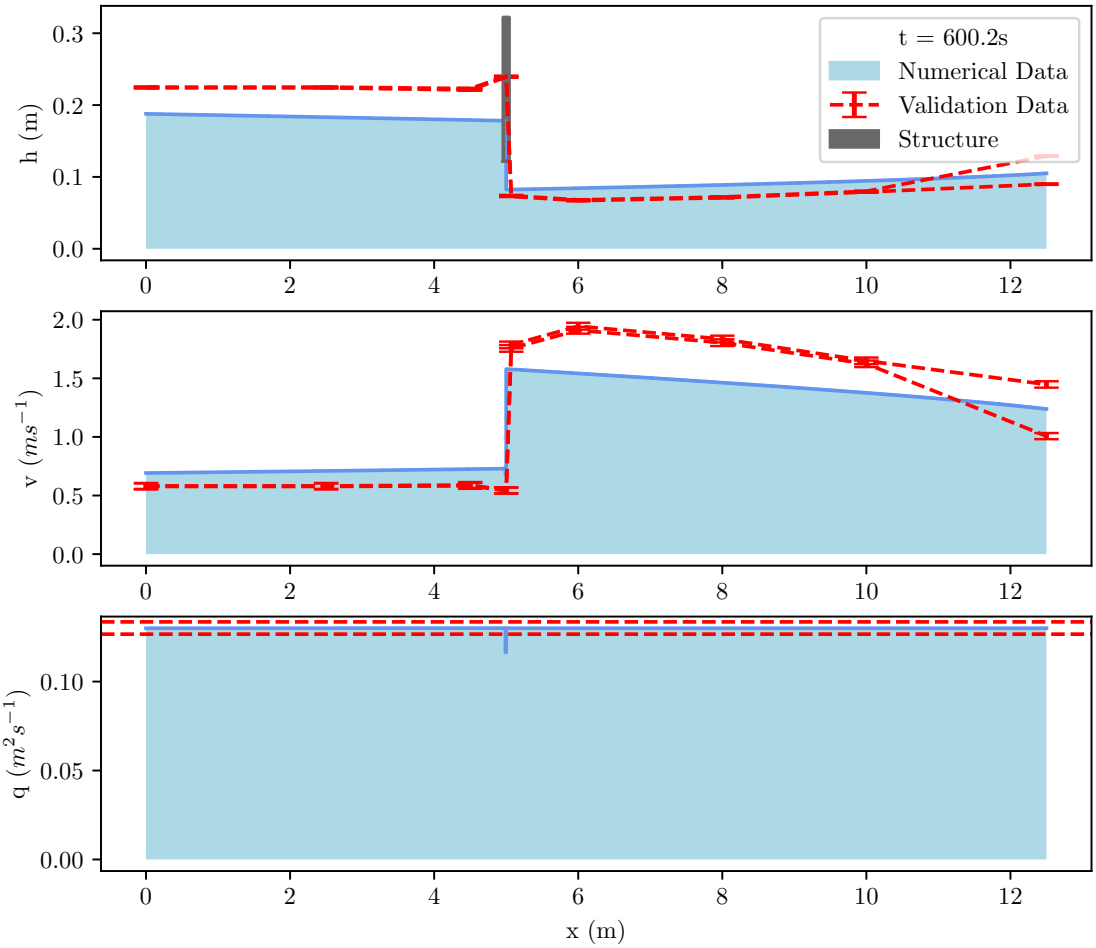

(a)

		x-Position									
		0.00m	2.50m	4.50m	5.00m	5.07m	6.00m	8.00m	10.00m	12.50m	
Average Depth (m)		0.2245	0.2245	0.2220	0.2395	0.0735	0.0675	0.0715	0.0795	0.1095	Experimental Data
Average Velocity (m/s)		0.5795	0.5795	0.5860	0.5432	1.7701	1.9274	1.8196	1.6365	1.1881	
Average Discharge (m^2/s)		0.1301	0.1301	0.1301	0.1301	0.1301	0.1301	0.1301	0.1301	0.1301	
Depth (m)		0.1878	0.1832	0.1790	0.1714	0.0824	0.0843	0.0888	0.0945	0.1050	Simulated Data
Velocity (m/s)		0.6922	0.7097	0.7262	0.6790	1.5769	1.5421	1.4633	1.3762	1.2385	
Discharge (m^2/s)		0.1300	0.1300	0.1300	0.1164	0.1300	0.1300	0.1300	0.1300	0.1300	
Depth (m)	Absolute Error	-0.0367	-0.0413	-0.0430	-0.0681	0.0089	0.0168	0.0173	0.0150	-0.0045	Error
	Percentage Error	16.3%	18.4%	19.4%	28.4%	12.2%	24.9%	24.3%	18.8%	4.1%	
Velocity (m/s)	Absolute Error	0.1127	0.1302	0.1402	0.1358	-0.1931	-0.3853	-0.3563	-0.2603	0.0504	
	Percentage Error	19.4%	22.5%	23.9%	25.0%	10.9%	20.0%	19.6%	15.9%	4.2%	
Discharge (m^2/s)	Absolute Error	-0.0001	-0.0001	-0.0001	-0.0137	-0.0001	-0.0001	-0.0001	-0.0001	-0.0001	
	Percentage Error	0.1%	0.1%	0.1%	10.5%	0.1%	0.1%	0.1%	0.1%	0.1%	

(b)

Figure 3.11: Comparison between numerical and experimental results for test case 2. Details of the numerical setup can be found in Section 3.3.1.

Inundated Bridge Structure

Figures 3.12 and 3.13 demonstrate that the solver is capable of adequately capturing the flow behaviour induced by an overtopped barrier. Figure 3.12a demonstrates that the solver contributed to the accurate prediction of the depth throughout the domain. Figure 3.12b supports this, with errors between the simulated and measured depths ranging between $0.1 - 21\%$. Similarly, depth predictions for Test Case 8 as shown in Figure 3.13a can be seen to be similarly accurate for a different barrier configuration at the same flow rate. For both of the presented test cases there is a small overestimation of the velocity downstream of the barrier which contributes to an underestimation of the downstream flow depth. As the barrier becomes more significantly overtopped, the predictions downstream of the barrier become less accurate however, the general behaviour is still within an acceptable range in comparison with the experimental data. Once more, this is likely a consequence of the simplistic velocity assignment as well as an increase in vertical motion immediately after the barrier; scenarios where the vertical velocity becomes significant violate the underlying assumptions for the conservation law and the scheme becomes unsuitable. Furthermore, it is important to only consider modelling cases for which the flow behaviour does not substantially violate the underlying assumptions for the conservation law and solution procedure. These primary assumptions include: a hydrostatic pressure distribution, that the pressure is atmospheric at the fluid surface and that the velocity in the vertical direction is negligible. However, for flood risk management applications at a catchment scale or greater, the inability to capture local behaviour in the vicinity of a structure, such as the water pouring over the top of the barrier as shown in Figure 3.13a, is relatively inconsequential since the depth and velocity, which is of primary concern, is otherwise accurate.

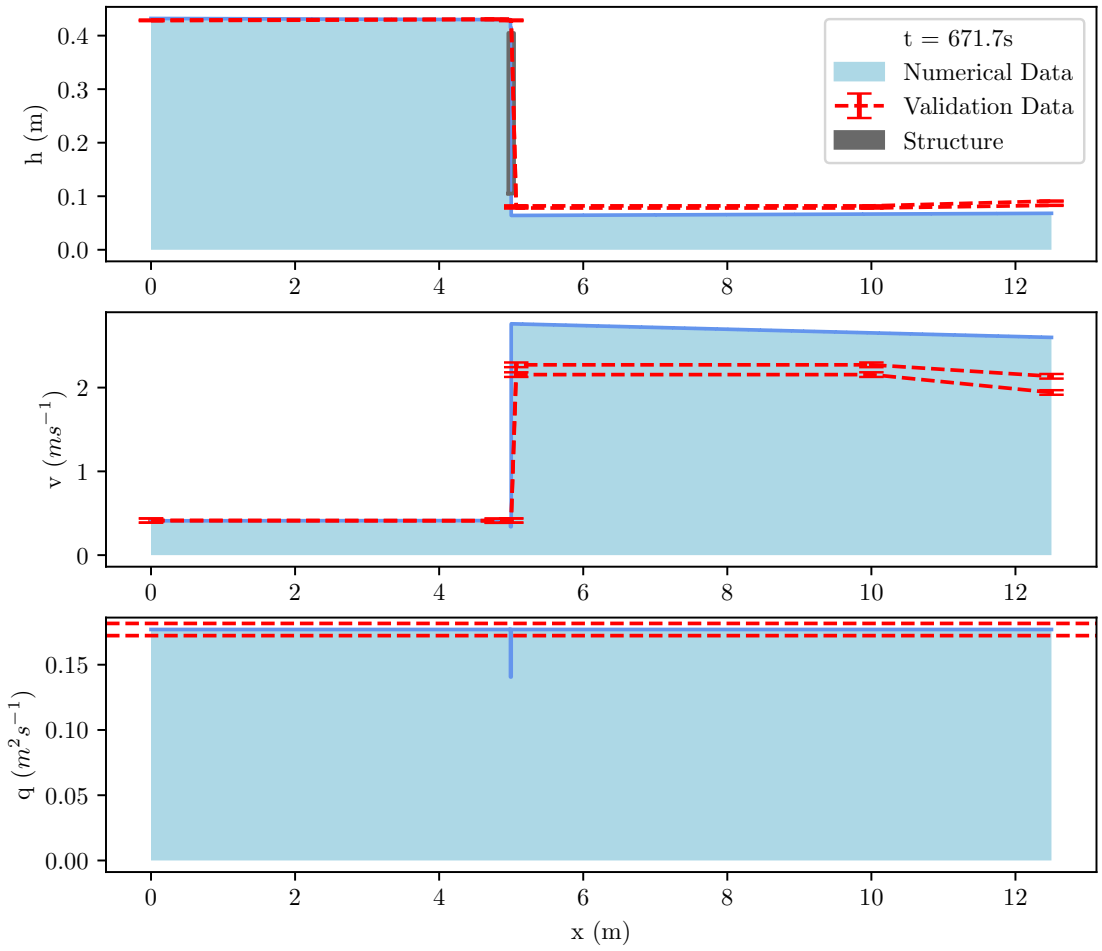

(a)

		x-Position						
		0.00m	4.80m	5.00m	5.07m	10.00m	12.50m	
Average Depth (m)		0.4285	0.4305	0.4285	0.0800	0.0800	0.0870	Experimental Data
Average Velocity (m/s)		0.4130	0.4110	0.4130	2.2119	2.2119	2.0339	
Average Discharge (m^2/s)		0.1770	0.1770	0.1770	0.1770	0.1770	0.1770	
Depth (m)		0.4321	0.4299	0.4147	0.0641	0.0667	0.0681	Simulated Data
Velocity (m/s)		0.4096	0.4117	0.3390	2.7602	2.6532	2.5990	
Discharge (m^2/s)		0.1770	0.1770	0.1406	0.1770	0.1770	0.1770	
Depth (m)	Absolute Error	0.0036	-0.0006	-0.0138	-0.0159	-0.0133	-0.0189	Error
	Percentage Error	0.8%	0.1%	3.2%	19.8%	16.6%	21.7%	
Velocity (m/s)	Absolute Error	-0.0033	0.0007	-0.0739	0.5483	0.4414	0.5651	
	Percentage Error	0.8%	0.2%	17.9%	24.8%	20.0%	27.8%	
Discharge (m^2/s)	Absolute Error	0.0000	0.0000	-0.0364	0.0000	0.0000	0.0000	
	Percentage Error	0.0%	0.0%	20.5%	0.0%	0.0%	0.0%	

(b)

Figure 3.12: Comparison between numerical and experimental results for test case 9. Details of the numerical setup can be found in Section 3.3.1.

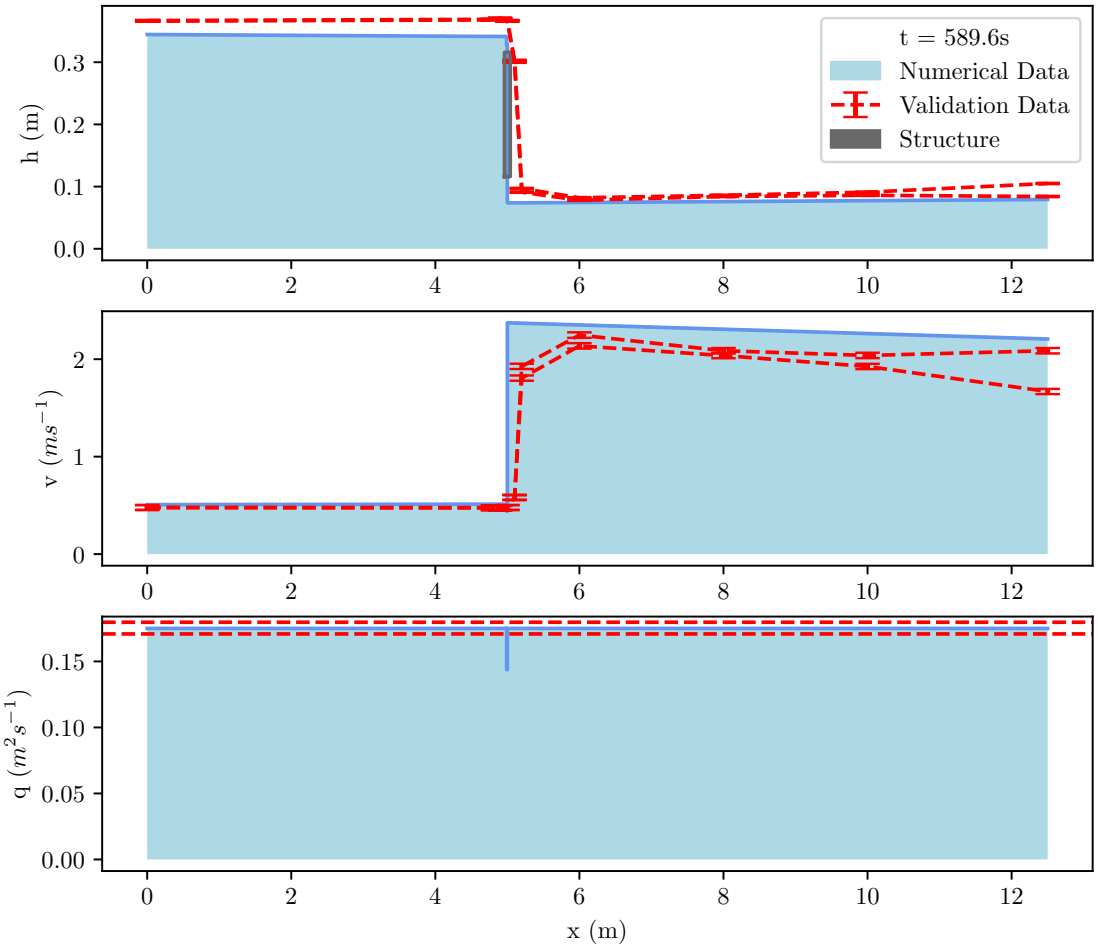

(a)

		x-Position								
		0.00m	4.80m	4.90m	5.00m	5.20m	6.00m	8.00m	10.00m	
Average Depth (m)		0.3665	0.3685	0.3700	0.3665	0.0940	0.0800	0.0850	0.0885	Experimental Data
Average Velocity (m/s)		0.4782	0.4756	0.4736	0.4782	1.8644	2.1906	2.0618	1.9802	
Average Discharge (m^2/s)		0.1753	0.1753	0.1753	0.1753	0.1753	0.1753	0.1753	0.1753	
Depth (m)		0.3448	0.3417	0.3416	0.3279	0.0740	0.0746	0.0760	0.0775	Simulated Data
Velocity (m/s)		0.5084	0.5131	0.5132	0.4393	2.3676	2.3500	2.3058	2.2615	
Discharge (m^2/s)		0.1753	0.1753	0.1753	0.1440	0.1753	0.1753	0.1753	0.1753	
Depth (m)	Absolute Error	-0.0217	-0.0268	-0.0284	-0.0386	-0.0200	-0.0054	-0.0090	-0.0110	Error
	Percentage Error	5.9%	7.3%	7.7%	10.5%	21.2%	6.8%	10.6%	12.4%	
Velocity (m/s)	Absolute Error	0.0303	0.0375	0.0395	-0.0388	0.5033	0.1593	0.2440	0.2813	
	Percentage Error	6.3%	7.9%	8.3%	8.1%	27.0%	7.3%	11.8%	14.2%	
Discharge (m^2/s)	Absolute Error	0.0000	0.0000	0.0000	-0.0312	0.0000	0.0000	0.0000	0.0000	
	Percentage Error	0.0%	0.0%	0.0%	17.8%	0.0%	0.0%	0.0%	0.0%	

(b)

Figure 3.13: Comparison between numerical and experimental results for test case 8. Details of the numerical setup can be found in Section 3.3.1.

Mesh Convergence Analysis

			x-Position (m)					
			0	4.8	5	5.07	10	12.5
Measured	Min	Depth (m)	0.428	0.43	0.428	0.078	0.078	0.083
	Max		0.429	0.431	0.429	0.082	0.082	0.091
	Min	Velocity (m/s)	0.414	0.412	0.414	2.272	2.272	2.135
	Max		0.412	0.41	0.412	2.155	2.155	1.942
	Min	Discharge (m^2/s)	0.177	0.177	0.177	0.177	0.177	0.177
	Max		0.177	0.177	0.177	0.177	0.177	0.177
Simulated	1cm Grid	Depth (m)	0.4321	0.4299	0.4147	0.0641	0.0667	0.0681
		Velocity (m/s)	0.4096	0.4117	0.3390	2.7602	2.6532	2.5990
		Discharge (m2/s)	0.1770	0.1770	0.1406	0.1770	0.1770	0.1770
	2cm Grid	Depth (m)	0.4321	0.4299	0.4147	0.0641	0.0667	0.0681
		Velocity (m/s)	0.4096	0.4117	0.3390	2.7599	2.6532	2.5990
		Discharge (m2/s)	0.1770	0.1770	0.1406	0.1770	0.1770	0.1770
	4cm Grid	Depth (m)	0.4321	0.4299	0.4147	0.0641	0.0667	0.0681
		Velocity (m/s)	0.4096	0.4117	0.3390	2.7597	2.6531	2.5994
		Discharge (m2/s)	0.1770	0.1770	0.1406	0.1770	0.1770	0.1770
	5cm Grid	Depth (m)	0.4321	0.4299	0.4147	0.0641	0.0667	0.0681
		Velocity (m/s)	0.4096	0.4117	0.3390	2.7592	2.6520	2.5990
		Discharge (m2/s)	0.1770	0.1770	0.1406	0.1770	0.1770	0.1770
	8cm Grid	Depth (m)	0.4321	0.4299	0.4147	0.0641	0.0667	0.0681
		Velocity (m/s)	0.4095	0.4116	0.3390	2.7594	2.6521	2.6002
		Discharge (m2/s)	0.1770	0.1770	0.1406	0.1770	0.1770	0.1770
	10cm Grid	Depth (m)	0.4321	0.4300	0.4147	0.0642	0.0668	0.0681
		Velocity (m/s)	0.4095	0.4121	0.3390	2.7588	2.6508	2.5989
		Discharge (m2/s)	0.1770	0.1772	0.1406	0.1770	0.1770	0.1770

Table 3.2: Comparison between the experimental data and simulated data for Test Case 9, for a range mesh resolutions.

The data in Table 3.2 demonstrates negligible differences in the results for the tested mesh resolutions which range between $1 - 10$cm ($\Delta x = 1 - 10$cm).

3.4 Conclusion

A novel Riemann solver capable of modelling the influence of structures on flood flows within 1D or 2D hydrodynamic flood models has been presented. The validation process demonstrates that the solver is able to adequately capture the flow behaviour for a range of partial barriers to flow at a range of flow rates. Accuracy of the predictions is mostly dependent on how well the velocity assignment process captures the vertical velocity profile at the barrier. As a result, further work to derive a more sophisticated and representative approach to determining the layer velocities for structure cells is proposed. However, in its current state the proposed solver still presents a unique physically based and robust approach to modelling hydraulic structures using a conservative form of the conservation laws. Furthermore, since the solution procedure only applies locally in the region surrounding an interface at which a structure is being modelled, implementation is feasible for both established and developing hydrodynamic models using finite volume schemes to solve the shallow water equations. The biggest barrier to implementation is the availability and resolution of the required data for structures and suitable meshing algorithms. The latter of which is also to be the subject of future work.

Addition of the capability to model a variety of in-channel hydraulic structures such as gates and bridges has the potential to significantly improve the accuracy and flexibility of inundation predictions and therefore contemporary hydrodynamic modelling practice. Further potential applications include but are not limited to:

- Infrastructure resilience modelling: particularly applications concerning the structural health monitoring of bridge structures.
- Flood risk management schemes involving the introduction or removal of control structures such as leaky barriers.

However, when using the solver, as for all solvers and numerical schemes, care must be taken to ensure that the underlying assumptions are not violated in order to ensure sufficient modelling accuracy is achieved. As a consequence, the solver can be considered appropriate for modelling the referenced hydraulic structures at a spatial scale whereby approximating the structure as a blockage existing at a cell interface is appropriate. In such cases, the additional energy losses, which are not included within the scheme, should be insignificant in contrast to the influence of the blockage of the flow by the structure, which has been demonstrated to be captured by the scheme. For flood risk management applications, whereby the upstream backwater depths are most relevant for assessing flood risk, the validation of the model suggests that the proposed method is suitable and superior to available alternatives. Considering the compatibility of the proposed solver with existing numerical schemes implemented within contemporary hydrodynamic models, the method presents a viable and relatively easy to implement solution. For detailed analyses of individual structures three-dimensional computational fluid dynamics (CFD) analyses are recommended.

In terms of further solver development, adding the capability to model vertical exchanges of momentum and non-hydrostatic pressure distributions would help to overcome some of the solvers current deficiencies. Although, addition of this further capability would also likely reduce the compatibility of the solver with existing numerical schemes.The inclusion of additional energy losses is also desirable however, explicit inclusion of energy losses as source terms would require altering the system of equations, once again reducing compatibility of the solver with existing numerical schemes.

Chapter 4

A Local Multi-Layer Approach to Modelling Interactions between Shallow Water Flows and Obstructions

The capability to accurately predict flood flows via numerical simulations is a key component of contemporary flood risk management practice. However, modern flood models lack the capacity to accurately model flow interactions with linear features, or hydraulic structures like bridges and gates, which act as partial barriers to flow. Presented within this paper is a new Riemann solver which represents a novel approach to modelling fluid-structure interactions within two-dimensional hydrodynamic models. The solution procedure models obstacles as existing at the interface between neighbouring cells and uses a combination of internal boundary conditions, different forms of the conservation laws and vertical discretisation of the neighbouring cells to resolve numerical fluxes across a partially obstructed interface. The predictive capacity of the solver has been validated through comparisons with experimental data collected from experiments conducted in a state-of-the-art hydraulic flume. Since the solution procedure is local, only applying to the cells within the immediate vicinity of a structure, the method is designed to be compatible with existing two-dimensional hydrodynamic models which use a finite volume scheme to solve the shallow water equations.

This chapter is available as a preprint and has been accepted for publication in Computer Methods in Applied Mechanics and Engineering: James Mckenna, Vassilis Glenis, Chris Kilsby, A Local Multi-Layer Approach to Modelling Interactions between Shallow Water Flows and Obstructions, arXiv:2304.10262 [physics.flu-dyn], 10.48550/arXiv.2304.10262.

4.1 Introduction

The ominous threat of anthropogenic climate change is driving the requirement for more effective flood risk management in order to better manage what is already a challenging and costly hazard; models estimate that forecasted average annual flood losses for the United States will increase from US$32 billion to more than US$40 billion by 2050 [483], with similar predictions of increasing flood risk being made on a global scale [222]. Hydrodynamic models play a vital role in contemporary flood risk management by providing evidence, via numerical predictions, upon which the quantification of flood risk and consequential future investment is based. It is therefore vital for effective flood risk management that hydrodynamic models produce accurate predictions.

Within catchments, channel structures, such as bridges, weirs and gates, can act as obstacles to flow, significantly influencing the local flow characteristics [109]. However, within contemporary hydrodynamic modelling practice, methods for modelling such features are relatively under-utilised, with industry standard models using coarse approximations, empirically based methods or even omitting such features entirely [54, 444, 81]. This is despite the fact that within academic literature there have been a number of contributions towards bridging this gap in modelling capacity.

A common approach to modelling partial barriers to flow is to represent hydraulic structures as existing at the interface between neighbouring cells, neglecting the width of the structure in the streamwise direction. An internal boundary condition can then be implemented to account for the effect of the structure. A variety of internal boundary conditions have been proposed within academic literature:

- Pepe et al. [359] modelled the effect of channel constrictions and obstructions as a stationary weak solution of the Saint Venant equations without friction.
- Cozzolino et al. [119] developed an approximate Riemann solver, based upon derived exact solutions for the dam-break problem across a partially lifted gate, to model flow under gates using a novel non-equilibrium gate formulation.
- Zhao et al. [498] proposed modification of the numerical flux across hydraulic structures in accordance with empirical discharge relations.
- Morales-Hernández et al. [322] proposed the use of gate equations to modify the conserved variables in the neighbouring cells in order to capture flow under gates.
- Jaafar and Merkley [237] considered the use of the method of characteristics to solve interior gate boundary conditions coupled with an approximate Riemann solver.
- Guerra et al. [190] derived coupling conditions based upon weir equations to solve a Riemann problem constructed across a weir.
- Ratia et al. [371] implemented a source term based upon a modified Borda-Carnot formulation to account for the head loss induced by flow through a unsubmerged, partially submerged or fully submerged bridge structure.
- Maranzoni and Mignosa [289] locally modified the conservation laws, using the Preissmann slot concept to capture the transition between free surface and pressurised flow through bridges.

- Dazzi et al. [129] extended the concept introduced by Morales-Hernández et al. to model low flow, partially pressurised, fully pressurised and overtopped flow conditions for hydraulic structures.
- Iguchi and Lannes [229] presented a general approach to solving one-dimensional initial boundary value problems for the purpose of modelling wave-structure interactions.

Unified approaches that don't neglect the streamwise width of the structure include the two-component pressure approach proposed by Cea et al. [96] and the congested shallow water model derived by Godlewski et al. [182].

In terms of modelling flow under barriers, the approach of Cozzolino et al. [119] is the most sophisticated, making significant advances on previous works, producing numerical results which are in agreement with the derived exact solutions and experimental validation. However, the application of the method is specifically desgined for flow under gates and therefore cannot be used as a general solver for partial barriers to flow without significant further advancements. Improvements in the empirical and physical understanding of combined flow over a weir and under a gate [393, 389, 464], in combination with advances in methods for solving initial boundary value problems for hyperbolic systems [229], may present avenues for extension of this method to include simultaneous weir flows, however, a solution of this type is currently unrealised. The work of Guerra et al. [190] introduces a method for coupling the weir equations; however, only validation through expert falsification is provided, and the method is restricted to modelling flow over a weir for subcritical initial data.

The works of Dazzi et al. [129] and Ratia et al. [371] are able to handle more general flow configurations however, these methods have their own respective drawbacks: the discharge formulae utilised by Dazzi et al. [129] are unsuitable for unsteady flows and both methods may require impractical calibration of uncertain parameters. Furthermore, the head loss source term proposed by Ratia et al. [371] may be unable to sufficiently capture nearfield flow effects including potential downstream supercritical flows.

Considering methods that address the vertical confinement of flow induced by structures, the two-component pressure approach proposed by Cea et al. [96] provides an alternative which requires less calibration. However, the method is also unable to accurately capture nearfield flows patterns with the additional disadvantage of being unable to handle overtopping. Similarly, the approach proposed by Maranzoni and Mignosa [289] is unable to handle overtopping and suffers from the well-established limitations of the Preissmann slot concept [287, 462]. The congested shallow water model derived by Godlewski et al. [182] is also restricted in its application due to the method's inability to model overtopping. Additionally, the requirement to implement the congestion constraint across the whole domain is an impractical feature for large-scale flood modelling. Restricting the implementation of the congested shallow water model to the cells which contain a structure with a ceiling could provide a potential compromise, however, a localised implementation may be challenging due to compatibility issues with standard solution methods applied to the classical shallow water equations; for the congested shallow water model, classical Godunov solvers are too dissipative and impose too much restriction on the timestep [137, 192].

It is therefore clear that, despite significant advancements within academic research, that

there is much progress still to be made in the search for a generalised treatment of partial barriers to flow which can accomodate all potential flow configurations (flow under, flow over and simultaneous flow under and over an obstacle), taking into account energy losses and the potential vertical confinement of the flow, whilst also producing satisfactory macroscale and nearfield flow predictions. Within the context of the outlined existing solutions, the aim of this paper is to present a new method for modelling partial barriers to flow which ignores the streamwise width of the structure, effects of vertical confinement and head loss but captures the nearfield and macroscale behaviour of the flow for all flow configurations. As such, the method presents an alternative to that of Dazzi et al. [129] and Ratia et al. [371], aiming to reduce the need for calibration, improve nearfield flow prediction accuracy and eliminate the use of empirical discharge relations which are invalid for unsteady flows. Ignoring the streamwise width of the structure, some energy losses and the effect of vertical confinement is justified by considering the modelling of structures at a scale for which the effect induced by the blockage of the flow by the structure dominates. It is considered that this is an appropriate assumption for the intended purpose of hydrodynamic flood modelling on spatial domains of relevance to flood risk management.

Within Mckenna et al. [303], the authors of this paper presented a new Riemann solver capable of resolving numerical fluxes across a partially obstructed interface. The proposed solution procedure represents structures as existing at the interface between neighbouring cells and uses a combination of internal boundary conditions and a different form of the conservation laws in the adjacent cells, to resolve numerical fluxes across the partially obstructed interface. Experimental validation, via experiments conducted in a state-of-the-art research flume, demonstrated the accuracy of the solver for a range of flow conditions and barrier configurations. Despite the successful validation of the solver, there is opportunity for enhancement of the method via more accurate discretisation of the horizontal velocity in the vertical plane. As such, this paper aims to use the basic conceptual idea underpinning the Riemann solver developed in [303], which is the decomposition of the Riemann problem in the vertical plane, to develop a new, more sophisticated and accurate method for representing structures within two-dimensional hydrodynamic models.

Whereas the method presented in [303] primarily accounts for the presence of an obstacle via a modification of the numerical flux, whereby the velocity profile is approximated based upon assumptions, the improved method introduces a vertical discretisation of the cells neighbouring an interface at which a structure is modelled in order to explicitly capture a more representative velocity profile. Since the structure cells require vertically discretised numerical fluxes, this necessitates the introduction of intermediate cells which act as a link between the neighbouring monolayer and multi-layer formulations. As for the development of the previous solver, considering the relative under-utilisation of methods for modelling obstructions within industry standard flood models, ease of implementation and compatibility of the method with existing flood models utilising two dimensional finite volume schemes to solve the shallow water equations was a key consideration throughout.

4.2 Mathematical Model

The proposed solution method divides the computational domain into structure cells, intermediate cells and normal cells with corresponding normal interfaces (NI), intermediate interfaces (II) and structure interfaces (SI) as shown in Figure 4.1. At a structure interface, the adjacent structure cells are vertically discretised into sub-cells with a limit flow depth corresponding to the dimensions of the idealised structure represented at the interface as shown in Figure 4.2. For example, the sub-cells $\mathbf{U}_{i,1}$ and $\mathbf{U}_{i+1,1}$ in Figure 4.2 have a limit flow depth of $H_{3/2} - H_{1/2}$ which is equivalent to $H_{3/2} - z_b$, which represents the difference in elevation between the base of the structure and the bed. For each intermediate or structure cell, the bed elevation is denoted as $H_{1/2} = z_b$ and the elevation of the base and cover of the structure are denoted as $H_{3/2}$ and $H_{5/2}$ respectively. The alignment of the sub-cells with the structure is necessary to enable the implementation of vertically variable boundary conditions at the structure interface, under the shallow water assumption that the flow direction is primarily horizontal. Intermediate cells act as a link between the mono-layer scheme utilised by the normal cells and the multi-layer scheme used by the structure cells.

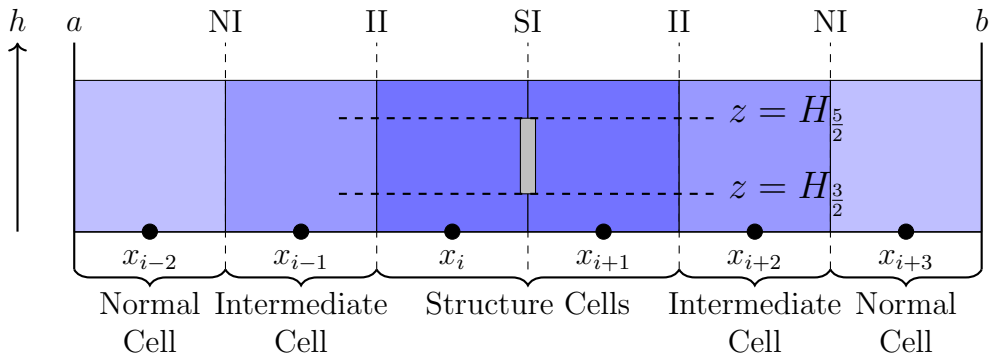

Figure 4.1: A simple computational domain $[a, b]$ illustrating the designation of structure, intermediate and normal cells with their corresponding interfaces. $H_{3/2}$ and $H_{5/2}$ represent the elevation of the projected base and cover of the idealised structure represented at the structure interface (see the horizontal dashed lines for illustration).

For normal interfaces and the corresponding adjacent normal or intermediate cells, a one-dimensional (1D) FV scheme is used to solve the 1D Shallow Water Equations (1D-SWE) given as:

$$\partial_t \mathbf{U} + \partial_x \mathbf{F}(\mathbf{U}) = \mathbf{S}(\mathbf{U}) \tag{4.1}$$

Where $\mathbf{U}$ is the vector of conserved variables, $\mathbf{F}(\mathbf{U})$ is the vector of fluxes and $\mathbf{S}(\mathbf{U})$ is a vector of sources comprising of $\mathbf{S}_0$, the bed slope source term and $\mathbf{S}_f$, the bed friction source term. These terms are given as follows:

$$\mathbf{U} = \begin{bmatrix} h \\ hu \end{bmatrix} \quad , \quad \mathbf{F} = \begin{bmatrix} hu \\ hu^2 + \frac{1}{2}gh^2 \end{bmatrix} \quad , \quad \mathbf{S}_0 = \begin{bmatrix} 0 \\ -gh\partial_x z \end{bmatrix} \quad , \quad \mathbf{S}_f = \begin{bmatrix} 0 \\ -\tau_f \end{bmatrix} \tag{4.2}$$

Whereby h denotes the depth of flow, u denotes the velocity component in the x direction, g is the acceleration due to gravity, z is the elevation of the bed and τ_f is the shear stress due to bed friction in accordance with Manning's equation:

$$\tau_f = C_f u|u| = \frac{gn^2}{\sqrt[3]{h}} u|u| \tag{4.3}$$

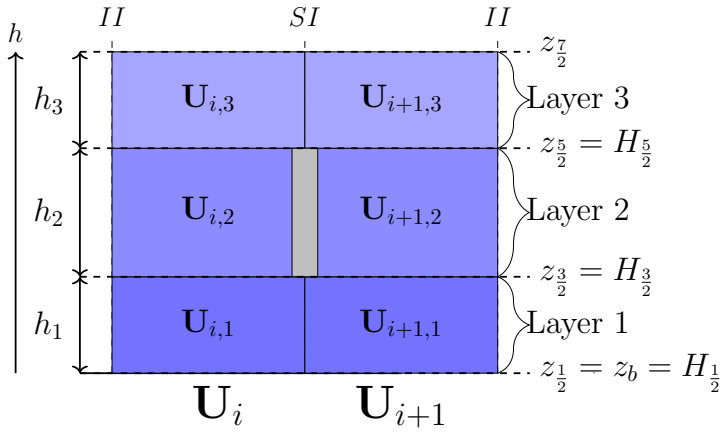

Figure 4.2: Division of structure cells into $N = 3$ sub-cells corresponding to the base ($H_{3/2}$) and cover ($H_{5/2}$) of the idealised structure modelled at the structure interface. The limit flow depth in the $U_{i,k}$ sub-cell, for $1 \leq k \leq N-1$, is equal to $H_{i,k+1/2} - H_{i,k-1/2}$. The uppermost layer, $U_{i,N}$ has no restriction applied to the flow depth. The upper and lower interfaces of layer k are denoted as $z_{k\pm1/2}$.

Where n is Manning's roughness coefficient.

For the structure and intermediate interfaces and corresponding adjacent structure and intermediate cells, a 1D FV scheme is used to solve a multi-layer 1D shallow water system based upon [418]:

$$\partial_t \mathbf{U}_k + \partial_x \mathbf{F}_k(\mathbf{U}_k) = \mathbf{S}_k(\mathbf{U}_k) \tag{4.4}$$

Where $\mathbf{U}_k$ is the vector of conserved variables for the layer k, $\mathbf{F}(\mathbf{U}_k)$ is the vector of fluxes for layer k and $\mathbf{S}_k(\mathbf{U}_k)$ is a vector of sources for layer k comprising of $\mathbf{S}_{k,0}$, the topographic source terms for layer k and $\mathbf{S}_{k,f}$, the friction source terms for layer k. These terms are given as follows:

$$\mathbf{U}_k = \begin{bmatrix} h_k \\ h_k u_k \end{bmatrix} \tag{4.5}$$

$$\mathbf{F}_k = \begin{bmatrix} h_k u_k \\ h_k u_k^2 + \frac{1}{2} g h_k^2 + g h_{k_{(+)}} h_k \end{bmatrix} = \begin{bmatrix} q_k \\ \sigma_k \end{bmatrix} \tag{4.6}$$

$$\mathbf{S}_{k,0} = \begin{bmatrix} 0 \\ -R_{k+\frac{1}{2}} + R_{k-\frac{1}{2}} \end{bmatrix} = \begin{bmatrix} 0 \\ g h_{k_{(+)}} \partial_x z_{k+1/2} - g(h_{k_{(+)}} + h_k) \partial_x z_{k-1/2} \end{bmatrix} \tag{4.7}$$

$$\mathbf{S}_{k,f} = \begin{bmatrix} 0 \\ \tau_{k+\frac{1}{2}} - \tau_{k-\frac{1}{2}} \end{bmatrix} =$$

$$\begin{bmatrix} 0 \\ (1-\delta_{nk}) \left(\frac{2\nu(u_{k+1}-u_k)}{h_{k+1}+h_k} - \frac{1}{2}(u'_{k+\frac{1}{2}})^2 \right) - \left((1-\delta_{1k}) \left(\frac{2\nu(u_k-u_{k-1})}{h_k+h_{k-1}} - \frac{1}{2}(u'_{k-\frac{1}{2}})^2 \right) - \delta_{1k} \frac{g n^2 u_k |u_k|}{\sqrt[3]{H}} \right) \end{bmatrix} \tag{4.8}$$

Where k refers to the index of the layer under consideration, labelled in ascending order from layer 1 at the bed, to layer N at the free surface. $k+1/2$ and $k-1/2$ refer respectively to the upper and lower interface of the flow in layer k. The subscript $k_{(+)}$ refers to the

properties of the flow above layer k where $h_{k_{(+)}}$ is defined as:

$$h_{k_{(+)}} = \sum_{j=k+1}^{N} h_j \tag{4.9}$$

$R_{k+1/2}$ and $R_{k-1/2}$ refer to the reaction forces exerted at the interfaces between the layers, with $R_{k+1/2}$ denoting the reaction force of layer k onto the fluid above and $R_{k-1/2}$ denoting the reaction force exerted on layer k by the fluid or bed beneath it. $\tau_{k+1/2}$ and $\tau_{k-1/2}$ represent the interlayer viscous friction effect induced at the upper and lower interfaces of layer k. The interlayer friction terms are derived for a multi-layer cell by applying a finite difference approximation, across the depth of the fluid layer k, to the Reynolds averaged stress component under the Boussinesq approximation [221]:

$$\begin{aligned}\int_{z_{k-\frac{1}{2}}}^{z_{k+\frac{1}{2}}} \frac{\partial}{\partial z}\left[2\nu\frac{\partial u}{\partial z} - K_E\right] dz &= \left(2\nu\frac{\partial u}{\partial z} - K_E\right)\Big|_{z_{k+\frac{1}{2}}} - \left(2\nu\frac{\partial u}{\partial z} - K_E\right)\Big|_{z_{k-\frac{1}{2}}} \\ \approx \frac{2\nu(u_{k+1}-u_k)}{h_{k+1}+h_k} - \frac{1}{2}\left(\frac{q_{k+1}+q_k}{h_{k+1}+h_k} - U\right)^2 &- \frac{2\nu(u_k-u_{k-1})}{h_k+h_{k-1}} + \frac{1}{2}\left(\frac{q_k+q_{k-1}}{h_k+h_{k-1}} - U\right)^2 \\ &= \tau_{k+\frac{1}{2}} - \tau_{k-\frac{1}{2}}\end{aligned} \tag{4.10}$$

Where $\nu = \nu_l + \nu_t$, is the total effective viscosity equal to the laminar viscosity ν_l, which is a physical property of the fluid and ν_t, which is the depth-averaged turbulent viscosity. The depth-averaged turbulent viscosity is evaluated, based on the assumption of a logarithmic velocity profile whereby bed-generated turbulence dominates over free layer turbulence as proposed in [500]:

$$\nu_t = \frac{\kappa}{6} U_* H \tag{4.11}$$

where κ is the von Kármán constant equal to 0.4, H is the total depth of flow and U_* is the depth-averaged shear velocity, which is given as:

$$U_* = \sqrt{\frac{gU^2}{C_z^2}} \equiv \sqrt{\frac{gn^2U^2}{H^{1/3}}} \tag{4.12}$$

where U is the depth-averaged velocity for the whole cell. K_E is the turbulent kinetic energy given as:

$$K_E = \frac{1}{2}u'u' \tag{4.13}$$

where u' is the variation of the velocity about the mean value. For the case where $k = 1$, considering the layer which flows over the bed, $\tau_{k-1/2} = \tau_b$ which is instead derived from Manning's equation (4.3), where H is the total depth of flow for the whole structure cell. The particular form of the viscous effect on the base of the fluid layer, $\tau_{k-1/2}$, is accounted for by the Kronecker delta in (4.8), which is defined as:

$$\delta_{\alpha k} = \begin{cases} 1 \text{ if } k = \alpha \\ 0 \text{ if } k \neq \alpha \end{cases} \tag{4.14}$$

The Kronecker delta also ensures that the $\tau_{k+1/2}$ term is zero at the free surface for layer N. The source terms for structure cells are also illustrated in Figure 4.3. Effects relating to stresses as a result of volumetric deformation are not considered necessary to include

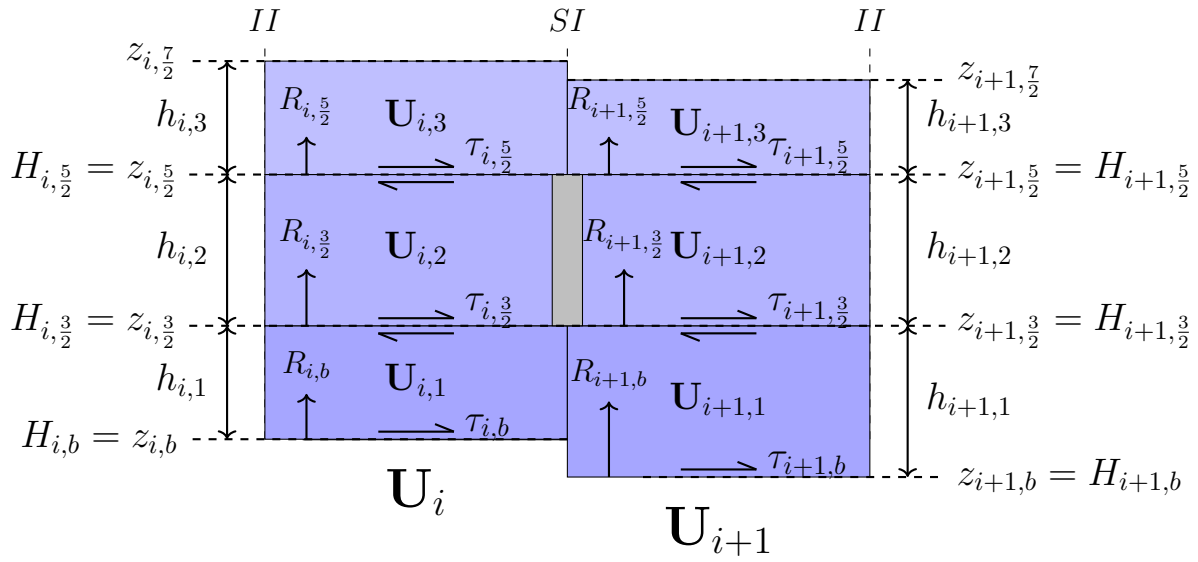

Figure 4.3: Annotation of the source terms for example structure cells and their component sub-cells on uneven bed topography. R represents a reaction force induced as a result of the uneven bed topography, τ represents a friction force acting at a layer interface, z denotes the elevation above the bed and h denotes the water depth in the sub-cell. $\mathbf{U}_i$ is the vector of conserved variables for the ith whole cell, which is equal to the sum of the conserved variables for the component sub cells $\mathbf{U}_{i,k}$.

due to their minor influence [468].

The domain is divided into cells $(\mathbf{V}_i)_{i\in\mathbb{Z}}$ and the discretised first-order finite volume scheme is given by:

$$\mathbf{U}_i^{n+1} = \mathbf{U}_i^n - \frac{\Delta t}{\Delta x}\left[\mathbf{F}_{i+\frac{1}{2}} - \mathbf{F}_{i-\frac{1}{2}}\right] + \Delta t \mathbf{S}\left(\mathbf{U}_i^n\right) \tag{4.15}$$

Where the subscript i represents the ith cell, the superscript n represents the nth time level and Δx and Δt represent the cell size and time step respectively. $\mathbf{F}_{i-1/2}$ and $\mathbf{F}_{i+1/2}$ represent the numerical fluxes at the $i \pm 1/2$ interfaces respectively. For the structure cells, it is the constituent sub-cells which are updated using the following modification of (4.15):

$$\mathbf{U}_{i,k}^{n+1} = \mathbf{U}_{i,k}^n - \frac{\Delta t}{\Delta x}\left[\mathbf{F}_{i+\frac{1}{2},k} - \mathbf{F}_{i-\frac{1}{2},k}\right] + \Delta t \mathbf{S}\left(\mathbf{U}_{i,k}^n\right) \tag{4.16}$$

Where $\mathbf{U}_{i,k}^n$ represents the conserved variables for the kth sub-cell in the ith structure cell at time level n. $\mathbf{F}_{i-1/2,k}$ and $\mathbf{F}_{i+1/2,k}$ represent the numerical fluxes at the kth layer of the $i \pm 1/2$ interfaces respectively. Although a 1D scheme is implemented in this case, implementation as a 2D scheme requires no fundamental changes to the method.

4.2.1 Derivation of the Decoupled Multi-layer Shallow Water System

The following derivation is based upon the two-layer system derived in Spinewine et al. [418] and is included here for completeness: consider a one-dimensional depth-averaged shallow water model divided into N horizontal layers of uniform density, operating under the classical assumption of immiscible fluid layers, as shown in Figure 4.4.

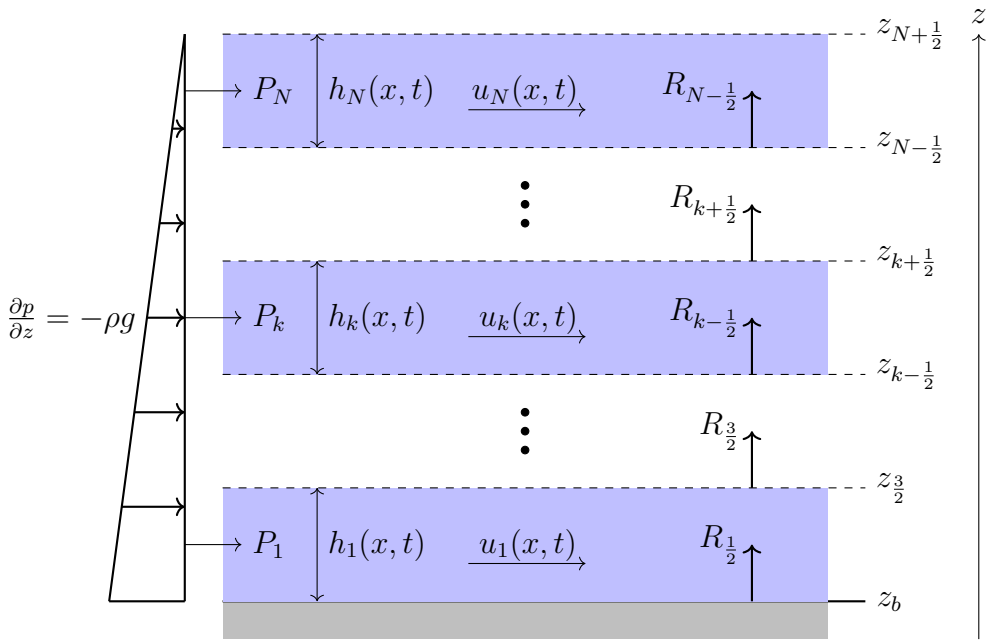

Figure 4.4: Details for a one-dimensional multi-layer shallow water system. Ellipses denote the presence of additional layers which aren't illustrated.

The continuity equation governing each layer can be expressed as follows:

$$\partial_t h_k + \partial_x q_k = 0 \ , \ 1 \leq k \leq N \tag{4.17}$$

where h_k is the depth of layer k, $q_k = h_k u_k$ is the unit discharge of layer k and u_k is the depth-averaged velocity of the flow in layer k.

Commencing with the highest layer, the momentum equation for layer N can be expressed as:

$$\partial_t \rho q_N + \partial_x \left(\rho h_N u_N^2 + P_N \right) = R_{N-\frac{1}{2}} \tag{4.18}$$

where P_N is the hydrostatic pressure force exerted onto layer N and $R_{N-1/2}$ is the interlayer reaction force exerted on layer N by layer $N-1$. Notably, the interlayer reaction force $R_{N-1/2}$ is implemented as a topographic source term; for each layer k, the *apparent topography* is defined as the sum of the cumulative thickness of layers beneath it plus the bed elevation. This approach differs from classical multi-layer shallow water systems, where this term represents a non-conservative pressure coupling term incorporated within the x-derivative of the flux. The presented form of the equations is based upon the assumption that the *apparent topography* is invariant in time, which is not strictly true except under special circumstances, such as when using a time-splitting method [70], or when redefining the layer properties to ensure alignment with a structure as described in Section 4.2.3. The layer redefinition process ensures that interlayer interfaces can only exist at the fixed elevations corresponding to $H_{k\pm1/2}$, whereas the free surface, for which the reaction force is equal to zero, is unrestricted. Hence, this assumption is valid for the proposed numerical scheme. The hydrostatic pressure force and interlayer reaction force are consequently given as:

$$\begin{cases} P_N = \dfrac{1}{2}\rho g h_N^2 \\ R_{N-\frac{1}{2}} = -\rho g h_N \partial_x z_{N-1/2} \end{cases} \tag{4.19}$$

Substituting (4.19) into (4.18) and dividing by ρ produces the following momentum equation for the top layer:

$$\partial_t q_N + \partial_x \left(h_N u_N^2 + \frac{1}{2} g h_N^2 \right) = -g h_N \partial_x z_{N-1/2} \tag{4.20}$$

where $z_{N-1/2}$ is equal to the fixed elevation $H_{N-1/2}$, corresponding to the elevation of the top of the structure modelled at the interface.

Considering next the lowest layer, layer 1, the momentum equation can be expressed as:

$$\partial_t \rho q_1 + \partial_x \left(\rho h_1 u_1^2 + P_1 \right) = R_{\frac{1}{2}} - R_{\frac{3}{2}} \tag{4.21}$$

where P_1 is the hydrostatic pressure force exerted onto layer 1, $R_{1/2}$ is the reaction force at the fixed bed and $R_{3/2}$ is the reaction force exerted by layer 1 onto layer 2. The hydrostatic pressure force and interlayer reaction forces are given as:

$$\begin{cases} P_1 = \left(\frac{1}{2} h_1 + h_{1_{(+)}} \right) \rho g h_1 \\ R_{\frac{1}{2}} = -\rho g \left(h_1 + h_{1_{(+)}} \right) \partial_x z_{1/2} \\ R_{\frac{3}{2}} = -\rho g h_{1_{(+)}} \partial_x z_{3/2} \end{cases} \tag{4.22}$$

where $h_{1_{(+)}}$ is calculated using (4.9). Substituting (4.22) into (4.21) and dividing by ρ produces:

$$\partial_t q_1 + \partial_x \left(h_1 u_1^2 + \frac{1}{2} g h_1^2 + g h_1 h_{1_{(+)}} \right) = g h_{1_{(+)}} \partial_x z_{3/2} - g \left(h_1 + h_{1_{(+)}} \right) \partial_x z_{1/2} \tag{4.23}$$

Following the same principles and assumptions, a general multi-layer formulation of the continuity and momentum equations can be derived:

$$\partial_t h_k + \partial_x q_k = 0 \tag{4.24}$$

$$\partial_t q_k + \partial_x \left(h_k u_k^2 + \frac{1}{2} g h_k^2 + g h_k h_{k_{(+)}} \right) = g h_{k_{(+)}} \partial_x z_{k+1/2} - g \left(h_k + h_{k_{(+)}} \right) \partial_x z_{k-1/2} \tag{4.25}$$

When friction terms are added and the system is written in vector conservation form, equations (4.24) and (4.25) correspond to equations (4.4)-(4.8). The eigenstructure of the system can be elucidated by casting the equations in the following non-conservation form:

$$\partial_t \mathbf{U} + \mathbf{A}(\mathbf{U}) \partial_x \mathbf{U} = \mathbf{S}(\mathbf{U}) \tag{4.26}$$

where the Jacobian matrix $\mathbf{A}$ is defined as:

$$\mathbf{A}(\mathbf{U}) = \frac{\partial \mathbf{F}(\mathbf{U})}{\partial \mathbf{U}} = \begin{bmatrix} \frac{\partial f_1}{\partial w_1} & \cdots & \frac{\partial f_1}{\partial w_N} \\ \vdots & \ddots & \vdots \\ \frac{\partial f_N}{\partial w_1} & \cdots & \frac{\partial f_N}{\partial w_N} \end{bmatrix} \tag{4.27}$$

with f_n denoting the nth component of the flux vector and w_n denoting the nth component of the vector of conserved variables. For the three layer system that is predominantly used

throughout, the vector of conserved variables and the vector of fluxes can be written in terms of the conserved variables as:

$$\mathbf{U} = \begin{bmatrix} w_1 \\ w_2 \\ w_3 \\ w_4 \\ w_5 \\ w_6 \end{bmatrix} = \begin{bmatrix} h_1 \\ h_1 u_1 \\ h_2 \\ h_2 u_2 \\ h_3 \\ h_3 u_3 \end{bmatrix} \ , \ \mathbf{F}(\mathbf{U}) = \begin{bmatrix} f_1 \\ f_2 \\ f_3 \\ f_4 \\ f_5 \\ f_6 \end{bmatrix} = \begin{bmatrix} w_2 \\ \frac{w_2^2}{w_1} + \frac{1}{2} g w_1^2 + g w_1 (w_3 + w_5) \\ w_4 \\ \frac{w_4^2}{w_3} + \frac{1}{2} g w_3^2 + g w_3 w_5 \\ w_6 \\ \frac{w_6^2}{w_5} + \frac{1}{2} g w_5^2 \end{bmatrix} \tag{4.28}$$

and the Jacobian is evaluated as:

$$\mathbf{A} = \begin{bmatrix} 0 & 1 & 0 & 0 & 0 & 0 \\ c_1^2 - u_1^2 & 2u_1 & g h_1 & 0 & g h_1 & 0 \\ 0 & 0 & 0 & 1 & 0 & 0 \\ 0 & 0 & c_2^2 - u_2^2 & 2u_2 & g h_2 & 0 \\ 0 & 0 & 0 & 0 & 0 & 1 \\ 0 & 0 & 0 & 0 & c_3^2 - u_3^2 & 2u_3 \end{bmatrix} \tag{4.29}$$

where the wave celerities for layer k, denoted as c_k are defined as:

$$\begin{cases} c_1 = \sqrt{g(h_1 + h_2 + h_3)} \\ c_2 = \sqrt{g(h_2 + h_3)} \\ c_3 = \sqrt{g h_3} \end{cases} \tag{4.30}$$

The eigenvalues of $\mathbf{A}$ are therefore real and distinct:

$$\begin{cases} S_1^- = u_1 - c_1 \ , \ S_1^+ = u_1 + c_1 \\ S_2^- = u_2 - c_2 \ , \ S_2^+ = u_2 + c_2 \\ S_3^- = u_3 - c_3 \ , \ S_3^+ = u_3 + c_3 \end{cases} \tag{4.31}$$

Whilst the simplifying assumptions result in an accessible eigenstructure with real and distinct eigenvalues (for $h > 0$) the underlying system remains ill-posed since the equations are unable to sufficiently model turbulent mixing. As noted by Sarno et al. [399], although numerical diffusion may produce results which do not appear oscillatory, artificial oscillations may still be present for schemes which use only the real eigenvalues or bounds of the moduli of the complex eigenvalues. As outlined within the review of the literature regarding multi-layer shallow water systems, the numerical solution of such systems remains an open problem. Despite the outlined issues, the validation process demonstrates that the presented model produces a strong approximation of the behaviour at a barrier. The eigenvalues computed for a two-layer system are in agreement with the eigenvalues for the relaxed model derived by Abgrall and Karni [4], which also utilises a decoupled formulation.

Classical Multi-Layer Shallow Water Equations

If the *apparent topographies* $z_{k-1/2}$ and $z_{k+1/2}$ are not fixed then the reaction forces cannot be written in terms of the constant values $z_{k\pm1/2} = H_{k\pm1/2}$:

$$R_{k-1/2} = -\rho g(h_k + h_{k_{(+)}})\partial_x z_{k-1/2} = -\rho g(h_k + h_{k_{(+)}})\partial_x \left(\sum_{j=1}^{k-1} h_j + z_{\frac{1}{2}}\right) \tag{4.32}$$

$$R_{k+1/2} = -\rho g h_{k_{(+)}}\partial_x z_{k+1/2} = -\rho g h_{k_{(+)}}\partial_x \left(\sum_{j=1}^{k} h_j + z_{\frac{1}{2}}\right) \tag{4.33}$$

and the classical multi-layer shallow water equations are recovered:

$$\partial_t h_k + \partial_x h_k u_k = 0 \tag{4.34}$$

$$\partial_t h_k u_k + \partial_x \left(h_k u_k^2 + \frac{1}{2} g h_k^2\right) = -g h_k \partial_x \left(\sum_{j=1}^{k-1} h_j + \sum_{j=k+1}^{N} h_j + z_{\frac{1}{2}}\right) \tag{4.35}$$

The classical multi-layer shallow water equations present two well known numerical challenges:

1. The equations are of mixed hyperbolic-elliptic type, with a local loss of hyperbolicity occurring due to the turbulent momentum exchanges which occur in the presence of Kelvin-Helmholtz instabilities, formed as a result of large relative velocities between superposed fluid layers [399, 419, 352].
2. The non-conservative product term generated by the pressure coupling between the layers is not well-defined for discontinuous solutions due to the difficulty establishing a suitable Rankine-Hugoniot condition [264, 265].

Despite the fact that the local loss of hyperbolicity indicates the invalidity of the model in the presence of Kelvin-Helmholtz instabilities, there is a desire to produce simplified approximations of these complex flows, since three-dimensional modelling is impractical for flood modelling applications. As a consequence, several approaches have been suggested to address the presented numerical challenges.

Audusse et al. [32] formulated a conditionally hyperbolic multi-layer system, providing a semi-discretisation of the horizontal velocity for a single continuity equation. As such, the assumption of layered immiscible fluids is removed, enabling mixing between the layers since a physical partitioning of the flow isn't enforced. An alternative multi-layer system with mass exchanges is presented by Fernández-Nieto et al. [159], which introduces a piecewise linear approximation of the vertical velocity within each fluid layer, enabling the definition of jump conditions across the interfaces. Comparisons with the numerical solution of the full Navier-Stokes equations demonstrate that this results in a more accurate determination of the vertical velocity component. Unfortunately, although this numerical approach has a number of desirable properties, it is unsuitable for the proposed application since vertical discretisation of both the momentum and continuity equations is required to model the effect of the structure using the outlined method. However, implementation of this method to describe the flow within a layer could provide a suitable method to improve the resolution of the approximated vertical velocity profile. This would correspond to a system of decoupled multi-layer systems, as opposed to the simpler decoupled system of monolayer systems that has been derived.

Castro Díaz et al. [140], present alternative methods to address the loss of hyperbolicity for a two-layer system, which can be extended to multi-layer systems. The authors first derive refined approximations for the eigenvalues of the system, based upon special cases ($h_1 = h_2$ and $u_1 = u_2$) for which exact eigenvalues can be obtained, producing sharper estimations of the non-hyperbolic sub-domains. Classical first order approximations of the eigenvalues can be found in Schijf and Schöfled [403]. Two friction treatments and a local change to a hyperbolic model are then presented as supplementary methods for handling local losses in hyperbolicity. However, within the context of the presented method for modelling structures, both of these methods are unsuitable.

The local friction treatment, based upon either the classical or improved approximation of the eigenvalues, is designed to shift the model from the non-hyperbolic region to its boundary within the hyperbolic region. This mimics the suspected repulsive behaviour of the elliptical region as commented on by [70], in which it is believed that the turbulent mixing of the layers causes the solution to rapidly evacuate the non-hyperbolic region to its boundary. However, since the proposed model is designed for applications involving uniform densities with large relative velocities between the layers, implementing a method which evacuates the solution from the non-hyperbolic region defeats the purpose of the model: the aim of the proposed scheme is to produce sensible simplified approximations of the complex flow that occurs within the non-hyperbolic regions of flow where they occur, not to avoid them. Furthermore, as identified by Castro Díaz et al. [140], the local friction treatment may produce non-physical behaviour under specific circumstances.

Locally changing the system, under the assumption of small variations in the free surface elevation, such that real and distinct eigenvalues can be obtained, is similar in nature to the simplifications imposed within the method presented within this paper. However, the aforementioned assumptions are more suited for oceanic applications where free surface variations are typically negligible with respect to the depth of flow, as opposed to potential transient shallow water flow interactions with barriers, where significant variations in the free surface may occur.

A further alternative solution proposed by Castro et al. [87], which was improved upon by Chertock et al. [102], introduces an intermediate layer which aims to broaden the hyperbolic sub-domain of the model by replicating the mixing layer that is produced by interfacial instabilities. However, this adaptation of the model is also unsuitable, since ensuring alignment of the interfaces with the structure following the introduction of an intermediate mixing layer poses a significant challenge. Furthermore, the expansion of the hyperbolic sub-domain of the model is likely not sufficient to ensure hyperbolicity of the model for the proposed application.

The relaxation approach presented by Abgrall and Karni [4], provides an alternative method to enable decoupling of the system in order to produce a more accessible eigenstructure. As for the proposed model, the underlying model is ill-posed but the scheme is shown to produce accurate numerical results for the showcased numerical tests. In this case, the formulation based upon the work of Spinewine et al. [418] is preferred due to the simplicity of the required numerical scheme which provides greater compatibility with the typical numerical schemes utilised by contemporary hydrodynamic models and a greater ease of implementation.

With regards to the non-conservative product term, produced by the pressure coupling between the layers, there are fewer available solutions. Non-conservative products present

a significant numerical challenge since the definition of weak solutions in accordance with classical theory is based upon the notion of distributions and non-conservative products are generally ambiguous in this regard [268]. The analytical theory developed by Dal Maso et al. [127], therefore presented a major breakthrough as it enabled the definition of weak solutions by means of a family of paths connecting the left and right states. A potential solution can therefore be produced by combining the theory of Dal Maso et al. [127], with the framework of path-conservative methods introduced by Parés [356] as shown in [89]. However, as displayed by Abgrall and Karni [3], even if the the correct path definition is known, such schemes will not in general converge to the assumed path. This is further complicated for shallow water systems as there is no clear path definition based upon the underlying physics. Furthermore, Castro et al. [90], determined that such schemes generate a *convergence error* source term which is a locally bounded error, provided that the total variation remains uniformly bounded. This means that the error measure may not be negligible in practice which is supported by the computations performed by Abgrall and Karni, who demonstrate that the relative errors are proportional to the strength of the shock. In the absence of further advances in the design of numerical schemes which guarantee convergence to the physically relevant weak solution for non-conservative hyperbolic systems, writings which seek to eliminate [418, 70, 59] or minimise [253] such terms, in physically justifiable ways, present a promising, albeit potentially limited, alternative.

Layer Coupling

As shown in [418, 3], evaluation of the flux Jacobian for the decoupled system (4.29) results in an eigensystem with real and distinct eigenvalues (4.31). However, this form of the equations does not account for the pressure coupling between the fluid layers within the wave structure of the problem. Furthermore, study of the Riemann invariants [418], demonstrates that the flow variables in an upper layer are constant across the waves present in a lower layer. As such, the system is closer to a system of superposed monolayer shallow water equations than the classical multi-layer system, which incorporates the coupling terms within the wave structure.

Under these assumptions, the coupling between the layers for the presented system is only weakly enforced via the source terms, with the fluid layers otherwise acting independently. There are strong physical arguments for incorporating the pressure coupling terms within the wave-structure of the problem, since the physical behaviour of real systems of layered immiscible fluids are strongly coupled by these terms. It is shown by Audusse [29] for example, that the decoupling of the propagation of the waves within the layers of a multi-layer system results in an underestimation of the external eigenvalues in comparison with the monolayer and coupled multi-layer systems. However, despite the simplifying assumptions, the decoupled formulation produces strong approximations of the corresponding monolayer solution, even within ill-posed regions of the solution [418, 3]. Since the partition of the flow in the structure and intermediate cells is arbitrary and not a consequence of layered immiscible fluids, the vertical discretisation of the flow into layers can be viewed simply as a tool to implement vertically variable internal boundary conditions and approximate a vertical velocity profile within a one- or two-dimensional monolayer context. In this regard, the internal mixing of the fluid layers is neglected, just as it is for the neighbouring monolayer formulations. As the chosen formulation and accompanying simplifying assumptions enable this in a way which is consistent with the

monolayer formulation, the choice of formulation is considered to be justified for this specific application. The approximation of the fluid in the presence of the structure as superposed independent layers of flow, is of course not perfectly representative of the true physical behaviour, however substantial simplifications are required due to the restrictive nature of the depth-averaged shallow water assumptions that hydrodynamic flood models are beholden to.

4.2.2 Numerical Flux Computation

The process for resolving fluxes is dependent on the type of interface (NI, II or SI). For structure and intermediate interfaces Harten-Lax-van Leer (HLL) approximate Riemann solvers [212] are used to resolve the intercell numerical fluxes. For normal interfaces, other suitable approximate Riemann solvers may be used, however, HLL approximate Riemann solvers are recommended for consistency.

Normal Interfaces

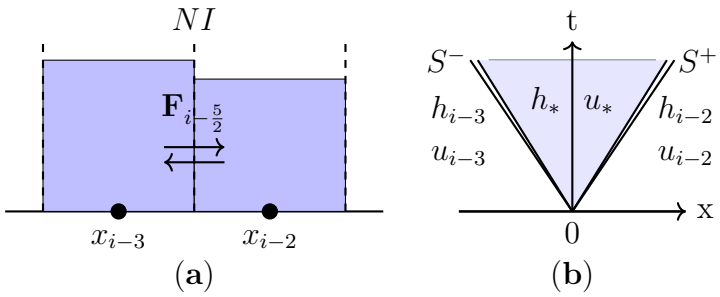

Figure 4.5: (a) Example normal interface with adjacent normal cells and (b) the general structure of the general solution of the Riemann problem for a normal interface. S^- is the left wave speed and S^+ is the right wave speed, as defined in Algorithm 2. h_* and u_* denote the conserved variables in the star region. $\mathbf{F}_{i-5/2}$ denotes the numerical flux at the interface.

A robust algorithm presented by Glenis et al. [179] is used to calculate wave speeds for the Riemann problem, which is outlined in Algorithm 2. Following calculation of the wave speeds, a standard HLL approximate Riemann solver (4.36) is used to determine numerical fluxes across the normal interface.

$$\mathbf{F}_{i+\frac{1}{2}} = \begin{cases} \mathbf{F}_i & \text{if } S^- > 0 \\ \mathbf{F}^{hll} = \frac{S^+\mathbf{F}_i - S^-\mathbf{F}_{i+1} + S^+S^-(\mathbf{U}_{i+1} - \mathbf{U}_i)}{S^+ - S^-} & \text{if } S^- \leq 0 \leq S^+ \\ \mathbf{F}_{i+1} & \text{if } S^+ < 0 \end{cases} \tag{4.36}$$

Structure Interfaces

At a structure interface the flow layers can be divided into *open* and *closed* as shown in Figure 4.6. *Open* layers are considered as having a transmissive boundary at the structure interface, with the portion of the structure interface shared by the adjacent sub-cells having no influence on the exchange of conserved variables. *Closed* layers are

Algorithm 2 Calculation of wave speeds [179]. An initial approximation (h_0) of the depth in the star region (h_*) using a two-rarefaction approximate state Riemann solver is used to determine whether a two-rarefaction or two-shock approximation is optimal. For the derived multi-layer system, the wave celerity is defined as $c_{i,k} = \sqrt{g(h_{i,k} + h_{i,k_{(+)}})}$, where $c_{i,k}$ is the celerity for cell i layer k, $h_{i,k}$ is the thickness of cell i, layer k and $h_{i,k_{(+)}}$ is the depth of water in cell i above layer k.

$g \leftarrow 9.81\text{ms}^{-2}$

if $h_i \wedge h_{i+1} > 0$ **then**

▷ Initial two-rarefaction approximation

$$c_i \leftarrow \sqrt{gh_i} \quad , \quad c_{i+1} \leftarrow \sqrt{gh_{i+1}}$$

$$h_0 \leftarrow \frac{1}{g}\left(\frac{1}{2}(c_i + c_{i+1}) + \frac{1}{4}(u_i - u_{i+1})\right)^2$$

if $h_0 \leq min(h_i, h_{i+1})$ **then**

▷ Use two-rarefaction approximate state Riemann solver

$$h_* \leftarrow h_0$$

else if $h_0 > min(h_i, h_{i+1})$ **then**

▷ Use two-shock approximate state Riemann solver

$$p_i \leftarrow \sqrt{\frac{g(h_0 + h_i)}{2h_0h_i}} \quad , \quad p_{i+1} \leftarrow \sqrt{\frac{g(h_0 + h_{i+1})}{2h_0h_{i+1}}}$$

$$h_* \leftarrow \frac{p_ih_i + p_{i+1}h_{i+1} + u_i - u_{i+1}}{p_i + p_{i+1}}$$

end if

$$\alpha_i \leftarrow \begin{cases} \frac{\sqrt{0.5(h_* + h_i)h_*}}{h_i} & \text{if } h_* > h_i \\ 1 & \text{if } h_* \leq h_i \end{cases} \quad , \quad \alpha_{i+1} \leftarrow \begin{cases} \frac{\sqrt{0.5(h_* + h_{i+1})h_*}}{h_{i+1}} & \text{if } h_* > h_{i+1} \\ 1 & \text{if } h_* \leq h_{i+1} \end{cases}$$

$$S^- \leftarrow u_i - \alpha_ic_i \quad , \quad S^+ \leftarrow u_{i+1} + \alpha_{i+1}c_{i+1}$$

else if $h_i = 0 \wedge h_{i+1} > 0$ **then**

▷ Left dry bed

$$S^- \leftarrow u_{i+1} - 2c_{i+1} \quad , \quad S^+ \leftarrow u_{i+1} + c_{i+1}$$

else if $h_{i+1} = 0 \wedge h_i > 0$ **then**

▷ Right dry bed

$$S^- \leftarrow u_i - c_i \quad , \quad S^+ \leftarrow u_i + 2c_i$$

end if

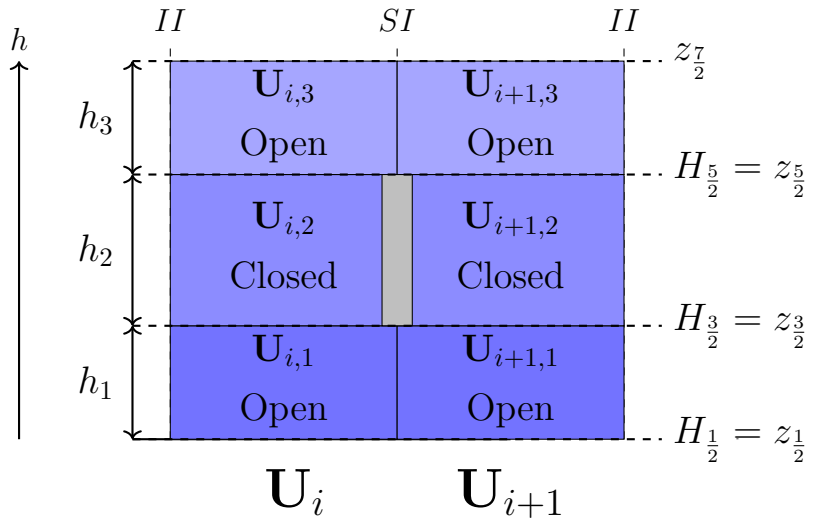

Figure 4.6: Designation of open and closed layers at a structure interface.

considered as having a reflective boundary at the structure interface due to the presence of the structure. For each open layer, a single Riemann problem must be constructed and solved whereas, at each closed layer two Riemann problems must be constructed and solved, as shown in Figure 4.7. Solution of two Riemann problems for a closed layer is necessary to implement the reflective boundary condition at the structure interface, which reflects the flow in both the left and right sub-cells. The reflective boundary condition is imposed, assuming a structure interface exists at $x_{i+1/2}$, by defining:

$$\begin{cases} h_k^{(L)} = h_{i,k} \\ u_k^{(L)} = -u_{i,k} \end{cases}, \quad \begin{cases} h_k^{(R)} = h_{i+1,k} \\ u_k^{(R)} = -u_{i+1,k} \end{cases} \tag{4.37}$$

as shown in Figure 4.7b. $h_k^{(L)}, u_k^{(L)}$ denotes to the depth and velocity of the ghost cell implemented for the reflective boundary condition at the left face of the structure for layer k and $h_k^{(R)}, u_k^{(R)}$ denotes the same properties for the right face of the structure for layer k.

This process is based on the assumption that the vertical velocity of the flow is negligible, which is a fundamental assumption for the derivation of the shallow water equations, and therefore the direction of the flow can be considered to be primarily parallel to the bed. The numerical flux for each layer is determined by applying (4.4) to each layer, where the numerical flux for a layer is given by equation (4.6), which can then be used to determine the flux at the interface using a standard HLL approximate Riemann solver (4.36). The method for determining the fluxes at a structure interface is summarised in Algorithm 3.

It is important to note that, when using standard procedures such as source term upwinding [57] to ensure well-balancing of the numerical scheme in the presence of uneven bottom topography, the following wave speed estimates [418] should be applied to all layers:

$$\begin{cases} S^- = \min(S_1^-, S_2^-, ..., S_N^-, 0) \\ S^+ = \max(S_1^+, S_2^+, ..., S_N^+, 0) \end{cases} \tag{4.38}$$

where S_k^- and S_k^+ are the left and right wave speeds for layers $1 \leq k \leq N$ calculated

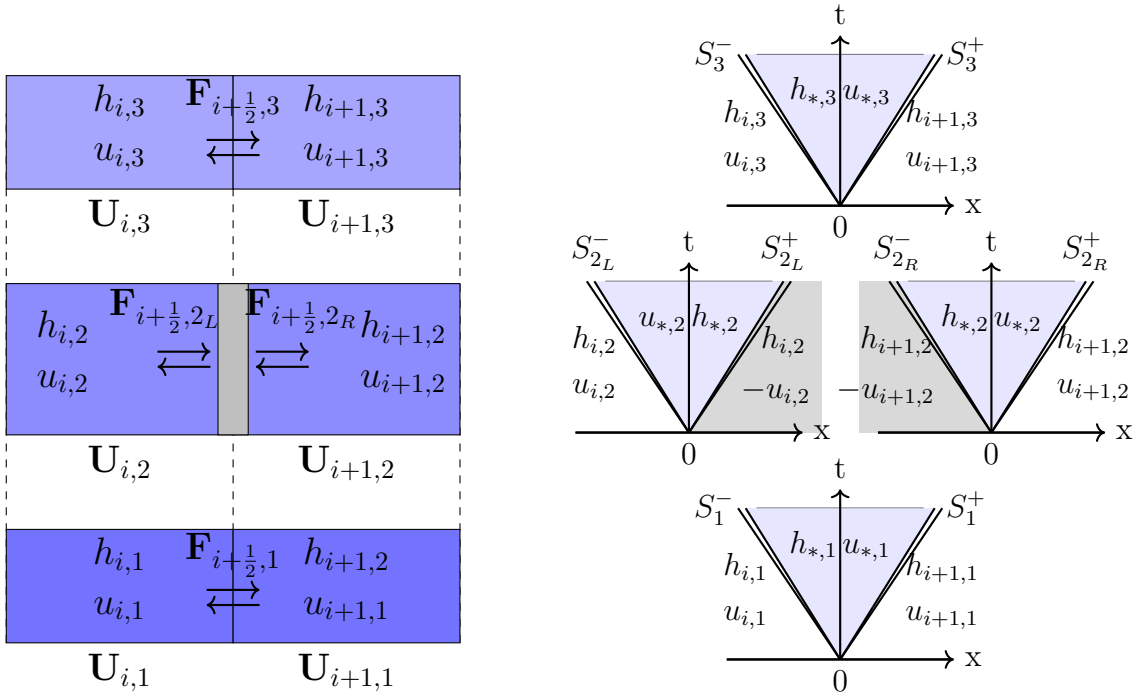

(a) Division of the structure cells into sub-cells and their respective properties. The subscripts L and R are used to differentiate between the left and right face of the structure interface.

(b) The general structure of the general solution of the Riemann problems for an example structure interface shown in (a). The introduction of fictitious ghost cells for the purpose of implementing reflective boundary conditions are denoted by grey shading.

Figure 4.7: Method for resolving fluxes for the sub-cells adjacent to a structure interface.

as shown in Algorithm 2 and S^- and S^+ are the wavespeed estimates used for all layers $1 \leq k \leq N$. This is equivalent to taking the left and right wave speeds in each layer of the cell as equal to the most extreme left and right wave speed present within any single layer of the cell. Although this makes the well-balancing process more convenient, it does come at the cost of overestimating the wave speed in some layers and consequently the addition of extra numerical diffusion within the numerical scheme.

Algorithm 3 Calculation of fluxes for an example structure interface as shown in Figure 4.7. k is the index of the layer under consideration, N is the total number of layers at the structure interface.

$g \leftarrow 9.81\text{ms}^{-2}$
$k \leftarrow 1$ ▷ For the open layers
while $k \leq N$ **do**
  calculate S_k^- , S_k^+ using Algorithm (1) ▷ Calculate wave speeds
  ▷ Calculate layer flux

$$\mathbf{F}_{i,k} \leftarrow \begin{bmatrix} h_{i,k}u_{i,k} \\ \frac{q_{i,k}^2}{h_{i,k}} + \frac{1}{2}gh_{i,k}^2 + gh_{i,k_{(+)}}h_{i,k} \end{bmatrix} , \mathbf{F}_{i+1,k} \leftarrow \begin{bmatrix} h_{i+1,k}u_{i+1,k} \\ \frac{q_{i+1,k}^2}{h_{i+1,k}} + \frac{1}{2}gh_{i+1,k}^2 + gh_{i+1,k_{(+)}}h_{i+1,k} \end{bmatrix}$$

$$\mathbf{F}_{i+\frac{1}{2},k} \leftarrow \begin{cases} \mathbf{F}_{i,k} \text{ if } S_k^- > 0 \\ \mathbf{F}^{hll} = \frac{S^+\mathbf{F}_{i,k} - S_k^-\mathbf{F}_{i+1,k} + S_k^+S_k^-(\mathbf{U}_{i+1,k} - \mathbf{U}_{i,k})}{S_k^+ - S_k^-} \text{ if } S_k^- \leq 0 \leq S_k^+ \\ \mathbf{F}_{i+1,k} \text{ if } S_k^+ < 0 \end{cases} \quad (6)$$

  $k \leftarrow k + 2$ ▷ Advance to next open layer
end while
$k \leftarrow 2$ ▷ For the closed layer
$h_{i+1,ghost} \leftarrow h_{i,k}$ ▷ Right ghost cell fluid depth
$u_{i+1,ghost} \leftarrow -u_{i,k}$ ▷ Right ghost cell fluid velocity
calculate $S_{k_L}^-$, $S_{k_L}^+$ using Algorithm (1) ▷ Calculate wave speeds
calculate $\mathbf{F}_{i+\frac{1}{2},k_L}$ using (6) ▷ Flux for the left side of the structure

$h_{i,ghost} \leftarrow h_{i+1,k}$ ▷ Left ghost cell fluid depth
$u_{i,ghost} \leftarrow -u_{i+1,k}$ ▷ Left ghost fluid velocity
calculate $S_{k_R}^-$, $S_{k_R}^+$ using Algorithm (1) ▷ Calculate wave speeds
calculate $\mathbf{F}_{i+\frac{1}{2},k_R}$ using (6) ▷ Flux for the right side of the structure

Intermediate Interfaces

In order to resolve fluxes with the adjacent sub-cells it is necessary to temporarily define layer properties for the intermediate cell as shown in Figure 4.8 (see also Figure 4.1 for wider context). The properties for the temporary layers in the intermediate interfaces

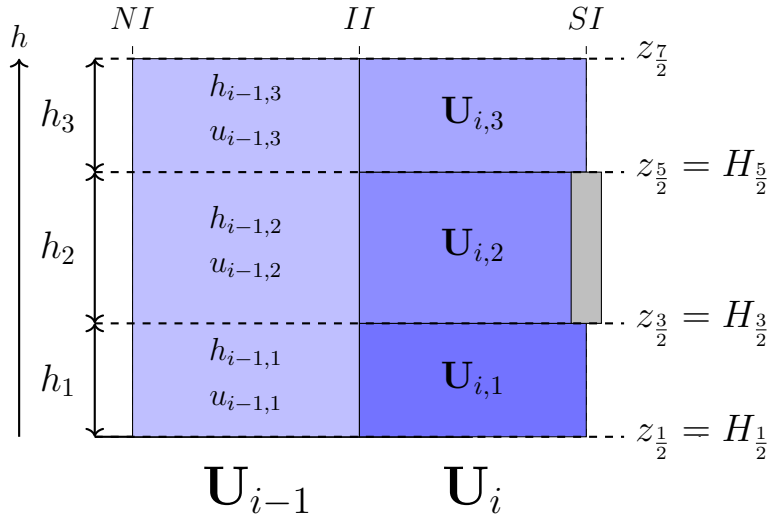

Figure 4.8: Temporary division of an intermediate cell into layers in order to resolve fluxes at a intermediate interface. $u_{i-1,1} = u_{i-1,2} = u_{i-1,3} = u_{i-1}$ where u_{i-1} represents the average velocity for the whole intermediate cell.

are defined by assuming that the velocity in each layer is equal to the average velocity of the whole intermediate cell and that the depth in each layer is restricted to the limit flow depth of the adjacent sub-cell, accounting for any differences in bed elevation. As such $H_{k\pm1/2}$ for the intermediate cell, is taken as equal to $H_{k\pm1/2}$ for the adjacent structure cell and the temporary layer depths are given as:

$$h^n_{i,k} = \min\left[\max\left(H^n_i - \sum_{j=1}^{k-1} h^n_{i,j}, 0\right), \max\left(H_{i\pm1,k+\frac{1}{2}} - \max(H_{i\pm1,k-\frac{1}{2}}, z_{i,\frac{1}{2}}), 0\right)\right] \quad (4.39)$$

$$\forall k \in \{k \in \mathbb{Z} : 1 \leq k \leq N-1\}$$

$$h^n_{i,N} = H^n_i - \sum_{j=1}^{N-1} h^n_{i,j}$$

where $h^n_{i,k}$ is the depth for the kth temporary layer, H^n_i is the total depth contained within the ith intermediate cell at time level n. $H_{i\pm1,k\pm\frac{1}{2}}$ is the elevation of the base or cover of the adjacent sub-cell which corresponds to the structure modelled at the interface ($H_{i+1,k\pm\frac{1}{2}}$ if the structure cell is to the right of the intermediate cell and $H_{i-1,k\pm\frac{1}{2}}$ if the structure cell is to the left) and $z_{i,\frac{1}{2}}$ is the bed elevation for the intermediate cell. The momentum is then simply defined as:

$$q^n_{i,k} = h^n_{i,k} u^n_i$$

where $q^n_{i,k}$ is the momentum for layer k, cell i at time n and u^n_i is the depth averaged velocity for the ith intermediate cell at time level n. This ensures that the total depth and momentum of the cell is conserved, that the upper and lower interfaces of the layers

are aligned with the relevant structure (except for at the free-surface and bed in some cases) and importantly that the total numerical flux for the temporarily defined layers is equal to the numerical flux for the whole intermediate cell. The fluxes for each layer can then be resolved using the process outlined for the open layers in Algorithm 3. Since the sum of the temporary layer fluxes are equal to that of the classical mono-layer shallow water equations, the layer fluxes $\mathbf{F}_k(\mathbf{U}_k)$ can be seen as a vertical decomposition of the mono-layer flux $\mathbf{F}(\mathbf{U})$, providing a compatible link between the neighbouring mono-layer and multi-layer systems. This can be viewed as a different implementation of the same concept presented by Bonaventura et al. [66], who present a more general framework for linking shallow water systems with a variable number of layers.

4.2.3 Conservative Updating of Conserved Variables

Once numerical fluxes have been resolved across all interfaces within the computational domain, the final procedure for each timestep is to update the conserved variables contained within each cell and sub-cell.

Normal Cells

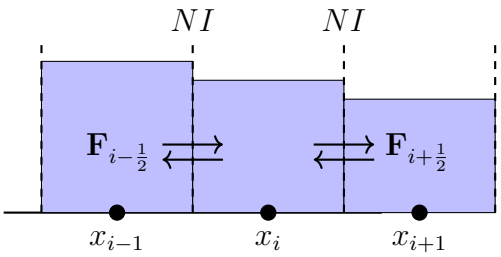

Figure 4.9: Illustration of the numerical fluxes at the normal interfaces bordering a normal cell.

The state variables for a normal cell are given as:

$$\mathbf{U}_i^n = \begin{bmatrix} h_i^n \\ h_i^n u_i^n \end{bmatrix} \tag{4.40}$$

which are updated using equation (4.15), as is standard for a one-dimensional Godunov type scheme. For cases involving variable bed topography, a well-balanced treatment of the topographic source terms can be achieved via the hydrostatic reconstruction method [31] or via upwinding of the source terms [57]. Suitable explicit or implicit treatment of the remaining source terms are both viable depending on the desired stability and admissible constraint of the stable timestep.

Intermediate Cells

The state variables for an intermediate cell are given as:

$$\mathbf{U}_i^n = \begin{bmatrix} h_i^n \\ h_i^n u_i^n \end{bmatrix} \tag{4.41}$$

and the same procedure for updating a normal cell is applied to an intermediate cell however, due to the fact that fluxes at a intermediate interface are calculated on a sub-cell basis (Figure 4.10), they must first be summated. For this case illustrated in Figure

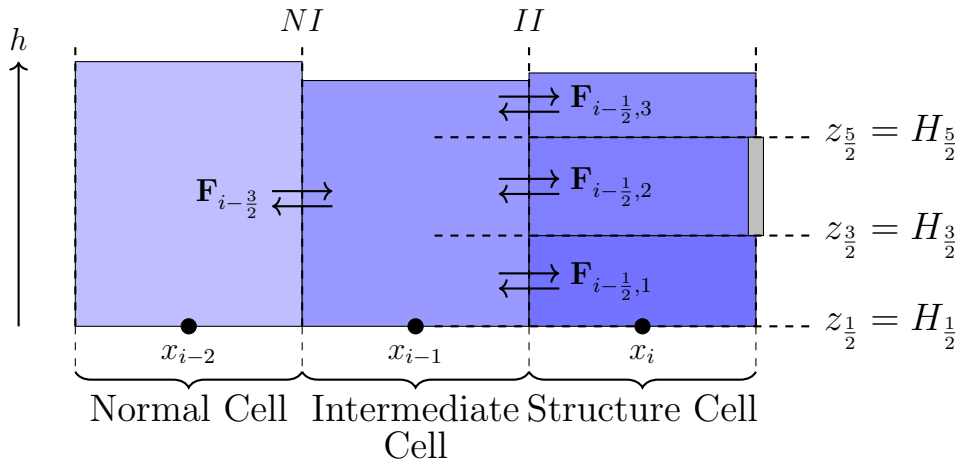

Figure 4.10: Illustration of the numerical fluxes used to update a intermediate cell.

4.10 this is equal to:

$$\mathbf{F}_{i-\frac{1}{2}} = \sum_{k=1}^{3} \mathbf{F}_{i-\frac{1}{2},k} \tag{4.42}$$

This sum is equal to the mono-layer shallow water flux provided that the layer velocities are equal to the depth averaged velocity for the whole cell. Where the layer velocities are variable, the flux is a first order approximation of the mono-layer shallow water flux plus a correction due to the more sophisticated vertical velocity profile.

Structure Cells

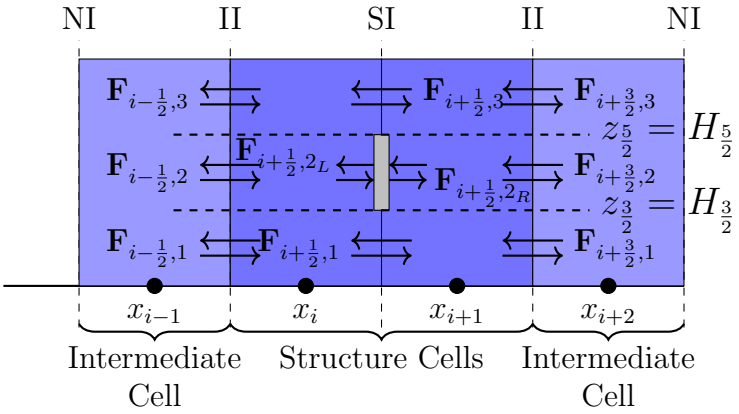

Figure 4.11: Illustration of the numerical fluxes used for updating the sub-cells of which a structure cells is comprised.

The state variables for the sub-cells contained within a structure cells are:

$$\mathbf{U}_{i,k}^{n} = \begin{bmatrix} h_{i,k}^{n} \\ h_{i,k}^{n} u_{i,k}^{n} \end{bmatrix} \tag{4.43}$$

In order to update a structure cell, a two step process is applied. In the first step, the constituent sub-cells are updated individually using the respective left and right fluxes as per:

$$\mathbf{U}_{i,k}^{n*} = \mathbf{U}_{i,k}^{n} - \frac{\Delta t}{\Delta x}\left[\mathbf{F}_{i+\frac{1}{2},k} - \mathbf{F}_{i-\frac{1}{2},k}\right] + \Delta t \mathbf{S}\left(\mathbf{U}_{i,k}^{n}\right) \tag{4.44}$$

Where $\mathbf{U}_{i,k}^{n}$ represents the vector of conserved variables for the kth sub-cell contained within the ith cell at time level n and $\mathbf{U}_{i,k}^{n*}$ represents an intermediate state. $\mathbf{F}_{i-1/2,k}$ and $\mathbf{F}_{i+1/2,k}$ represent the left and right fluxes for the kth layer of the ith cell. The intermediate state is necessary, since the updating of the conserved variables via (4.44) may cause the depth of flow within a sub-cell to exceed the limit flow depth ($H_{k+1/2}-H_{k-1/2}$). The second step of the solution process is therefore to exchange mass and momentum between the sub-cells to ensure that the limit flow depth is respected and consequently ensure, where there is sufficient depth of flow, that the layer interfaces are aligned with the obstruction modelled at the interface. Crucially, this layer redefinition procedure conserves the total depth and momentum of the structure cell. The updated layer depths h_k^{n+1} are given as:

$$h_k^{n+1} = \min\left(\max\left(H - \sum_{j=1}^{k-1} h_j^{n+1}, 0\right), H_{k+\frac{1}{2}} - H_{k-\frac{1}{2}}\right) \quad \forall k \in \{k \in \mathbb{Z} : 1 \leq k \leq N-1\}$$

$$h_N^{n+1} = H - \sum_{j=1}^{N-1} h_j^{n+1} \tag{4.45}$$

where $H = \sum_{j=1}^{N} h_j^{n*}$ is the total depth of flow contained within the structure cell at the intermediate state $\mathbf{U}_{i,k}^{n*}$ and $H_{k\pm1/2}$ is the static elevation of the base/cover of the kth sub-cell, which corresponds to the elevation of the base/cover of the obstruction modelled at the interface. The updated momentum for the sub-cells contained within the structure cell is given as:

$$q_k^{n+1} = h_k^{n+1} u_k^{n+1} =$$
$$\sum_{j=1}^{N}\left[\min\left(\max\left[\sum_{j=1}^{k} h_j^{n+1} - \max\left(\sum_{m=1}^{j-1} h_m^{n*}, H_{k-\frac{1}{2}}\right), 0\right], \max\left(\sum_{m=1}^{j} h_m^{n*} - H_{k-\frac{1}{2}}, 0\right), h_j^{n*}\right) u_j^{n*}\right]$$
$$\forall k \in \{k \in \mathbb{Z} : 1 \leq k \leq N-1\}$$

$$q_N^{n+1} = Q - \sum_{j=1}^{N-1} q_j^{n+1} \tag{4.46}$$

where $Q = \sum_{j=1}^{N} q_j^{n*}$ is the total depth of momentum contained within the structure cell at the intermediate state $\mathbf{U}_{i,k}^{n*}$. Formula (4.45) states that the depth of flow in layer k is equal to the total depth of flow (H), minus the depth of flow already assigned to lower layers ($\sum_{j=1}^{k-1} h_j^{n+1}$), which cannot be smaller than zero due to the requirement for depth positivity, or larger than the capacity of the sub-cell ($H_{k+\frac{1}{2}} - H_{k-\frac{1}{2}}$). Formula (4.46) states that the corresponding momentum of the flow in the redefined layer k, is equal to the sum over all layers contained within the structure cell, of the contribution of the intermediate layer depth h_k^{n*} to the redefined layer depth h_k^{n+1}, multiplied by the corresponding intermediate depth-averaged velocity u_j^{n*}. The layer redefinition process is also illustrated in Figure 4.12. As mentioned previously, this is similar to the process used by Bonaventura et al. [66], when linking shallow water models with a variable number of layers. As noted by Bonaventura et al., the local loss of accuracy which occurs when approximating the vertical velocity profile in this way has limited impact on the overall accuracy of the method as demonstrated by the numerical results.

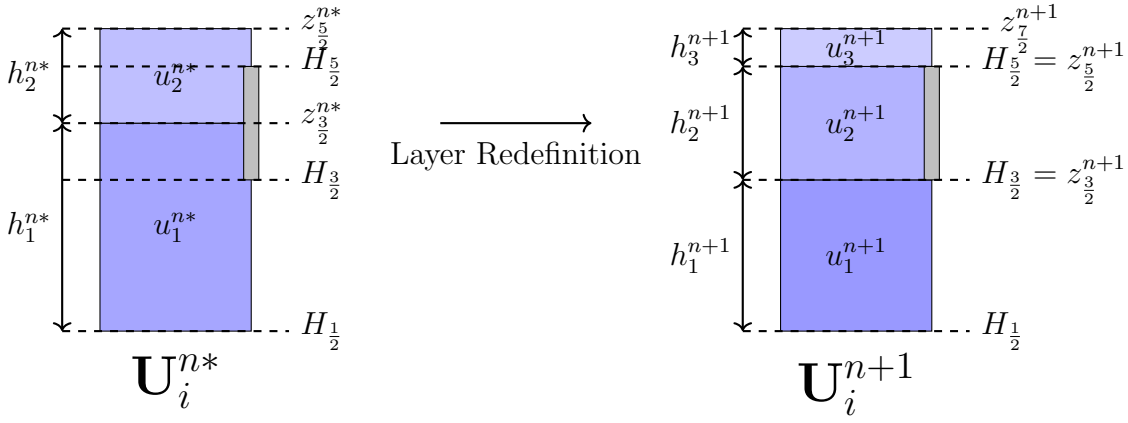

Figure 4.12: Illustration of the layer redefinition process after updating the conserved variables $\mathbf{U}^n_{i,k}$ to the intermediate state $\mathbf{U}^{n*}_{i,k}$. The redefinition process is required to re-align the layer interfaces, $z_{3/2}$ and $z_{5/2}$, with the base/cover of the structure, $H_{3/2}$ and $H_{5/2}$. The sum of the conserved variables at the intermediate state, $\mathbf{U}^{n*}_i$, is equal to the sum of the conserved variables at the new time level, $\mathbf{U}^{n+1}_i$, and hence the layer redefinition process conserves the total depth and momentum of the structure cell.

As for the normal cells, a well-balanced treatment of the topographic source terms may be achieved via the hydrostatic reconstruction method or via upwinding of the source terms. As mentioned previously, special treatment of the wave speed estimation may be required to ensure the well-balancing of the scheme if upwinding the source terms. The remaining source terms may be treated using suitable explicit or implicit methods depending on the desired stability and constraint of the timestep.

At the sub-cell interfaces containing a structure there are two numerical fluxes as illustrated in Figure 4.11, as a consequence of the two reflective boundaries implemented at each side of the structure. Since not all of the external forces are accounted for, these fluxes may be unequal, with the difference in the sum of the fluxes at the left face of the structure interface ($\mathbf{F}^{(-)}$) and the right face of the structure interface ($\mathbf{F}^{(+)}$) equal to $(\Delta t/\Delta x(\mathbf{F}^{(+)} - \mathbf{F}^{(-)}))$ at each timestep. When the fluid velocity is equal to zero in the closed layers adjacent to the structure $\mathbf{F}^{(+)} - \mathbf{F}^{(-)}$ is equal to the resultant hydrostatic pressure force exerted on the structure.

4.3 Model Validation

Previously published validation data [303], collected from experiments conducted in Newcastle University's Armfield S100 Research Flume, is used to validate the accuracy of the proposed Riemann solver. The S100 Research Flume is a 12.5m long, 1m wide, 0.8m deep flume capable of producing flow rates up to 400ls^{-1}. The user can select a desired flow rate which is then produced by the two pumps which draw water from the sump. The flow rate is maintained and corrected via a proportional-integral-derivative control loop, which uses a electromagnetic flow meter (Euromag Model MUT2200EL) to ensure that flow rate within the inflow pipe matches the desired flow rate. According to Euromag technical sheet [155], each sensor is calibrated on a hydraulic test rig equipped with an ISO17025 traceable weighing system, which ensures that the accuracy of the sensor is equal to $0.2\% \pm 2$mms^{-1} with a repeatability of approximately 0.1%. A summary of the

maximum permissible error limits for the instrument, provided by the manufacturer, is presented in Table 4.1.

Maximum Permissible Error limits for Euromag Model MUT2200EL DN 350 PN 10			
Flow Rate: Q (m^3h^{-1})	$12.8 < Q < 20.48$	$20.48 < Q < 280$	$Q > 280$
Instrument Error	$\pm$ 4.99%	$\pm$ 2.00%	$\pm$ 0.49 – 2.00%

Table 4.1: Maximum permissible error limits for the electromagnetic flow meter for a range of flow rates within the inflow pipe (adapted from [155] p.4).

The validation experiments consisted of running the flume at a range of flow rates, with a range of different barrier geometries placed within the flume cross-section, at a distance of 5m downstream. The flume tilt was set to 0% for all validation experiments in order to eliminate any potential numerical errors introduced as a result of topographic source terms. Once steady state flow conditions were achieved for each experiment, depth measurements were obtained using vernier point gauges. The full validation dataset is available as supplementary material from the referenced publication [303].

4.3.1 Numerical Setup

All numerical simulations were conducted on a 12.5m 1D spatial domain, discretised into a structured grid comprised of 0.1m cells ($\Delta x = 0.1$m). In order to ensure satisfaction of the Courant-Friedrichs-Lewy condition, a Courant number of $C = (0.95\Delta x)/(S^n_{max})$ was used to determine a stable timestep, where S^n_{max} is the maximum absolute wave speed at time level n. Since the bed slope is set to 0% this has the intended effect of simplifying the source terms, only requiring the friction source term to be resolved, facilitating clearer analysis of the accuracy of the Riemann solver. The friction source terms are resolved using the splitting method proposed by Liang and Marche [275]:

$$q_i^{n+1} = q_i^{n*} - \Delta t S^n_{i,c} = q_i^{n*} - \Delta t \left(\frac{\tau_{i,f}}{1 + \Delta t \frac{\partial \tau_{i,f}}{\partial q_i}} \right)^n = q_i^{n*} - \Delta t \left(\frac{C_i u_i |u_i|}{1 + \frac{2\Delta t C_{i,f} |q_i|}{h_i^2}} \right)^n \tag{4.47}$$

Where $q_i^{n*} = h_i^{n*} u_i^{n*}$ is the discharge following solution of the homogeneous advection problem. The following adaptation is used to resolve the friction source terms for the structure cells:

$$q_i^{n+1} = q_i^{n*} + \Delta t \left(\frac{\left(\tau^n_{i,k+\frac{1}{2}} - \tau^n_{i,k-\frac{1}{2}} \right)}{1 - \Delta t \left(\left(\frac{\partial \tau_{i,k+1/2}}{\partial q_{i,k}} \right)^n - \left(\frac{\partial \tau_{i,k-1/2}}{\partial q_{i,k}} \right)^n \right)} \right) \tag{4.48}$$

The following simple limiter is also used to ensure stability in regions where the water depth approaches zero:

$$S^n_{i,c} = \frac{q_i^n}{\Delta t} \text{ if } |\Delta t S^n_{i,c}| > |q_i^n| \tag{4.49}$$

A Manning's n equal to 0.012 and a kinematic viscosity of $1.0034 \times 10^{-6} \mathrm{m^2 s^{-1}}$ is assumed for all numerical simulations.

The upstream and downstream boundary conditions are both implemented using exterior ghost cells. In order to replicate the constant inflow produced by the S100 flume, an

inflow boundary condition is defined at the upstream end utilising relationships derived from the Riemann invariants across a rarefaction wave. At the downstream boundary a critical depth boundary condition is imposed. Full details for the implementation of the boundary conditions are presented in [303].

4.4 Results

The following validation test cases, as shown in Table 4.2 [303], can be categorised into three primary flow configurations:

- Flow under a barrier.
- Flow under a barrier, producing a downstream stationary hydraulic jump.
- Flow over and under a barrier.

Selected Validation Test Cases				
Test Case	q (ls^{-1})	z_1 (mm)	z_2 (mm)	Description
Test 1	130	116	316	Flow under barrier.
Test 2	130	122	322	Flow under barrier.
Test 5	24	32	232	Flow under barrier with hydraulic jump.
Test 6	20	32	232	Flow under barrier with hydraulic jump.
Test 8	175	116	316	Overtopped barrier.
Test 9	177	105	405	Overtopped barrier.

Table 4.2: Selected validation test conditions from Mckenna et al. [303]. q is the flow rate, z_1 is the elevation of the base of the barrier above the flume bed and z_2 is the elevation of the top of the barrier.

Through comparisons between the experimental and numerical data for the six presented validation test cases, the suitability and accuracy of the proposed solver is demonstrated. Comparisons are also provided with the solution method presented in Mckenna et al. [303], referred to hereafter as Solver 1. The solution method presented within this publication is referred to as Solver 2. To provide a fair comparison between the solvers, Solver 1 has been updated to utilise the same wavespeed estimation algorithm presented by [179].

4.4.1 Flow Under a Barrier

For test case one and test case two, involving flow under a barrier producing downstream supercritical flow, Solver 2 can be seen to produce accurate predictions, capturing the interaction of the flow with the obstruction, particularly in the immediate vacinity of the obstruction (Figure 4.15 and Figure 4.16). This is supported by the calculation of the contraction coefficient C_c, defined as the ratio of the depth at the *vena contracta* to the gate opening, for test case one:

$$C_c^{Exp} = \frac{0.0725}{0.116} = 0.625 \pm 0.043 \quad , \quad C_c^{Num} = \frac{0.0680}{0.116} = 0.586 \tag{4.50}$$

where the superscripts *Exp* and *Num* refer to the experimental and numerical data respectively. For test case two, an accurate estimate of the contraction coefficient is also

obtained, although there is a greater discrepancy since the model does not capture the increase in flow velocity which occurs within the $1m$ region downstream of the barrier:

$$C_c^{Exp} = \frac{0.067}{0.122} = 0.549 \pm 0.014 \quad , \quad C_c^{Num} = \frac{0.0742}{0.122} = 0.608 \tag{4.51}$$

The depths immediately upstream, h_1, and downstream, h_2, of the barrier are however, accurately predicted:

$$\frac{h_2^{Exp}}{h_1^{Exp}} = \frac{0.0735}{0.2395} = 0.307 \pm 0.008 \quad , \quad \frac{h_2^{Num}}{h_1^{Num}} = \frac{0.0742}{0.2374} = 0.313 \tag{4.52}$$

For both test cases it can be seen that the numerical results approximate the validation data most accurately at the barrier, with accuracy degrading towards the boundaries of the domain. For all test cases the downstream boundary condition has a strong influence on the downstream profile and particularly for test case two, the implementation of the boundary condition is complicated by the difficulty obtaining accurate measurements of shallow depths in the presence of significant variations prior to the outfall.

The slight decrease in the headwater depth, which occurs just upstream of the barrier, is not captured by the model since the shallow water equations are unable to adequately capture the energy dissipation that occurs at the barrier. Despite this, the errors in the estimation of the backwater effect are small for both cases, with upstream percentage errors falling within the range of $0.9 - 7.0\%$.

The comparison between the results for Solver 1 and Solver 2 demonstrate significant improvements for Solver 2 across both of the test cases. For Solver 1, an approximate vertical velocity profile is captured by assuming that the flow velocity behind the barrier is exactly equal to zero, which is only strictly true exactly at the interface between the barrier and the fluid, and consequently the velocity of the flow within the open layers is approximated as the total momentum of the cell divided by the sum of the open layer depths. Since the cell is updated on a monolayer basis by summating the component fluxes, significant averaging occurs degrading the approximation of the velocity profile. Figures 4.13 and 4.14 show the respective vertical profiles for the horizontal velocity for the two cells either side of the structure interface for test case one and test case two respectively.

The figures demonstrate similarities between the respective velocity profiles; both solvers produce a larger velocity in the lower layer, underneath the barrier, with a lower velocity in the layer adjacent to the barrier. The primary difference between the two Solvers can be seen for the left structure cell whereby the more complex discretisation of the structure cells for Solver 2 enables the scheme to produce a non-zero velocity immediately behind the barrier. Although, no experimental data is available for the velocity profile, it is expected that the non-zero velocity produced by Solver 2 is more physically representative than the zero velocity produced by Solver 1 and this is supported by the greater accuracy of the upstream results.

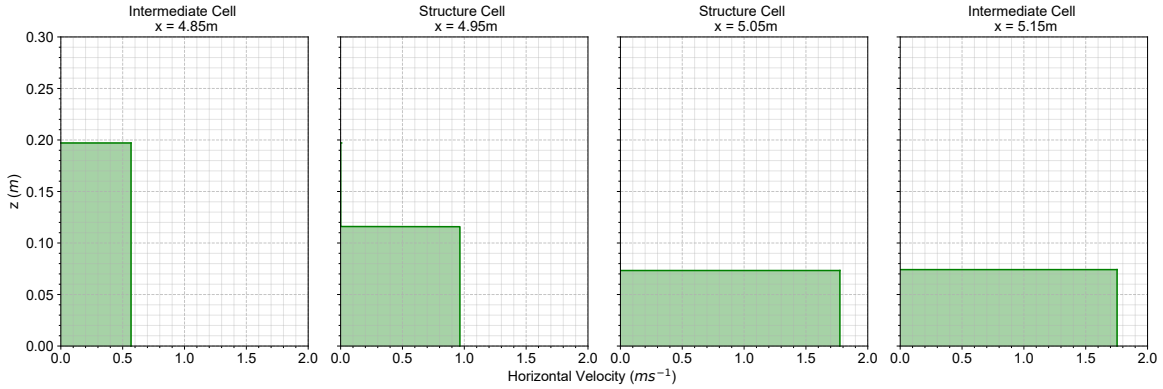

(a)

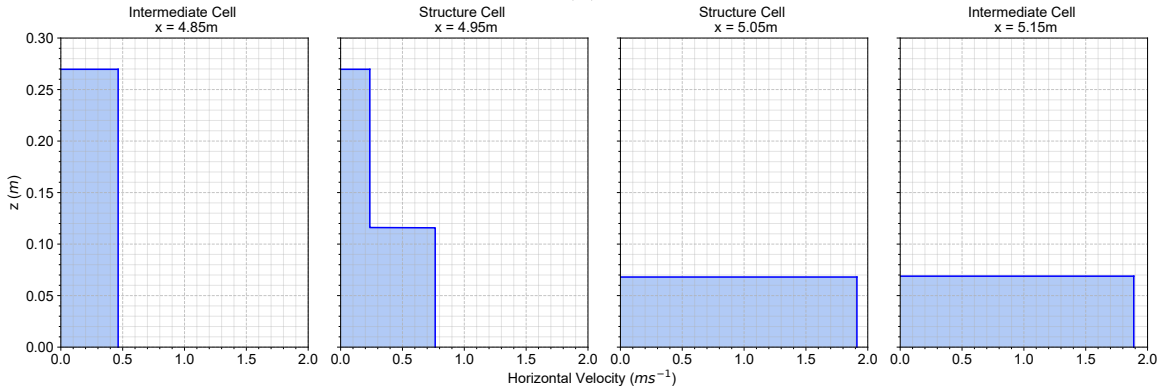

(b)

Figure 4.13: Comparison between the velocity profiles for test case one for Solver 1 (a) and Solver 2 (b) for the two cells either side of the structure interface.

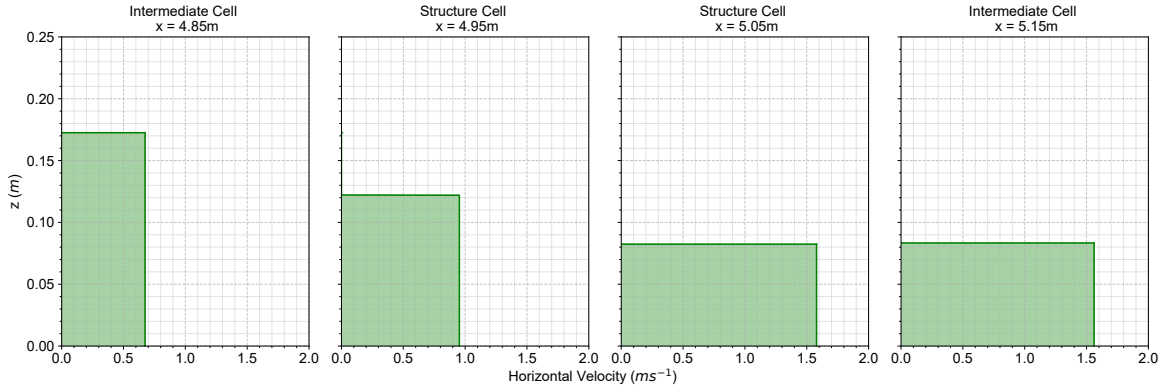

(a)

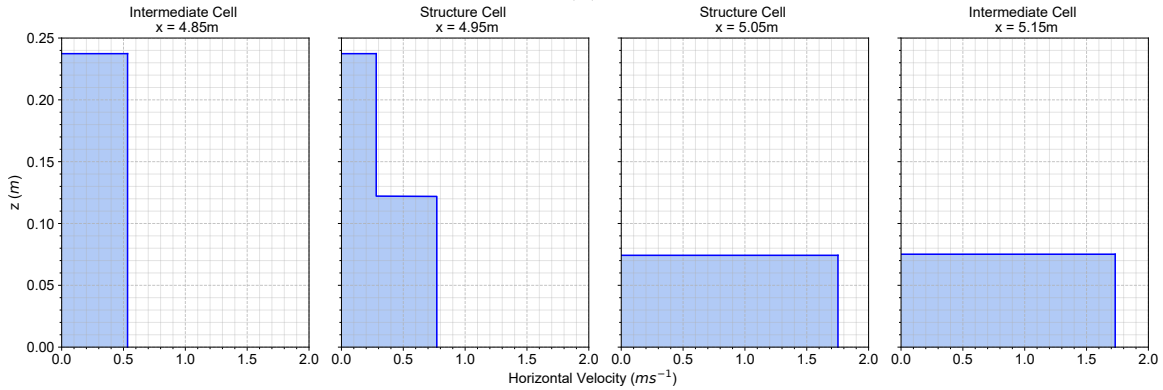

(b)

Figure 4.14: Comparison between the velocity profiles for test case two for Solver 1 (a) and Solver 2 (b) for the two cells either side of the structure interface.

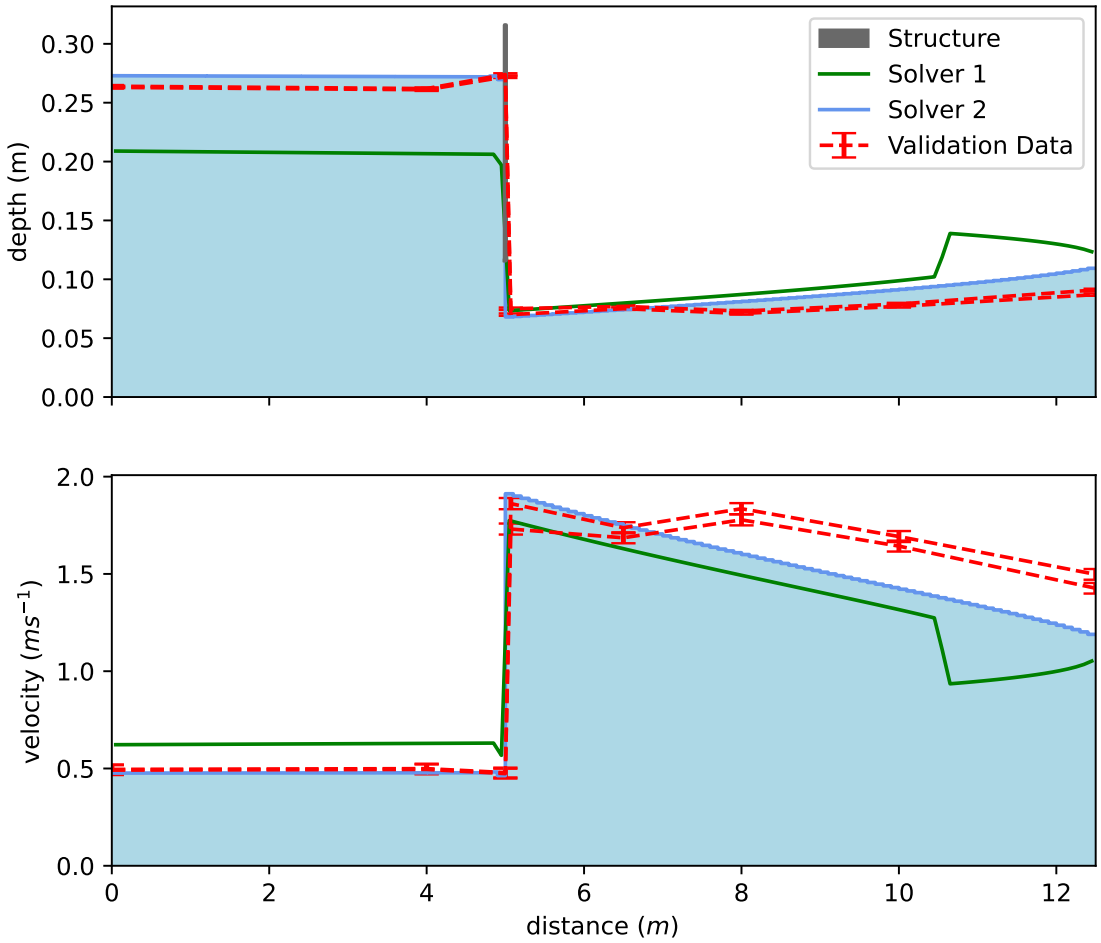

(a)

		Distance								
		0.00m	4.00m	5.00m	5.07m	6.50m	8.00m	10.00m	12.50m	
Average Depth (m)		0.2635	0.2615	0.2730	0.0725	0.0760	0.0720	0.0780	0.0890	Validation Data
Average Velocity (m/s)		0.4935	0.4973	0.4764	1.7938	1.7112	1.8063	1.6673	1.4612	
Average Discharge (m^2/s)		0.1301	0.1301	0.1301	0.1301	0.1301	0.1301	0.1301	0.1301	
Depth (m)		0.2729	0.2721	0.2697	0.0680	0.0743	0.0811	0.0912	0.1093	Numerical Data
Velocity (m/s)		0.4765	0.4779	0.4634	1.9121	1.7514	1.6043	1.4256	1.1894	
Discharge (m^2/s)		0.1301	0.1301	0.1301	0.1301	0.1301	0.1301	0.1301	0.1301	
Depth (m)	Absolute Error	0.0094	0.0106	-0.0033	-0.0045	-0.0017	0.0091	0.0132	0.0203	Error
	Percentage Error	3.6%	4.1%	1.2%	6.2%	2.3%	12.6%	17.0%	22.9%	
Velocity (m/s)	Absolute Error	-0.0171	-0.0195	-0.0130	0.1183	0.0402	-0.2019	-0.2417	-0.2718	
	Percentage Error	3.5%	3.9%	2.7%	6.6%	2.4%	11.2%	14.5%	18.6%	
Discharge (m^2/s)	Absolute Error	0.0000	0.0000	0.0000	0.0000	0.0000	0.0000	0.0000	0.0000	
	Percentage Error	0.0%	0.0%	0.0%	0.0%	0.0%	0.0%	0.0%	0.0%	

(b)

Figure 4.15: Comparison between numerical and experimental results for test case 1. Details of the numerical setup can be found in Section 4.3.1. Details of the experimental setup can be found in Mckenna et al. [303]

.

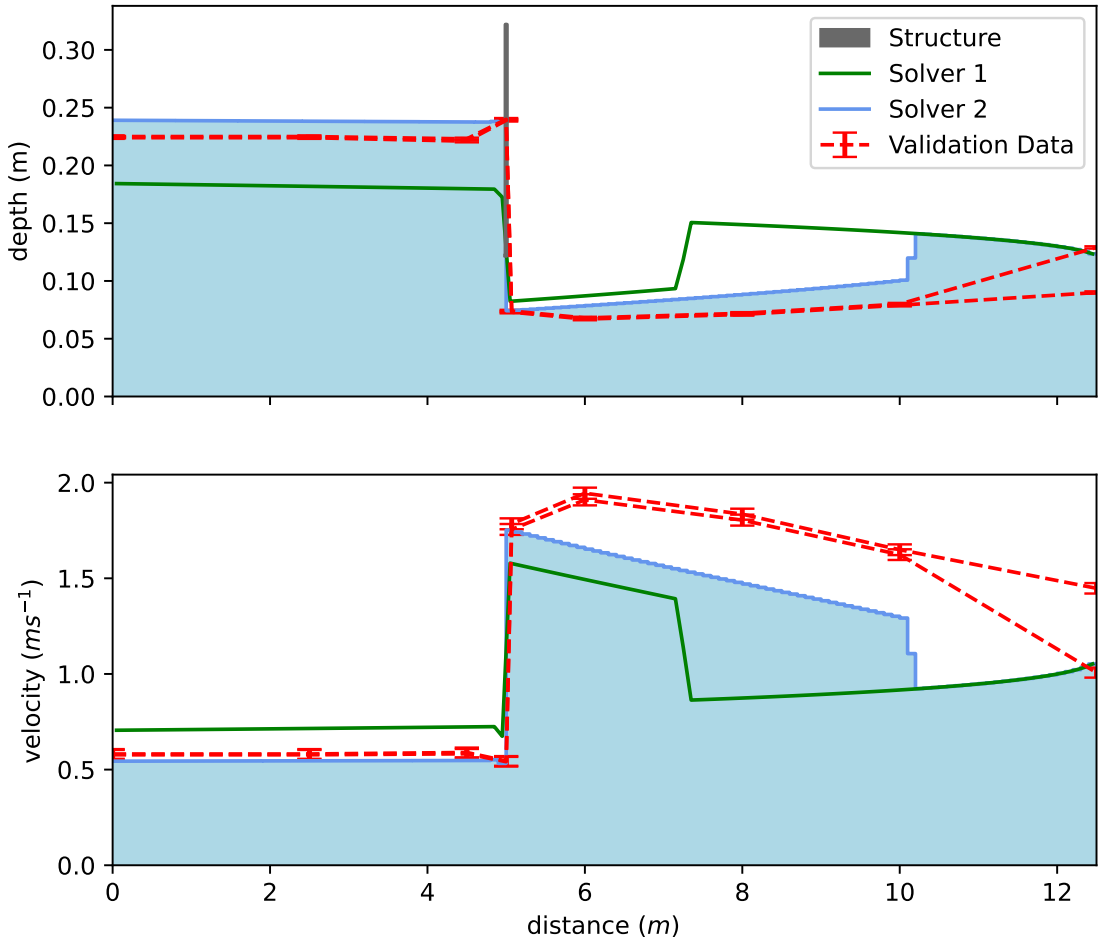

(a)

		Distance									
		0.00m	2.50m	4.50m	5.00m	5.07m	6.00m	8.00m	10.00m	12.50m	
Average Depth (m)		0.2245	0.2245	0.2220	0.2395	0.0735	0.0675	0.0715	0.0795	0.1095	Validation Data
Average Velocity (m/s)		0.5795	0.5795	0.5860	0.5432	1.7701	1.9274	1.8196	1.6365	1.1881	
Average Discharge (m^2/s)		0.1301	0.1301	0.1301	0.1301	0.1301	0.1301	0.1301	0.1301	0.1301	
Depth (m)		0.2391	0.2383	0.2376	0.2374	0.0742	0.0785	0.0882	0.1003	0.1235	Numerical Data
Velocity (m/s)		0.5441	0.5459	0.5475	0.5328	1.7522	1.6572	1.4745	1.2969	1.0523	
Discharge (m^2/s)		0.1301	0.1301	0.1301	0.1265	0.1301	0.1301	0.1301	0.1301	0.1299	
Depth (m)	Absolute Error	0.0146	0.0138	0.0156	-0.0021	0.0007	0.0110	0.0167	0.0208	0.0140	Error
	Percentage Error	6.5%	6.1%	7.0%	0.9%	1.0%	16.3%	23.4%	26.2%	12.8%	
Velocity (m/s)	Absolute Error	-0.0354	-0.0336	-0.0386	-0.0104	-0.0179	-0.2702	-0.3451	-0.3395	-0.1358	
	Percentage Error	6.1%	5.8%	6.6%	1.9%	1.0%	14.0%	19.0%	20.7%	11.4%	
Discharge (m^2/s)	Absolute Error	0.0000	0.0000	0.0000	-0.0036	0.0000	0.0000	0.0000	0.0000	-0.0002	
	Percentage Error	0.0%	0.0%	0.0%	2.8%	0.0%	0.0%	0.0%	0.0%	0.1%	

(b)

Figure 4.16: Comparison between numerical and experimental results for test case 2. Details of the numerical setup can be found in Section 4.3.1. Details of the experimental setup can be found in Mckenna et al. [303]

4.4.2 Stationary Hydraulic Jump

Test case five and test case six showcase the capacity of the solver to accurately resolve scenarios involving stationary hydraulic jumps. The two presented test cases use the same barrier configuration with different flow rates, resulting in the formation of different stationary hydraulic jumps for each scenario. As for test case one and two, Solver 2 accurately predicts the contraction coefficient for test case five:

$$C_c^{Exp} = \frac{0.018}{0.032} = 0.563 \pm 0.043 \quad , \quad C_c^{Num} = \frac{0.0177}{0.032} = 0.553 \tag{4.53}$$

and for test case six:

$$C_c^{Exp} = \frac{0.0185}{0.032} = 0.578 \pm 0.059 \quad , \quad C_c^{Num} = \frac{0.0185}{0.032} = 0.578 \tag{4.54}$$

For test case five there is an overestimation of the upstream depth and for test case six there is a slight underestimation of the upstream depth. It should be considered that since these test cases involve small inflows of $20.3 - 20.5ls^{-1}$ and $23.9 - 24.2ls^{-1}$ respectively, that the uncertainty in the inflow rate is larger than for the other presented test cases for which the flow rates exceeds $130ls^{-1}$. As outlined in the Euromag Sensors Instruction Manual [154], the inflow pipe must operate at full bore with minimal aeration, since the conversion between the measured potential to the estimated flow rate is based upon the assumed electrical conductivity of a volume of water, not an air-water mixture. The presence of air bubbles within the flow produces oscillating measurements, which were observed for all test cases (the average range in the measured inflow rate across the validation data set is equal to $0.32ls^{-1}$), whereas the presence of air pockets, which may form due to insufficient pressures and fluid velocities, produces systematic errors in the flow measurement. The maximum permissible errors provided by the manufacturer, summarised in Table 4.1, suggest that the error bound for flow rates of $\approx 20ls^{-1}$ is $\pm 2\%$, however, in the absence of in-situ verification the provided error bounds should be taken as guidelines only. Nonetheless, it can be demonstrated that adjusting the inflow rate within the range of the provided error estimates ($\pm 2\%$) produces an accurate prediction of the upstream depth, with indistinguishable differences downstream of the barrier, for both test cases (see A.1 and A.2).

In both cases, Solver 2 correctly predicts the formation of a stationary hydraulic jump downstream of the barrier. The robust wave estimation algorithm (Algorithm 2) was determined to be crucial for accurately capturing and maintaining the stationary hydraulic jumps for the relevant numerical simulations. For test case six, the location of the foot of the jump is accurately predicted however, for test case five, the prediction of the hydraulic jump is premature, occurring at approximately $x = 0.5$m upstream of the actual location. For test case five the downstream depth of the jump is accurately predicted whereas for test case five the downstream depth of the jump is underestimated. However, in general, the errors resulting from the inexact capturing of the hydraulic jump should not necessarily be attributed to Solver 2; as shown by Zhou and Stansby [500], for a given flow rate, the location at which a jump forms is dependent on small changes in the bed roughness, the position of the hydraulic jump is also sensitive to the implementation of the downstream boundary condition as shown in Figure 4.20 and the mesh resolution is clearly insufficient to sharply capture the slope of the jump in any case. Furthermore, in both cases the numerical results predict jumps with a zero length roller, characterised by a sharp discontinuity in the depth of flow at the toe of the jump, which is a feature

of the classical shallow water equations; since there is no internal energy transcribed within the classical shallow water equations, energy loss through a shock discontinuity is instead captured via Rankine-Hugoniot relations arising from the conservation of mass and momentum [432]. This is insufficient to capture the complex behaviour which occurs within the transition region of turbulent hydraulic jumps with a Froude number of greater than 1.5. Methods to overcome the shortcomings of the classical shallow water equations, such as the work of Richard and Gavrilyuk [376], are not appropriate nor necessary for the desired application of flood risk modelling. Since the purpose of the presented solution procedure is to capture the interaction of the flow with the barrier, the accurate reproduction of the flow characteristics immediately upstream and downstream of the barrier, as has been demonstrated, is of utmost importance when considering the models utility.

Once more, Solver 2 provides a significant improvement over Solver 1 in the accurate prediction of the upstream flow characteristics as a consequence of the more sophisticated solution procedure. Figure 4.17 and 4.18 show the respective vertical velocity profiles.

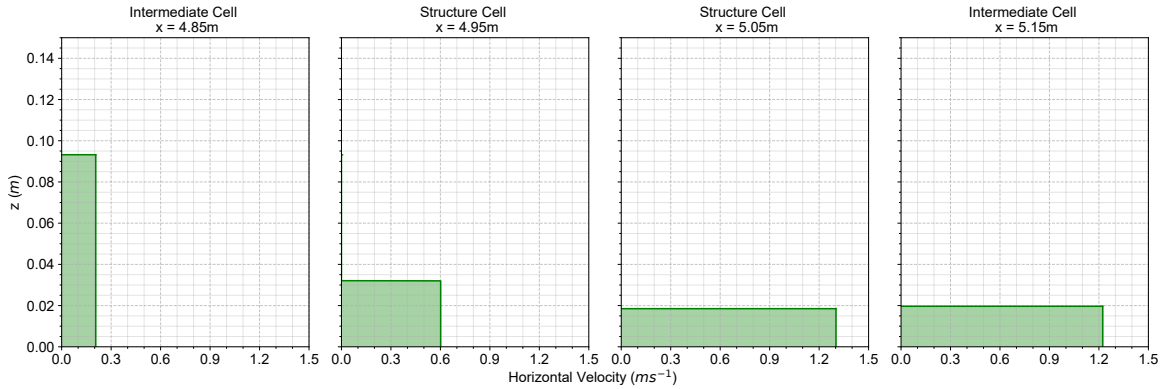

(a)

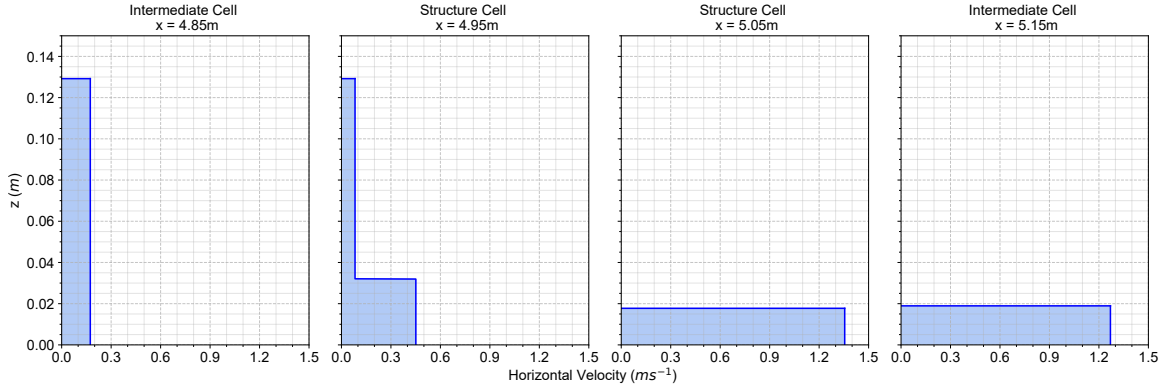

(b)

Figure 4.17: Comparison between the velocity profiles for test case five for Solver 1 (a) and Solver 2 (b) for the two cells either side of the structure interface.

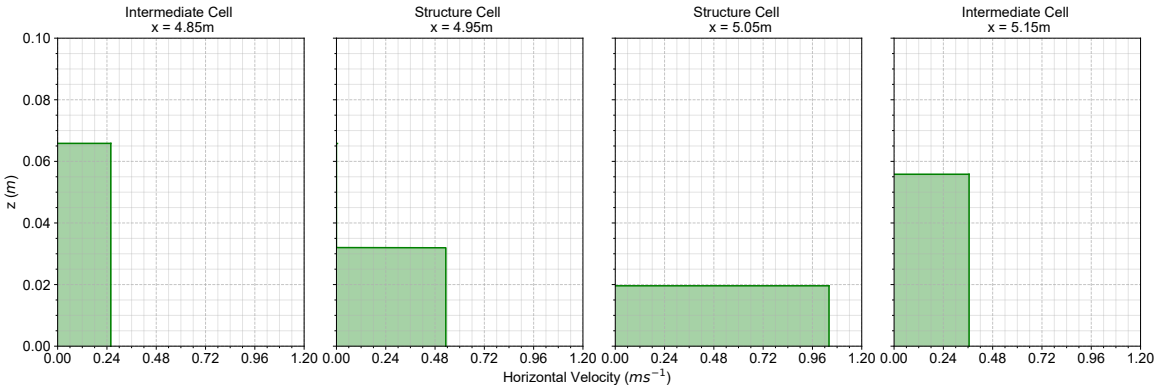

(a)

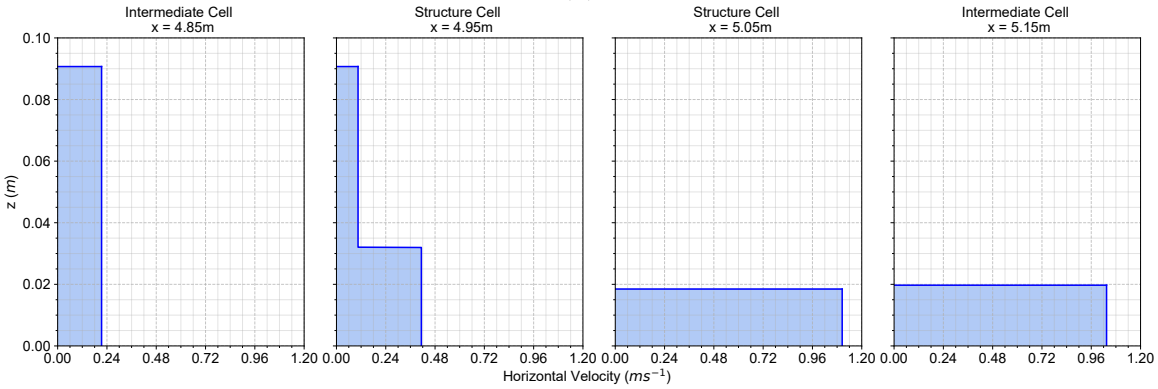

(b)

Figure 4.18: Comparison between the velocity profiles for test case six for Solver 1 (a) and Solver 2 (b) for the two cells either side of the structure interface.

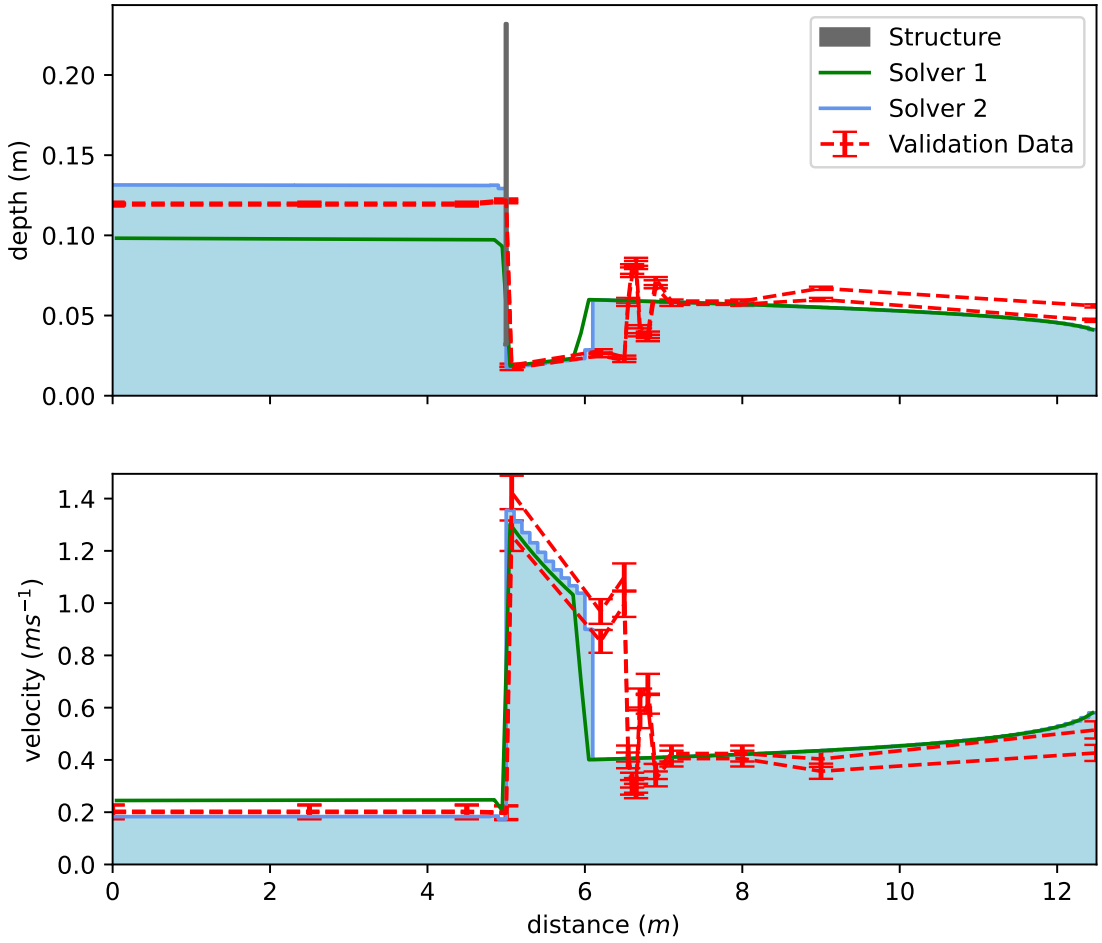

(a)

		Distance											
		0.00m	4.50m	5.07m	6.20m	6.50m	6.55m	6.60m	6.90m	7.10m	8.00m	9.00m	12.50m	
Average Depth (m)		0.1195	0.1195	0.0180	0.0265	0.0230	0.0585	0.0780	0.0705	0.0580	0.0580	0.0635	0.0515	Validation Data
Average Velocity (m/s)		0.2013	0.2013	1.3361	0.9075	1.0457	0.4111	0.3083	0.3411	0.4147	0.4147	0.3787	0.4670	
Average Discharge (m^2/s)		0.0241	0.0241	0.0241	0.0241	0.0241	0.0241	0.0241	0.0241	0.0241	0.0241	0.0241	0.0241	
Depth (m)		0.1315	0.1311	0.0177	0.0597	0.0593	0.0592	0.0591	0.0587	0.0584	0.0570	0.0551	0.0412	Numerical Data
Velocity (m/s)		0.1829	0.1834	1.3550	0.4024	0.4050	0.4055	0.4059	0.4090	0.4111	0.4215	0.4356	0.5803	
Discharge (m^2/s)		0.0240	0.0240	0.0240	0.0240	0.0240	0.0240	0.0240	0.0240	0.0240	0.0240	0.0240	0.0239	
Depth (m)	Absolute Error	0.0120	0.0116	-0.0003	0.0332	0.0363	0.0007	-0.0189	-0.0118	0.0004	-0.0010	-0.0084	-0.0103	Error
	Percentage Error	10.0%	9.7%	1.4%	125.3%	157.8%	1.2%	24.2%	16.7%	0.7%	1.8%	13.2%	20.0%	
Velocity (m/s)	Absolute Error	-0.0183	-0.0179	0.0189	-0.5052	-0.6407	-0.0057	0.0976	0.0678	-0.0036	0.0068	0.0568	0.1133	
	Percentage Error	9.1%	8.9%	1.4%	55.7%	61.3%	1.4%	31.7%	19.9%	0.9%	1.7%	15.0%	24.3%	
Discharge (m^2/s)	Absolute Error	0.0000	0.0000	0.0000	0.0000	0.0000	0.0000	0.0000	0.0000	0.0000	0.0000	0.0000	-0.0001	
	Percentage Error	0.0%	0.0%	0.0%	0.1%	0.2%	0.2%	0.2%	0.2%	0.2%	0.2%	0.2%	0.5%	

(b)

Figure 4.19: Comparison between numerical and experimental results for test case 5. Details of the numerical setup can be found in Section 4.3.1. Details of the experimental setup can be found in Mckenna et al. [303].

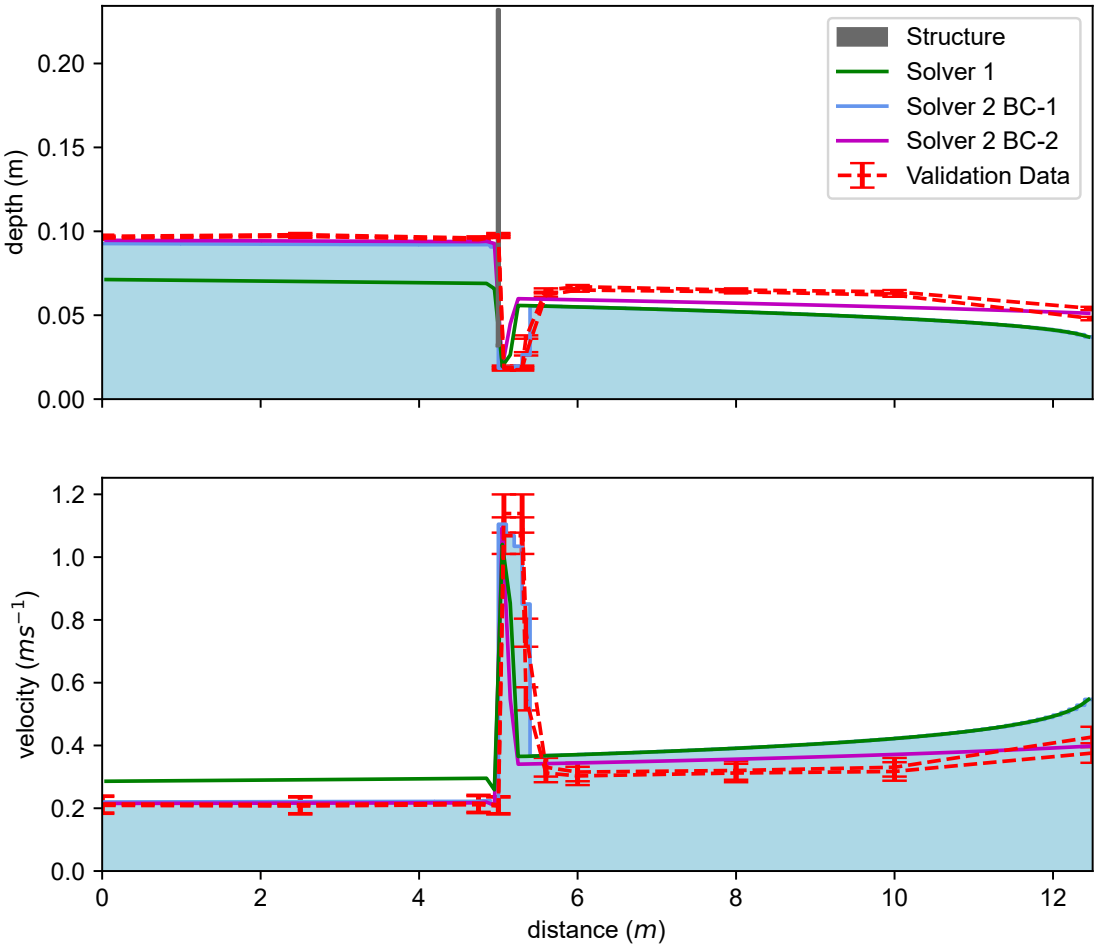

(a)

		Distance											
		0.00m	2.50m	4.75m	5.00m	5.07m	5.35m	5.60m	6.00m	8.00m	10.00m	12.50m	
Average Depth (m)		0.0965	0.0975	0.0955	0.0975	0.0185	0.0320	0.0635	0.0660	0.0645	0.0630	0.0510	Validation Data
Average Velocity (m/s)		0.2114	0.2092	0.2136	0.2092	1.1027	0.6375	0.3213	0.3091	0.3163	0.3238	0.4000	
Average Discharge (m^2/s)		0.0204	0.0204	0.0204	0.0204	0.0204	0.0204	0.0204	0.0204	0.0204	0.0204	0.0204	
Depth (m)		0.0927	0.0923	0.0919	0.0907	0.0185	0.0264	0.0554	0.0549	0.0521	0.0482	0.0371	Numerical Data
Velocity (m/s)		0.2200	0.2210	0.2220	0.2138	1.1048	0.8506	0.3675	0.3708	0.3911	0.4222	0.5468	
Discharge (m^2/s)		0.0204	0.0204	0.0204	0.0194	0.0204	0.0225	0.0204	0.0204	0.0204	0.0203	0.0203	
Depth (m)	Absolute Error	-0.0038	-0.0052	-0.0036	-0.0068	0.0000	-0.0056	-0.0081	-0.0111	-0.0124	-0.0148	-0.0139	Error
	Percentage Error	3.9%	5.4%	3.8%	7.0%	0.2%	17.5%	12.7%	16.8%	19.3%	23.5%	27.3%	
Velocity (m/s)	Absolute Error	0.0086	0.0118	0.0084	0.0046	0.0021	0.2131	0.0462	0.0617	0.0748	0.0983	0.1468	
	Percentage Error	4.0%	5.6%	3.9%	2.2%	0.2%	33.4%	14.4%	20.0%	23.6%	30.4%	36.7%	
Discharge (m^2/s)	Absolute Error	0.0000	0.0000	0.0000	-0.0010	0.0000	0.0021	0.0000	0.0000	0.0000	-0.0001	-0.0001	
	Percentage Error	0.0%	0.0%	0.0%	4.9%	0.0%	10.1%	0.2%	0.2%	0.2%	0.2%	0.6%	

(b)

Figure 4.20: Comparison between numerical and experimental results for test case 6. Solver 2 BC-1 illustrates the results for the standard critical depth boundary condition which is implemented for all test cases. Solver 2 BC-2 provides a comparison of the results for a fixed depth boundary condition ($h = 0.051m$) to demonstrate the significance of the downstream boundary condition on the downstream flow. Table 4.20b presents data relating to Solver 1 BC-1. Details of the numerical setup can be found in Section 4.3.1. Details of the experimental setup can be found in Mckenna et al. [303].

4.4.3 Flow Over and Under a Barrier

Test case eight and nine involve combined flow over a weir and under a gate, with significant vertical flows occurring as a result of the flow over the barrier, which presents a significant challenge for depth-averaged shallow water models since the vertical component of the velocity is neglected. Furthermore, energy losses induced by the conversion of potential energy to kinetic energy during weir flow are also not incorporated within the model. Nonetheless, the overall results remain accurate and the general behaviour is well captured: Solver 2 accurately captures the behaviour of the flow for test eight (Figure 4.23) and test case nine (Figure 4.24).

For test case eight, the validation data demonstrates significant vertical flows immediately downstream of the barrier which obviously cannot be captured by a depth-averaged one- or two-dimensional shallow water model. Despite this, the errors in the predicted depths and velocity upstream are small, ranging from $0.2 - 1.6\%$, with errors downstream at $x = 5.20m$ and $x = 6.00m$ between $9.0\% - 11.0\%$. For test case nine, the horizontal scale of the vertical flow is much smaller and as a result the immediate downstream profile is more accurately predicted. However, upstream accuracy is comparatively worse than for test case eight, although errors remain acceptably small ($6.4 - 8.5\%$). As for all of the presented test cases, the downstream boundary condition is a source of error however, the accuracy of the presented methodology can still be ascertained from the data in close proximity to the barrier.

It is possible to incorporate energy losses associated with weir flow within the model by introducing an internal boundary condition above the barrier based upon a weir equation, an outline of a simple implementation of this method is provided in A.3 and the corresponding results are provided in A.4 and A.5. However, for test case eight and nine the results are quasi-indistinguishable from the results presented in Figure 4.23 and 4.24 suggesting that neglecting energy losses is not the primary cause of the errors for the presented test cases. As such, the errors in the results are likely primarily caused by the quality of the approximation of the velocity profile.

Through comparison of the results for Solver 1 and Solver 2 it can be seen that, for both cases, Solver 1 underestimates the upstream depth and overestimates the velocity relative to Solver 1, producing a larger velocity and shallower corresponding depth downstream of the barrier. This can be explained through analysis of the velocity profiles presented in Figure 4.21 and 4.22: the velocity assignment assumptions for Solver 1 result in a larger and equal velocity in both open layers, relative to Solver 1, which results in a larger numerical flux and consequently upstream depths are comparatively lower and downstream velocities are comparatively higher. Overall it is hard to distinguish, purely based on the presented test cases, which of the two solvers is most accurate for modelling combined weir and gate flows. However, Solver 2 has the advantage in that the quality of the approximation of the velocity profile can be improved by introducing further vertical discretisation within each structure cell as well as the possibility of introducing more structure cells around a structure interface to extend the region in which the velocity profile is approximated. However, the results demonstrate that despite the complexity of the flow, both Solver 1 and Solver 2 produce adequate numerical results for combined weir and gate flow.

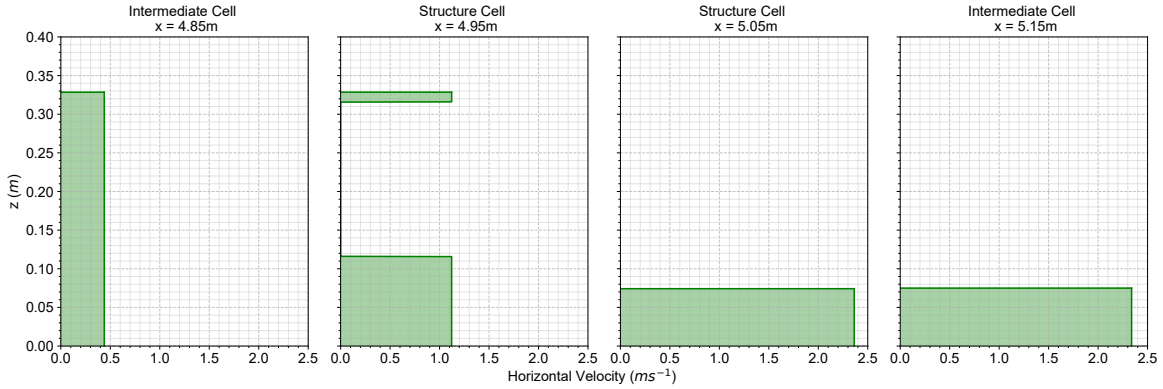

(a)

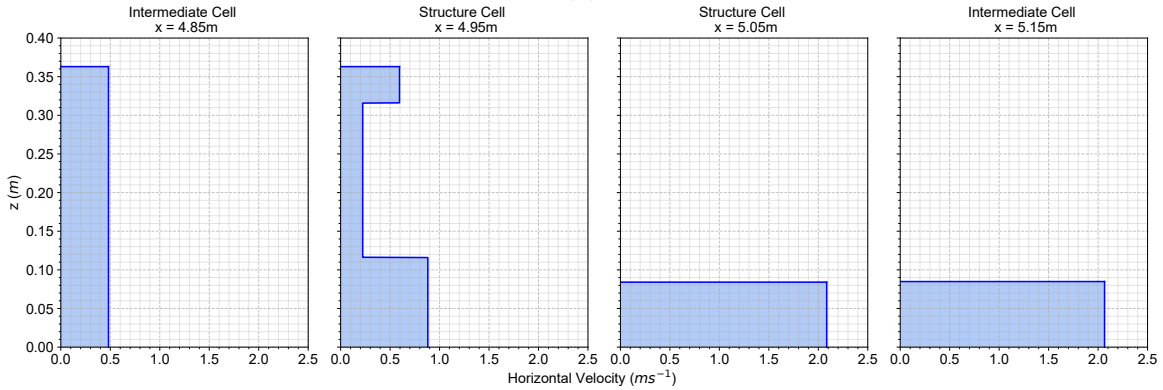

(b)

Figure 4.21: Comparison between the velocity profiles for test case eight for Solver 1 (a) and Solver 2 (b) for the two cells either side of the structure interface.

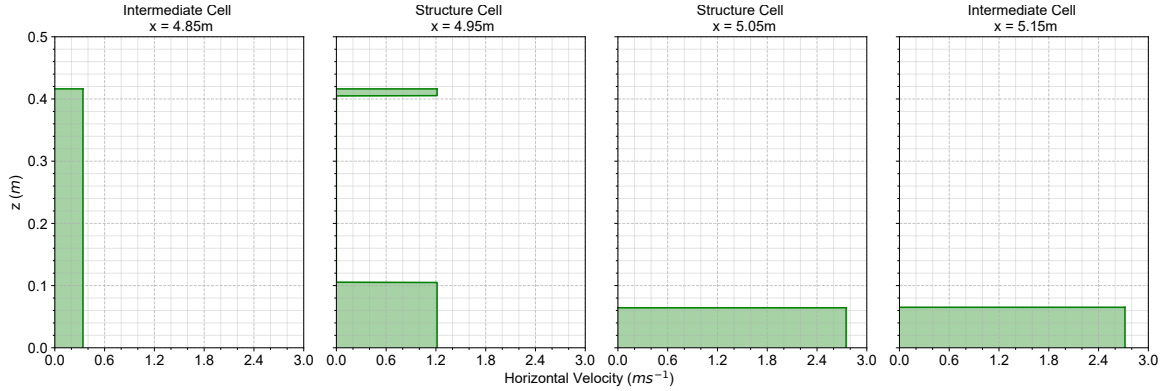

(a)

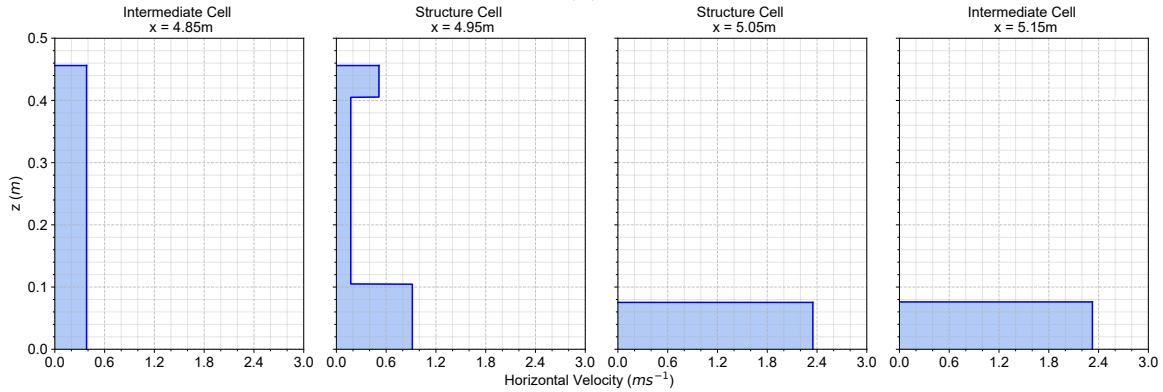

(b)

Figure 4.22: Comparison between the velocity profiles for test case nine for Solver 1 (a) and Solver 2 (b) for the two cells either side of the structure interface.

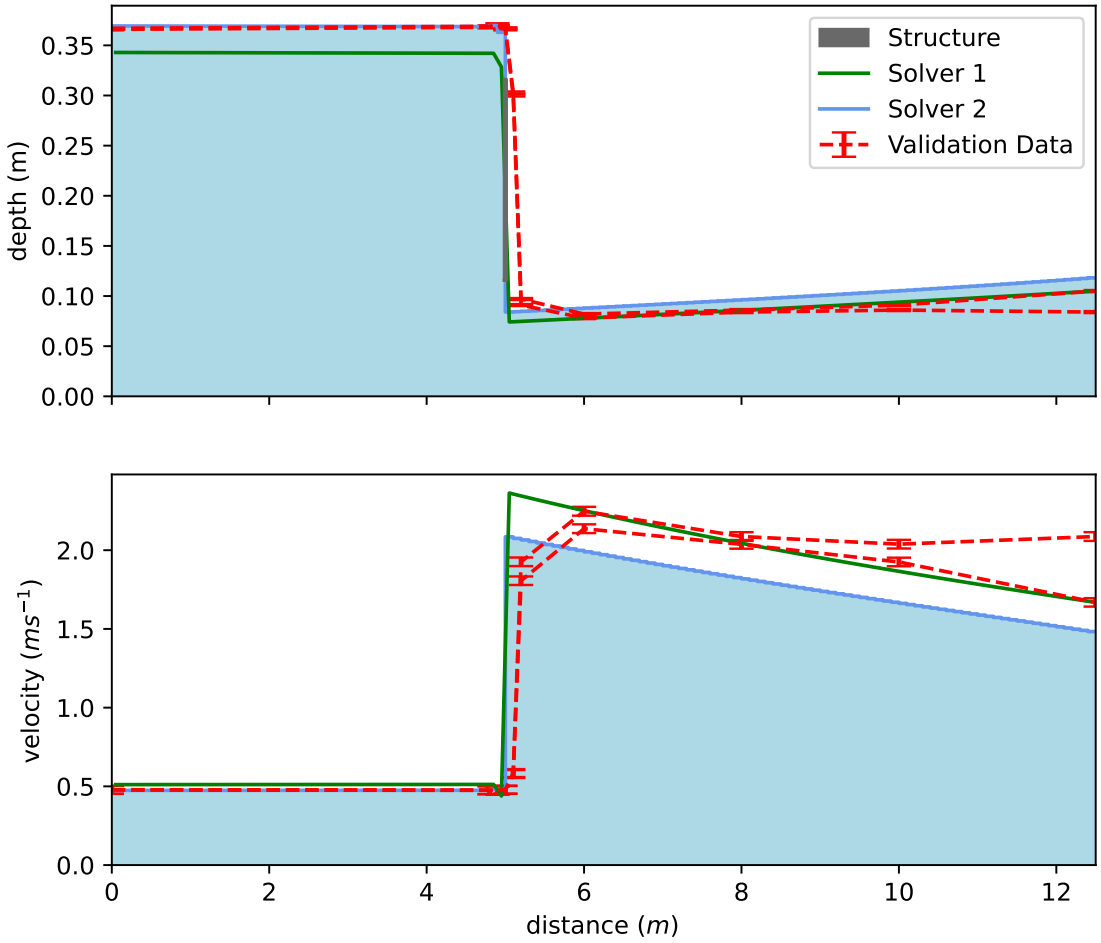

(a)

		Distance									
		0.00m	4.80m	4.90m	5.00m	5.20m	6.00m	8.00m	10.00m	12.50m	
Average Depth (m)		0.3665	0.3685	0.3700	0.3665	0.0940	0.0800	0.0850	0.0885	0.0945	Validation Data
Average Velocity (m/s)		0.4782	0.4756	0.4736	0.4782	1.8644	2.1906	2.0618	1.9802	1.8545	
Average Discharge (m^2/s)		0.1753	0.1753	0.1753	0.1753	0.1753	0.1753	0.1753	0.1753	0.1753	
Depth (m)		0.3693	0.3693	0.3664	0.3630	0.0847	0.0879	0.0962	0.1052	0.1181	Numerical Data
Velocity (m/s)		0.4745	0.4781	0.4813	0.4815	2.0701	1.9944	1.8218	1.6659	1.4833	
Discharge (m^2/s)		0.1752	0.1766	0.1763	0.1748	0.1753	0.1753	0.1753	0.1753	0.1753	
Depth (m)	Absolute Error	0.0028	0.0008	-0.0036	-0.0035	-0.0093	0.0079	0.0112	0.0167	0.0236	Error
	Percentage Error	0.8%	0.2%	1.0%	0.9%	9.9%	9.8%	13.2%	18.9%	25.0%	
Velocity (m/s)	Absolute Error	-0.0037	0.0026	0.0076	0.0034	0.2058	-0.1962	-0.2399	-0.3143	-0.3712	
	Percentage Error	0.8%	0.5%	1.6%	0.7%	11.0%	9.0%	11.6%	15.9%	20.0%	
Discharge (m^2/s)	Absolute Error	0.0000	0.0013	0.0011	-0.0004	0.0000	0.0000	0.0000	0.0000	0.0000	
	Percentage Error	0.0%	0.7%	0.6%	0.2%	0.0%	0.0%	0.0%	0.0%	0.0%	

(b)

Figure 4.23: Comparison between numerical and experimental results for test case 8. Details of the numerical setup can be found in Section 4.3.1. Details of the experimental setup can be found in Mckenna et al. [303].

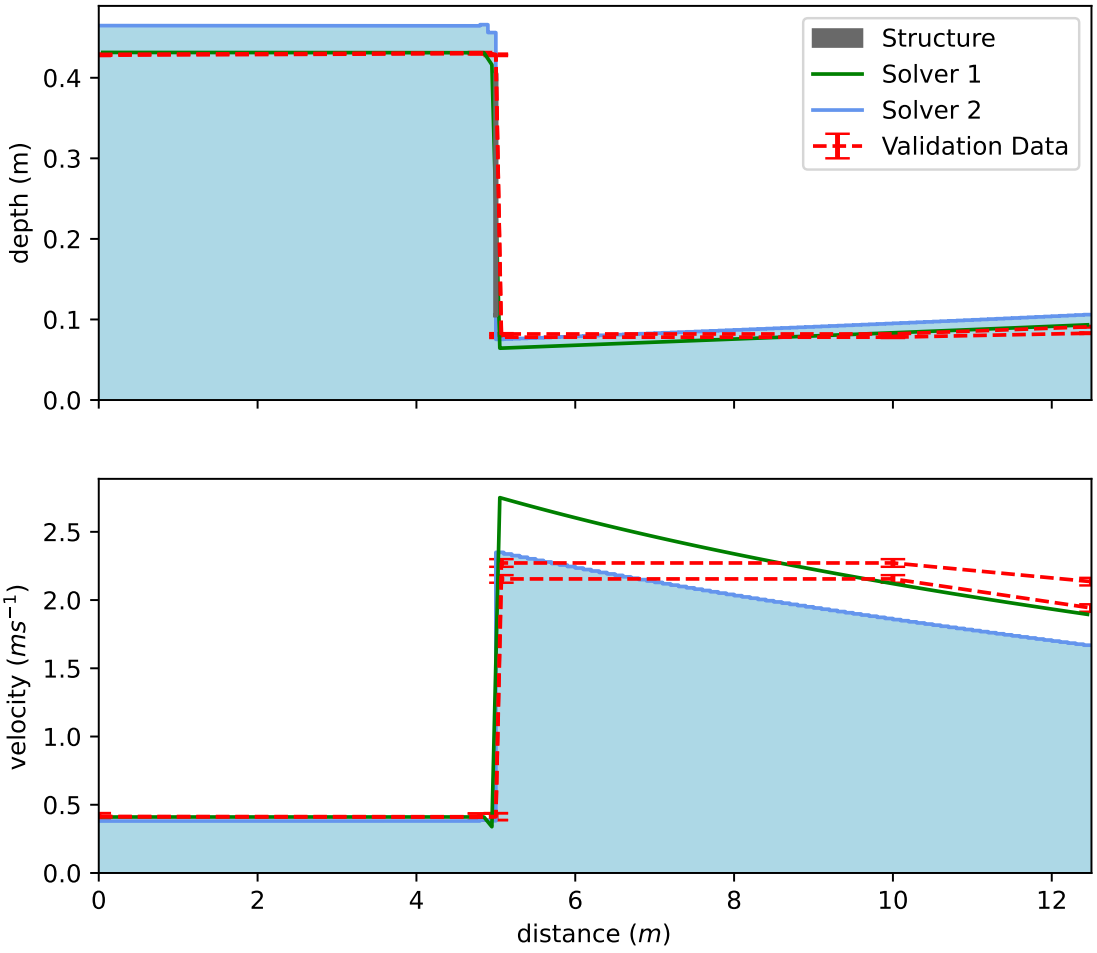

(a)

		Distance						
		0.00m	4.80m	5.00m	5.07m	10.00m	12.50m	
Average Depth (m)		0.4285	0.4305	0.4285	0.0800	0.0800	0.0870	Validation Data
Average Velocity (m/s)		0.4130	0.4110	0.4130	2.2119	2.2119	2.0339	
Average Discharge (m^2/s)		0.1770	0.1770	0.1770	0.1770	0.1770	0.1770	
Depth (m)		0.4648	0.4652	0.4561	0.0753	0.0951	0.1060	Numerical Data
Velocity (m/s)		0.3807	0.3843	0.3826	2.3496	1.8610	1.6693	
Discharge (m^2/s)		0.1769	0.1788	0.1745	0.1770	0.1770	0.1770	
Depth (m)	Absolute Error	0.0363	0.0347	0.0276	-0.0047	0.0151	0.0190	Error
	Percentage Error	8.5%	8.1%	6.4%	5.9%	18.9%	21.8%	
Velocity (m/s)	Absolute Error	-0.0322	-0.0267	-0.0304	0.1377	-0.3509	-0.3646	
	Percentage Error	7.8%	6.5%	7.4%	6.2%	15.9%	17.9%	
Discharge (m^2/s)	Absolute Error	0.0000	0.0018	-0.0025	0.0000	0.0000	0.0000	
	Percentage Error	0.0%	1.0%	1.4%	0.0%	0.0%	0.0%	

(b)

Figure 4.24: Comparison between numerical and experimental results for test case 9. Details of the numerical setup can be found in Section 4.3.1. Details of the experimental setup can be found in Mckenna et al. [303].

4.4.4 Mesh Convergence Analysis

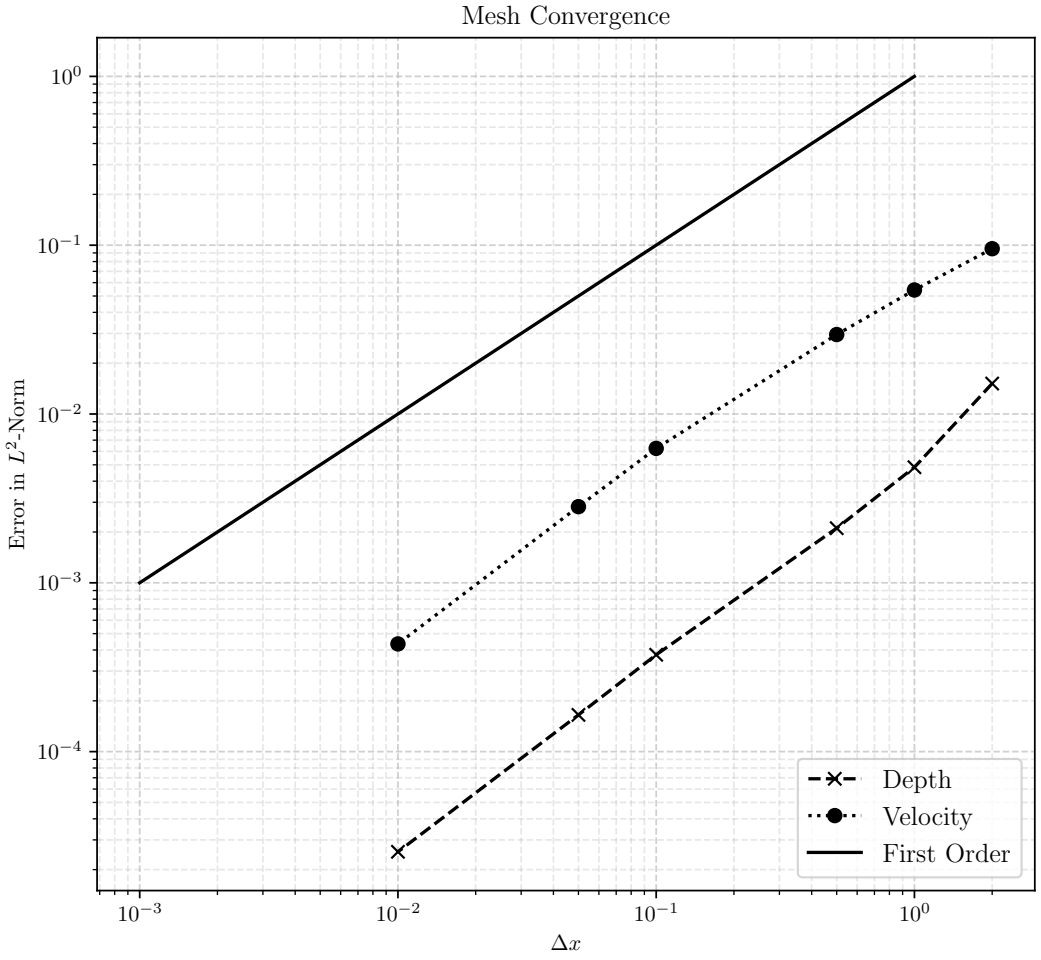

Table 4.3: The error in the L^2-norm, computed using a 0.005m mesh as a reference solution in absence of an analytical solution.

In the absence of an available analytical solution, the convergence of the scheme, shown in Figure 4.3, is assessed by computing the error in the L^2-norm with respect to a reference solution produced using a refined mesh resolution ($\Delta x = 0.005$m).

4.5 Conclusion

A new Riemann solver, capable of resolving numerical fluxes across a partially obstructed interface, has been presented. Via the validation process, it has been demonstrated that the solver is able to adequately capture fluid-structure interactions for a range of barrier configurations and flow rates. Furthermore, via the comparison process, it has been demonstrated that the solver represents a significant improvement on the previously published solver [303].

It is clear that the new solution procedure addresses the identified weakness of the previous solver by more accurately capturing the vertical variation in the horizontal velocity profile at a structure interface. This results in the more accurate determination of the flow characteristics, particularly the upstream flow characteristics. However, this does come at the cost of increased computational demands and implementation complexity although, due to the local nature of the solution procedure and the proportionally small number of structure cells within a computational domain, the increase in computational expense in unlikely to be prohibitive. As for the previous solver, the biggest barrier to implementation is the scarcity of the required data for structures and the availability of suitable meshing algorithms, which remains the subject of further work. The solver presented in [303] maintains utility as a viable, albeit comparatively less accurate, alternative with a greater ease of implementation.

The capability of the solver to resolve numerical fluxes across a partially obstructed interface has significant implications for modelling a variety of structures within two-dimensional hydrodynamic models. This has important applications in terms of improving flood inundation modelling capabilities as well as enabling the modelling of infrastructure resilience modelling and the structural health monitoring of hydraulic structures. Moreover, the greater accuracy of the solver combined with the vertical discretisation of the structure cells presents new opportunities such as the possibility of modelling the transport of solutes in conjunction with flows around obstacles.

As for all models, the underlying assumptions must be considered in order to ascertain the limitations of the model and as such the solver should be considered appropriate for modelling structures at a spatial scale whereby approximating the structure as a partial obstruction existing at a cell interface is appropriate. Although, the proposed model does not capture all of the energy losses which occur as a result of the fluid-structure interaction, such effects are insignificant at this spatial scale in comparison with the effect induced by the blockage of the flow by the structure, which is well captured as shown by the validation results. For detailed analyses of individual structures 3D CFD analyses are recommended.

Avenues for further development of the solver include increased vertical discretisation of structure cells, to enhance the quality of the approximation of the velocity profile (Figure 4.25) and the use of more structure cells per structure interface, to horizontally extend the region in which the vertical velocity profile is captured (Figure 4.26). Increased vertical discretisation of the structure cells is relatively straightforward albeit at potentially significant computational cost on a per structure cell basis. The use of more structure cells, to extend horizontally the region in which the approximate vertical velocity profile is captured, can potentially result in complex meshing requirements for 2D models. This is primarily as a result of the fact that a single cell may be close enough to two or

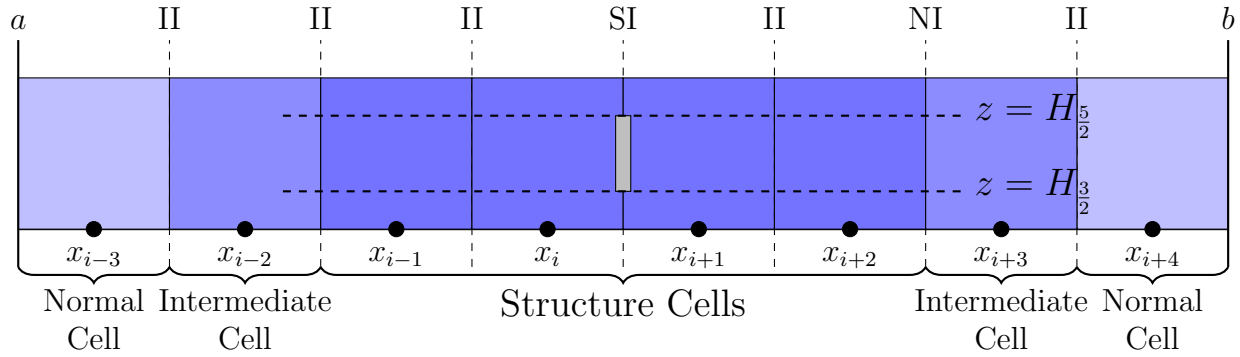

Figure 4.25: A simple computational domain $[a, b]$ illustrating the implementation of additional structure cells.

more structure interfaces and as a consequence, would require vertical discretisation into sub-cells aligned with all relevant structure interfaces. This is especially problematic if increased vertical discretisation of the structure cells is also introduced, as the number of layers per structure cell could become unrealistic. An alternative approach would be to describe the flow within a sub-cell using a multi-layer system with mass exchanges [32, 159] as this would enable a higher quality approximation of the velocity profile within a sub-cell without introducing additional unnecessary continuity equations.

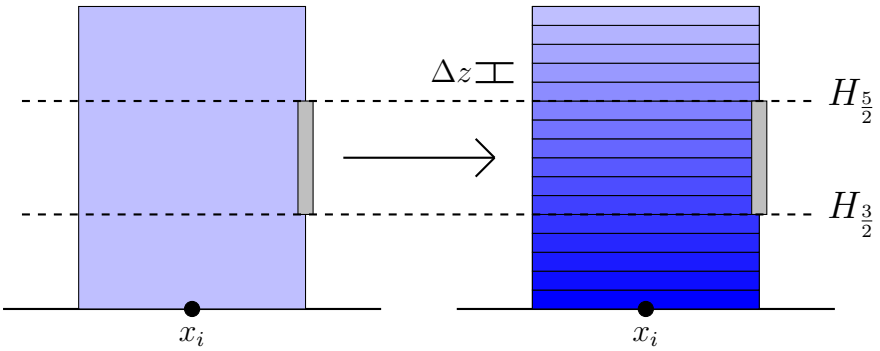

Figure 4.26: An example of further vertical discretisation of a Structure cell.

Another option for potential further development of the solver would be to develop a more sophisticated treatment of the relatively simplistic layer redefinition process. Flows which are inherently vertical in nature, such as water spilling over the top of a structure, also present a major challenge however, this is difficult to address without compromising the compatibility of the solver with the numerical schemes utilised by contemporary flood models due to the fundamental nature of the shallow water equations.

Chapter 5

A Local Multi-Layer Approach to Modelling Depth-Integrated Solute Transport through Obstructions

Modelling the mixing and transport of solutes is important for a variety of environmental engineering applications. Within typical domains, features such as bridges, gates and weirs act as partial barriers to flow and the advection and diffusion of a scalar quantity in the presence of such features has been seldom explored within academic literature. In order to address this gap in modelling capability, the advection and diffusion of a well-mixed dissolved solute within the context of shallow water interactions with partial barriers to flow is explored using the local multi-layer approach to modelling shallow water interactions with obstructions presented by Mckenna et al. in [arXiv preprint arXiv:2304.10262, physics.flu-dyn, (2023)]. A simple first order upwind scheme utilising a Harten-Lax-van Leer Contact solver to resolve numerical fluxes is implemented for the coupled modelling of a shallow water system with the advection-diffusion equations. The numerical results are validated via planar concentration analyses, in which the scattering and absorption of incident light by an injected dissolved fluorescent tracer mass enables the nonintrusive determination of the fieldwise concentration for the duration of the experiment.

This chapter is to be submitted for publication, pending successful publication of Chapter 4 and the completion of significant further work.

5.1 Introduction

Accurately modelling the mixing and transport of solutes is crucial for various environmental engineering applications, including studies assessing the environmental impact of soluble pollutants on surface water quality and the transportation of nutrients for fertigation. For vertically well-mixed solutes, depth-averaged approximations may be applied, with the computational demands of hydrodynamic flood modelling at scales pertinent to flood risk management necessitating such an approach.

Within academic literature finite difference ([136, 273]), finite element ([183]), finite volume ([439, 321]) and Lattice Boltzmann methods [358, 499, 357] for modelling advection-diffusion equations have been presented. State-of-the-art urban hydrodynamic modelling and more generally the approximation of hyperbolic conservation laws, is dominated by finite volume models due to the inherent conservation properties, flexibility of implementation on structured and unstructured grids, strong stability properties and simplicity of implementation and as such, finite volume models are the primary focus of this publication. For finite volume methods solving systems including advection-diffusion equations specifically, it is common to present a flexible implementation on irregular unstructured grids ([30, 53, 249, 271, 456, 321, 199, 94]) in order to provide greater meshing flexibility for complex geometries. Although the versatility of using either regular structured meshes or irregular unstructured meshes is clearly desirable, practitioners should be aware that although irregular unstructured meshes provide an advantageous degree of flexibility when meshing complex geometries, this does not necessarily guarantee higher accuracy; as explained by Bouche et al. [69], when methods are formally referred to as *first order* or *second order* with regards to the order of spatial accuracy, this indicates that the scheme exhibits a first or second order truncation error on uniform Cartesian grids, it is not known whether the same order of spatial accuracy is achieved for unstructured grids. Furthermore, Bouche et al. [69] demonstrate that, in general, the truncation error for unstructured grids *does not* tend to zero as the mesh size is refined.

Within the literature relating to finite volume solutions for systems containing advection-diffusion equations a number of key numerical challenges can be identified. The first of which is the case of pure advection, for which numerical schemes should minimise artificial diffusion and oscillations in order to conserve solute concentration profiles for long duration simulations. Since it is well established that first-order upwind schemes are diffusive, such schemes are typically unsuitable in this regard, producing increasingly smeared concentration profiles with a corresponding reduction in peak concentrations over the duration of the simulation [199, 331, 321, 330]. Extension of the scheme to second order spatial accuracy to remedy this, is however, not straightforward, with the choice of flux limiter having a strong influence on the quality of the results [53, 83]. Furthermore, Murillo et al. [331] demonstrated that it is not possible to simultaneously obtain second order spatial accuracy for both the conserved variables and the solute concentration; a choice must be made as to which requires a higher order of spatial accuracy. This is as a consequence of the fact that the solute concentration, which is a primitive variable, is independent of the eigenstructure of the system and therefore the monotonicity properties of the numerical scheme apply only to the solute mass not the concentration. As a consequence, it is also non-trivial to ensure bounded values of concentration. This means that it is necessary to enforce, when updating cell properties, that the updated value of the concentration is bounded by the neighbouring minimum and maximum concentration

values. A solution to this problem is introduced via a conservative redistribution of the updating contributions in [333], with further discussion and implementation being explored in [330, 331, 332, 83] for conservative upwind schemes utilising Roe approximate Riemann solvers [381]. In this regard, the treatment of wet/dry fronts also requires special numerical consideration [332, 40, 48].

The minimisation of numerical diffusion and oscillations can also be achieved via the implementation of higher order accuracy schemes as shown by Cai et al. [84], who implemented a fourth order central weighted essentially non-oscillatory reconstruction with an adaptive semi-discrete central upwind scheme. This scheme can achieve an arbitrary order of spatial accuracy in the absence of source terms however, the second order discretisation of the source terms presented within the paper proves to be of high-resolution and non-oscillatory. It should be noted however, that Cai et al. only consider the case of pure advection with no diffusion.

An alternative method for minimising artificial diffusion and oscillations is the decoupled modelling of the solute transport using a non-diffusive numerical method. Chertock et al. [101] and Touma and Saleh [440] both utilise a hybrid finite-volume-particle method approach in which the solution of the shallow water system is achieved via a central-upwind scheme and the subsequent advection of the solute is achieved using a particle method. This is beneficial since central upwind schemes are unable to sufficiently resolve the contact waves across which the pollutant concentration is discontinuous and the particle method is non-dissipative with filters being used to remove oscillations. It should however be noted that both of the referenced methods consider only the pure advection of a scalar quantity. For conservative upwind schemes, it has been shown by Burguete et al. [83], that decoupled discretisation of the solute transport results in significant numerical challenges that require special corrections [334]. This is further supported by Bai and Jin [40], who demonstrate the same numerical issues for decoupled schemes. Historically, decoupled treatment of the advection of a solute has presented a popular solution since it enables the implementation of simple and computationally efficient schemes, with decoupling justified, in ignorance of the numerical difficulties, by the negligible influence of the solute on the flow dynamics for low concentrations. Adaptive mesh refinement, as implemented by Benkhaldoun [53], also presents a potential solution to reduce numerical diffusion, albeit at the cost of greater implementation complexity.

For first order upwind schemes with sufficient physical diffusion, Murillo and García-Navarro [330] proposed an innovative solution involving the modification of the physical diffusion to ensure that the total diffusion, equal to the sum of the numerical and physical diffusion, is as close of an estimate of the physical diffusion as possible. This technique has been demonstrated to produce quasi-second-order spatial accuracy for first order upwind schemes [321], with promising results also being demonstrated for second order schemes. This technique is particularly pertinent for upwind schemes considering the aforementioned discovery of Murillo et al. [331], that you cannot simultaneously enforce second order spatial accuracy for both the conserved variables and the solute concentration.

The computational efficiency of the scheme is also an important consideration since the addition of the capacity to model solute advection and diffusion increases the computational burden, with many applications also demanding long simulation durations. As a consequence, the stability of the scheme and the resulting restriction on the timestep is an important consideration. The choice of treatment of the source terms relating to the

diffusion of the solute is therefore a key consideration, with implicit treatment resulting in no further restriction of the timestep albeit requiring a potentially expensive iterative solution. The alternative is to use an explicit treatment which is computationally simpler but imposes a greater restriction on the timestep. Techniques which expand the region of stability, such as [329], are also valuable tools. Similarly, the sub step explicit resolution of the diffusion terms introduced by Morales-Hernández [321] prevents reduction of the time step for the shallow water system, enabling a more efficient computation for explicit treatment of the source terms in a decoupled scheme.

In the majority of cases, the advection-diffusion equations are considered to be hyperbolic under the assumption of dominant advection however, the advection-diffusion(-reaction) equations are in fact parabolic in nature. Montecinos and Toro [320] address this by using Cattaneo's relaxation approach [91] to reformulate the system into a hyperbolic system with stiff sources. In Vanzo et al. [456], this technique can be seen to produce a scheme with a favourable stability range, producing robust second order accurate approximations. The assumption of dominant advection is suitable for most common applications in which the shallow water assumptions also hold, such as pollutant spills in rivers or fertigation applications, however, the more rigorous treatment of the equations provides a more robust and versatile solution. It should be noted however, that due to the potential for application specific complexities, the general application of a advection-diffusion model to specific scenarios may encounter challenges. For example, when considering applications involving meandering channels, spiral motion induced by an imbalance of centripetal and pressure forces becomes an important consideration as shown in Caleffi and Valiani [85]. Another example of a problem specific modification is provided by Cea and Vázquez-Cendón [94], who demonstrate that for applications involving rainfall runoff, a well-balanced discretisation of the friction source terms, in addition to the topographic source terms, is required. This demonstrates the challenges involved in developing a general model for simulating advection-diffusion.

The aim of this paper is to complement the outlined advances with the derivation of a method to handle the interaction between shallow water flows, dissolved solutes and partial obstructions to flow, which has seldom been explored within academic literature. As such, presented within this article is a newly developed numerical method, which builds upon the work presented by Mckenna et al. [302], which details a method for modelling partial barriers to flow within one- or two-dimensional hydrodynamic models. In [302] a local implementation of a multi-layer shallow water model is used to capture fluid-structure interactions. Within this publication, further development of the model, in order to add the capability to model the advection and diffusion of a well-mixed dissolved solute, is outlined and experimentally validated. This capability is particularly relevant to urban and riverine environments which usually contain a number of the aforementioned barriers such as bridges, weirs and gates. The flexibility of the method also enables the modelling of complex barrier geometries including natural flood risk management solutions such as leaky barriers.

The proposed numerical method utilises the same local multi-layer approach to modelling interactions between shallow water flows and obstructions as presented in [302], with modifications to the conservation laws implemented to augment species equations describing the advection and diffusion of passive scalars. As a consequence, Harten-Lax-van Leer Contact (HLLC) [435], as opposed to Harten-Lax-van Leer (HLL) [212], approximate Riemann solvers are utilised within the structure cells in order to resolve the numerical

fluxes for the depth-averaged solute mass across the restored contact discontinuity wave. The predictive capacity of the model is validated via experiments conducted in a state-of-the-art hydraulic flume. These validation experiments consisted of planar concentration analyses (PCA), based upon the methodologies presented by [23, 386], whereby the scattering and absorption of incident light by an injected dissolved fluorescent tracer mass enables the nonintrusive determination of the fieldwise concentration for the duration of the experiment.

5.2 Mathematical Model

As described in [302] the computational domain is divided into normal cells, intermediate cells and structure cells, with corresponding normal interfaces (NI), intermediate interfaces (II) and structure interfaces (SI) as shown in Figure 5.1.

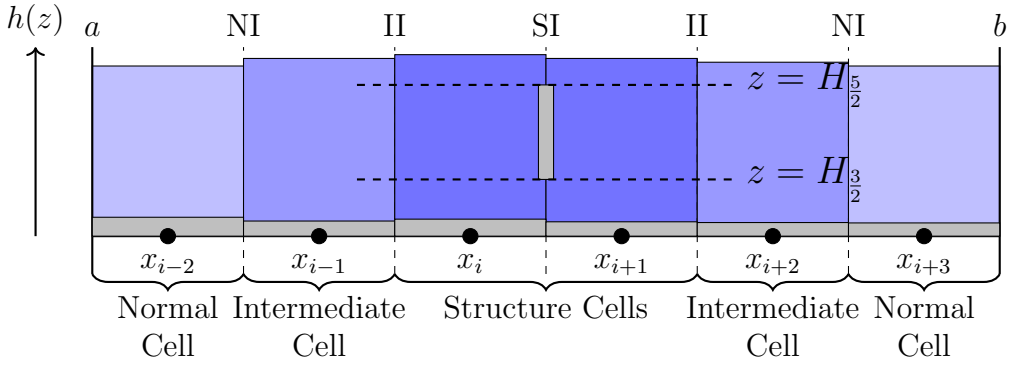

Figure 5.1: A simple computational domain $[a, b]$ with variable bed topography illustrating the designation of structure, intermediate and normal cells with their corresponding interfaces. $H_{3/2}$ and $H_{5/2}$ represent the elevation of the base and cover of the idealised structure represented at the structure interface.

The mathematical model for the normal and intermediate cells is derived by augmenting the two-dimensional shallow water equations with an additional species equation describing the transport of a passive scalar:

$$\partial_t \mathbf{U} + \partial_x \mathbf{F}(\mathbf{U}) + \partial_y \mathbf{G}(\mathbf{U}) = \mathbf{S}(\mathbf{U}) \tag{5.1}$$

Where $\mathbf{U}$ is the vector of conserved variables, $\mathbf{F}(\mathbf{U})$ and $\mathbf{G}(\mathbf{U})$ are the vector of fluxes in the x and y directions and $\mathbf{S}(\mathbf{U})$ is a vector of sources comprising of $\mathbf{S}_0$, the bed slope source term, $\mathbf{S}_f$, the bed friction source term and $\mathbf{S}_D$, the dispersion-diffusion source term. These terms are given as follows:

$$\mathbf{U} = \begin{bmatrix} h \\ hu \\ hv \\ h\psi \end{bmatrix} \quad , \quad \mathbf{F} = \begin{bmatrix} hu \\ hu^2 + \frac{1}{2}gh^2 \\ huv \\ hu\psi \end{bmatrix} \quad , \quad \mathbf{G} = \begin{bmatrix} hv \\ huv \\ hv^2 + \frac{1}{2}gh^2 \\ hv\psi \end{bmatrix} \tag{5.2}$$

$$\mathbf{S}_0 = \begin{bmatrix} 0 \\ -gh\partial_x z \\ -gh\partial_y z \\ 0 \end{bmatrix} \quad , \quad \mathbf{S}_f = \begin{bmatrix} 0 \\ \tau_{f,x} \\ \tau_{f,y} \\ 0 \end{bmatrix} \quad , \tag{5.3}$$

$$\mathbf{S}_D = \begin{bmatrix} 0 \\ 0 \\ 0 \\ \partial_x \left(hD_{xx}\partial_x\psi + hD_{xy}\partial_y\psi \right) + \partial_y \left(hD_{yx}\partial_x\psi + hD_{yy}\partial_y\psi \right) + \psi_s \end{bmatrix} \tag{5.4}$$

The conserved variables are h which denotes the depth of flow, u which denotes the velocity component in the x direction, v which denotes the velocity component in the y direction and ψ which represents the depth-averaged concentration of a solute. Within the topographic source term, $\mathbf{S}_0$, g is the acceleration due to gravity and z is the elevation of the bed measured from a fixed reference elevation. Within the bed friction source term, $\mathbf{S}_f$, $\tau_{f,x}$ and $\tau_{f,y}$ represent the x and y components of the shear stress at the bed, defined in accordance with Manning's equation:

$$\begin{cases} \tau_{f,x} = \dfrac{-ghq_x}{|\mathbf{q}|} \left(\dfrac{n^2 |\mathbf{q}|^2}{h^{\frac{10}{3}}} \right) = -C_f u |\mathbf{u}| \\ \tau_{f,y} = \dfrac{-ghq_y}{|\mathbf{q}|} \left(\dfrac{n^2 |\mathbf{q}|^2}{h^{\frac{10}{3}}} \right) = -C_f v |\mathbf{u}| \end{cases} \tag{5.5}$$

Where n is Manning's roughness coefficient, $|\mathbf{q}|$ is the modulus of the discharge vector $\mathbf{q} = (q_x, q_y)^T$, where $q_x = hu$ and $q_y = hv$ are the respective x and y components, $|\mathbf{u}|$ is the modulus of the velocity vector $\mathbf{u} = (u, v)^T$ and C_f is the Manning's bed friction coefficient:

$$|\mathbf{q}| = \sqrt{q_x^2 + q_y^2} = \sqrt{(hu)^2 + (hv)^2} \quad , \quad |\mathbf{u}| = \sqrt{u^2 + v^2} \quad , \quad C_f = \frac{gn^2}{h^{\frac{1}{3}}}$$

Within the dispersion-diffusion source term, $\mathbf{S}_D$, D_{xx}, D_{xy}, D_{yx} and D_{yy} are the turbulent mixing components of the tensor-rotated dispersion-diffusion tensor of depth averaged mixing [364]:

$$\begin{cases} D_{xx} = \dfrac{\sqrt{g}h \left(\epsilon_l u^2 + \epsilon_t v^2 \right)}{C_z \sqrt{u^2 + v^2}} \\ D_{xy} = D_{yx} = \dfrac{\sqrt{g}h \left(\epsilon_l - \epsilon_t \right) uv}{C_z \sqrt{u^2 + v^2}} \\ D_{yy} = \dfrac{\sqrt{g}h \left(\epsilon_l v^2 + \epsilon_t u^2 \right)}{C_z \sqrt{u^2 + v^2}} \end{cases} \tag{5.6}$$

where C_z is the Chezy coefficient defined, based upon the Manning equation, as:

$$C_z = \frac{h^{\frac{1}{6}}}{n} \tag{5.7}$$

ϵ_l is a dimensionless constant representing the longitudinal dispersion and ϵ_t is a dimensionless constant representing the turbulent diffusion. Elder [149] empirically estimated the values of these dimensionless constants as $\epsilon_l = 5.93$ and $\epsilon_t = 0.15$ for fully developed boundary layer flows in straight channels. As these dimensionless constants are influenced by the turbulence intensity of the flow, an application specific estimation is required in most cases. Within academic literature, there is a wealth of publications dedicated to the estimation of the longitudinal dispersion coefficients [7, 27, 37, 39, 38, 341]. The final term, ψ_s, represents a source or sink that contributes or removes solute such as naturally occurring pollutant decay or growth. Although the method is presented for a single pollutant species, it is trivial to extend the method to model a family of pollutant species via the addition of further transport equations.

5.2.1 Local Multi-Layer Model

In order to capture fluid structure interactions a modification of the local multi-layer model presented in [302] is employed within the structure cells:

$$\partial_t \mathbf{U}_k + \partial_x \mathbf{F}_k(\mathbf{U}_k) + \partial_y \mathbf{G}_k(\mathbf{U}_k) = \mathbf{S}_k(\mathbf{U}_k) \tag{5.8}$$

Where $\mathbf{U}_k$ is the vector of conserved variables for layer k, $\mathbf{F}(\mathbf{U}_k)$ and $\mathbf{G}(\mathbf{U}_k)$ are the vector of fluxes for layer k in the x and y directions and $\mathbf{S}_k(\mathbf{U}_k)$ is a vector of sources for layer k, comprising of $\mathbf{S}_{k,0}$, the topographic source terms for layer k, $\mathbf{S}_{k,f}$, the friction source terms for layer k and $\mathbf{S}_{k,D}$, the dispersion-diffusion source term for layer k. These vectors of conserved variables and fluxes are are given as follows:

$$\mathbf{U}_k = \begin{bmatrix} h_k \\ h_k u_k \\ h_k v_k \\ h_k \psi_k \end{bmatrix} \quad , \quad \mathbf{F}_k = \begin{bmatrix} h_k u_k \\ h_k u_k^2 + \frac{1}{2} g h_k^2 + g h_{k_{(+)}} h_k \\ h_k u_k v_k \\ h_k u_k \psi \end{bmatrix} \quad , \quad \mathbf{G}_k = \begin{bmatrix} h_k v_k \\ h_k u_k v_k \\ h_k v_k^2 + \frac{1}{2} g h_k^2 + g h_{k_{(+)}} h_k \\ h_k v_k \psi \end{bmatrix} \tag{5.9}$$

and the components of the vector of sources are given as:

$$\mathbf{S}_{k,0} = \begin{bmatrix} 0 \\ g h_{k_{(+)}} \partial_x z_{k+1/2} - g(h_{k_{(+)}} + h_k) \partial_x z_{k-1/2} \\ g h_{k_{(+)}} \partial_y z_{k+1/2} - g(h_{k_{(+)}} + h_k) \partial_y z_{k-1/2} \\ 0 \end{bmatrix} \tag{5.10}$$

$$\mathbf{S}_{k,f} = \begin{bmatrix} 0 \\ \tau_{k+\frac{1}{2},x} - \tau_{k-\frac{1}{2},x} \\ \tau_{k+\frac{1}{2},y} - \tau_{k-\frac{1}{2},y} \\ 0 \end{bmatrix} =$$

$$\begin{bmatrix} 0 \\ (1-\delta_{nk}) \left(\frac{2\nu(u_{k+1}-u_k)}{h_{k+1}+h_k} - K_{E,k+\frac{1}{2}} \right) - \left((1-\delta_{1k}) \left(\frac{2\nu(u_k-u_{k-1})}{h_k+h_{k-1}} - K_{E,k-\frac{1}{2}} \right) - \delta_{1k} C_f u_k \left| \mathbf{u}_k \right| \right) \\ (1-\delta_{nk}) \left(\frac{2\nu(v_{k+1}-v_k)}{h_{k+1}+h_k} - K_{E,k+\frac{1}{2}} \right) - \left((1-\delta_{1k}) \left(\frac{2\nu(v_k-v_{k-1})}{h_k+h_{k-1}} - K_{E,k-\frac{1}{2}} \right) - \delta_{1k} C_f v_k \left| \mathbf{u}_k \right| \right) \\ 0 \end{bmatrix} \tag{5.11}$$

$$\mathbf{S}_{k,D} = \begin{bmatrix} 0 \\ 0 \\ 0 \\ \partial_x \left(h_k D_{k,xx} \partial_x \psi + h_k D_{k,xy} \partial_y \psi_k \right) + \partial_y \left(h_k D_{k,yx} \partial_x \psi + h_k D_{k,yy} \partial_y \psi_k \right) + \psi_{k,s} \end{bmatrix} \tag{5.12}$$

Where k refers to the index of the layer under consideration, labelled in ascending order from layer 1 at the bed, to layer N at the free surface. $k+1/2$ and $k-1/2$ refer respectively to the upper and lower interface of the flow in layer k. The subscript $k_{(+)}$ refers to the properties of the flow above layer k where $h_{k_{(+)}}$ is defined as:

$$h_{k_{(+)}} = \sum_{j=k+1}^{N} h_j \tag{5.13}$$

The topographic sources are equal to $R_{k+1/2} - R_{k-1/2}$ which refer to the reaction forces exerted at the interfaces between the layers or bed, with $R_{k+1/2}$ denoting the reaction force of layer k onto the fluid above and $R_{k-1/2}$ denoting the reaction force exerted on layer k by the fluid or bed beneath it. $\tau_{k+1/2}$ and $\tau_{k-1/2}$ represent the interlayer turbulent friction effect induced at the upper and lower interfaces of layer k. The interlayer friction terms are derived for a multi-layer cell by applying a finite difference approximation, across the depth of the fluid layer k, to the Reynolds averaged stress component under the Boussinesq approximation [221]:

$$\begin{aligned}\int_{z_{k-\frac{1}{2}}}^{z_{k+\frac{1}{2}}} \frac{\partial}{\partial z}\left[2\nu\frac{\partial u}{\partial z} - K_E\right] dz &= \left(2\nu\frac{\partial u}{\partial z} - K_E\right)\Big|_{z_{k+\frac{1}{2}}} - \left(2\nu\frac{\partial u}{\partial z} - K_E\right)\Big|_{z_{k-\frac{1}{2}}} \\ \approx \frac{2\nu(u_{k+1}-u_k)}{h_{k+1}+h_k} - K_{E,k+\frac{1}{2}} - \frac{2\nu(u_k-u_{k-1})}{h_k+h_{k-1}} + K_{E,k-\frac{1}{2}} &= \tau_{k+\frac{1}{2},x} - \tau_{k-\frac{1}{2},x}\end{aligned} \tag{5.14}$$

$$\begin{aligned}\int_{z_{k-\frac{1}{2}}}^{z_{k+\frac{1}{2}}} \frac{\partial}{\partial z}\left[2\nu\frac{\partial v}{\partial z} - K_E\right] dz &= \left(2\nu\frac{\partial v}{\partial z} - K_E\right)\Big|_{z_{k+\frac{1}{2}}} - \left(2\nu\frac{\partial v}{\partial z} - K_E\right)\Big|_{z_{k-\frac{1}{2}}} \\ \approx \frac{2\nu(v_{k+1}-v_k)}{h_{k+1}+h_k} - K_{E,k+\frac{1}{2}} - \frac{2\nu(u_k-u_{k-1})}{h_k+h_{k-1}} + K_{E,k-\frac{1}{2}} &= \tau_{k+\frac{1}{2},y} - \tau_{k-\frac{1}{2},y}\end{aligned} \tag{5.15}$$

Where $\nu = \nu_l + \nu_t$, is the total effective viscosity equal to the laminar viscosity ν_l, which is a physical property of the fluid and ν_t, which is the depth-averaged turbulent viscosity. The depth-averaged turbulent viscosity is evaluated, based on the assumption of a logarithmic velocity profile whereby bed-generated turbulence dominates over free layer turbulence as proposed in [500]:

$$\nu_t = \frac{\kappa}{6} U_* H \tag{5.16}$$

where κ is the von Kármán constant equal to 0.4, H is the total depth of flow and U_* is the depth-averaged shear velocity, which is given by the following equation:

$$U_* = \frac{\sqrt{g(U^2+V^2)}}{C_z} = \frac{n\sqrt{g(U^2+V^2)}}{H^{\frac{1}{6}}} \tag{5.17}$$

where U and V and H represent the depth-averaged velocity in the x direction, depth-averaged velocity in the y direction and total depth for the whole multi-layer cell. K_E is the turbulent kinetic energy given as:

$$K_E = \frac{1}{2}\left(u'u' + v'v'\right) \tag{5.18}$$

where u' and v' denotes the variation of the velocity component about the mean value. $K_{E,k\pm1/2}$ in equations (5.14)-(5.15) therefore represents an approximation of the turbulent kinetic interface at the layer interfaces, approximated as:

$$\begin{aligned}K_{E,k+\frac{1}{2}} = \frac{1}{2}\left(u'_{k+\frac{1}{2}}u'_{k+\frac{1}{2}} + v'_{k+\frac{1}{2}}v'_{k+\frac{1}{2}}\right) = \\ \frac{1}{2}\left(\left(\frac{q_{k+1,x}+q_{k,x}}{h_{k+1}+h_k} - U\right)^2 + \left(\frac{q_{k+1,y}+q_{k,y}}{h_{k+1}+h_k} - V\right)^2\right)\end{aligned} \tag{5.19}$$

$$K_{E,k-\frac{1}{2}} = \frac{1}{2}\left(u'_{k-\frac{1}{2}}u'_{k-\frac{1}{2}} + v'_{k-\frac{1}{2}}v'_{k-\frac{1}{2}}\right) = \frac{1}{2}\left(\left(\frac{q_{k,x}+q_{k-1,x}}{h_k+h_{k-1}} - U\right)^2 + \left(\frac{q_{k,y}+q_{k-1,y}}{h_k+h_{k-1}} - V\right)^2\right) \quad (5.20)$$

For the case where $k = 1$, considering the layer which flows over the bed, $\tau_{k-1/2} = \tau_b$ which is instead derived from Manning's equation (5.5), where H is the total depth of flow for the whole structure cell. The particular form of the viscous effect on the base of the fluid layer, $\tau_{k-1/2}$, is accounted for by the Kronecker delta in (5.11), which is defined as:

$$\delta_{\alpha k} = \begin{cases} 1 \text{ if } k = \alpha \\ 0 \text{ if } k \neq \alpha \end{cases} \quad (5.21)$$

The Kronecker delta also ensures that $\tau_{N+1/2} = 0$, which corresponds to zero friction at the free surface. The depth-averaged mixing coefficients are also evaluated on a layer-by-layer basis:

$$\begin{cases} D_{k,xx} = \dfrac{\sqrt{g}h\left(\epsilon_l u_k^2 + \epsilon_t v_k^2\right)}{C\sqrt{u_k^2+v_k^2}} \\ D_{k,xy} = D_{k,yx} = \dfrac{\sqrt{g}h_k\left(\epsilon_l - \epsilon_t\right)u_k v_k}{C\sqrt{u_k^2+v_k^2}} \\ D_{k,yy} = \dfrac{\sqrt{g}h\left(\epsilon_l v_k^2 + \epsilon_t u_k^2\right)}{C\sqrt{u_k^2+v_k^2}} \end{cases} \quad (5.22)$$

5.3 Experimental Validation: Planar Concentration Analysis

As prior mentioned, the nonintrusive determination of the fieldwise concentration for the duration of the experiment is achieved via a planar concentration analysis (PCA), adapting the method of Arques et al. [23] and the hydro-optical theory presented by Rummel [386] and von Carmer [86]. Detailed references for more general hydro-optical theory are provided by Kondratyev and Filatov [248], Bukata et al. [82] and Arst [25].

5.3.1 Experimental Setup

The PCA was conducted in the S100 Research flume housed within the Novak Laboratory at Newcastle University. A detailed description of the flume, including error estimates for the electromagnetic flow meter are provided in Mckenna et al. [302]. Initial experiments were conducted to determine optimal barrier and flow rate configurations and the chosen configuration is presented in Figure 5.2. Two Sony SNC-VB770 cameras were mounted above the flume in order to capture the required footage, with each camera observing an area of the flume equal to approximately $1.20m$ x $1.00m$. Raw footage was captured at a maximum frame rate of 30Hz, producing frames of 3840 x 2160 pixels, shot in intelligent screen capture (low noise) mode. Unlike cameras which operate using charge-coupled devices (CCDs), which introduce spurious noise during the digitisation process [386], the modern $35mm$ full frame Exmor complementary metal-oxide-semiconductor (CMOS) sensor utilised by the Sony SNC-VB770 drastically reduces the signal-to-noise ratio. This

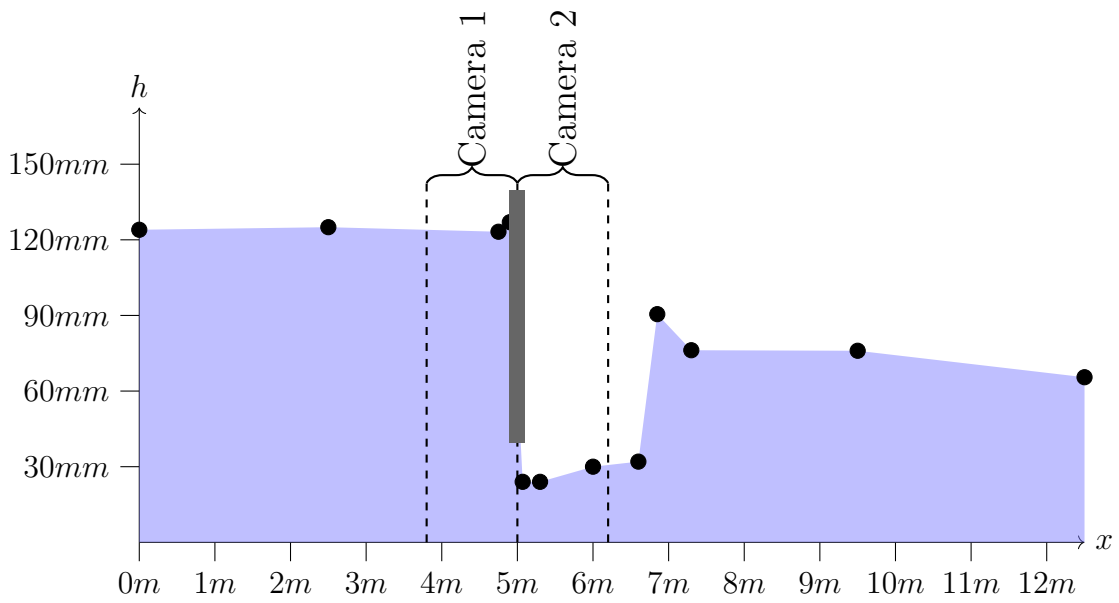

Figure 5.2: Sketch of the experimental setup for the planar concentration analysis. The flow rate is equal to $33ls^{-1}$ and the base of the barrier is at an elevation of $39.5mm$ above the flume bed. Black circles denote the average measured depths.

essentially eliminates the requirement to perform noise reduction post-processing techniques, such as time-averaging the outputs, increasing the temporal and spatial resolution of the final outputs. Since the primary focus is on the interaction of the flow and the dissolved solute with the barrier, placed $5m$ downstream from the inlet, the two measurement areas were centered around the barrier, with Camera 1 observing the upstream end and Camera 2 observing the downstream end, as shown in Figure 5.2.

As for the experiments detailed in Section 3.3 and Section 4.3, depth measurements were obtained using a vernier depth gauge. At each measurement point a maximum depth was observed via raising the depth gauge to the maximum elevation above the flume bed such that the tip of the gauge experiences temporary submergence. Conversely, minimum depth measurements were obtained by lowering the depth gauge to the minimum elevation above the flume bed such that the tip of the gauge is permanently submerged. Due to a lack of appropriate equipment for the measurement of the fluid velocity, the fluid velocity is derived from the flow rate, as measured by the electromagnetic flow meter, and the corresponding depth measurement. Hence, depth measurements were obtained with an absolute uncertainty of $\pm$1mm, with the difference between the maximum and minimum depth measurements being determined by the unsteadiness of the flow at the measurement point. A minimum and maximum velocity is therefore obtained considering the uncertainty in the respective measurements of the flow rate and the depth, from which the velocity is derived.

Rhodamine water tracing (WT) dye, was selected as the conservative tracer, procured in the form of a 20% solution in water. As a result, an array of six 50W LED arrays were used to illuminate the flume with green light ($555-585nm$), since this specific wavelength range aligns with the peak of the emission spectrum for Rhodamine WT [374, 378, 411]. Although efforts were made to ensure a uniform illumination of the flume, perfectly homogeneous illumination is essentially impossible in practice [86], especially since the use

of a light diffuser was deemed too impractical within the constraints of the laboratory. To account for the inhomogeneities in the incident irradiance, a calibration process was performed in order to derive the spatial dependency of the photometric response for known, well mixed, concentrations, such that a transfer algorithm may be defined to enable conversion between the observed intensity of the upwelling irradiance and the concentration of the tracer. A camera calibration process was also conducted in order to eliminate lens distortion. A detailed description of the calibration process is provided in Section 5.3.1. It should be noted that since Rhodamine WT was obtained in 20% aqueous form, concentrations hereafter refer to the concentration of the 20% aqueous solution, not pure Rhodamine WT.

For each experiment, injections of diluted Rhodamine WT solution were manually performed, using a micropipette, to simulate the instantaneous release of a pollutant slug. Injections were performed approximately $4.5m$ upstream of the measurement area to ensure that the dye had sufficient time to vertically well-mix and satisfy the depth-averaged assumptions of the numerical model and the calibration process.

Calibration

In order to perform the camera calibration process, machine vision algorithms provided by Open Computer Vision (OpenCV) [74] were used to identify the corners of a chessboard pattern placed at the corresponding water surface height for each camera frame. Since the distance between the chessboard corners is uniform and known, this enables the definition of a new *camera matrix*. The new *camera matrix* is obtained via OpenCV's undistort method, whereby the new *camera matrix* represents a geometric transformation, with bilinear interpolation used to estimate pixel values at non-integer coordinates, that can be applied to all subsequent frames to remove the effect of lens distortion. Through alignment of the northern chessboard edge with the wall of the flume and the respective western (for Camera 1) and eastern (for Camera 2) edges with the barrier slot, a coordinate system can be defined for each of the cameras. Following detection of the corners and application of the new *camera matrix*, horizontal lines of best fit are then drawn through the undistorted corner coordinates in both cardinal directions, as shown in Figure 5.3, which can then be used to rotate the image such that it is aligned with the direction of flow.

The mean error in the transformation process is estimated using the re-projection error, which is calculated by comparing the image points obtained by the corner detection algorithm and the points obtained using the known three-dimensional objects points:

$$\epsilon = \frac{1}{n_{proj}} \sum_{j=1}^{n} ||p_{proj} - p_{img}||_2 \tag{5.23}$$

$$\epsilon_{avg} = \frac{1}{n} \sum_{k=1}^{n} \epsilon_k \tag{5.24}$$

ϵ_{avg} was calculated as 0.036 pixels for Camera 1 and 0.027 pixels for Camera 2. The accuracy of the transformation process can be further verified using the average coefficient of determination, R^2, for the vertical (R_y^2) and horizontal (R_x^2) lines drawn through the

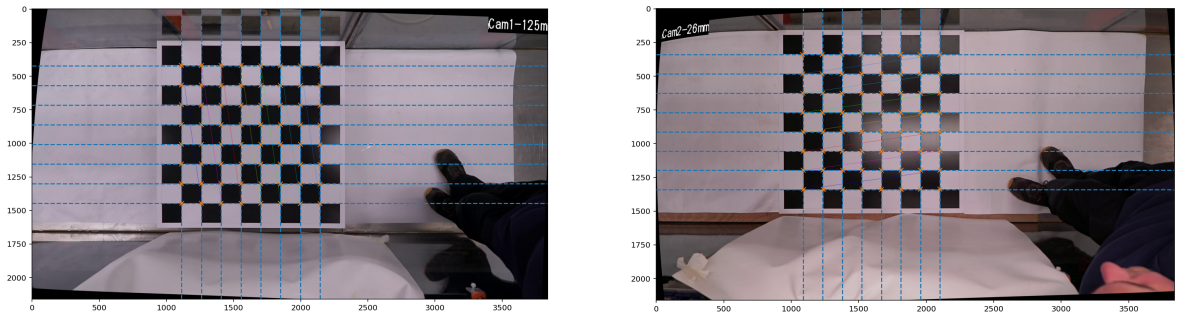

(a) Camera 1 (b) Camera 2

Figure 5.3: Undistorted and rotated camera frames for Camera 1 (Figure 5.3a) and Camera 2 (Figure 5.3b) following the identification of the corners of the chessboard pattern and definition of a new camera matrix. Units for the axes are pixels. A white background was utilised to assist the machine vision algorithm in accurately determining the corner locations.

undistorted corner coordinates:

$$\text{Camera 1} : \begin{cases} R_x^2 = 0.999999 \\ R_y^2 = 0.999992 \end{cases} \quad , \quad \text{Camera 2} : \begin{cases} R_x^2 = 0.999979 \\ R_y^2 = 0.999998 \end{cases} \tag{5.25}$$

In order to account for the spatial inhomogeneity of the incident irradiance, a second calibration process is required in order to define a transfer algorithm, enabling conversion between the observed green light intensity of each pixel(s) and the corresponding solute concentration. The first step in this process is to hydraulically isolate the areas observed by each camera. Under the established experimental illumination conditions, which must be maintained thereafter, the spatial calibration process is then performed by first filling the respective hydraulically isolated calibration zones with water, to the average depth of the flow in that region (see Figure 5.2). Through the sequential recording of the calibration zones and subsequent addition of Rhodamine WT, which must be well mixed to ensure homogeneity, a relationship between the known discrete concentration values and the measured green light intensity can be obtained, referred to as the photometric response. Since the photometric response is dependent on the depth of flow, it was therefore necessary to select a flow rate and barrier configuration that produced near constant depths within the observed regions of the flow (Figure 5.2). The spatial variation in the median observed green light intensity for each of the nine calibration concentrations for both cameras is provided in A.6.1-A.7.10. This data is used to define a calibration matrix, $G_{cal}(c_i, x, y)$, which enables conversion between from the measured monochromatic luminance, $G(x, y)$, into a depth-averaged solute concentration, $c(x, y)$.

An initial cropping of the observed domain for each camera is performed to eliminate areas contaminated by shadows introduced by the hydraulic isolation of the calibration zones, as shown in Figure 5.4. Since the hydraulic isolation of the individual calibration zones requires sealing the central barrier, the calibration of the immediate upstream and downstream zones is also compromised since the experimental illumination conditions, once the barrier is raised, do not correspond to the illumination conditions for the calibration process.

The ideal calibration process would be to sequentially mix the entire volume of the sump

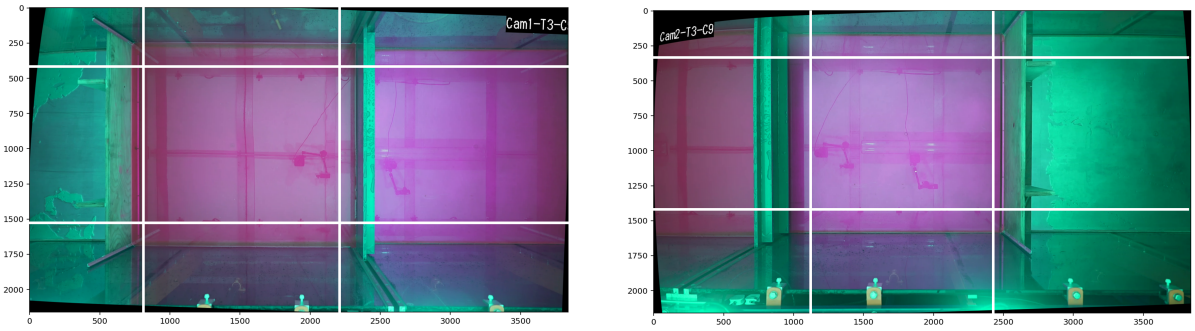

(a) Camera 1 (b) Camera 2

Figure 5.4: Figure 5.4a and Figure 5.4b illustrate the cropped area, via the superimposed white lines, for the planar concentration analysis. The area of the cropped frame for Camera 1 is $0.95m \times 0.76m = 0.722m^2$. The area of the cropped frame for Camera 2 is $0.9m \times 0.76m = 0.684m^2$.

to the desired calibration concentrations, performing the calibration recordings under the pre-defined flume configuration. This would result in the highest consistency of illumination conditions with the additional benefit of removing incongruencies resulting from the differing hydro-optical behaviour of a stationary fluid and the variations in the depth. Incongruencies in the hydro-optical behaviour of a stationary fluid are demonstrated within Figure 5.4 and A.6.1-A.7.10, where the presence of strong surface reflections emerge as the concentration increases. For a fluid in motion, the small variations in the free surface of the flow disturbs and distorts these surface reflections resulting in a reduced validity of the calibrated photometric response for higher concentrations. Similar effects are induced by the rippling motion of the free surface immediately upstream of the barrier and the random turbulent fluctuations in the flow immediately downstream of the barrier. Further errors may be introduced during the mixing process, as the oil based sealant, used to ensure water-tight hydraulic isolation, may be disturbed and contribute to thin-film interference of the incident light [324]. However, performing the calibration in this manner is essentially impossible in practice since the variable velocity of the flow within the flume would result in non-uniform concentrations which cannot be accurately determined. A more feasible dynamic calibration involves removing the barrier and operating the flume at a constant flow rate which produces a depth of flow corresponding to the average upstream depth, then repeating the process for the average downstream depth. However, this would still necessitate cropping the area immediately surrounding where the barrier is placed and wouldn't capture the intricate flow characteristics that occur in the presence of the barrier during the experiment. There are also significant practical challenges to consider:

1. Accurate estimation of the volume of fluid contained within the sump and consequently the calibration concentrations is complicated by the presence of leaks. Although accurate measurement of the initial fluid volume could be achieved via filling of the sump through a water meter.

2. The required volume of Rhodamine WT is potentially cost-inefficient with the process required to ensure homogeneous mixing being time-inefficient.

3. Following the calibration process, the sump must be emptied and replaced meaning that the experiment cannot be conducted within a single working day and as a result,

the exact maintenance of illumination conditions is more challenging. Furthermore, when subjected to experimental illumination conditions for long durations, the photolysis of Rhodamine WT introduces errors in the estimation of the concentration [425].

As such, calibration via hydraulic isolation provides a satisfactory balance of accuracy and practical feasibility.

The transfer algorithm is initialised by spatially averaging the pixels, via grouping into cells, and applying a hydro-optical model to the photometric response for each cell, as shown in Figure 5.5. The the mathematical form of the curve fitted to the calibration

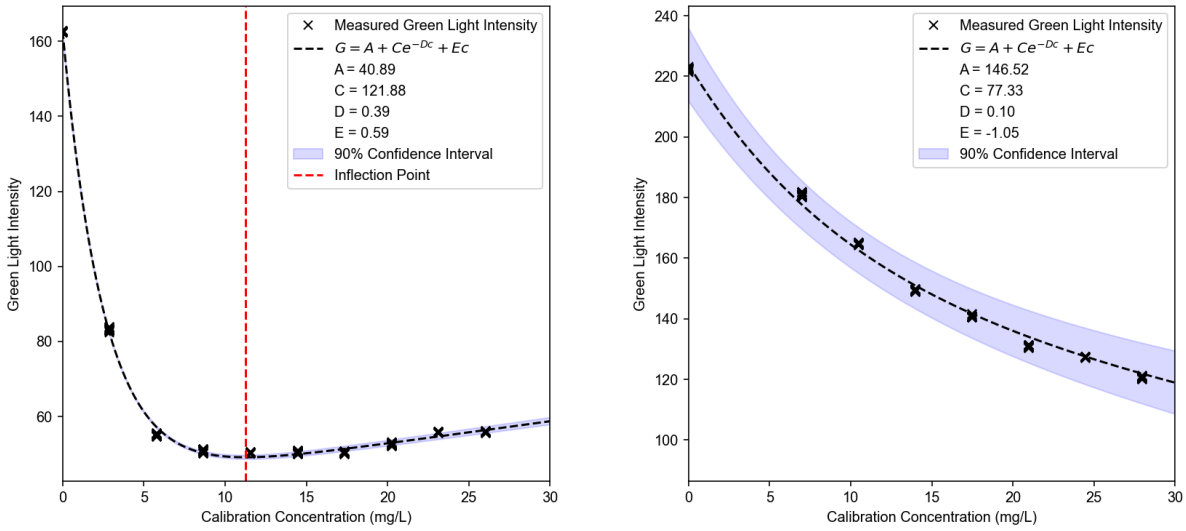

(a) Camera 1

(b) Camera 2

Figure 5.5: Sample photometric responses for Camera 1 (Figure 5.5a) and Camera 2 (Figure 5.5b). Multiple monochromatic luminance intensities are recorded for each calibration concentration and the 10% most extreme values are filtered. As shown by the tight grouping of the measurements for each calibration concentration, the variance in the measurements is small.

data is derived from optical principals, based upon the hydro-optical model presented by Rummel et al. [386]:

$$G = f(c) = A + Ce^{-Dc} + Ec \tag{5.26}$$

where, G denotes the monochromatic luminance intensity, which is a function of the depth averaged concentration c. $A + C$ represents the green light intensity for which the concentration of Rhodamine WT is zero and A corresponds to the saturation of Rhodamine WT which results in no further scattering of incident light. e^{-Dc} reflects the attenuation of incident light assuming homogeneous concentration along the optical path. D describes the scattering of incident light and Ec embeds the reflection at the water surface, with E being the reflectivity of the water. The error compensation term, B, introduced by Rummel et al. [386] is dropped in this case since it yields a value of zero provided the distribution of calibration points is optimal. For a less optimal distribution of calibration points, a curve of the form $G = A + (Bc + C)e^{-Dc} + Ec$ should be used. The process used to determine the parameters of the the hydro-optical model fitted to the calibrated photometric response for each cell is outlined in Algorithm 4. Analysis of

the value of E, denoting the reflectivity of the water, for each cell, as shown in Figure 5.6, demonstrates that the deeper upstream depth of water produces a positive value of E, whereas, the shallower downstream depths produce a negative value of E. Within the plots, the surface reflections of ceiling features and the cameras and their mounts can be discerned.

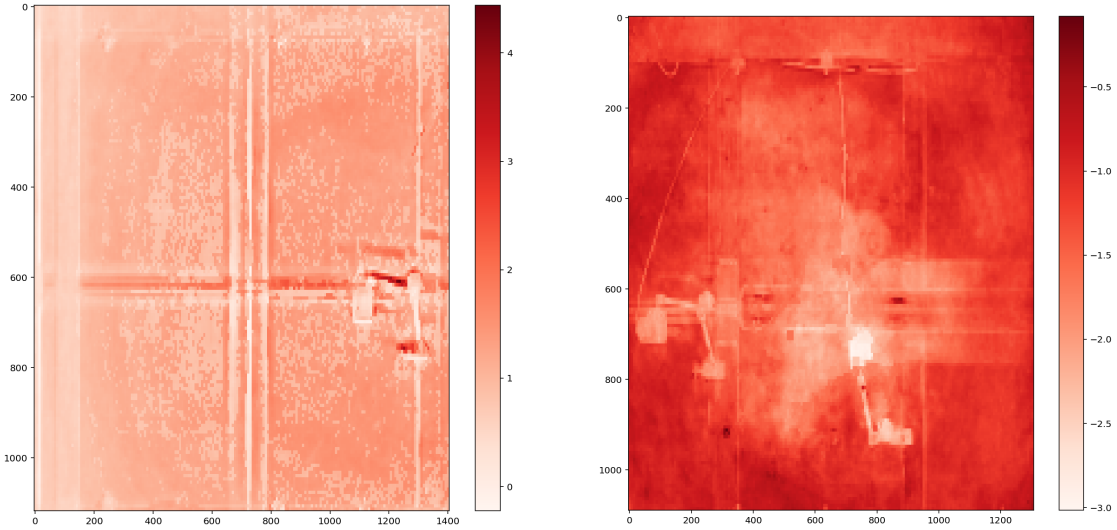

(a) Camera 1 (b) Camera 2

Figure 5.6: The spatial variation in the calibrated value of E for each cell, which denotes the reflectivity of the water. The upstream calibration produces optimised values of $E \geq 0$ whereas, the downstream calibration produces optimised values of $E \leq 0$.

As a consequence of the positivity of E for the upstream calibration, the upstream calibration curves are non-monotonic, resulting in an ill-posed transfer algorithm. To ensure that the transfer algorithm is well-posed the maximum observed concentration must be restricted to the monotonic subdomain $[0, c_{ip}^{min}]$, where c_{ip}^{min} is the smallest upstream cell concentration value corresponding to the inflection point:

$$c_{ip} = \frac{\log(DC) - \log(E)}{D} \tag{5.27}$$

For this analysis the maximum permissible concentration value was determined to be equal to $10.01 mg/L$. Due to this restriction, it is imperative to ensure strong agreement between the measured green light intensity for $0 mg/L$ of Rhodamine WT and the y-intercept of each curve. Algorithm 4 achieves this by using a penalisation technique to ensure that the y-intercept of the curve lies within the range of the filtered measured intensities. After initial optimisation of the curve parameters to fit the data, a comparison between the y-intercept of the curve, equal to $A + C$, and the filtered green light intensities for a concentration of $0 mg/L$ is performed. If the y-intercept does not lie within the range of the corresponding filtered green light intensities then an attempt is made to refine the curve parameters. A residual function is defined as follows:

$$\epsilon(G, c, x, y) = G(x, y) - (A_0 + C_0 e^{-D_0 c(x,y)} + E_0 c(x, y)) - p \tag{5.28}$$

where G is an observed green light intensity for a concentration of $0 mg/L$, $A_0 + C_0 e^{-D_0 c(x,y)} + E_0 c(x, y)$ is the initial optimisation of the hydro-optical model and p is a penalisation defined as $p = k(A_0 + C_0 - G_0)$ where $A_0 + C_0$ is the y-intercept of the initial curve, G_0 is

the median of the filtered green light intensities for a concentration of $0mg/L$ and k is a constant used to scale the weighting of the penalisation on the calculation of the residual error. A value of $k = 100$ was empirically determined to produce satisfactory results for this specific PCA configuration. A new optimisation is then performed in order to fit the residual function to the photometric response data before finally applying a least squares regression to further refine the parameters.

In order to reduce the impact of strong surface reflections, which tend to produce greater residual errors in the fitting process, a spatial smoothing is introduced using a second pass of Algorithm 4 which is performed for cells with residuals errors above a threshold value. In this second attempt at fitting a hydro-optical model to the photometric response, the photometric response data from the eight surrounding cells is used. This process reduces the spatial resolution of the response data for the selected cells in order to provide a larger sample of measurements, which are ideally unaffected by the same surface reflections, in an attempt to smooth sharp discontinuities in the optical response produced by the surface reflections of the cameras, camera mounts and ceiling beams. Although this does reduce the spatial accuracy of the photometric response of the selected cells, the cells are of sufficient resolution such that the difference in optical path to the neighbouring cells is minimal. The time-averaging process used by Arques et al. [23] to filter direct reflections was found to be ineffective in this case, potentially as a result of insufficient motion of the water surface during the calibration process. As noted by Arques et al., direct surface reflections are a major source of error when performing a PCA and require careful management.

The results of the application of Algorithm 4 are shown in Figure 5.7, whereby red denotes cells for which the spatial smoothing was applied. The spatial smoothing process is applied to the cells with residuals in the 85th percentile and above and it can be seen that for Camera 1, the spatial distribution of these cells corresponds to the location of the surface reflections. For Camera 2, which exhibits a negative reflectivity, the surface reflections have a minor effect. Nonetheless, the smoothing process is still applied in order to improve the quality of the curve fitting process for the cells with the largest residuals.

Via experimentation it was determined that a cell size of approximately 50 pixels, equating to an area of approximately $5mm^2$ provided the greatest accuracy. If the cell size is too large then the spatially varied photometric response for the pixels contained within the cell may not be well captured by the spatially averaged output and the resolution of the final outputs may also be inadequate. If the cell size is reduced too much, it can result in an inadequate number of pixels within each cell in order to perform an effective spatial averaging and filtering of the data to remove spurious measurements. Further refinement also reduces the effectiveness of the smoothing process, since the scale of the cells may be too small relative to the scale of the reflections, resulting in a suboptimal spatial averaging process when only utilising the data from the neighbouring cells. A viable alternative approach would be to search for viable nearest neighbouring cells, restricting the search to within a permissible maximum distance, rather than just the immediate neighbours. (A.8) illustrates the cell-wise residual errors for cell sizes of $10mm$, $5mm$ and $2mm$.

Completion of the transfer algorithm is achieved via the calculation of a time-averaged background concentration for each cell, measured immediately prior to the injection of the Rhodamine WT for each experiment. As shown in Figure 5.8b, the background con-

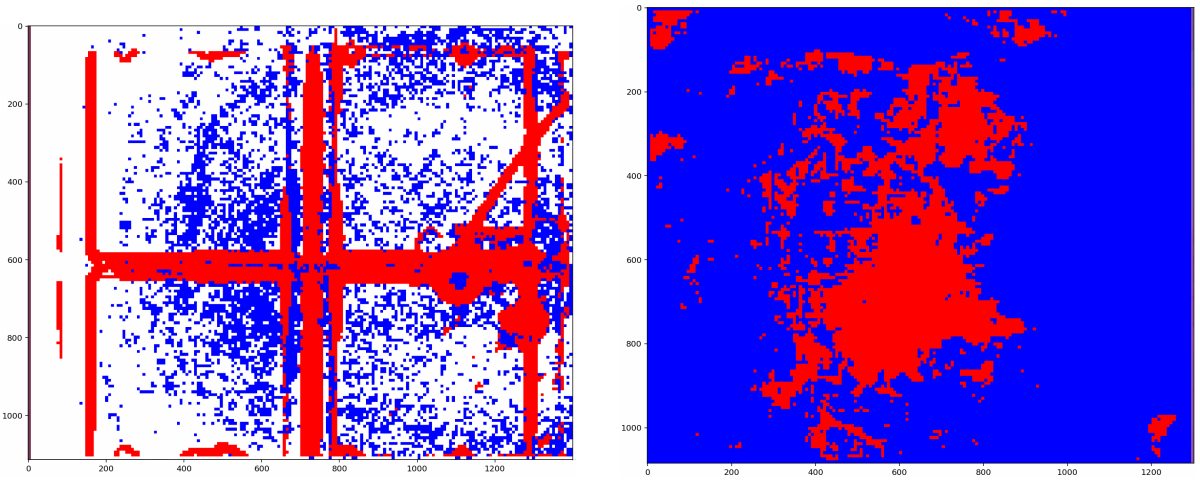

(a) Camera 1 (b) Camera 2

Figure 5.7: Colour map detailing the application of Algorithm 4 to optimise the parameters of a hydro-optical model in accordance with the calibrated photometric response for each cell. White cells correspond to the cells in which the initial optimisation of the parameters resulted in a suitable fit. Blue cells denote cells which required penalisation to ensure satisfactory agreement of the y-intercept. Red cells denote the cells for which spatial smoothing was applied.

centration is subtracted from the derived raw concentration value. This is a necessary process since the flume operates in a closed circuit configuration, in which the pumps draw from the same sump that the flume outflows into. Since the duration of each experiment ($\approx 10 - 15s$) is significantly shorter than the recirculation time the subtraction of the background concentration avoids the requirement to drain the sump following each experiment. Furthermore, the considerable volume of water contained within the sump ($\approx 95m^3$) compared to the total volume of Rhodamine WT used during each experiment (on the order of mL), ensures that background concentrations remain negligible. The calculated background concentration levels for the two experiments are presented in A.9.

The synchronisation of the cameras, to the nearest frame, is achieved via the flash of torch within the mutually observed area directly above the barrier. This process is demonstrated within Figure 5.9.

Algorithm 4 Definition of the transfer algorithm and application of the hydro-optical model to the measured photometric response. A penalisation process is used to ensure agreement between the measured y-intercept for the photometric response and the optimised hydro-optical model. In the event that the hydro-optical model does not sufficiently fit the measured data, a piecewise linear interpolation is used. The optimisation functions from the SciPy library [471] are used to optimise the model parameters.

$\epsilon_{\max} \leftarrow 10^6$ ▷ Maximum permissible residual error
$k \leftarrow 10^2$ ▷ Penalisation weighting factor
for all cells **do**
    $Gs \leftarrow [G_0, G_1, ..., G_N]$ ▷ G_i contains the measured intensities for calibration i of N total
    $Cs \leftarrow [c_0, c_1, ..., c_N]$ ▷ c_i is the calibration concentration for calibration i of N total

    $A, C, D, E \leftarrow$ scipy.optimize.curve_fit ▷ Fit $G = A + Ce^{Dc} + Ec$ to $G = Gs$, $c = Cs$
    $\epsilon \leftarrow$ residuals ▷ Initial curve fit error estimation
    $y_0 \leftarrow A + C$ ▷ y-intercept for initial curve

    if $min(G_0) \leq y_0 \leq max(G_0)$ **then** ▷ If the y-intercept falls within the measured intensities
        pass
    else ▷ If the y-intercept doesn't fall within the measured intensities
        $p \leftarrow k\,|y_0 - \text{median}(G_0)|$ ▷ Define a penalisation to force curve fitting through y-intercept
        function PENALISED_RESIDUALS(G_i, c_i, A, C, D, E) ▷ Define a penalised residual function
            Return$(G_i - (A + Ce^{Dc_i} + Ec_i) - p)$
        end function
        $A, C, D, E \leftarrow$ scipy.optimise.curve_fit ▷ Fit penalised residual function to $G = Gs$, $c = Cs$
        $A, C, D, E \leftarrow$ scipy.optimise.leastsq ▷ Least squares regression to refine parameters
        $\epsilon \leftarrow$ residuals ▷ Refined curve fit error estimation
    end if

    if $\epsilon \leq \epsilon_{\max}$ **then**
        curve $\leftarrow A + Ce^{Dc} + Ec$ ▷ Apply optimised parameters for hydro-optical model
    else
        curve $\leftarrow$ scipy.interpolate.interp1d ▷ Fit a piecewise linear interpolated curve
    end if
end for

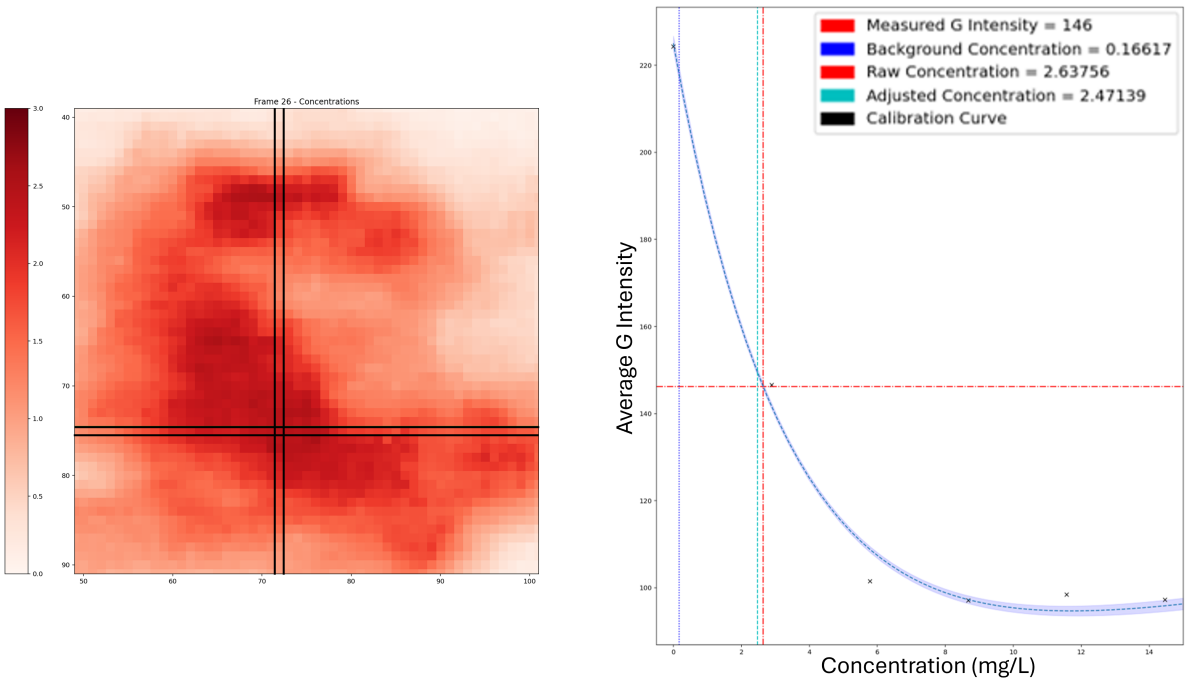

(a) Concentration Map

(b) Photometric Response

Figure 5.8: Figure 5.8a shows a concentration map derived from the transfer algorithm. For the cell highlighted using the black lines superimposed on Figure 5.8a, Figure 5.8b demonstrates how the concentration value is derived from the photometric response by the transfer algorithm. The measured average green light intensity is converted into a raw concentration value using the hydro-optical model (line of best fit). The background concentration, recorded before the injection is performed, is then subtracted from the raw concentration value, to determine the concentration value.

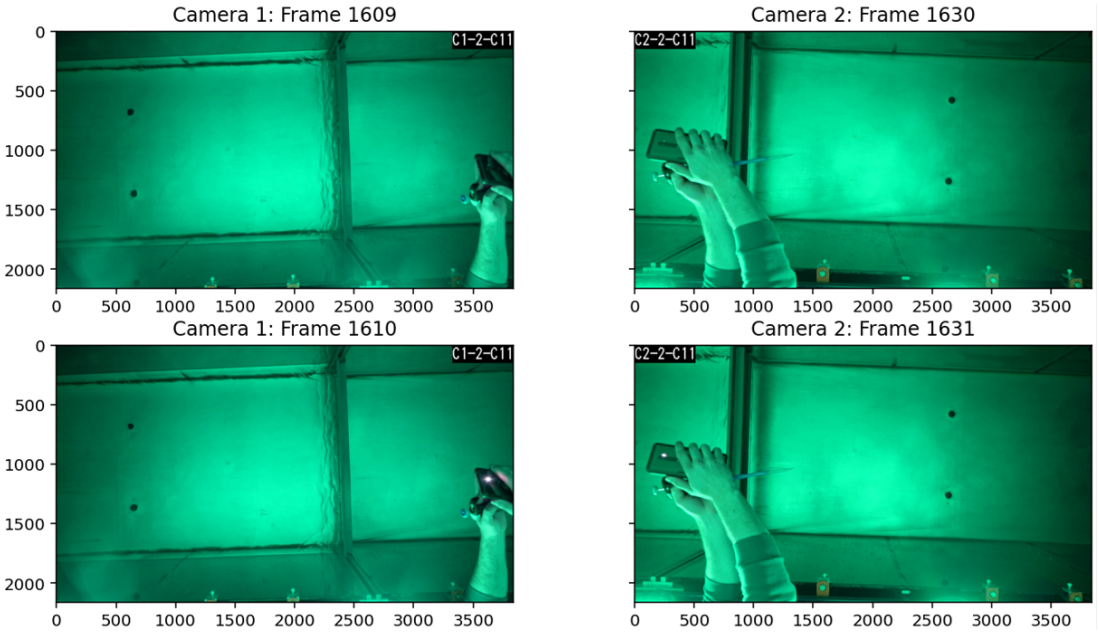

(a) Camera 1 (b) Camera 2

Figure 5.9: Synchronisation of the cameras via the flashing of a torch light. The left frames correspond to Camera 1 and the right frames correspond to Camera 2. The frames are presented in chronological order from top to bottom, with the bottom left and right frames showing the first frame in which the torch flash is visible for both cameras.

5.3.2 Analysis

As proposed by Arques et al. [23], a temporal averaging process is applied throughout the analysis to filter spurious measurements such as camera noise and direct surface reflections. Via experimentation, it was determined that averaging over 3 consecutive frames ($0.1s$) resulted in the optimal results. In this regard, the noise reduction technology provided by the Exmor CMOS sensors provides an advantage in terms of the maximum temporal resolution of the final outputs, since longer duration time-averaging of the results is required for cameras utilising sensors with a higher signal to noise ratio. Similarly, a higher frame rate would have been beneficial. In total sixteen experiments were conducted, with each pair of experiments consisting of the injection of a decreasing concentration of Rhodamine WT. Since observed upstream concentrations are required to be bounded by the maximum permissible concentration of $10.01mg/L$, to ensure a well posed transfer algorithm, the two experiments in which a $10 \pm 1mL$ slug injection of $1500 \pm 80.5mg/L$ Rhodamine WT solution, referred to hereafter as Experiment 1 and Experiment 2, are selected as the most suitable validation data sets. Lower concentrations result in a higher measurement sensitivity since the gradient of the photometric response is larger however, as the concentration values become smaller the proportion of the measurements comprising of noise increases. The selected experiments provide the greatest compromise between these competing considerations within the provided maximum concentration constraints.

Final Outputs

Figures 5.10-5.15, present snapshots of the concentration maps derived from the PCA analysis for Experiment 1 and Experiment 2 at times $2.5s$, $4s$ and $5s$.

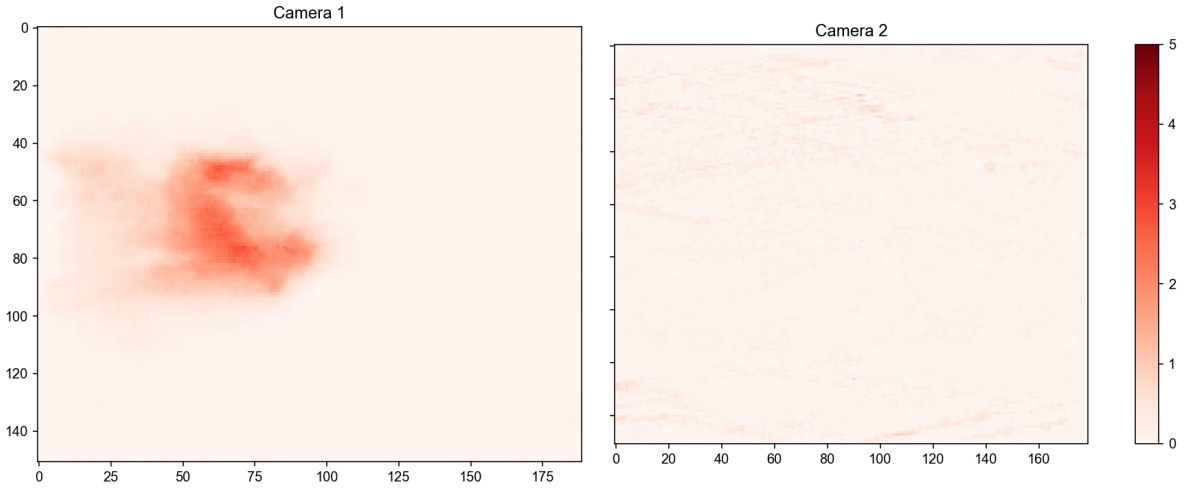

Figure 5.10: PCA output for Experiment 1 at $t = 2.5s$. The colour map corresponds to the spatial distribution of the Rhodamine WT solution concentration (mg/L), as per the colour bar on the right hand side. Small erroneous measurements can be observed for Camera 2 due to the emergence of turbulent disturbances downstream of the barrier.

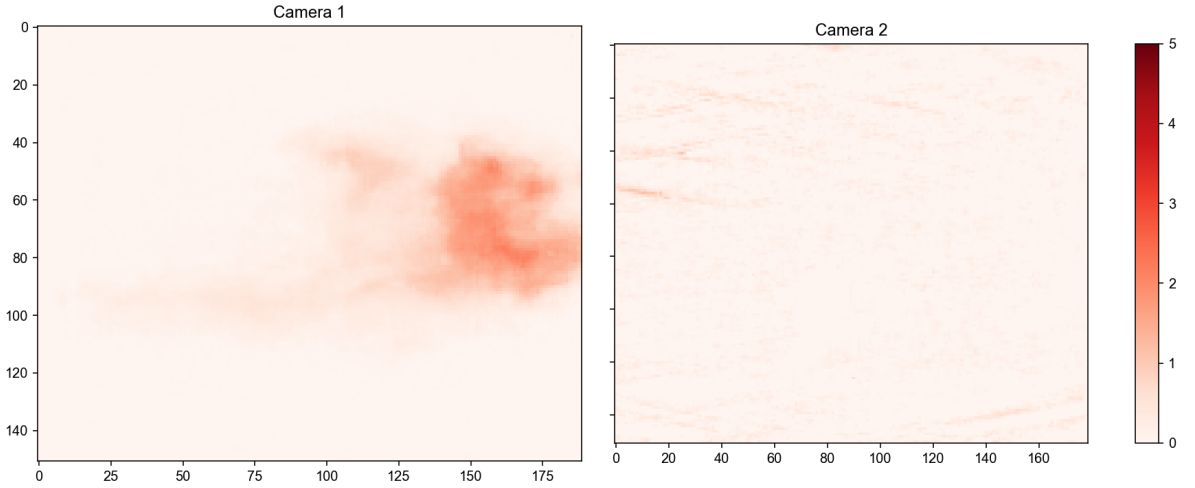

Figure 5.11: PCA output for Experiment 1 at $t = 4s$. The colour map corresponds to the spatial distribution of the Rhodamine WT solution concentration (mg/L), as per the colour bar on the right hand side. Small erroneous measurements can be observed for Camera 2 due to the emergence of turbulent disturbances downstream of the barrier.

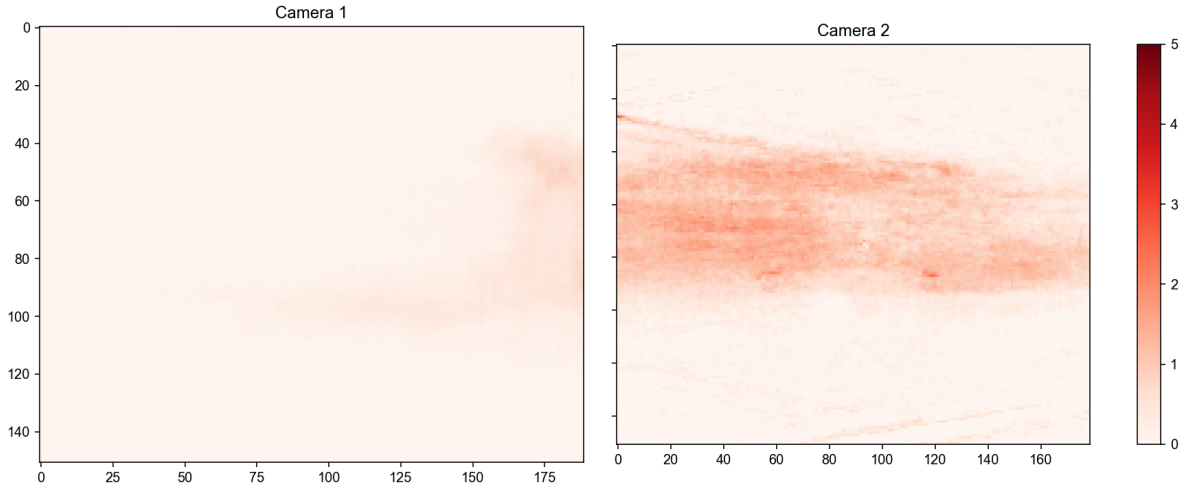

Figure 5.12: PCA output for Experiment 1 at $t = 5s$. The colour map corresponds to the spatial distribution of the Rhodamine WT solution concentration (mg/L), as per the colour bar on the right hand side.

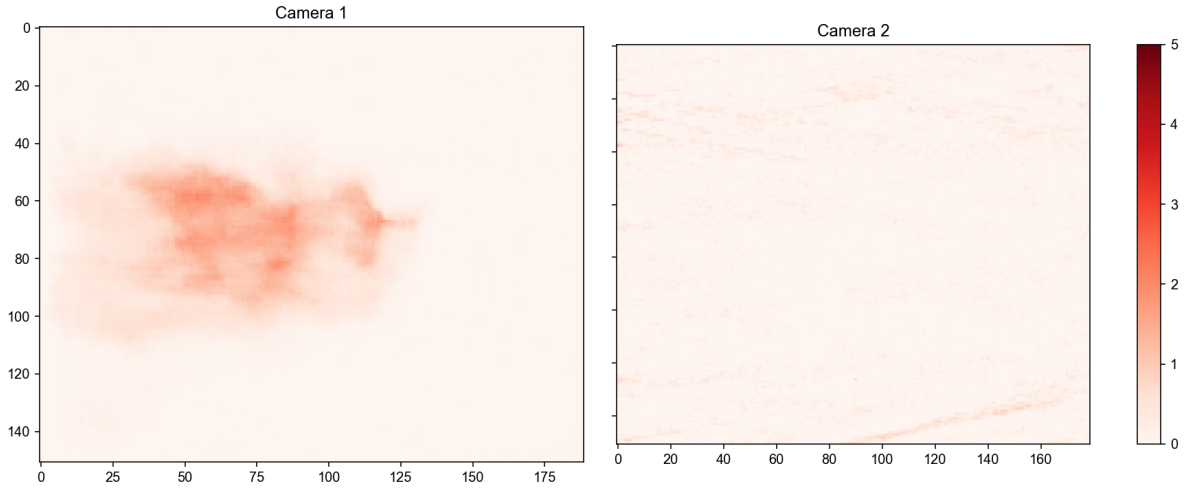

Figure 5.13: PCA output for Experiment 2 at $t = 2.5s$. The colour map corresponds to the spatial distribution of the Rhodamine WT solution concentration (mg/L), as per the colour bar on the right hand side. Small erroneous measurements can be observed for Camera 2 due to the emergence of turbulent disturbances downstream of the barrier.

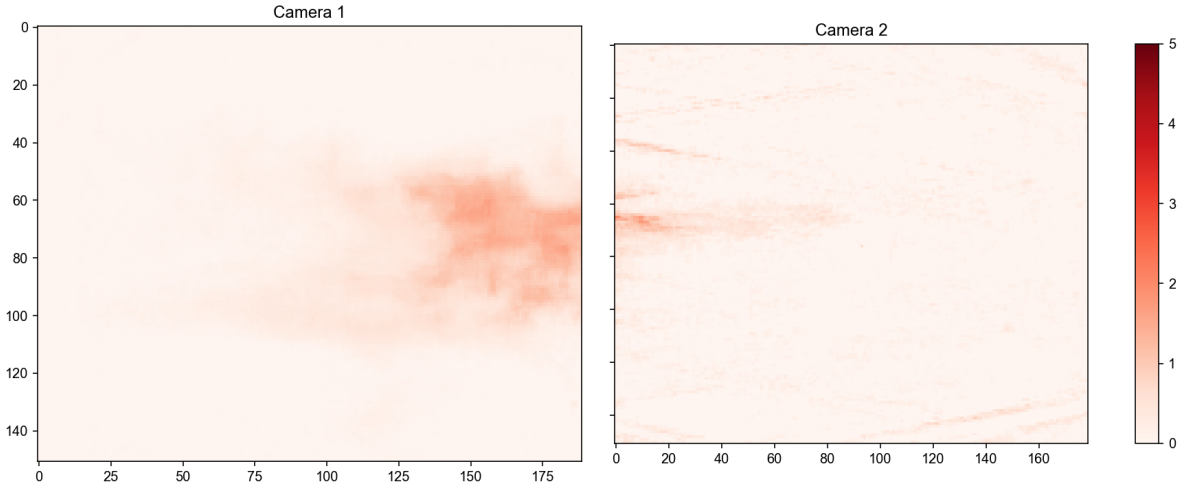

Figure 5.14: PCA output for Experiment 2 at $t = 4s$. The colour map corresponds to the spatial distribution of the Rhodamine WT solution concentration (mg/L), as per the colour bar on the right hand side. Small erroneous measurements can be observed for Camera 2 due to the emergence of turbulent disturbances downstream of the barrier.

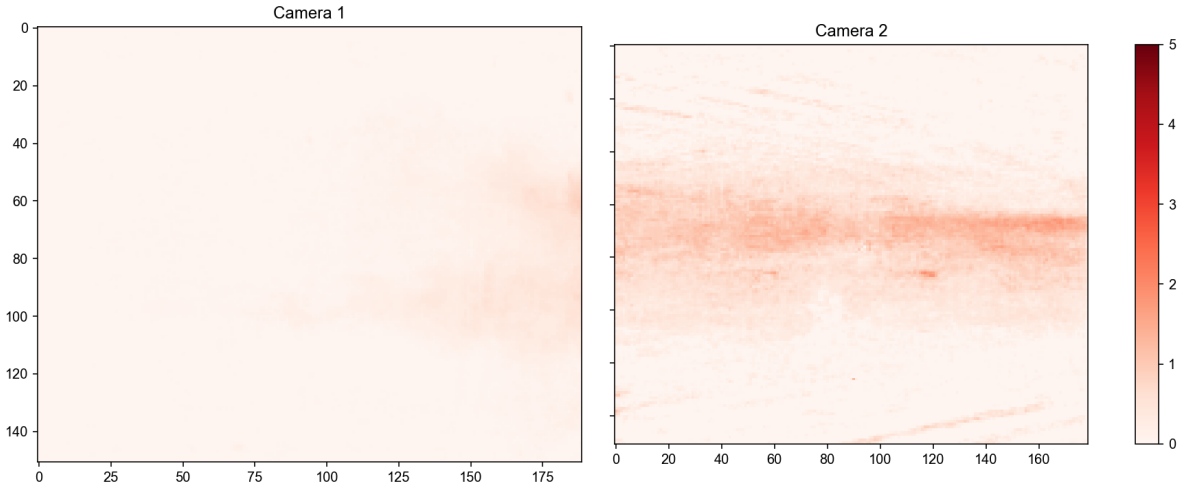

Figure 5.15: PCA output for Experiment 2 at $t = 5s$. The colour map corresponds to the spatial distribution of the Rhodamine WT solution concentration (mg/L), as per the colour bar on the right hand side.

Mass Analysis

By aggregating the derived concentration values for all cells over the duration of the experiment, the total mass of detected Rhodamine WT solution can be estimated and used to verify the accuracy of the PCA. However, since the camera frames are discontinuous, it is challenging to validate the mass-conservation of the PCA. As seen in Figure 5.16, for the period of time between $\approx 2-4s$, in which the entirety of the tracer is contained within the frame of Camera 1, the peak observed mass is relatively stable and corresponds to a mass value which is approximately equal to the injected mass. The top left and right plots within Figure 5.16 show the raw data which includes spurious measurements of concentration prior to the solute mass entering the frame and following the exit of the solute mass from the frame. The lower plots in Figure 5.16 show the data following subtracting of the average background noise and application of a Savitzky-Golay filtering [402] to smooth the data further. The peak solute mass, $15.23mg$ for Experiment 1 and $14.99mg$ for Experiment 2, is consistent with the injected mass ($15 \pm 0.81mg$) as well as demonstrating a high level of consistency across the two experiments.

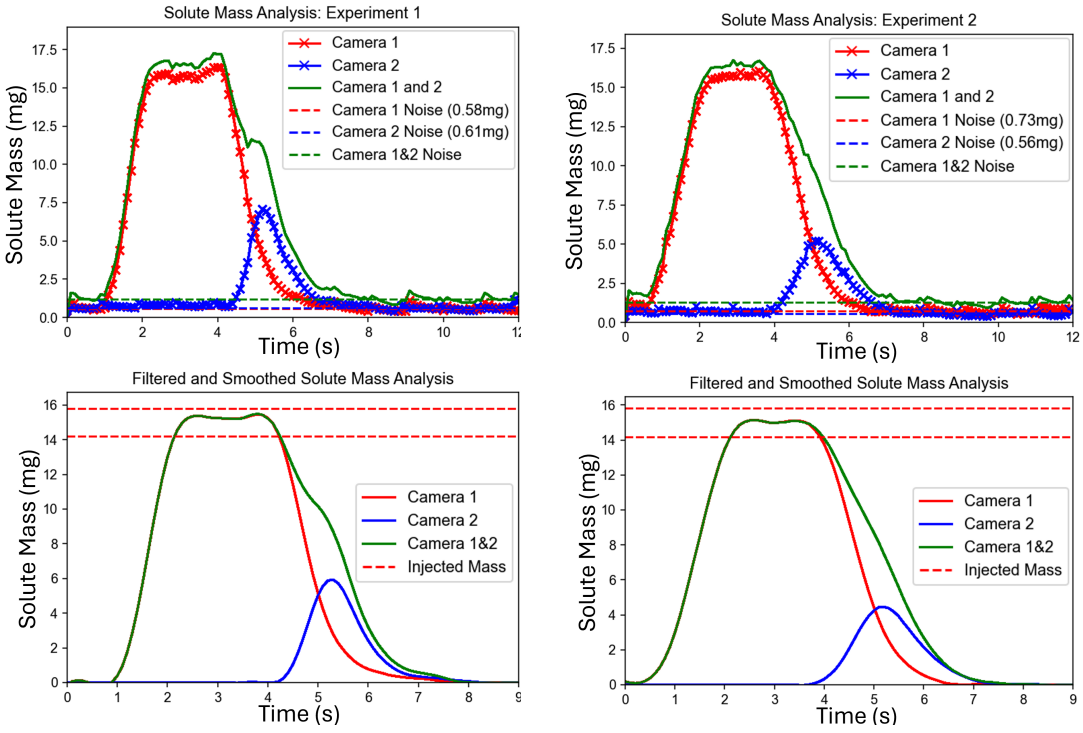

(a) Experiment 1 (b) Experiment 2

Figure 5.16: Solute mass analysis for the two conducted PCA. The adjusted solute mass is following removal of the background noise and application of Savitzky-Golay filtering [402] to smooth the data. Framewise ($0.1s$) solute mass per camera is estimated by multiplying the cell concentration by the interpolated cell volume.

5.4 Numerical Results

Preliminary results for the modelling of a flow interactions with a lifted gate including the transport of a solute mass are presented for a simple first order upwind scheme. An analytical test case is provided in order to validate the numerical treatment of the

advection and diffusion of a solute for simple flow conditions within a two-dimensional domain. A one-dimensional analysis of the data obtained from the PCAs for Experiment 1 and Experiment 2 is then used to perform an initial validation of the numerical model. Since the duration of the experiment is short ($\approx 10s$), the configuration is identical in the plane aligned with the flow direction, the transverse velocity is negligible and consequently transverse diffusion effects are also negligible, application of a one-dimensional model is considered to be justified for an initial validation. A rigorous validation of the numerical model and suitable treatment of the highlighted numerical challenges outlined within the review of the literature, such as ensuring the boundedness of the solute concentration, are to be the focus of future publications.

5.4.1 Numerical Scheme

The domain is divided into cells $(\mathbf{V}_{i,j})_{i,j\in\mathbb{Z}}$, which are perfect quadrilaterals of area $\Delta x \times \Delta y$, and the discretised first order finite volume scheme is given as:

$$\mathbf{U}^*_{ij} = U^n_{ij} + \frac{\Delta t}{\Delta x}\left[\mathbf{F}_{i-\frac{1}{2},j} - \mathbf{F}_{i+\frac{1}{2},j}\right] + \frac{\Delta t}{\Delta y}\left[\mathbf{G}_{i,j-\frac{1}{2}} - \mathbf{G}_{i,j+\frac{1}{2}}\right] \tag{5.29}$$

Where the subscript i, j represents the index of the cell, the superscripts n, $n + 1/2$ and $*$ represent the nth, $n + 1/2$th and intermediate time levels. $\mathbf{U}^*_{ij}$ is therefore the solution to the homogeneous advection problem at an intermediate time level. Δx and Δy represent the dimensions of the cell in the x and y directions and Δt is the time step used to advance the scheme, determined in accordance with the Courant-Friedrichs-Lewy condition as:

$$\Delta t = C_{\text{CFL}} \times \min_{i,j}\left(\frac{\Delta x}{|S^{\text{n,x}}_{i,j}|}, \frac{\Delta y}{|S^{\text{n,y}}_{i,j}|}\right) \tag{5.30}$$

where $S^{\text{n,x}}_{i,j}$ and $S^{\text{n,y}}_{i,j}$ are the maximum wavespeed present at time level n in the x and y directions respectively and $0 \leq C_{\text{CFL}} \leq 0.5$ is taken as equal to 0.45. $\mathbf{F}_{i-1/2,j}$ and $\mathbf{F}_{i+1/2,j}$ represent the numerical fluxes resolved across the $i \pm 1/2, j$ interfaces in the x-direction. $\mathbf{G}_{i,j-1/2}$ and $\mathbf{G}_{i,j+1/2}$ represent the numerical fluxes resolved across the $i, j \pm 1/2$ interfaces in the y-direction. The numerical fluxes are resolved using a HLLC solver as follows:

$$\mathbf{F}^{hllc}_{i+\frac{1}{2},j} = \begin{cases} \mathbf{F}_L \text{ if } 0 \leq S^-_x \\ \mathbf{F}_{*L} \text{ if } S^-_x \leq 0 \leq S^*_x \\ \mathbf{F}_{*R} \text{ if } S^*_x \leq 0 \leq S^+_x \\ \mathbf{F}_R \text{ if } 0 \geq S^+_x \end{cases} \quad , \quad \mathbf{G}^{hllc}_{i,j+\frac{1}{2}} = \begin{cases} \mathbf{G}_L \text{ if } 0 \leq S^-_y \\ \mathbf{G}_{*L} \text{ if } S^-_y \leq 0 \leq S^*_y \\ \mathbf{G}_{*R} \text{ if } S^*_y \leq 0 \leq S^+_y \\ \mathbf{G}_R \text{ if } 0 \geq S^+_y \end{cases} \tag{5.31}$$

with the intermediate fluxes $\mathbf{F}_{*L}$, $\mathbf{G}_{*L}$ and $\mathbf{F}_{*R}$, $\mathbf{G}_{*L}$ determined via application of the Rankine-Hugoniot conditions across each of the waves of speed S^-, S^+ and S^+:

$$S^-\text{: } \mathbf{F}_{*L} = \mathbf{F}_L + S^-_x(\mathbf{U}_{*L} - \mathbf{U}_L) \quad , \quad \mathbf{G}_{*L} = \mathbf{G}_L + S^-_y(\mathbf{U}_{*L} - \mathbf{U}_L) \tag{5.32}$$

$$S^*\text{: } \mathbf{F}_{*R} = \mathbf{F}_{*L} + S^*_x(\mathbf{U}_{*R} - \mathbf{U}_{*L}) \quad , \quad \mathbf{G}_{*L} + S^*_y(\mathbf{U}_{*R} - \mathbf{U}_{*L}) \tag{5.33}$$

$$S^+\text{: } \mathbf{F}_{*R} = \mathbf{F}_R + S^+_x(\mathbf{U}_{*R} - \mathbf{U}_R) \quad , \quad \mathbf{G}_{*R} = \mathbf{G}_R + S^+_y(\mathbf{U}_{*R} - \mathbf{U}_R) \tag{5.34}$$

Wavespeeds are calculated as shown in Algorithm 5. An efficient implementation of the HLLC solver can be achieved via use of a HLL solver to determine the mass fluxes, $\mathbf{F}_1$,

$\mathbf{G}_1$, and the momentum fluxes in the respective principle directions, $\mathbf{F}_2$, $\mathbf{G}_3$, as:

$$\mathbf{F}_{i+\frac{1}{2},j} = \begin{cases} \mathbf{F}_{i,j} & \text{if } S_x^- > 0 \\ \mathbf{F}^{hll} = \frac{S^+\mathbf{F}_{i,j} - S^-\mathbf{F}_{i+1,j} + S_x^+ S_x^- (\mathbf{U}_{i+1,j} - \mathbf{U}_{i,j})}{S_x^+ - S_x^-} & \text{if } S_x^- \leq 0 \leq S_x^+ \\ \mathbf{F}_{i+1,j} & \text{if } S_x^+ < 0 \end{cases} \tag{5.35}$$

$$\mathbf{G}_{i,j+\frac{1}{2}} = \begin{cases} \mathbf{G}_{i,j} & \text{if } S_y^- > 0 \\ \mathbf{G}^{hll} = \frac{S^+\mathbf{F}_{i,j} - S^-\mathbf{F}_{i,j+1} + S_y^+ S_y^- (\mathbf{U}_{i,j+1} - \mathbf{U}_{i,j})}{S_y^+ - S_y^-} & \text{if } S_y^- \leq 0 \leq S_y^+ \\ \mathbf{G}_{i,j+1} & \text{if } S_y^+ < 0 \end{cases} \tag{5.36}$$

with the tangential momentum flux, $\mathbf{F}_3$ and $\mathbf{G}_2$, as:

$$\mathbf{F}_{i+\frac{1}{2},j} = \begin{cases} v_{i,j}\mathbf{F}_1 & \text{if } S_x^+ > 0 \\ v_{i+1,j}\mathbf{F}_1 & \text{if } S_x^+ < 0 \end{cases}, \quad \mathbf{G}_{i,j+\frac{1}{2}} = \begin{cases} u_{i,j}\mathbf{G}_1 & \text{if } S_y^+ > 0 \\ u_{i,j+1}\mathbf{G}_1 & \text{if } S_y^+ < 0 \end{cases} \tag{5.37}$$

and solute mass flux, $\mathbf{F}_4$ and $\mathbf{G}_4$, subsequently calculated given as:

$$\mathbf{F}_{i+\frac{1}{2},j} = \begin{cases} \psi_{i,j}\mathbf{F}_1 & \text{if } S_x^+ > 0 \\ \psi_{i+1,j}\mathbf{F}_1 & \text{if } S_x^+ < 0 \end{cases}, \quad \mathbf{G}_{i,j+\frac{1}{2}} = \begin{cases} \psi_{i,j}\mathbf{G}_1 & \text{if } S_y^+ > 0 \\ \psi_{i,j+1}\mathbf{G}_1 & \text{if } S_y^+ < 0 \end{cases} \tag{5.38}$$

The friction source terms are resolved using the splitting method proposed by Liang and Marche [275]:

$$q_{i,j,d}^{n+1} = q_{i,j,d}^{n*} - \Delta t S_{i,j,d}^n = q_{i,j,d}^{n*} - \Delta t \left(\frac{\tau_{f,d}}{1 + \Delta t \frac{\partial \tau_{f,d}}{\partial q_{i,j,d}}} \right)^n \tag{5.39}$$

Where $d = x, y$ denotes the direction and $q_{i,j,x}^{n*} = h_{i,j}^{n*} u_{i,j}^{n*}$, $q_{i,j,y}^{n*} = h_{i,j}^{n*} v_{i,j}^{n*}$ is the discharge at the intermediate time level following solution of the homogeneous advection problem in the x- and y-direction respectively. The following simple limiter is used to ensure stability in regions where the water depth approaches zero:

$$S_{i,j,d}^n = \frac{q_{i,j,d}^n}{\Delta t} \text{ if } |\Delta t S_{i,j,d}^n| > |q_{i,j,d}^n| \tag{5.40}$$

The dispersion-diffusion source terms are solved using a second-order central difference scheme:

$$\begin{aligned}
(\psi h)_{i,j}^{n+1} = (\psi h)_{i,j}^* + & \\
& \frac{1}{\Delta x}\left[(hD_{xx})_{i+\frac{1}{2},j}^* \left(\frac{(\psi)_{i+1,j}^* - (\psi)_{i,j}^*}{\Delta x} \right) - (hD_{xx})_{i-\frac{1}{2},j}^* \left(\frac{(\psi)_{i,j}^* - (\psi)_{i-1,j}^*}{\Delta x} \right) \right] \\
+ \frac{1}{2\Delta x}\left[(hD_{xy})_{i+1,j}^* \left(\frac{(\psi)_{i+1,j+1}^* - (\psi)_{i+1,j-1}^*}{2\Delta y} \right) - (hD_{xy})_{i-1,j}^* \left(\frac{(\psi)_{i-1,j+1}^* - (\psi)_{i-1,j-1}^*}{2\Delta y} \right) \right] & \\
+ \frac{1}{2\Delta y}\left[(hD_{yx})_{i,j+1}^* \left(\frac{(\psi)_{i+1,j+1}^* - (\psi)_{i-1,j+1}^*}{2\Delta x} \right) - (hD_{yx})_{i,j-1}^* \left(\frac{(\psi)_{i+1,j-1}^* - (\psi)_{i-1,j-1}^*}{2\Delta x} \right) \right] & \\
+ \frac{1}{\Delta y}\left[(hD_{yy})_{i,j+\frac{1}{2}}^* \left(\frac{(\psi)_{i,j+1}^* - (\psi)_{i,j}^*}{\Delta y} \right) - (hD_{yy})_{i,j-\frac{1}{2}}^* \left(\frac{(\psi)_{i,j}^* - (\psi)_{i,j-1}^*}{\Delta y} \right) \right] &
\end{aligned}$$

Algorithm 5 Calculation of wave speeds as proposed by Glenis et al. [179]. An initial approximation (h_0) of the depth in the star region (h_*) using a two-rarefaction approximate state Riemann solver is used to determine whether a two-rarefaction or two-shock approximation is optimal. $h_L = h_{i,j}$, $u_L = u_{i,j}$ and $h_R = h_{i+1,j}$, $u_R = u_{i+1,j}$ for $S^{n,x}_{i,j}$. $h_L = h_{i,j}$, $u_L = v_{i,j}$ and $h_R = h_{i,j+1}$, $u_R = v_{i,j+1}$ for $S^{n,y}_{i,j}$.

$g \leftarrow 9.81\text{ms}^{-2}$
if $h_L \wedge h_R > 0$ **then** ▷ Initial two-rarefaction approximation
  $c_L \leftarrow \sqrt{gh_L}$
  $c_R \leftarrow \sqrt{gh_R}$
  $h_0 \leftarrow \frac{1}{g}\left(\frac{1}{2}(c_L + c_R) + \frac{1}{4}(u_L - u_R)\right)^2$
  if $h_0 \leq \min(h_L, h_R)$ **then** ▷ Use two-rarefaction approximate state Riemann solver
    $h_* \leftarrow h_0$
    $u_* \leftarrow \frac{1}{2}(u_L + u_R)$
  else if $h_0 > \min(h_L, h_R)$ **then** ▷ Use two-shock approximate state Riemann solver
    $p_L \leftarrow \sqrt{\frac{g(h_0+h_L)}{2h_0h_L}}$
    $p_R \leftarrow \sqrt{\frac{g(h_0+h_R)}{2h_0h_R}}$
    $h_* \leftarrow \frac{p_Lh_L+p_Rh_R+u_L-u_R}{p_L+p_R}$
    $u_* = \frac{1}{2}(u_L + u_R) + \frac{1}{2}(p_R(h_* - h_R) - p_L(h_* - h_L))$
  end if
  if $h_* > h_L$ **then** ▷ Left shock wave
    $\alpha_L \leftarrow \frac{\sqrt{0.5(h_*+h_L)h_*}}{h_L}$
  else if $h_* \leq h_L$ **then** ▷ Left rarefaction wave
    $\alpha_R \leftarrow 1$
  end if
  if $h_* > h_R$ **then** ▷ Right shock wave
    $\alpha_R \leftarrow \frac{\sqrt{0.5(h_*+h_R)h_*}}{h_R}$
  else if $h_* \leq h_R$ **then** ▷ Right rarefaction wave
    $\alpha_R \leftarrow 1$
  end if
  $S^- \leftarrow u_L - \alpha_L c_L$ ▷ Left wavespeed
  $S^* \leftarrow u_*$ ▷ Central contact discontinuity
  $S^+ \leftarrow u_R + \alpha_R c_R$ ▷ Right wavespeed
else if $h_L = 0 \wedge h_R > 0$ **then** ▷ Left dry bed
  $S^- \leftarrow u_R - 2c_R$ ▷ Left wavespeed
  $S^+ \leftarrow u_R + c_R$ ▷ Right wavespeed
  $S^* \leftarrow S^-$ ▷ Contact discontinuity
else if $h_R = 0 \wedge h_L > 0$ **then** ▷ Right dry bed
  $S^- \leftarrow u_L - c_L$ ▷ Left wavespeed
  $S^+ \leftarrow u_L + 2c_L$ ▷ Right wavespeed
  $S^* \leftarrow S^+$ ▷ Contact discontinuity
end if

To overcome the limitations induced by the diffusive properties of a first order scheme, anti-diffusion measures proposed by Murillo and García-Navarro [330] are implemented. The anti-diffusion measures seek to reduce the physical diffusion, modelled by the diffusion source terms, by an amount equal to the numerical diffusion, produced by the truncation error which arises as a consequence of the first order discretisation, such that the total diffusion is consistent with the intended physical diffusion. Consider the following one-dimensional linear advection equation:

$$\partial_t q + a\partial_x q = 0 \tag{5.41}$$

which describes the advection of a quantity q at a constant velocity a. Applying a first order upwind scheme results in:

$$q_i^{n+1} = q_i^n - \frac{a\Delta t}{\Delta x}\left(q_i^n - q_{i-1}^n\right) \tag{5.42}$$

where q_i^n represents the approximate solution at time level n for cell i. By rearranging the upwind scheme (5.42) as a direct discretisation of the partial differential equation (5.41), replacing the approximate solution with the exact solution, $q(x,t)$, and expanding the terms about $q(x,t)$ using Taylor series (assuming a smooth solution), the local truncation error can be determined as:

$$L_k(x,t) = \frac{1}{2}a\Delta t\left(a - \frac{\Delta x}{\Delta t}\right)q_{xx}(x,t) + \mathcal{O}(\Delta t^2) \tag{5.43}$$

$$L_k(x,t) = \mathcal{O}(\Delta t) \quad \text{as} \quad \Delta t \to 0 \tag{5.44}$$

for a fixed mesh ratio $\Delta t/\Delta x = \text{constant}$. A modified equation can therefore be defined as:

$$q_t + aq_x = \frac{1}{2}a\Delta x\left(1 - v\right)q_{xx} \tag{5.45}$$

which represents an advection-diffusion equation. The presence of the diffusion term of the form Dq_{xx}, where D is the diffusion coefficient, dictates the qualitative behaviour of the solution: the solution propagates at the correct speed, a, but diffuses at a rate proportional to D at each timestep, resulting in a smeared solution. The diffusion coefficient is given by $\frac{1}{2}a\Delta x(1-v)$, where $v = a\Delta t/\Delta x$ is the Courant number. Using $D_{num} = \frac{1}{2}a\Delta x(1-v)$ as an estimate of the numerical diffusion introduced by the numerical scheme, the modified physical diffusion $\mathcal{D}$ can be defined as:

$$\mathcal{D}_{dd} = \max\left(D_{dd} - D_{num,d}, 0\right) \tag{5.46}$$

where d represents the x or y direction and the advection velocity a is taken equal to the either u, for the x-direction or v, for the y-direction. Despite requiring smoothness assumptions when applying the Taylor series expansions, the modified equation remains a good model of the qualitative behaviour of the true solution in the presence of discontinuities since the diffusive terms result in a smearing of discontinuities, as occurs for the numerical solution, ensuring satisfaction of the smoothness assumptions [268]. Overall, the implemented anti-diffusion measures result in a numerical treatment of the diffusion process which is more consistent with the intended diffusion, however, the effectiveness of the measures is dependent on the relative magnitude of D_{dd} and $D_{num,d}$. Therefore, the

implementation of a higher order numerical scheme presents a more rigorous solution and is recommended where feasible.

In order to simplify the numerical solution the bed slope is set to 0% and therefore solution of the topographic source terms is not required. For cases involving variable bed topography, a well-balanced treatment of the topographic source terms can be achieved via the hydrostatic reconstruction method [31] or via upwinding of the source terms [57].

For the multi-layer components of the scheme the same numerical scheme for the mono-layer system is applied on a layer by layer basis as detailed in Mckenna et al. [302].

5.4.2 Analytical Test Case

The analytical solution, for advection and diffusion phenomena occurring in a frictionless infinite two-dimensional domain with uniform one-dimensional flow in the direction of the x-axis ($v = 0$ and $D_{xy} = D_{yx} = 0$) is given as [273]:

$$\psi(x, y, t) = \frac{\psi_0}{4\pi t\sqrt{D_{xx}D_{yy}}} \exp\left(-\frac{(x - x_0 - ut)^2}{4D_{xx}t} - \frac{(y - y_0)^2}{4D_{yy}t}\right)$$

where ψ_0 is the initial concentration of the solute instantaneously added to the water at position (x_0, y_0). t is the time in seconds measured from the time of injection, $t_0 = 0$. u is the velocity in the x-direction and D_{xx}, D_{yy} are the turbulent mixing coefficients in the x and y directions respectively.

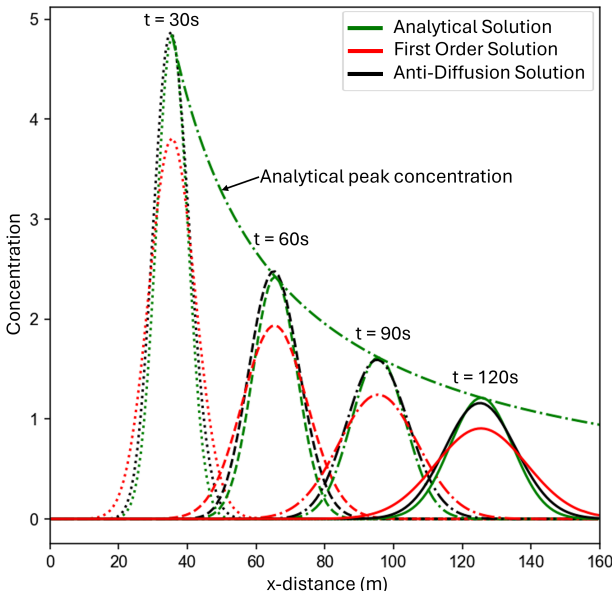

Figure 5.17: The longitudinal concentration profile, at $30s$ (dotted), $60s$ (dashed), $90s$ (dash-dot) and $120s$ (solid), for the analytical solution (green), first order numerical solution (red), first order numerical solution with diffusion correction (black) along the line $y = 80.5m$. The green dash-dot curve represents the analytical peak concentration at time $t = x$.

A test domain of 160×160 cells, $\Delta x = \Delta y = 1m$, is used to simulate the advection and diffusion of an initial solute mass injection of $M = 100$, at $(x_0, y_0) = (5.5m, 80.5m)$ for

a duration of $120s$. Longitudinal and lateral dispersion coefficients are set to constant values of $\epsilon_l = 5.93$ and $\epsilon_t = 0.15$ respectively. The depth is set to a uniform value of $1m$ and the horizontal velocity is set to a uniform value of $u = 1m/s$, with a corresponding tangential velocity $v = 0m/s$, replicating the required flow conditions. Figure 5.17 shows a comparison between the analytical concentration profiles and the respective computed numerical results for the presented first order scheme, with and without the diffusion correction, along the line $y = 80.5m$. As expected for the unmodified first order scheme, excessive numerical diffusion increasingly smears the concentration profile as the simulation duration increases. The use of the diffusion correction proposed by Murillo and García-Navarro [330] results in approximations which are much more consistent with the analytical results.

5.4.3 One-dimensional Validation

Following the analytical validation of the two-dimensional scheme for a simple flow configuration, a one-dimensional simplification of the presented numerical scheme, including the use of the first order diffusion correction, is used to validate the transport of a solute in the presence of a partial obstruction to flow. Figure 5.18 illustrates the accuracy of the model in capturing the flow characteristics for the experimental configuration. The area observed by Camera 1 spans from $x = 3.97m$ to $x = 4.93m$, the area observed by Camera 2 spans from $x = 5.15m$ to $x = 6.05m$.

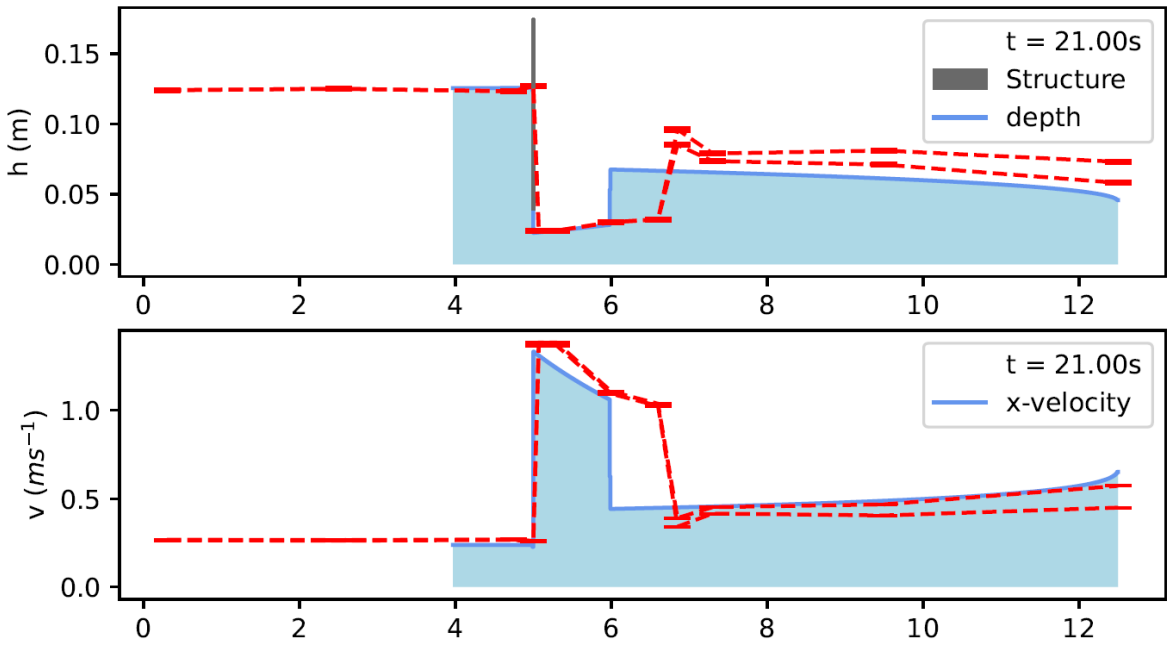

Figure 5.18: Experimental validation of the numerical results for the depth and velocity.

The numerical simulations are performed on a $8.54m$ one-dimensional spatial domain, which spans from the left boundary at a distance of $3.97m$ from the flume inlet to the flume outlet at $12.5m$, discretised into a structured grid comprised of $0.01m$ cells ($\Delta x = 0.01m$). The bed slope is set to 0%, simplifying the source terms, requiring only the resolution of the friction and diffusion source terms. A constant Manning's n equal to 0.012 and a kinematic viscosity of $1.0034 \times 10^{-6} m^2 s^{-1}$ is assumed. The discharge is equal to $29.8ls^{-1}$.

Do to the small errors in the numerical approximation of the depth and velocity, when analysing the transport of the solute compensations must be made to ensure a fair comparison. The underestimation of the velocity and overestimation of the will contribute to an underestimation of the concentration with a corresponding phase error in the propagation speed. Errors in the estimation of the discharge may also be present due to the relatively small inflow rate [302].

Boundary Conditions

The injection of the Rhodamine WT solution is captured using the PCA data. The inflow of Rhodamine WT solution arriving within the area observed by Camera 1 for each frame ($\approx 0.1s$) is captured by analysing the solute mass contained within the first five columns of cells at the left boundary, where 5 cells $= 0.025m \approx v_{avg} \times \Delta t$, with $v_{avg} = 0.26ms^{-1}$ and $\Delta t = 0.1s$. Since the cell size is discrete ($5mm$), this represents a slight underestimation of the average distance travelled by the solute within a single frame. As a consequence, the shape of the curve is obtained by repeating this process for each of the first five columns, whereby the analysed cells comprise of the start cell column plus the proceeding four cell columns. The average shape of the obtained curves is then determined, to filter any potential errors introduced by a defective column of cells. The curve is then linearly scaled such that the maximum value is consistent with the respective values determined from the mass analysis (Figure 5.16). The derived graphs, which plot the cumulative solute mass entering the domain over time for each of the two experiments are shown in Figure 5.19.

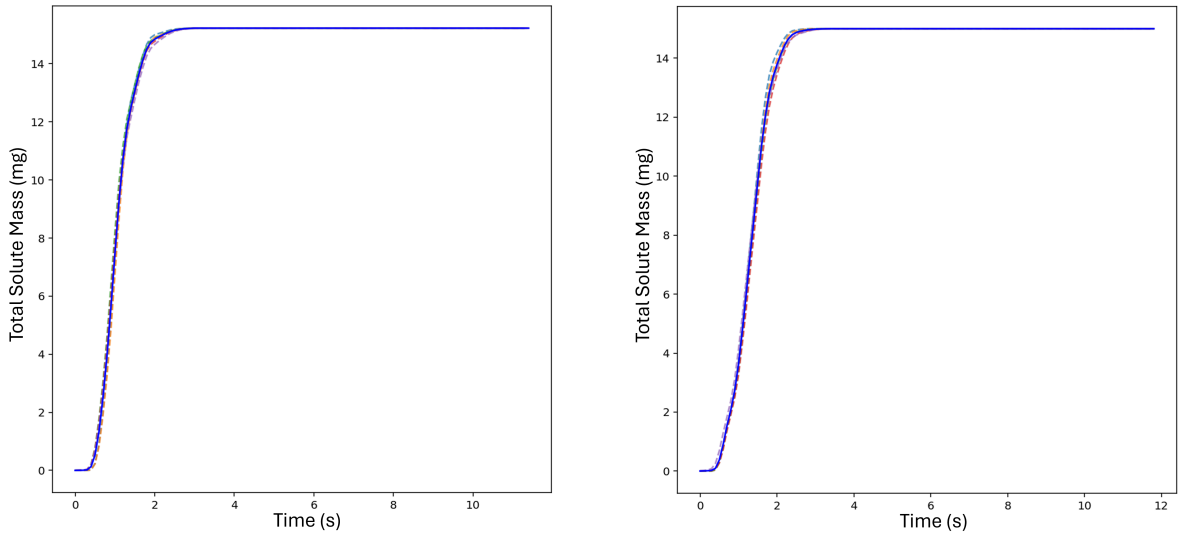

(a) Experiment 1

(b) Experiment 2

Figure 5.19: The derived graphs of cumulative mass of Rhodamine WT solution which has entered the frame of Camera 1 over time for Experiment 1 (Figure 5.19a) and Experiment 2 (Figure 5.19b). The curves are scaled such that the total mass of Rhodamine WT solution is consistent with the peak measured mass of Rhodamine WT solution and the known injected mass of Rhodamine WT solution.

The upstream solute injection is then modelled via manipulation of the boundary flux

$\mathbf{F}^3 = \mathbf{F}^1\psi_k$. Using the Riemann invariant:

$$u_L - 2a_L = u_R - 2a_R$$

and substituting:

$$\begin{aligned} Q_{in} &= h_L u_L \\ u_L &= \frac{Q_{in}}{h_L} \\ a_k &= \sqrt{gh_k} \end{aligned}$$

Gives:

$$\frac{Q_{in}}{h_L} - 2\sqrt{gh_L} = u_R - 2\sqrt{gh_R}$$

Which can be rearrange to give the following function:

$$\begin{aligned} \frac{Q_{in}}{h_L} - 2\sqrt{gh_L} - u_R + 2\sqrt{gh_R} &= 0 \\ \frac{Q_{in}}{h_L} + 2\sqrt{g}(\sqrt{h_R} - \sqrt{h_L}) - u_R &= 0 \end{aligned}$$

let:

$$\begin{aligned} f(h_L, h_R, u_R) &= \frac{Q_{in}}{h_L} + 2\sqrt{g}(\sqrt{h_R} - \sqrt{h_L}) - u_R \\ \frac{d}{dh_L} f(h_L, h_R, u_R) &= -\frac{Q_{in}}{h_L^2} - \frac{\sqrt{g}}{\sqrt{h_L}} \end{aligned}$$

This can then be solved to find h_L using the Newton-Raphson method with an initial guess of $h_0 = h_R$:

$$x_{n+1} = x_n - \frac{f(x_n)}{f'(x_n)}$$

Using a suitable tolerance (10^{-6}) and a maximum number of iterations (1000). Finally u_L may be determined using:

$$u_L = \frac{Q_{in}}{h_L}$$

For $h > 0, u > 0$, which is satisfied providing water is entering the domain, $u_* > 0$ and hence:

$$\mathbf{F}^3 = h_L u_L \psi_L = \mathbf{F}^1 \psi_L$$

where ψ_L is the concentration in the ghost cell. Using the Figure 5.19, the required ghost cell concentration, ψ_L, can be determined. Using a first order accurate upwind scheme:

$$\mathbf{U}_i^{n+1} = \mathbf{U}_i^n - \frac{\Delta t}{\Delta x}\left[\mathbf{F}_{i+\frac{1}{2}} - \mathbf{F}_{i-\frac{1}{2}}\right] - \frac{\Delta t}{\Delta x}\left[\mathbf{G}_{i+\frac{1}{2}} - \mathbf{G}_{i-\frac{1}{2}}\right] + \Delta t \mathbf{S}\left(\mathbf{U}_i^{(s)}\right)$$

Assuming the solute mass injection occurs in the x-direction, across the left boundary of the domain:

$$\Delta \mathbf{U}_{in} = \frac{\Delta t}{\Delta x}\left[\mathbf{F}_{i-\frac{1}{2}}\right] \tag{5.47}$$

$$(\psi h)_{inj} = \frac{\Delta t}{\Delta x}\mathbf{F}^{3}_{i-\frac{1}{2}} = \frac{\Delta t}{\Delta x}\left(h_L u_L \psi_L\right) \tag{5.48}$$

Where $\Delta \mathbf{U}_{in}$ represents the conserved variable entering the domain via the left flux and $(\psi h)_{inj}$ is specifically the injected solute mass entering the domain. Therefore the required ghost cell concentration, ψ_L, can be determined by rearranging:

$$\frac{(\psi h)_{inj}\Delta x}{\Delta t h_L u_L} = \psi_L$$

Where $(\psi h)_{inj}$ can be determined by finding the difference between the total solute mass which has entered previously entered the domain at $t = t^n$ and the cumulative solute mass which is projected to have entered the domain at time $t = t^{n+1}$, interpolated from the data contained within Figure 5.19. Since the PCA measurements used to determine the inflow rate are contained within the frame of Camera 1, this must be accounted for within the numerical model by either further truncating the domain or via shifting the data in Figure 5.19 by $0.1s$.

At the downstream end a critical depth boundary condition is implemented as detailed in [303].

Mass Analysis and Comparison

Figure 5.22 and Figure 5.23 show the total mass of Rhodamine WT solution observed during the PCA for each of the cameras, for Experiment 1 and Experiment 2 respectively. In both cases the numerical model replicates the initial movement of the slug injection into the observation area for Camera 1, as shown by the alignment of the rising limb of the plots for Camera 1 for both experiments. This demonstrates that the proposed inflow boundary condition reasonably replicates the experiment observations.

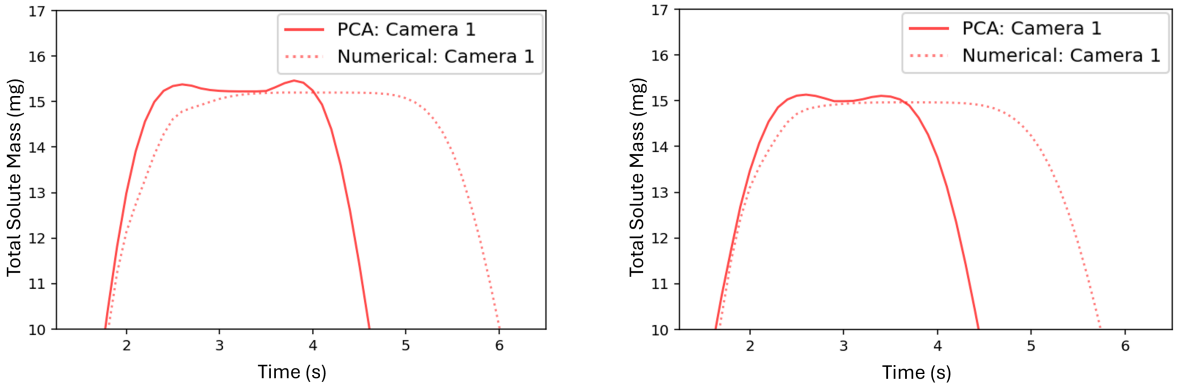

(a) Experiment 1

(b) Experiment 2

Figure 5.20: Zoomed focus on the results for Camera 1 between $2s - 6s$ for Experiment 1 as shown in Figure 5.20a taken from Figure 5.22 and for Experiment 2 as shown in in Figure 5.20b taken from Figure 5.23.

As shown in Figure 5.20, the gradient of the rising limb decreases in relation to the observations at approximately $2s$ for both experiments. This suggests that the decreasing of the gradient of the mass inflow rate towards the peak in Figure 5.19 artificially reduces the mass inflow rate in the numerical simulation. As a consequence the tail of the plume for the numerical experiments should be expected to be smeared in comparison with the observations. However, the overall effect is relatively small since it only impacts the final $3mg$ of Rhodamine WT solution entering the domain.

For both experiments, the correct intended peak mass is attained and maintained demonstrating the expected conservation properties of the scheme. Whilst the rate of inflow isn't perfectly replicated, the intended total mass inflow is achieved. However, due to incongruencies in the hydrodynamic variables as shown in Figure 5.18, the numerical solute takes longer to reach the right edge of the observation area for Camera 1 in both experiments. This is demonstrated by the maintenance of the peak solute mass for an additional $1s$ for both Experiment 1 Experiment 2. The consistency in the lag time across both experiments supports the fact that it is the underlying inaccuracy of the hydrodynamic variables which is contributing to this error and not the treatment of the diffusion process. The falling limb of the mass data can be seen to be roughly parallel in both cases suggesting that the shape of the solute slug is relatively consistently modelled despite differences in transit time.

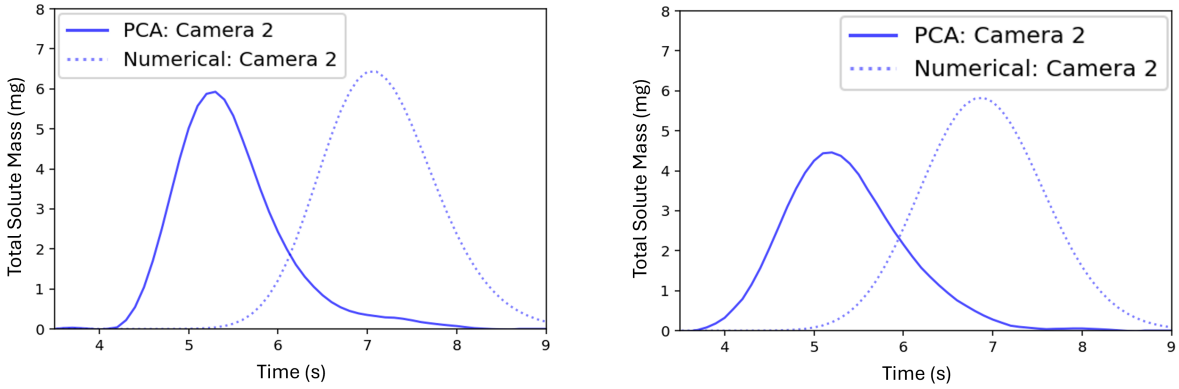

(a) Experiment 1 (b) Experiment 2

Figure 5.21: Zoomed focus on the results for Camera 1 between $3.5s - 9s$ for Experiment 1 as shown in Figure 5.21a taken from Figure 5.22 and for Experiment 2 as shown in in Figure 5.21b taken from Figure 5.23.

For Camera 2, as shown in Figure 5.21, the lag time between the numerical results and experiment observations is increased however, the numerical results approximate the observations well neglecting the phase shift. The main difference that can be observed is that the numerical results do not capture the trailing decrease in the observed mass for Experiment 1 however, it is likely that this observation is a product of uncertainty in the observations which are increasingly hard to distinguish from the background noise as the total value diminishes.

For both experiments the peak solute mass observed for Camera 2 is slightly overestimated which can be attributed to the slower velocity; the underestimation of the downstream velocity means it takes longer for the solute to exit the camera frame and therefore there is a greater potential for a larger total mass of solute to be observed within a single time

frame. Similarly the longer duration for which the solute is observed within the frame of Camera 2 can be attributed to the same issue.

The difference in lag time observed upstream of the barrier is approximately consistent with the lag time observed downstream of the barrier in terms of the time at which the slug is first detected within Camera 2. In the downstream region the uncertainty in the PCA results is higher, since the depth is approximated as constant, and the error in the prediction of the hydrodynamics is also larger as seen in Figure 5.18.

Overall the behaviour of the advection diffusion process through the barrier is observed to be generally captured by the numerical model. This can be seen via the apparent self-similarity of the numerical and experimental results for both of the presented experiments, despite the obvious scaling and phase errors. However, due to the uncertainty in the validation data and the underlying errors in the hydrodynamic predictions of the model, rigorous validation of the quality of the numerical approximations is unfeasible at this stage.

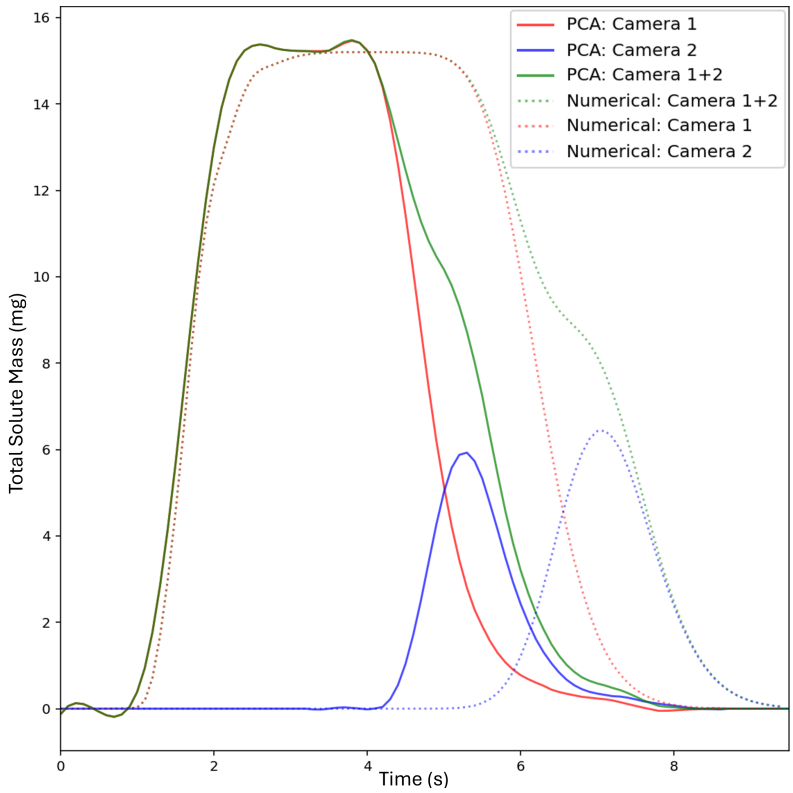

Figure 5.22: A comparison between the numerical and experimental total mass of Rhodamine WT for the individual and combined camera observation areas for Experiment 1.

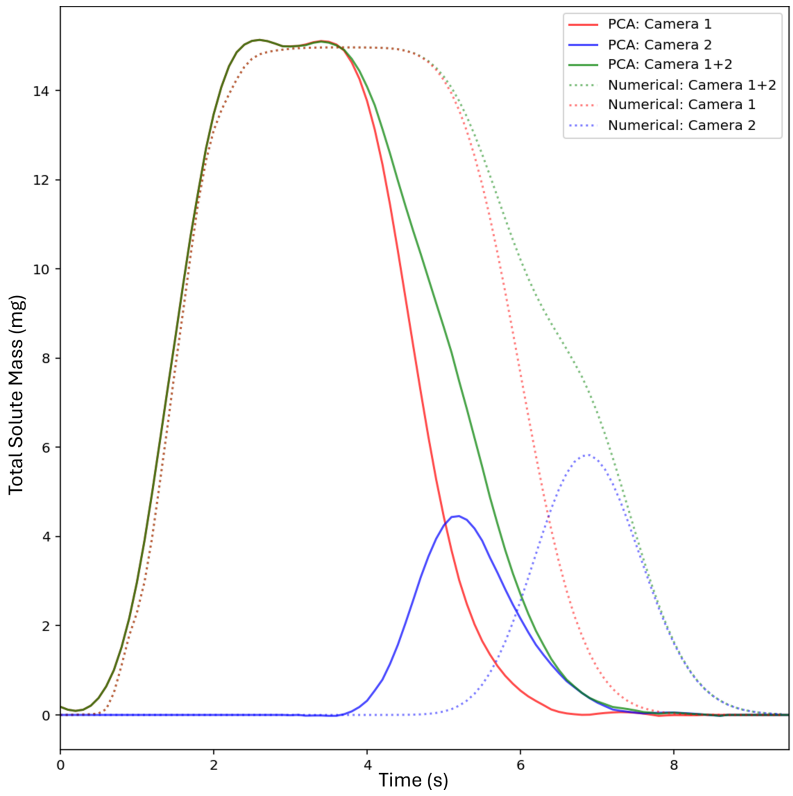

Figure 5.23: A comparison between the numerical and experimental total mass of Rhodamine WT for the individual and combined camera observation areas for Experiment 2.

5.5 Conclusion

The presented work investigates the augmented capacity of the local multi-layer approach to modelling shallow water interactions with obstacles to flow, presented in [302], to model the transport of a depth-integrated solute through an obstruction. The presented validation experiment conducted via a series of PCAs provides a valuable insight into the advection diffusion process across a partial barrier to flow. Partial barriers to flow such as gates, bridges and weirs are prevalent throughout relevant urban domains and the accurate modelling of their impact upon the dynamic flow processes as well as the transport process is important to capture. The modelling of the transport process has a variety of potential applications including but not limited to: point source pollution identification [18, 42], ecological modelling [474, 408], quantitative microbial risk assessment [293, 6, 78], eutrophication prediction [365, 19], flood-induced pollution events [423], accidental pollution spills [492] and protecting drinking water source areas [397, 141, 493, 306]. The advances presented herein therefore contribute to the accuracy of models where flows interact with partial barriers to flow, enhancing the potential effectiveness in the outlined applications.

The conducted PCA experiments enabled the nonintrusive determination of the fieldwise concentration for a series of experiments involving a slug injection of a fluorescent tracer being transported through a gate structure. New techniques have been implemented to overcome challenges related to the experiment configuration and suboptimal lighting conditions when analysing the photometric response of the fluorescent tracer. Analysis of the mass conservation for the upstream observation area corresponds to the known injected solution mass, inspiring confidence in the validity of the experimental data. However, due to the discontinuous nature of the observation areas, mass conservation for the downstream observation area is challenging to verify, resulting in uncertainty in the downstream validation data.

Following implementation of the outlined solver within a simple first order upwind scheme, the numerical results have been validated against the results from PCA experiments. The comparison between the numerical results and the experimental observations demonstrates that the proposed solution procedure is capable of capturing the transport process across a gate type structure. However, errors in the prediction of the hydrodynamic properties of the flow, which is prerequisite to the modelling of the advection diffusion process, limit the potential for rigorous validation. However, the presentation of numerical results validated by experiments is rare for applications related to transport processes for shallow water models and the experimental data is therefore valuable in and of itself for the validation of similar solvers and for understanding the underlying physical processes involved and the consequent suitability of two-dimensional shallow water models for capturing such phenomena. In particular, Mignot et al. [310] identified a lack of experimental data related to the processes associated with hydrodynamic modelling such as pollutant transport in urban environments and this experimental data, in a small way, works towards bridging the identified gap.

Therefore, further work to improve the experimental and numerical results is proposed. It is clear that the PCA experiments would benefit greatly from an expansion of the observation areas the use of a light diffuser. The expansion of the observation areas, which should ideally be designed to be a single continuous series of observation areas spanning the length of the flume, will enable verification of the mass conservation across the en-

tire domain. The use of a light diffuser will enable the optimisation of the illuminance conditions and minimisation of the problematic surface reflections which diminish the capability to analyse the photometric response of the tracer. Through the identification of flow and barrier configurations that reduce turbulent disturbances in the free surface, the use lower tracer concentrations, for which the photometric response is more sensitive, may be permitted enabling a higher accuracy analysis.

For the numerical results, the inaccuracies in the hydrodynamic predictions are to be addressed via the implementation of the proposed solver within a higher order numerical scheme. It it therefore proposed that the updated scheme be based upon the combination of arbitrary high order derivative (ADER) schemes using a weighted essentially non-oscillatory (WENO) reconstruction technique [219, 433, 436, 434]. Such schemes are anti-diffusive and non-oscillatory, offering the potential for a high order of spatial accuracy which does not degrade to first order accuracy in the presence of discontinuities [437]. This therefore addresses identified issues related to the choice of limiter, which may strongly influencing the quality of the numerical results [53, 83]. Furthermore, high order reconstruction in the primitive variables [491], as opposed to the conserved variables, addresses issues related to shock capturing fidelity [328] and ensures a high order of spatial accuracy for the concentration.

Chapter 6

Conclusion

6.1 Conclusions

6.1.1 Summary

The overarching aim of the thesis has been successfully achieved through the development and validation of two new Riemann solvers:

> **Aim:** *To contribute to advances in contemporary hydrodynamic modelling via the development of improved methods for modelling linear features such as bridges, gates and weirs within two-dimensional flood models.*

The innovative Riemann solvers enable the accurate modelling of partial barriers to flow within one- or two-dimensional hydrodynamic models. As identified within the presented literature review, precise modelling of flow interactions with obstacles is crucial for flood hazard and vulnerability assessment. Therefore, the presented Riemann solvers represent advances over existing methods for modelling obstacles which act as partial barriers to flow, offering distinct advantages over the limited available alternatives.

Both of the presented solvers are capable of representing any obstacle to flow which may be idealised as existing at the interface between neighbouring cells. The capability of the solvers to resolve numerical fluxes for a range of barrier and flow configurations has been verified via a validation process involving comparisons between the numerical predictions and the observed flow characteristics for experiments conducted within a state-of-the-art research flume. Both of the presented solvers are physically based and do not require impractical calibration to obtain physically meaningful results. Furthermore, neither of the solvers rely on empirical discharge relations which are only valid under certain flow conditions and limit the effectiveness of existing solutions. The proposed solution procedures therefore also preclude the requirement for additional logical conditions to determine the flow regime as implemented in other similar internal boundary conditions. For example, alternative methods for modelling gates will tentatively determine the depth at the *vena contracta* and the corresponding conjugate depth to determine the transition between submerged and free flow conditions.

The first solver, referred to as Solver 1, represents a simple and easily implemented method which is highly compatible with existing numerical schemes. The proposed solution procedure represents structures as existing at the interface between neighbouring cells and

under the shallow water assumption of primarily horizontal flow, the two-layer shallow water equations are leveraged to enable a vertical discretisation of the numerical flux in accordance with the structure modelled at the interface. As the method lacks the capacity to capture the vertical variation of the horizontal component of the velocity, it is necessary to approximate the velocity profile based upon physical considerations. Despite the simplicity of the method, the validation process demonstrates the suitability of the method in determining the corresponding upstream and downstream depth profiles. The determination of the local velocity is less accurate but still satisfactory. The errors in the approximated flow variables are attributed to the relatively simplistic assumptions used to approximate the velocity profile at the barrier.

Solver 2, addresses the limitations of Solver 1 by providing a permanent vertical discretisation of the neighbouring cells facilitating the more accurate determination of the velocity profile via the numerical scheme, which locally implements a decoupled formulation of the multi-layer shallow water equations. As a result of the permanent vertical discretisation of the neighbouring cells it is necessary to implement intermediate cells either side of the cells neighbouring the structure to couple the mono-layer and multi-layer domains. A layer redefinition process is also required to maintain alignment between the structure modelled at the interface and the layer interfaces. The multi-layer shallow water equations present a significant numerical challenge due to the potential for a local loss of hyperbolicity and the presence of non-conservative product terms. The proposed formulation therefore utilises mathematical manipulations and simplifying assumptions to minimise the effect of the non-conservative product terms, avoiding the need to implement flawed path-conservative schemes, whilst maximising the stability of the scheme in spite of the potential for a local loss of hyperbolicity. Although, it should be noted that these mechanisms also have the potential to reduce the accuracy of the scheme.

However, via comparisons with Solver 1 and the validation data, it is demonstrated that Solver 2 represents a significant improvement upon Solver 1. The more sophisticated treatment of the flow at the barrier results in a more accurate determination of the flow characteristics, which is particularly visible upstream of the barrier. This does come at the cost of increased computational demand and implementation complexity in comparison with Solver 1, however, due to the local nature of the solution procedure the increase in computational expense in unlikely to be prohibitive.

Due to the greater accuracy exhibited by Solver 2, the potential to add the capacity to also model the advection and diffusion of a scalar quantity was explored. Via the conducted planar concentration analyses, the experimental study of the advection diffusion process for a slug injection passing through a partial barrier to flow was investigated, for what appears to be the first time within academic literature. Due to the suboptimal experimental conditions, novel techniques were implemented within the analyses of the observed photometric response and the mass balance, where verifiable, appears conservative with respect to the known injection mass. Although, further work is required to improve the experimental validation procedure and to upgrade the order of accuracy of the numerical scheme to enable a more rigorous validation process. Despite the simplicity of the implemented scheme and the errors and uncertainties in the hydrodynamic predictions and experimental observations, the presented validation procedure demonstrates that the solver is capable of capturing the overall behaviour of the interaction. As a lack of data, validation and process understanding have been identified by leading experts as major obstacles to progress, the presented combination of numerical and experimental results

represents positive progress in this regard.

6.1.2 Key Research Outcomes

Objective 1: To develop and experimentally validate a novel approximate Riemann solver (Solver 1) capable of resolving numerical fluxes across a linear fixed immiscible partial barrier to flow, with a focus upon ease of implementation and compatibility with existing flood models to promote uptake in practice.

- The developed solver is capable of resolving numerical fluxes across a range of linear fixed immiscible partial barriers to flow as demonstrated by the validation process.
- The proposed solver is simple and easy to implement, requiring no calibration and acting only on the numerical flux. The flux calculation process is highly compatible with existing established approximate Riemann solvers and common finite volume numerical schemes.
- The avoidance of using empirical discharge relations ensures that the solver does not suffer from a loss of rigorous validity under unsteady and transient flow conditions.

Objective 2: To develop and experimentally validate an improved approximate Riemann solver (Solver 2) capable of resolving numerical fluxes across a linear fixed immiscible partial barrier to flow, with a focus upon maximising accuracy.

- The developed solver is capable of resolving numerical fluxes across a range of linear fixed immiscible partial barriers to flow as demonstrated by the validation process.
- The solver provides increased accuracy with respect to the previous solver, due to the more sophisticated treatment of the flow in the neighbouring cells.
- The natural extension of the method via increased vertical discretisation or an expansion in the horizontal direction promises further possibilities to improve the accuracy of the method.
- The simplifying assumptions and mathematical manipulations ensure stability in spite of the potential for a local loss of hyperbolicity and avoid the requirement to implement path-conservative methods for the treatment of non-conservative product terms.
- The avoidance of using empirical discharge relations ensures that the solver does not suffer from a loss of rigorous validity under unsteady and transient flow conditions.

Objective 3: To develop and experimentally validate the capability to model the transport of well-mixed dissolved scalar quantities through linear fixed immiscible partial barriers to flow for Solver 2.

- The successful execution of the planar concentration analysis provides an experimental insight into advection diffusion phenomena that is currently lacking.
- The use of new techniques helped to overcome suboptimal experimental illumination conditions for the calibration and analysis of the photometric response for the planar concentration analysis.
- The produced validation dataset provides an opportunity for the future further development of the proposed solver and the development and validation of similar

solvers by other researchers within the academic community.

- Despite uncertainties in the experimental data and discrepancies in the prediction of the hydrodynamic variables, the comparisons between the numerical predictions and the experimental observations demonstrate the capability of the solver to capture the behaviour of the transport process through obstacles.

6.1.3 Future Work

There are opportunities to further validate the capacity of the solvers for a variety of useful and thus far, unexplored applications. First and foremost, is the opportunity to validate the transient capabilities of the solvers for gate flow and weir flow individually, using the analytical solutions provided by Cozzolino et al. [117, 119]. Depending on the results there may be further opportunities to enhance the solvers. Likewise, a thorough comparison between the presented solvers and comparable published solvers across an exhaustive set of validation test cases would be valuable for both developers and practitioners.

It may also be worth investigating and comparing the results obtained by implementing a path-conservative scheme and numerically computing the exact external eigenvalues for Solver 2, to determine if the results are improved. From a practical perspective it would be useful to know whether the results are improved by an exact computation of the external eigenvalues, even if it is potentially computationally expensive and also the extent to which the solvers differ with a path conservative treatment.

An ideal scenario would be to implement the solvers within a mature state-of-the-art numerical code, such as Newcastle University's CityCAT, for field-scale application and field-scale validation of the solvers. However, this may require significant further work relating to the automatic identification and meshing of linear partial barriers to flow such that the method is practical for use in realistic scenarios. Furthermore, topographic source terms, which have been neglected throughout, would be necessary to include for any realistic field-scale application. As briefly discussed, a well-balanced treatment of the topographic source terms may be facilitated via the hydrostatic reconstruction method [31] or via upwinding of the source terms [57]. For solver 1, this is a straightforward process since the numerical solution procedure is compatible with both methods. For solver 2 the process is less straightforward when upwinding the source terms to achieve a well-balanced treatment of the topographic sources, as excess numerical diffusion may be introduced since it is necessary to set the wavespeed in each layer to the maximum wavespeed present within a single layer. The hydrostatic reconstruction method is therefore a more straightforward solution.

Provided a suitable meshing algorithm can be developed and a well-balanced treatment of topographic source terms is implemented, then a thorough comparison between the presented solvers and alternative methods, particularly those commonly used within contemporary industry practice, would be extremely valuable in order to promote commercial uptake.

It would also be interesting to explore, on a smaller scale, the detailed modelling of an urban intersection considering intruding flows and micro-scale topography, as explored by Dewals et al. [138] and Mignot et al. [315]. The flexible nature of the presented solvers potentiates the possibility of a general treatment of all barriers to flow and the proposed scenario is a perfect sandbox for maximally testing this capacity. This is likely to be of

commercial interest to insurance and/or reinsurance companies as existing methods of estimating exposure are relatively simplistic and may result in a significant underestimation or overestimation of the expected damages induced by a flood event. By modelling explicitly, the intrusion of flows into buildings it would be possible to more accurately ascertain the expected damages. However, this is an ambitious target since the mechanisms enabling intrusion of flood flows into properties are highly uncertain and current surveying practices provide inadequate data resolution (providing information only on the building footprint). Furthermore, for solver 2, there may be significant challenges related to the computational burden and practical implementation of the solution procedure if a large percentage of the domain includes partial barriers to flow.

Regarding the conducted planar concentration analyses, further work to reduce surface reflections, enabling the use of lower concentrations which confer higher sensitivity would be valuable. As would further exploration of methods to enable expansion of the observation areas to facilitate the analysis of the mass conservation across the domain. Furthermore, it would be useful to explore other scenarios such as weir flow and combined gate and weir flow to truly ascertain the limitations of the proposed solver.

With regards to the development of the solver there is clearly much progress still to be made. Whilst the initial results demonstrate promise, the development of a sophisticated method which is capable of minimising numerical diffusion, ensuring boundedness of concentration values and a high order of spatial accuracy for primitive and conserved variables is challenging and requires careful investigation. The proposal to explore the application of high order central weighted essentially non-oscillatory reconstruction, with particular focus on the reconstruction of the primitive variables appears promising in this regard.

Bibliography

[1] K.E.K. Abderrezzak et al. "Division of critical flow at three-branch open-channel intersection". In: *Journal of Hydraulic Research* 49.2 (2011), pp. 231–238. DOI: 10.1080/00221686.2011.558174.

[2] M. Abdulkareem and H. Elkadi. "From engineering to evolutionary, an overarching approach in identifying the resilience of urban design to flood". In: *International Journal of Disaster Risk Reduction* 28 (2018), pp. 176–190. ISSN: 2212-4209. DOI: 10.1016/j.ijdrr.2018.02.009.

[3] R. Abgrall and S. Karni. "A comment on the computation of non-conservative products". In: *Journal of Computational Physics* 229.8 (2010), pp. 2759–2763. ISSN: 00219991. DOI: 10.1016/j.jcp.2009.12.015.

[4] R. Abgrall and S. Karni. "Two-Layer Shallow Water System: A Relaxation Approach". In: *SIAM Journal on Scientific Computing* 31.3 (2009), pp. 1603–1627. ISSN: 1064-8275 1095-7197. DOI: 10.1137/06067167x.

[5] S.R. Abt et al. "Human Stability in a high flood hazard zone". In: *JAWRA Journal of the American Water Resources Association* 25.4 (1989), pp. 881–890. DOI: 10.1111/j.1752-1688.1989.tb05404.x.

[6] W. Addison-Atkinson et al. "Modelling urban sewer flooding and quantitative microbial risk assessment: A critical review". In: *Journal of Flood Risk Management* 15.4 (2022), e12844. DOI: 10.1111/jfr3.12844.

[7] Z. Ahmad. "Prediction of longitudinal dispersion coefficient using laboratory and field data: relationship comparisons". In: *Hydrology Research* 44.2 (2013), pp. 362–376. ISSN: 0029-1277 2224-7955. DOI: 10.2166/nh.2012.047.

[8] F. Ahmed et al. "Strengthening the Bridge Between Academic and the Industry Through the Academia-Industry Collaboration Plan Design Model". In: *Frontiers in Psychology* 13 (2022), p. 875940. DOI: 10.3389/fpsyg.2022.875940.

[9] W. Ahmed et al. "A review on microbial contaminants in stormwater runoff and outfalls: Potential health risks and mitigation strategies". In: *Science of The Total Environment* 692 (2019), pp. 1304–1321. ISSN: 0048-9697. DOI: 10.1016/j.scitotenv.2019.07.055.

[10] J.M. Ahn et al. "Predicting Cyanobacterial Blooms Using Hyperspectral Images in a Regulated River". In: *Sensors* 21.2 (2021). DOI: 10.3390/s21020530.

[11] F. Alcrudo. *Mathematical modelling techniques for flood propagation in urban areas.* Report. 2004.

[12] F. Alcrudo. *Mathematical modelling techniques for flood propagation in urban areas*. Tech. rep. EU IMPACT. URL: https://www.yumpu.com/en/document/view/52385789/mathematical-modelling-techniques-for-flood-propagation-impact (visited on 03/03/2024).

[13] F. Alcrudo and F. Benkhaldoun. "Exact solutions to the Riemann problem of the shallow water equations with a bottom step". In: *Computers & Fluids* 30.6 (2001), pp. 643–671. ISSN: 0045-7930. DOI: 10.1016/S0045-7930(01)00013-5.

[14] F. Alcrudo and J. Mulet-Marti. "Urban inundation models based upon the Shallow Water equations. Numerical and practical issues Marrakesh July 2005". In: *Finite Volumes for Complex Applications IV. Problems and Perspectives*. Ed. by F Benkhaldoun, D Ouazar, and S Raghay. Marrakesh: Hermes Science Pub, 2005, pp. 1–12.

[15] F. Alcrudo et al. "The model city flooding experiment". In: *Proc. 2nd Project Workshop EC Contract EVG1-CT-2001-00037 IMPACT Investigation of Extreme Flood Processes and Uncertainty. Mo i Rana (Norway)*. 2002, p. 17.

[16] A. Ali. *Flood Inundation Modeling and Hazard Mapping under Uncertainty in the Sungai Johor Basin, Malaysia*. 1st. CRC Press, 2018. DOI: 10.1201/9780429469015.

[17] O. Alminagorta and G.P. Merkley. "Transitional flow between orifice and nonorifice regimes at a rectangular sluice gate". In: *Journal of Irrigation and Drainage Engineering* 135.3 (2009), pp. 382–387. DOI: 10.1061/(ASCE)IR.1943-4774.0000071.

[18] S. Amiri, M. Mazaheri, and J. Mohammad Vali Samani. "Introducing a general framework for pollution source identification in surface water resources (theory and application)". In: *Journal of Environmental Management* 248 (2019), p. 109281. ISSN: 0301-4797. DOI: 10.1016/j.jenvman.2019.109281.

[19] E. Anagnostou, A. Gianni, and I. Zacharias. "Ecological modeling and eutrophication-A review". In: *Natural Resource Modeling* 30.3 (2017), e12130. DOI: 10.1111/nrm.12130.

[20] I. Anderson et al. "Analysis of bridge and stream conditions of over 300 Vermont bridges damaged in Tropical Storm Irene". In: *Structure and Infrastructure Engineering* 13.11 (2017), pp. 1437–1450. DOI: 10.1080/15732479.2017.1285329.

[21] I. Anderson et al. "Stream Power Application for Bridge-Damage Probability Mapping Based on Empirical Evidence from Tropical Storm Irene". In: *Journal of Bridge Engineering* 22.5 (2017), p. 05017001. DOI: 10.1061/(ASCE)BE.1943-5592.0001022.

[22] M. Andrle and A. El Badia. "On an inverse source problem for the heat equation. Application to a pollution detection problem, II". In: *Inverse Problems in Science and Engineering* 23.3 (2015), pp. 389–412. DOI: 10.1080/17415977.2014.906415.

[23] S.R Arques et al. "Cost effective measuring technique to simultaneously quantify 2D velocity fields and depth-averaged solute concentrations in shallow water flows". In: *Flow Measurement and Instrumentation* 64 (2018), pp. 213–223. ISSN: 09555986. DOI: 10.1016/j.flowmeasinst.2018.10.022.

[24] C. Arrighi, M. Pregnolato, and F. Castelli. "Indirect flood impacts and cascade risk across interdependent linear infrastructures". In: *Natural Hazards and Earth System Sciences* 21.6 (2021), pp. 1955–1969. DOI: 10.5194/nhess-21-1955-2021.

[25] H. Arst. *Optical Properties and Remote Sensing of Multicomponental Water Bodies*. 1st ed. Springer Berlin, Heidelberg, 2003. ISBN: 978-3-540-00629-9.

[26] A.H. Arthington et al. "Preserving the biodiversity and ecological services of rivers: new challenges and research opportunities". In: *Freshwater Biology* 55.1 (2010), pp. 1–16. DOI: 10.1111/j.1365-2427.2009.02340.x.

[27] N. Arya Azar, S. Ghordoyee Milan, and Z. Kayhomayoon. "The prediction of longitudinal dispersion coefficient in natural streams using LS-SVM and ANFIS optimized by Harris hawk optimization algorithm". In: *J Contam Hydrol* 240 (2021), p. 103781. ISSN: 1873-6009 (Electronic) 0169-7722 (Linking). DOI: 10.1016/j.jconhyd.2021.103781.

[28] R.M. Ashley et al. "Flooding in the future–predicting climate change, risks and responses in urban areas". In: *Water Sci Technol* 52.5 (2005), pp. 265–273.

[29] E. Audusse. "A multilayer Saint-Venant model: Derivation and numerical validation". In: *Discrete and Continuous Dynamical Systems - B* 5.2 (2005), pp. 189–214. ISSN: 1531-3492. DOI: 10.3934/dcdsb.2005.5.189.

[30] E. Audusse and M.O. Bristeau. "Transport of Pollutant in Shallow Water A Two Time Steps Kinetic Method". In: *ESAIM: Mathematical Modelling and Numerical Analysis* 37.2 (2003), pp. 389–416. ISSN: 0764-583X 1290-3841. DOI: 10.1051/m2an:2003034.

[31] E. Audusse et al. "A Fast and Stable Well-Balanced Scheme with Hydrostatic Reconstruction for Shallow Water Flows". In: *SIAM Journal on Scientific Computing* 25.6 (2004), pp. 2050–2065. DOI: 10.1137/S1064827503431090.

[32] E. Audusse et al. "A multilayer Saint-Venant system with mass exchanges for shallow water flows. Derivation and numerical validation". In: *ESAIM: Mathematical Modelling and Numerical Analysis* 45.1 (2011), pp. 169–200. DOI: 10.1051/m2an/2010036.

[33] Australian Government. *Charter: National Water Quality Management Strategy*. Canberra: Department of Agriculture and Water Resources, Mar. 2018. URL: https://waterquality.gov.au.

[34] Autorità di Bacino del Po. *Regole per la costruzione in sicurezza e la verifica dei ponti sui corsi d'acqua contenute*. Italian. Deliberazione 11 maggio 1999, no. 2/99. 1999.

[35] M.T. Ayvaz. "A hybrid simulation-optimization approach for solving the areal groundwater pollution source identification problems". In: *Journal of Hydrology* 538 (2016), pp. 161–176. ISSN: 0022-1694. DOI: 10.1016/j.jhydrol.2016.04.008.

[36] M.T. Ayvaz. "A linked simulation-optimization model for solving the unknown groundwater pollution source identification problems". In: *Journal of Contaminant Hydrology* 117.1 (2010), pp. 46–59. ISSN: 0169-7722. DOI: 10.1016/j.jconhyd.2010.06.004.

[37] K. Baek. "Flowchart on Choosing Optimal Method of Observing Transverse Dispersion Coefficient for Solute Transport in Open Channel Flow". In: *Sustainability* 10.5 (2018). ISSN: 2071-1050. DOI: 10.3390/su10051332.

[38] K.O. Baek and I.W. Seo. "On the methods for determining the transverse dispersion coefficient in river mixing". In: *Advances in Water Resources* 90 (2016), pp. 1–9. ISSN: 03091708. DOI: 10.1016/j.advwatres.2016.01.009.

[39] K.O. Baek and I.W. Seo. "Prediction of transverse dispersion coefficient using vertical profile of secondary flow in meandering channels". In: *KSCE Journal of Civil Engineering* 12.6 (2008), pp. 417–426. ISSN: 1226-7988 1976-3808. DOI: 10.1007/s12205-008-0417-1.

[40] L.H. Bai and S. Jin. "A Conservative Coupled Flow/Transport Model with Zero Mass Error". In: *Journal of Hydrodynamics* 21.2 (2009), pp. 166–175. ISSN: 1001-6058 1878-0342. DOI: 10.1016/s1001-6058(08)60134-1.

[41] V. Bakhtiari et al. "A critical review for the application of cutting-edge digital visualisation technologies for effective urban flood risk management". In: *Sustainable Cities and Society* 99 (2023), p. 104958. ISSN: 2210-6707. DOI: 10.1016/j.scs.2023.104958.

[42] M. Barati Moghaddam, M. Mazaheri, and J. Mohammad Vali Samani. "Inverse modeling of contaminant transport for pollution source identification in surface and groundwaters: a review". In: *Groundwater for Sustainable Development* 15 (2021), p. 100651. ISSN: 2352-801X. DOI: 10.1016/j.gsd.2021.100651.

[43] G.K. Batchelor. *An Introduction to Fluid Dynamics*. Cambridge University Press, 1967. ISBN: 978-0-521-66396-0.

[44] P.D. Bates, M.S. Horritt, and T.J. Fewtrell. "A simple inertial formulation of the shallow water equations for efficient two-dimensional flood inundation modelling". In: *Journal of Hydrology* 387.1 (2010), pp. 33–45. ISSN: 0022-1694. DOI: 10.1016/j.jhydrol.2010.03.027.

[45] P.H. Bazin, E. Mignot, and A. Paquier. "Computing flooding of crossroads with obstacles using a 2D numerical model". In: *Journal of Hydraulic Research* 55.1 (2017), pp. 72–84. DOI: 10.1080/00221686.2016.1217947.

[46] P.H. Bazin et al. "Influence of Detailed Topography when Modeling Flows in Street Junction During Urban Flood". In: *Journal of Disaster Research* 7.5 (2012), pp. 560–566. URL: https://hal.inrae.fr/hal-02597823.

[47] J. Bear. *Dynamics of Fluids in Porous Media*. New York: Dover Publications, 1988.

[48] L. Begnudelli and B.F. Sanders. "Unstructured Grid Finite-Volume Algorithm for Shallow-Water Flow and Scalar Transport with Wetting and Drying". In: *Journal of Hydraulic Engineering* 132.4 (2006), pp. 371–384. ISSN: 0733-9429 1943-7900. DOI: 10.1061/(asce)0733-9429(2006)132:4(371).

[49] L. Begnudelli, B.F. Sanders, and S.F. Bradford. "Adaptive Godunov-Based Model for Flood Simulation". In: *Journal of Hydraulic Engineering* 134.6 (2008), pp. 714–725. DOI: 10.1061/(ASCE)0733-9429(2008)134:6(714).

[50] L. Begnudelli, A. Valiani, and B.F. Sanders. "A balanced treatment of secondary currents, turbulence and dispersion in a depth-integrated hydrodynamic and bed deformation model for channel bends". In: *Advances in Water Resources* 33.1 (2010), pp. 17–33. ISSN: 0309-1708. DOI: 10.1016/j.advwatres.2009.10.004.

[51] C.E. Behlke and H.D. Pritchett. "The design of supercritical flow channel junctions". In: *Transportation Research Record* 123 (1966).

[52] F. Behzadi, B. Shamsaei, and J.C. Newman. "Solution of fully-coupled shallow water equations and contaminant transport using a primitive-variable Riemann method". In: *Environmental Fluid Mechanics* 18.2 (2017), pp. 515–535. ISSN: 1567-7419 1573-1510. DOI: 10.1007/s10652-017-9571-7.

[53] F. Benkhaldoun, I. Elmahi, and M. Seaïd. "Well-balanced finite volume schemes for pollutant transport by shallow water equations on unstructured meshes". In: *Journal of Computational Physics* 226.1 (2007), pp. 180–203. ISSN: 00219991. DOI: 10.1016/j.jcp.2007.04.005.

[54] J.R. Benn et al. *Afflux at Bridges and Culverts. Review of current knowledge and practice*. Report. JBA Consulting, 2004.

[55] R. Beretta et al. "Simulating the Influence of Buildings on Flood Inundation in Urban Areas". In: *Geosciences* 8.2 (2018). ISSN: 2076-3263. DOI: 10.3390/geosciences8020077.

[56] M.J. Berger and P. Colella. "Local adaptive mesh refinement for shock hydrodynamics". In: *Journal of Computational Physics* 82.1 (1989), pp. 64–84. ISSN: 0021-9991. DOI: 10.1016/0021-9991(89)90035-1.

[57] A. Bermudez and E. Vazquez. "Upwind methods for hyperbolic conservation laws with source terms". In: *Computers & Fluids* 23.8 (1994), pp. 1049–1071. DOI: 10.1016/0045-7930(94)90004-3.

[58] R. Bernetti, V.A. Titarev, and E.F. Toro. "Exact solution of the Riemann problem for the shallow water equations with discontinuous bottom geometry". In: *Journal of Computational Physics* 227.6 (2008), pp. 3212–3243. ISSN: 0021-9991. DOI: 10.1016/j.jcp.2007.11.033.

[59] C. Berthon, F. Foucher, and T. Morales. "An efficient splitting technique for two-layer shallow-water model". In: *Numerical Methods for Partial Differential Equations* 31.5 (2015), pp. 1396–1423. DOI: 10.1002/num.21949.

[60] Chebbo G. Bertrand-Krajewski J. and Saget A. "Distribution of pollutant mass vs volume in stormwater discharges and the first flush phenomenon". In: *Water Research* 32 (1998), pp. 2341–2356.

[61] R. Bertsch, V. Glenis, and C. Kilsby. "Building level flood exposure analysis using a hydrodynamic model". In: *Environmental Modelling & Software* 156 (2022), p. 105490. ISSN: 1364-8152. DOI: 10.1016/j.envsoft.2022.105490.

[62] J.L. Best and I. Reid. "Separation zone at open-channel junctions". In: *Journal of Hydraulic Engineering* 110.11 (1984), pp. 1588–1594.

[63] G. Bickford et al. "Aquatic Ecological and Human Health Risk Assessment of Chemicals in Wet Weather Discharges in the Sydney Region, New South Wales, Australia". In: *Marine Pollution Bulletin* 39.1 (1999), pp. 335–345. ISSN: 0025-326X. DOI: 10.1016/S0025-326X(99)00057-0.

[64] M. Bijankhan, V. Ferro, and S. Kouchakzadeh. "New stage-discharge relationships for free and submerged sluice gates". In: *Flow Measurement and Instrumentation* 28 (2012), pp. 50–56. ISSN: 0955-5986. DOI: 10.1016/j.flowmeasinst.2012.07.004.

[65] M.L. Blau, F. Luz, and T. Panagopoulos. "Urban River Recovery Inspired by Nature-Based Solutions and Biophilic Design in Albufeira, Portugal". In: *Land* 7.4 (2018). ISSN: 2073-445X. DOI: 10.3390/land7040141.

[66] L Bonaventura et al. "Multilayer shallow water models with locally variable number of layers and semi-implicit time discretization". In: *Journal of Computational Physics* 364 (2018), pp. 209–234. ISSN: 0021-9991. DOI: 10.1016/j.jcp.2018.03.017.

[67] R. Borsche, R.M. Colombo, and M. Garavello. "On the coupling of systems of hyperbolic conservation laws with ordinary differential equations". In: *Nonlinearity* 23.11 (2010), pp. 2749–2770. ISSN: 0951-7715 1361-6544. DOI: 10.1088/0951-7715/23/11/002.

[68] U. Bosi et al. "A spectral/hpelement depth-integrated model for nonlinear wave-body interaction". In: *Computer Methods in Applied Mechanics and Engineering* 348 (2019), pp. 222–249. ISSN: 00457825. DOI: 10.1016/j.cma.2019.01.020.

[69] D. Bouche, J.M. Ghidaglia, and F. Pascal. "Error Estimate and the Geometric Corrector for the Upwind Finite Volume Method Applied to the Linear Advection Equation". In: *SIAM Journal on Numerical Analysis* 43.2 (2005), pp. 578–603. ISSN: 0036-1429 1095-7170. DOI: 10.1137/040605941.

[70] F. Bouchut and T. Morales de Luna. "An entropy satisfying scheme for two-layer shallow water equations with uncoupled treatment". In: *ESAIM: Mathematical Modelling and Numerical Analysis* 42.4 (2008), pp. 683–698. ISSN: 0764-583X 1290-3841. DOI: 10.1051/m2an:2008019.

[71] C. E. Bowers. "Hydraulic model studies for Whiting Field Naval Air Station, Part V: Studies of open-channel junctions". In: *Technical Papers, Series B, St. Anthony Falls Laboratory, Univ. of Minnesota, Minneapolis* (1966).

[72] G.E. P. Box, A. Luñeño, and M.d.C Paniagua-Quiñones. *Statistical Control By Monitoring and Adjustment*. John Wiley & Sons, 2009.

[73] G.E.P. Box and A. Luñeño. *Statistical Control: By Monitoring and Feedback Adjustment*. John Wiley & Sons, 1997.

[74] G. Bradski. "The OpenCV Library". In: *Dr. Dobb's Journal of Software Tools* (2000).

[75] L. Brandimarte and M.K. Woldeyes. "Uncertainty in the estimation of backwater effects at bridge crossings". In: *Hydrological Processes* 27.9 (2013), pp. 1292–1300. DOI: 10.1002/hyp.9350.

[76] G Braschi and M Gallatti. "Simulation of level-breaking submersion of planes and urban areas". In: *Hydrocomp 89. Proceedings Int. Conf. on Computational Modeling and Experimental methods in Hydraulics*. Elsevier Applied Science. 1989.

[77] M.O. Bristeau, N. Goutal, and J. Sainte-Marie. "Numerical simulations of a non-hydrostatic shallow water model". In: *Computers & Fluids* 47.1 (2011), pp. 51–64. ISSN: 00457930. DOI: 10.1016/j.compfluid.2011.02.013.

[78] A.F. Brouwer, N.B. Masters, and J.N.S. Eisenberg. "Quantitative Microbial Risk Assessment and Infectious Disease Transmission Modeling of Waterborne Enteric Pathogens". In: *Current Environmental Health Reports* 5.2 (2018), pp. 293–304. ISSN: 2196-5412. DOI: 10.1007/s40572-018-0196-x.

[79] J.D. Brown, T. Spencer, and I. Moeller. "Modeling storm surge flooding of an urban area with particular reference to modeling uncertainties: A case study of Canvey Island, United Kingdom". In: *Water Resources Research* 43.6 (2007). ISSN: 0043-1397. DOI: 10.1029/2005WR004597.

[80] P Brufau, P Garcıa-Navarro, and M E Vázquez-Cendón. "Zero mass error using unsteady wetting–drying conditions in shallow flows over dry irregular topography". In: *International Journal for Numerical Methods in Fluids* 45.9 (2004), pp. 1047–1082. DOI: 10.1002/fld.729.

[81] G.W. Brunner. *HEC-RAS Hydraulic Reference Manual*. US Army Corps of Engineers. Hydrologic Engineering Center, California, 2020.

[82] R.P. Bukata et al. *Optical Properties and Remote Sensing of Inland and Coastal Waters*. 1st ed. CRC Press, 1995. ISBN: 9780367579678.

[83] J. Burguete, P. García-Navarro, and J. Murillo. "Preserving bounded and conservative solutions of transport in one-dimensional shallow-water flow with upwind numerical schemes: Application to fertigation and solute transport in rivers". In: *International Journal for Numerical Methods in Fluids* 56.9 (2007), pp. 1731–1764. ISSN: 0271-2091 1097-0363. DOI: 10.1002/fld.1576.

[84] Li Cai et al. "Computations of transport of pollutant in shallow water". In: *Applied Mathematical Modelling* 31.3 (2007), pp. 490–498. ISSN: 0307904X. DOI: 10.1016/j.apm.2005.11.011.

[85] V. Caleffi and A. Valiani. "A 2D local discontinuous Galerkin method for contaminant transport in channel bends". In: *Computers & Fluids* 88 (2013), pp. 629–642. ISSN: 00457930. DOI: 10.1016/j.compfluid.2013.10.023.

[86] C.F. von Carmer. "Shallow turbulent wake flows: momentum and mass transfer due to large-scale coherent vortical structures". Thesis. 2005. DOI: 10.5445/ksp/1000003453.

[87] M. Castro et al. "On the Hyperbolicity of Two- and Three-Layer Shallow Water Equations". In: *Hyperbolic Problems*. Series in Contemporary Applied Mathematics. Singapore: World Scientific Publishing, 2012, pp. 337–345. ISBN: 978-981-4417-06-8. DOI: 10.1142/9789814417099%5F0030.

[88] M. J. Castro, A. Pardo Milanés, and C. Parés. "Well-balanced numerical schemes based on a generalized hydrostatic reconstruction technique". In: *Mathematical Models and Methods in Applied Sciences* 17.12 (2007), pp. 2055–2113. DOI: 10.1142/S021820250700256X.

[89] M.J. Castro, T. Morales de Luna, and C. Parés. "Chapter 6 - Well-Balanced Schemes and Path-Conservative Numerical Methods". In: *Handbook of Numerical Methods for Hyperbolic Problems*. Ed. by R. Abgrall and C.W. Shu. Vol. 18. Handbook of Numerical Analysis. Elsevier, 2017, pp. 131–175. DOI: 10.1016/bs.hna.2016.10.002.

[90] M.J. Castro et al. "Why many theories of shock waves are necessary: Convergence error in formally path-consistent schemes". In: *Journal of Computational Physics* 227.17 (2008), pp. 8107–8129. ISSN: 0021-9991. DOI: 10.1016/j.jcp.2008.05.012.

[91] C. Cattaneo. "Sulla conduzione del calore". In: *Atti Semin. Mat. Fis. Univ. Modena* 3 (1949), pp. 83–101.

[92] L. Cea and P. Costabile. "Flood Risk in Urban Areas: Modelling, Management and Adaptation to Climate Change. A Review". In: *Hydrology* 9.3 (2022). ISSN: 2306-5338. DOI: 10.3390/hydrology9030050.

[93] L. Cea and A. López-Núñez. "Extension of the two-component pressure approach for modeling mixed free-surface-pressurized flows with the two-dimensional shallow water equations". In: *International Journal for Numerical Methods in Fluids* 93.3 (2021), pp. 628–652. ISSN: 0271-2091. DOI: 10.1002/fld.4902.

[94] L. Cea and M. E. Vázquez-Cendón. "Unstructured finite volume discretisation of bed friction and convective flux in solute transport models linked to the shallow water equations". In: *Journal of Computational Physics* 231.8 (2012), pp. 3317–3339. ISSN: 00219991. DOI: 10.1016/j.jcp.2012.01.007.

[95] L. Cea and M. E. Vázquez-Cendón. "Unstructured finite volume discretization of two-dimensional depth-averaged shallow water equations with porosity". In: *International Journal for Numerical Methods in Fluids* 63.8 (2009), pp. 903–930. ISSN: 0271-2091 1097-0363. DOI: 10.1002/fld.2107.

[96] L. Cea et al. "Hydraulic Modeling of Bridges in Two-Dimensional Shallow Water Models". In: *Journal of Hydraulic Engineering* 148.8 (2022). ISSN: 0733-9429 1943-7900. DOI: 10.1061/(asce)hy.1943-7900.0001992.

[97] L. Cea et al. "IberWQ: new simulation tool for 2D water quality modelling in rivers and shallow estuaries". In: *Journal of Hydroinformatics* 18.5 (May 2016), pp. 816–830. ISSN: 1464-7141. DOI: 10.2166/hydro.2016.235.

[98] Y. C. Chang. "Lateral mixing in meandering channels". PhD thesis. Iowa University, 1971.

[99] Y. Chen et al. "In Situ Simultaneous Analysis of Nitrogen and Phosphorus Migration in Urban Black Odorous Runoff". In: *International Journal of Environmental Research and Public Health* 19.20 (Oct. 2022), p. 13240. DOI: 10.3390/ijerph192013240.

[100] Y. Chen et al. "Urban river restoration in Hong Kong: Assessment, impact, and improvement strategies". In: *Sustainable Cities and Society* 99 (2023), p. 104885. ISSN: 2210-6707. DOI: 10.1016/j.scs.2023.104885.

[101] A. Chertock, A. Kurganov, and G. Petrova. "Finite-Volume-Particle Methods for Models of Transport of Pollutant in Shallow Water". In: *Journal of Scientific Computing* 27.1-3 (2006), pp. 189–199. ISSN: 0885-7474 1573-7691. DOI: 10.1007/s10915-005-9060-x.

[102] A. Chertock et al. "Three-Layer Approximation of Two-Layer Shallow Water Equations". In: *Mathematical Modelling and Analysis* 18.5 (2013), pp. 675–693. ISSN: 1392-6292 1648-3510. DOI: 10.3846/13926292.2013.869269.

[103] V.T. Chow. *Open-Channel Hydraulics*. New York: McGraw-Hill, 1959.

[104] D. Clarke. *A Review of the Floods in Northern England and North Wales January 2005*. Tech. rep. Environment Agency, Bristol, 2005.

[105] A. Cook and V. Merwade. "Effect of topographic data, geometric configuration and modeling approach on flood inundation mapping". In: *Journal of Hydrology* 377.1 (2009), pp. 131–142. ISSN: 0022-1694. DOI: 10.1016/j.jhydrol.2009.08.015.

[106] C. Copeland. "Clean Water Act: a summary of the law". In: Congressional research service, Library of Congress Washington, DC. 1999.

[107] P. Costabile, C. Costanzo, and F. Macchione. "Performances and limitations of the diffusive approximation of the 2-D shallow water equations for flood simulation in urban and rural areas". In: *Applied Numerical Mathematics* 116 (2017), pp. 141–156. DOI: 10.1016/j.apnum.2016.07.003.

[108] P. Costabile and F. Macchione. "Analysis of One-Dimensional Modelling for Flood Routing in Compound Channels". In: *Water Resources Management* 26.5 (2012), pp. 1065–1087. ISSN: 1573-1650. DOI: 10.1007/s11269-011-9947-2.

[109] P. Costabile et al. "Comparison of Scenarios with and without Bridges and Analysis of Backwater Effect in 1-D and 2-D River Flood Modeling". In: *Computer Modeling in Engineering & Sciences* 109-110.2 (2015), pp. 81–103. ISSN: 1526-1506. DOI: 10.3970/cmes.2015.109.081.

[110] P. Costabile et al. "Flood mapping using LIDAR DEM. Limitations of the 1-D modeling highlighted by the 2-D approach". In: *Natural Hazards* 77.1 (2015), pp. 181–204. ISSN: 1573-0840. DOI: 10.1007/s11069-015-1606-0.

[111] P. Costabile et al. "Is local flood hazard assessment in urban areas significantly influenced by the physical complexity of the hydrodynamic inundation model?" In: *Journal of Hydrology* 580 (2020), p. 124231. ISSN: 0022-1694. DOI: 10.1016/j.jhydrol.2019.124231.

[112] P. Costabile et al. "Representing skewed bridge crossing on 1-D and 2-D flood propagation models: compared analysis in practical studies". In: *Proceedings of the International Conference on Fluvial Hydraulics, River Flow 2014*. Ed. by Anton J Schleiss et al. CRC Press/Balkema, Taylor & Francis Group, 2014, pp. 733–741.

[113] P. Costabile et al. "Terrestrial and airborne laser scanning and 2-D modelling for 3-D flood hazard maps in urban areas: new opportunities and perspectives". In: *Environmental Modelling & Software* 135 (2021), p. 104889. ISSN: 1364-8152. DOI: 10.1016/j.envsoft.2020.104889.

[114] R. Courant, K.O. Friedrichs, and H. Lewy. *On the partial difference equations of mathematical physics*. NYO-7689. Translated from German. Institute for Mathematical Sciences, New York University, 1956.

[115] L. Cozzolino et al. "A Broad-crested Weir Boundary Condition in Finite Volume Shallow-water Numerical Models". In: *Procedia Engineering* 70 (2014), pp. 353–362. ISSN: 1877-7058. DOI: 10.1016/j.proeng.2014.02.040.

[116] L. Cozzolino et al. "A well-balanced spectral volume scheme with the wetting-drying property for the shallow-water equations". In: *Journal of Hydroinformatics* 14.3 (2012), pp. 745–760. ISSN: 1464-7141. DOI: 10.2166/hydro.2012.035.

[117] L. Cozzolino et al. "Boundary conditions in finite volume schemes for the solution of shallow-water equations: the non-submerged broad-crested weir". In: *Journal of Hydroinformatics* 16.6 (2014), pp. 1235–1249. ISSN: 1464-7141. DOI: 10.2166/hydro.2014.100.

[118] L. Cozzolino et al. "Exact Solution of the Dam-Break Problem for Constrictions and Obstructions in Constant Width Rectangular Channels". In: *Journal of Hydraulic Engineering* 143.11 (2017), p. 04017047. DOI: 10.1061/(ASCE)HY.1943-7900.0001368.

[119] L. Cozzolino et al. "Mathematical and numerical modelling of rapid transients at partially lifted sluice gates". In: *Advances in Water Resources* 181 (2023). ISSN: 03091708. DOI: 10.1016/j.advwatres.2023.104562.

[120] L. Cozzolino et al. "Multiple Solutions for the Riemann Problem in the Porous Shallow Water Equations". In: *HIC 2018. 13th International Conference on Hydroinformatics*. Ed. by Goffredo La Loggia et al. Vol. 3. EPiC Series in Engineering. EasyChair, 2018, pp. 476–484. DOI: 10.29007/31n4.

[121] L. Cozzolino et al. "Numerical solution of the discontinuous-bottom Shallow-water Equations with hydrostatic pressure distribution at the step". In: *Advances in Water Resources* 34.11 (2011), pp. 1413–1426. ISSN: 0309-1708. DOI: 10.1016/j.advwatres.2011.07.009.

[122] L. Cozzolino et al. "The analytic solution of the Shallow-Water Equations with partially open sluice-gates: The dam-break problem". In: *Advances in Water Resources* 80 (2015), pp. 90–102. ISSN: 0309-1708. DOI: 10.1016/j.advwatres.2015.03.010.

[123] L. Cozzolino et al. "The solution of the dam-break problem in the Porous Shallow water Equations". In: *Advances in Water Resources* 114 (2018), pp. 83–101. ISSN: 0309-1708. DOI: 10.1016/j.advwatres.2018.01.026.

[124] J. A. Cunge, F. M. Holly, and A. Verwey. *Practical aspects of computational river hydraulics*. Boston: Pitman, 1980.

[125] J. A. Cunge and M. Wegner. "Intégration numérique des équations d'écoulement de barré de Saint-Venant par un schéma implicite de différences finies". In: *La Houille Blanche* 50.1 (1964), pp. 33–39. DOI: 10.1051/lhb/1964002.

[126] F. Cupola, M. G. Tanda, and A. Zanini. "Contaminant release history identification in 2-D heterogeneous aquifers through a minimum relative entropy approach". In: *SpringerPlus* 4.1 (2015). DOI: 10.1186/s40064-015-1465-x.

[127] G. DalMaso, P.G. LeFloch, and F. Murat. "Definition and weak stability of nonconservative products". In: *Journal de Mathématiques Pures et Appliquées* 74 (1995), pp. 483–548.

[128] R.J. Dawson, R. Peppe, and M. Wang. "An agent-based model for risk-based flood incident management". In: *Natural Hazards* 59.1 (2011), pp. 167–189. ISSN: 1573-0840. DOI: 10.1007/s11069-011-9745-4.

[129] S Dazzi, R Vacondio, and P Mignosa. "Internal boundary conditions for a GPU-accelerated 2D shallow water model: Implementation and applications". In: *Advances in Water Resources* 137 (2020). ISSN: 03091708. DOI: 10.1016/j.advwatres.2020.103525.

[130] A. Defina. "Two-dimensional shallow flow equations for partially dry areas". In: *Water Resources Research* 36.11 (2000), pp. 3251–3264. ISSN: 0043-1397. DOI: 10.1029/2000WR900167.

[131] A. Defina, L. D'Alpaos, and B. Mattichio. "A new set of equations for very shallow water and partially dry areas suitable to 2D numerical models". In: *Proceedings of the specialty conference "Modelling flood propagation over initially dry areas"*. Ed. by Pierpaolo Molinaro and Luigi Natale. New York: American Society of Civil Engineers, 1994, pp. 82–101.

[132] A. Defina and F.M. Susin. "Hysteretic behavior of the flow under a vertical sluice gate". In: *Physics of Fluids* 15.9 (2003), pp. 2541–2548. ISSN: 1070-6631. DOI: 10.1063/1.1596193.

[133] V.V. Degtyarev et al. "Comparison of theory and experiment in simulation of dam break in a rectangular channel with a sudden change in cross-sectional area". In: *Journal of Applied Mechanics and Technical Physics* 55.6 (2014), pp. 999–1004. ISSN: 1573-8620. DOI: 10.1134/S0021894414060108.

[134] O. Delestre and F. Marche. "A Numerical Scheme for a Viscous Shallow Water Model with Friction". In: *Journal of Scientific Computing* 48.1 (2011), pp. 41–51. ISSN: 1573-7691. DOI: 10.1007/s10915-010-9393-y.

[135] A. I. Delis and Th Katsaounis. "A Generalized Relaxation Method for Transport and Diffusion of Pollutant Models in Shallow Water". In: *Computational Methods in Applied Mathematics* 4.4 (2004), pp. 410–430. ISSN: 1609-9389 1609-4840. DOI: 10.2478/cmam-2004-0023.

[136] A.I. Delis, H. Guillard, and Y.C. Tai. "Numerical simulations of hydraulic jumps with the Shear Shallow Water model". en. In: *The SMAI Journal of computational mathematics* 4 (2018), pp. 319–344. DOI: 10.5802/smai-jcm.37.

[137] S. Dellacherie. "Analysis of Godunov type schemes applied to the compressible Euler system at low Mach number". In: *Journal of Computational Physics* 229.4 (Feb. 2010), pp. 978–1016. DOI: 10.1016/j.jcp.2009.09.044.

[138] B. Dewals et al. "Can the 2D shallow water equations model flow intrusion into buildings during urban floods?" In: *Journal of Hydrology* 619 (2023), p. 129231. ISSN: 0022-1694. DOI: 10.1016/j.jhydrol.2023.129231.

[139] E. Diamanti-Kandarakis et al. "Endocrine-disrupting chemicals: an Endocrine Society scientific statement". In: *Endocrine reviews* 30.4 (2009), pp. 293–342. DOI: 10.1210/er.2009-0002.

[140] M.J. Castro Diaz et al. "Discussion on Different Numerical Treatments of the Loss of Hyperbolicity for the Two-Layer Shallow Water System". In: *Advances in Water Resources* 182 (2023).

[141] X. Ding and P. Fang. "Accident Trend Prediction of Heavy Metal Pollution in the Heshangshan Drinking Water Source Area Based on Integrating a Two-Dimensional Water Quality Model and GIS". In: *Sustainability* 11.15 (2019). ISSN: 2071-1050. DOI: 10.3390/su11153998.

[142] B. Diskin and J.L. Thomas. "Notes on accuracy of finite-volume discretization schemes on irregular grids". In: *Applied Numerical Mathematics* 60.3 (2010), pp. 224–226. ISSN: 0168-9274. DOI: 10.1016/j.apnum.2009.12.001.

[143] S. Djordjević, D. Prodanović, and C. Maksimović. "An approach to simulation of dual drainage". In: *Water Science and Technology* 39.9 (1999), pp. 95–103. ISSN: 0273-1223. DOI: 10.1016/S0273-1223(99)00221-8.

[144] B. Dong et al. "Experimental and numerical model studies on flash flood inundation processes over a typical urban street". In: *Advances in Water Resources* 147 (2021), p. 103824. ISSN: 0309-1708. DOI: 10.1016/j.advwatres.2020.103824.

[145] J. G. Duan. "Simulation of flow and mass dispersion in meandering channels". In: *Journal of Hydraulic Engineering* 130.10 (2004), pp. 964–976.

[146] M. Dumbser and E. F. Toro. "A simple extension of the Osher Riemann solver to non-conservative hyperbolic systems". In: *Journal of Scientific Computing* 48.1-3 (2011), pp. 70–88. DOI: 10.1007/s10915-010-9408-0.

[147] I. Echeverribar et al. "Analysis of the performance of a hybrid CPU/GPU 1D2D coupled model for real flood cases". In: *Journal of Hydroinformatics* 22.5 (July 2020), pp. 1198–1216. ISSN: 1464-7141. DOI: 10.2166/hydro.2020.032.

[148] Organisation for Economic Co-operation and Development (OECD). *Financial Management of Flood Risk*. 2016, p. 136. DOI: 10.1787/9789264257689-en.

[149] J.W. Elder. "The dispersion of marked fluid in turbulent shear flow". In: *J. Fluid Mech.* 5 (1959), pp. 544–560.

[150] J. Ellis. "Gates and shallow water waves". In: *Proc. Inst. Civ. Eng., Part 2* 61.3 (1976), pp. 507–523. DOI: 10.1680/iicep.1976.3404.

[151] B. Engquist and S. Osher. "One-sided difference approximations for nonlinear conservation laws". In: *Journal of Computational Physics* 36 (1981), pp. 321–351.

[152] Environment Agency, Department for Environment, Food and Rural Affairs, The Water Services Regulation Authority, and Rebecca Pow MP. *Progress made but too many water companies still falling short*. Press release. July 2021. URL: https://www.gov.uk/government/news/progress-made-but-too-many-water-companies-still-falling-short.

[153] E.V. Escobar-Silva et al. "Assessing the Extent of Flood-Prone Areas in a South-American Megacity Using Different High Resolution DTMs". In: *Water* 15.6 (2023). ISSN: 2073-4441. DOI: 10.3390/w15061127.

[154] Euromag International. *Electromagnetic Flowmeters. Sensors. Instruction Manual*. Euromag International. Mestrino (Padova), Italy, 2019.

[155] Euromag International. *Sensor MUT2200EL Electromagnetic Flowmeter*. Euromag International. Mestrino (Padova), Italy, 2021.

[156] European Commission. *The European Union Water Initiative*. EUWI Background Document at the World Summit on Sustainable Development, Johannesburg. Available at https://www.euwi.net/. Aug. 2002. URL: https://www.euwi.net.

[157] European Parliament and the Council. *Directive 2007/60/EC on the Assessment and Management of Flood Risks*. EU: Brussels, Belgium. 2007.

[158] Federal Highway Administration. *Highways in the River Environment*. Tech. rep. Technical Report No. 90-016; 683. 1990.

[159] E. D. Fernández-Nieto, E. H. Koné, and T. Chacón Rebollo. "A Multilayer Method for the Hydrostatic Navier-Stokes Equations: A Particular Weak Solution". In: *Journal of Scientific Computing* 60.2 (2013), pp. 408–437. ISSN: 0885-7474 1573-7691. DOI: 10.1007/s10915-013-9802-0.

[160] D. Fernández-Nóvoa et al. "Numerical simulation of the deadliest flood event of Portugal: Unravelling the causes of the disaster". In: *Science of The Total Environment* 896 (2023), p. 165092. ISSN: 0048-9697. DOI: 10.1016/j.scitotenv.2023.165092.

[161] J. Fernández-Pato and P. García-Navarro. "An Efficient GPU Implementation of a Coupled Overland-Sewer Hydraulic Model with Pollutant Transport". In: *Hydrology* 8.4 (2021). ISSN: 2306-5338. DOI: 10.3390/hydrology8040146.

[162] A. Ferrari and R. Vacondio. "An augmented HLLEM ADER numerical model parallel on GPU for the porous Shallow Water Equations". In: *Computers & Fluids* 238 (2022), p. 105360. ISSN: 0045-7930. DOI: 10.1016/j.compfluid.2022.105360.

[163] A. Ferrari, R. Vacondio, and P. Mignosa. "A second-order numerical scheme for the porous shallow water equations based on a DOT ADER augmented Riemann solver". In: *Advances in Water Resources* 140 (2020), p. 103587. ISSN: 0309-1708. DOI: 10.1016/j.advwatres.2020.103587.

[164] A. Ferrari et al. "A 1D-2D Shallow Water Equations solver for discontinuous porosity field based on a Generalized Riemann Problem". In: *Advances in Water Resources* 107 (2017), pp. 233–249. ISSN: 0309-1708. DOI: 10.1016/j.advwatres.2017.06.023.

[165] A. Ferrari et al. "Flood inundation modeling in urbanized areas: A mesh-independent porosity approach with anisotropic friction". In: *Advances in Water Resources* 125 (2019), pp. 98–113. ISSN: 0309-1708. DOI: 10.1016/j.advwatres.2019.01.010.

[166] T. J. Fewtrell et al. "Evaluating the effect of scale in flood inundation modelling in urban environments". In: *Hydrological Processes* 22.26 (2008), pp. 5107–5118. ISSN: 0885-6087. DOI: 10.1002/hyp.7148.

[167] P. Finaud-Guyot et al. "An approximate-state Riemann solver for the two-dimensional shallow water equations with porosity". In: *International Journal for Numerical Methods in Fluids* 62.12 (2010), pp. 1299–1331. DOI: 10.1002/fld.2066.

[168] P. Finaud-Guyot et al. "Experimental insight for flood flow repartition in urban areas". In: *Urban Water Journal* 15.3 (2018), pp. 242–250. DOI: 10.1080/1573062X.2018.1433861.

[169] *Flood Modeller Pro / Flood Modeller Free Release Notes Version 4.5*. Jacobs. 2023. URL: https://help.floodmodeller.com/docs/latest-release-notes.

[170] S. Soares Frazão et al. "The Impact European Research Project on Flood Propagation in Urban Areas: Experimental and Numerical Modelling of the Influence of Buildings on the Flow". In: *Flood Risk Management in Europe: Innovation in Policy and Practice*. Ed. by Selina Begum, Marcel J. F. Stive, and Jim W. Hall. Dordrecht: Springer Netherlands, 2007, pp. 191–211. ISBN: 978-1-4020-4200-3. DOI: 10.1007/978-1-4020-4200-3_11.

[171] S. Soares Frazão et al. *The isolated building test case: results from the IMPACT benchmark*. Tech. rep. EU IMPACT. URL: https://www.yumpu.com/en/document/view/52447241/isolated-building-benchmark-tests-impact (visited on 03/03/2024).

[172] Z.F. Fu et al. "Discharge Coefficient of Combined Orifice-Weir Flow". In: *Water* 10.6 (2018). ISSN: 2073-4441. DOI: 10.3390/w10060699.

[173] S. Fuchs et al. "Flood risk perception and adaptation capacity: a contribution to the socio-hydrology debate". In: *Hydrology and Earth System Sciences* 21.6 (2017), pp. 3183–3198. DOI: 10.5194/hess-21-3183-2017.

[174] H.A. Gallegos, J.E. Schubert, and B.F. Sanders. "Two-dimensional, high-resolution modeling of urban dam-break flooding: A case study of Baldwin Hills, California". In: *Advances in Water Resources* 32.8 (2009), pp. 1323–1335. ISSN: 0309-1708. DOI: 10.1016/j.advwatres.2009.05.008.

[175] H.A. Gallegos, J.E. Schubert, and B.F. Sanders. "Two-dimensional, high-resolution modeling of urban dam-break flooding: A case study of Baldwin Hills, California". In: *Advances in Water Resources* 32.8 (2009), pp. 1323–1335. ISSN: 0309-1708. DOI: 10.1016/j.advwatres.2009.05.008.

[176] T.W. Gallien, J.E. Schubert, and B.F. Sanders. "Predicting tidal flooding of urbanized embayments: a modeling framework and data requirements". In: *Coastal Engineering* 58.6 (2011), pp. 567–577.

[177] G. García-Alén et al. "Iber-Pest: Automatic Calibration in Fully Distributed Hydrological Models Based on the 2D Shallow Water Equations". In: *SSRN* (2024). Preprint. DOI: http://dx.doi.org/10.2139/ssrn.4745388. eprint: 4745388.

[178] P. García-Navarro, E. Playán, and N. Zapata. "Solute Transport Modeling in Overland Flow Applied to Fertigation". In: *Journal of Irrigation and Drainage Engineering* 126.1 (2000), pp. 33–40. DOI: 10.1061/(ASCE)0733-9437(2000)126:1(33).

[179] V. Glenis, V. Kutija, and C.G. Kilsby. "A fully hydrodynamic urban flood modelling system representing buildings, green space and interventions". In: *Environmental Modelling & Software* 109 (2018), pp. 272–292. ISSN: 1364-8152. DOI: 10.1016/j.envsoft.2018.07.018.

[180] V. Glenis et al. "Flood modelling for cities using Cloud computing". In: *Journal of Cloud Computing: Advances, Systems and Applications* 2.1 (2013), p. 7. ISSN: 2192-113X. DOI: 10.1186/2192-113X-2-7.

[181] K. Glińska-Lewczuk et al. "The impact of urban areas on the water quality gradient along a lowland river". In: *Environmental Monitoring and Assessment* 188.11 (2016), p. 624. DOI: 10.1007/s10661-016-5638-z.

[182] E Godlewski et al. "Congested shallow water model: roof modeling in free surface flow". In: *ESAIM: M2AN* 52.5 (2018), pp. 1679–1707. DOI: 10.1051/m2an/2018032.

[183] H. Gómez et al. "A finite element formulation for a convection-diffusion equation based on Cattaneo's law". In: *Computer Methods in Applied Mechanics and Engineering* 196.9 (2007), pp. 1757–1766. ISSN: 0045-7825. DOI: 10.1016/j.cma.2006.09.016.

[184] G. Gordillo et al. "A GPU-based 2D shallow water quality model". In: *Journal of Hydroinformatics* 22.5 (July 2020), pp. 1182–1197. DOI: 10.2166/hydro.2020.030.

[185] J.A. Gore, ed. *The Restoration of Rivers and Streams: Theories and Experience*. Ann Arbor, MI: Butterworth, 1985.

[186] M. S. Goudiaby and G. Kreiss. "Existence result for the coupling of shallow water and Borda-Carnot equations with Riemann data". In: *Journal of Hyperbolic Differential Equations* 17.01 (2020), pp. 185–212. ISSN: 0219-8916. DOI: 10.1142/S021989162050006X.

[187] F. Greco, P. Lonetti, and P. Nevone Blasi. "Impact mitigation measures for bridges under extreme flood actions". In: *Journal of Fluids and Structures* 106 (2021), p. 103381. ISSN: 0889-9746. DOI: 10.1016/j.jfluidstructs.2021.103381.

[188] T. Gschnitzer et al. "Towards a robust assessment of bridge clogging processes in flood risk management". In: *Geomorphology* 279 (2017), pp. 128–140. ISSN: 0169-555X. DOI: 10.1016/j.geomorph.2016.11.002.

[189] M. Guan et al. "Bottom-up multilevel flood hazard mapping by integrated inundation modelling in data scarce cities". In: *Journal of Hydrology* 617 (2023), p. 129114. ISSN: 0022-1694. DOI: 10.1016/j.jhydrol.2023.129114.

[190] G. Guerra, M. Herty, and F. Marcellini. "Modeling and analysis of pooled stepped chutes". In: *Networks & Heterogeneous Media* 6.4 (2011), pp. 665–679. ISSN: 1556-181X. DOI: 10.3934/nhm.2011.6.665.

[191] S.B. Guerreiro et al. "Pluvial Flooding in European Cities-A Continental Approach to Urban Flood Modelling". In: *Water* 9.4 (2017). ISSN: 2073-4441. DOI: 10.3390/w9040296.

[192] Hervé Guillard and Angelo Murrone. "On the behavior of upwind schemes in the low Mach number limit: II. Godunov type schemes". In: *Computers & Fluids* 33.4 (2004), pp. 655–675. ISSN: 0045-7930. DOI: 10.1016/j.compfluid.2003.07.001.

[193] V. Guinot. "Consistency and bicharacteristic analysis of integral porosity shallow water models. Explaining model oversensitivity to mesh design". In: *Advances in Water Resources* 107 (2017), pp. 43–55. ISSN: 0309-1708. DOI: 10.1016/j.advwatres.2017.06.008.

[194] V. Guinot. "Multiple porosity shallow water models for macroscopic modelling of urban floods". In: *Advances in Water Resources* 37 (2012), pp. 40–72. ISSN: 03091708. DOI: 10.1016/j.advwatres.2011.11.002.

[195] V. Guinot and C. Delenne. "Macroscopic modelling of urban floods". In: *La Houille Blanche* 6 (2014), pp. 19–25. DOI: 10.1051/lhb/2014058.

[196] V. Guinot, B.F. Sanders, and J.E. Schubert. "Dual integral porosity shallow water model for urban flood modelling". In: *Advances in Water Resources* 103 (2017), pp. 16–31. ISSN: 03091708. DOI: 10.1016/j.advwatres.2017.02.009.

[197] V. Guinot and S. Soares-Frazão. "Flux and source term discretization in two-dimensional shallow water models with porosity on unstructured grids". In: *International Journal for Numerical Methods in Fluids* 50.3 (2006), pp. 309–345. ISSN: 0271-2091. DOI: 10.1002/fld.1059.

[198] K. Guo, M. Guan, and D. Yu. "Urban surface water flood modelling - a comprehensive review of current models and future challenges". In: *Hydrology and Earth System Sciences* 25.5 (2021), pp. 2843–2860. DOI: 10.5194/hess-25-2843-2021.

[199] W. D. Guo et al. "Finite-Volume Multi-Stage Scheme for Advection-Diffusion Modeling in Shallow Water Flows". In: *Journal of Mechanics* 27.3 (2011), pp. 415–430. ISSN: 1727-7191 1811-8216. DOI: 10.1017/jmech.2011.44.

[200] S. K. Gurram and K. S. Karki. "Subcritical open-channel junction flow: Discussion". In: *Journal of Hydraulic Engineering* 126.1 (2000), pp. 87–89.

[201] S. K. Gurram, K. S. Karki, and W. H. Hager. "Subcritical junction flow". In: *Journal of Hydraulic Engineering* 123.5 (1997), pp. 447–455.

[202] G. Gzyl et al. "Contaminant source and release history identification in groundwater: A multi-step approach". In: *Journal of Contaminant Hydrology* 157 (2014), pp. 59–72. ISSN: 0169-7722. DOI: 10.1016/j.jconhyd.2013.11.006.

[203] A. Habibzadeh, A.R. Vatankhah, and N. Rajaratnam. "Role of energy loss on discharge characteristics of sluice gates". In: *ASCE Journal of Hydraulic Engineering* 137.9 (2011), pp. 1079–1084. DOI: 10.1061/(ASCE)HY.1943-7900.0000406.

[204] J. Hadamard. *Lectures on Cauchy's Problem in Linear Partial Differential Equations*. New Haven: Yale University Press, 1923.

[205] W. H. Hager. "Transitional flow in channel junctions". In: *Journal of Hydraulic Engineering* 115.2 (1989), pp. 243–259.

[206] S. Haider. "Contribution A La Modelisation D'une Inondation En Zone Urbanisee. Approche Bidimensionnelle Par Les Equations De Saint Venant". Thesis. 2001.

[207] S. Haider et al. "Urban flood modelling using computational fluid dynamics". In: *Proceedings of the Institution of Civil Engineers - Water and Maritime Engineering* 156.2 (2003), p. 6. ISSN: 1472-4561. DOI: doi.org/10.1680/wame.2003.156.2.129.

[208] F.M. Hailemariam, L. Brandimarte, and F. Dottori. "Investigating the influence of minor hydraulic structures on modeling flood events in lowland areas". In: *Hydrological Processes* 28.4 (2014), pp. 1742–1755. DOI: 10.1002/hyp.9717.

[209] A. Hamdi and I. Mahfoudhi. "Inverse source problem based on two dimensionless dispersion-current functions in 2D evolution transport equations". In: *Journal of Inverse and Ill-posed Problems* 24.6 (2016), pp. 663–685. DOI: doi:10.1515/jiip-2014-0051.

[210] A. Hamdi and I. Mahfoudhi. "Inverse source problem in a one-dimensional evolution linear transport equation with spatially varying coefficients: application to surface water pollution". In: *Inverse Problems in Science and Engineering* 21.6 (2013), pp. 1007–1031. DOI: 10.1080/17415977.2013.764871.

[211] E. Han and G. Warnecke. "Exact Riemann solutions to shallow water equations". In: *Quarterly of Applied Mathematics* 72.3 (2014), pp. 407–453. ISSN: 0033-569X 1552-4485. DOI: 10.1090/s0033-569x-2014-01353-3.

[212] A. Harten, P.D. Lax, and B. van Leer. "On Upstream Differencing and Godunov-Type Schemes for Hyperbolic Conservation Laws". In: *Upwind and High-Resolution Schemes*. Ed. by M.Y. Hussaini, B. van Leer, and J. Van Rosendale. Berlin, Heidelberg: Springer Berlin Heidelberg, 1997, pp. 53–79. DOI: 10.1007/978-3-642-60543-7_4.

[213] A. Hazart et al. "Inverse transport problem of estimating point-like source using a Bayesian parametric method with MCMC". In: *Signal Processing* 96 (2014), pp. 346–361. ISSN: 0165-1684. DOI: 10.1016/j.sigpro.2013.08.013.

[214] Q. He et al. "Water quality improvement for upgrading urban landscapes". In: *Water-Wise Cities and Sustainable Water Systems: Concepts, Technologies, and Applications*. IWA Publishing, Jan. 2021. ISBN: 9781789060768. DOI: 10.2166/9781789060768_0357.

[215] F.M. Henderson. *Open Channel Flow*. New York: The McMillan Co., 1966.

[216] H.R. Henry. "Discussion of 'Diffusion of submerged jets' by M.L. Albertson, Y.B. Doi, R.A. Jensen ad H. Rouse". In: *Trans. ASCE* 115 (1950), pp. 687–694. DOI: 10.1061/TACEAT.0006368.

[217] D. Henstra, A. Minano, and J. Thistlethwaite. "Communicating disaster risk? An evaluation of the availability and quality of flood maps". In: *Natural Hazards and Earth System Sciences* 19.1 (2019), pp. 313–323. DOI: 10.5194/nhess-19-313-2019.

[218] Jean-Michel Hervouet, René Samie, and Benoit Moreau. "Modelling urban areas in dam-break flood-wave numerical simulations". In: *RESCDAM Seminar*. Sinajöki, Finland, Sept. 2000. URL: https://api.semanticscholar.org/CorpusID:220925302.

[219] A. Hidalgo and M. Dumbser. "ADER Schemes for Nonlinear Systems of Stiff Advection-Diffusion-Reaction Equations". In: *Journal of Scientific Computing* 48.1 (2011), pp. 173–189. ISSN: 1573-7691. DOI: 10.1007/s10915-010-9426-6.

[220] Highways England. *Highway Structures & Bridges Design CD 356: Design of highway structures for hydraulic action (formerly BA 59/94), Revision 1*. Technical Report CD 356. Guildford, UK: Highways England, 2020.

[221] J.O. Hinze. *Turbulence*. New York: McGraw Hill Publishing Co., 1975.

[222] Y. Hirabayashi et al. "Global flood risk under climate change". In: *Nature Climate Change* 3.9 (2013), pp. 816–821. ISSN: 1758-678X 1758-6798. DOI: 10.1038/nclimate1911.

[223] A.O. Hopland and S.F. Kvamsdal. "Drinking water contamination and treatment costs". In: *Water Resources and Economics* 43 (2023), p. 100225. ISSN: 2212-4284. DOI: 10.1016/j.wre.2023.100225.

[224] T.Y. Hou and P.G. Le Floch. "Why Nonconservative Schemes Converge to Wrong Solutions: Error Analysis". In: *Mathematics of Computation* 62.206 (1994), pp. 497–530. ISSN: 00255718, 10886842. DOI: 10.2307/2153520.

[225] C.C. Hsu, W.J. Lee, and C.H. Chang. "Subcritical open-channel junction flow". In: *Journal of Hydraulic Engineering* 124.8 (1998), pp. 847–855.

[226] C.C. Hsu et al. "Subcritical 90° equal-width open-channel dividing flow". In: *Journal of Hydraulic Engineering* 128.7 (2002), pp. 716–720.

[227] J.C. Huang, L.J. Weber, and Y.G. Lai. "Three-dimensional numerical study of flows in open-channel junctions". In: *Journal of Hydraulic Engineering* 128.3 (2002), pp. 268–280.

[228] S.A. Hughes. *Physical Modelling and Laboratory Techniques in Coastal Engineering*. Singapore: World Scientific Publishing Co. Pte. Ltd., 1995.

[229] T. Iguchi and D. Lannes. "Hyperbolic Free Boundary Problems and Applications to Wave Structure Interactions". In: *Indiana University Mathematics Journal* (2019).

[230] C. Iliadis and C. Glenis V.and Kilsby. "Representing buildings and urban features in hydrodynamic flood models". In: *Journal of Flood Risk Management* (Sept. 2023). DOI: 10.1111/jfr3.12950.

[231] C. Iliadis, V. Glenis, and C. Kilsby. "Cloud Modelling of Property-Level Flood Exposure in Megacities". In: *Water* 15.19 (2023). ISSN: 2073-4441. DOI: 10.3390/w15193395.

[232] C. Iliadis, V. Glenis, and C. Kilsby. "Cloud Modelling of Property-Level Flood Exposure in Megacities". In: *Water* 15.19 (2023). ISSN: 2073-4441. DOI: 10.3390/w15193395.

[233] *InfoWorks ICM: Key Concepts*. Innovyze. 2023. URL: https://help2.innovyze.com/infoworksicm/Content/HTML/ICM_IN_ILCM/InfoWorks_Key_Concepts.htm.

[234] Innovyze. *Inline Banks in InfoWorks ICM*. https://www.innovyze.com/en-us/blog/inline-banks-in-infoworks-icm. Accessed: 2022-06-29. 2014.

[235] A. T. Ippen. "Mechanics of supercritical flow, 1st paper of high-velocity flow in open channels: a symposium". In: *Transactions, Engineering Journal of ASCE; Proceedings of the American Society of Civil Engineers* 116 (1951), pp. 268–295.

[236] T Ishigaki, K Toda, and K Inoue. "Hydraulic model tests of inundation in urban area with underground space". In: *Proceedings of the 30th IAHR Congress*. Vol. B. AUTh, Greece, 2003, pp. 487–493.

[237] H.H. Jaafar and G.P. Merkley. "High-Resolution Method for Modeling Hydraulic Regime Changes at Canal Gate Structures". In: *Journal of Irrigation and Drainage Engineering* 136.12 (2010), pp. 795–808. DOI: 10.1061/(ASCE)IR.1943-4774.0000263.

[238] M. Jia and H. Jia. "LID-BMPs for urban runoff pollutant source control". In: *Water-Wise Cities and Sustainable Water Systems: Concepts, Technologies, and Applications*. IWA Publishing, Jan. 2021. ISBN: 9781789060768. DOI: 10.2166/9781789060768_0325.

[239] T. Jin et al. "A data-driven model for real-time water quality prediction and early warning by an integration method". In: *Environmental Science and Pollution Research* 26.29 (2019), pp. 30374–30385. ISSN: 1614-7499. DOI: 10.1007/s11356-019-06049-2.

[240] S.N. Jonkman and E. Penning-Rowsell. "Human Instability in Flood Flows". In: *JAWRA Journal of the American Water Resources Association* 44.5 (2008), pp. 1208–1218. DOI: 10.1111/j.1752-1688.2008.00217.x.

[241] Kelly J. Kaatz and Wesley P. James. "Analysis of Alternatives for Computing Backwater at Bridges". In: *Journal of Hydraulic Engineering* 123.9 (1997), pp. 784–792. DOI: 10.1061/(ASCE)0733-9429(1997)123:9(784).

[242] S.C. Kao et al. "Towards the Development of An Operational Hydrodynamic Flood Simulation Capability - A Multi-GPU TRITON Framework". In: *AGU Fall Meeting Abstracts*. Vol. 2020. Dec. 2020, H196-0011, H196–0011.

[243] A. Keating et al. *Operationalizing Resilience Against Natural Disaster Risk: Opportunities, Barriers, and a Way Forward*. May 2014. URL: opim.wharton.upenn.edu/risk/library/zurichfloodresiliencealliance_ResilienceWhitePaper_2014.pdf.

[244] K. Kerenyi, T. Sofu, and J. Guo. "Hydrodynamic forces on inundated bridge decks". In: *Journal of Hydraulic Research* 47.4 (2009), pp. 473–480.

[245] A.A. Khan, R. Cadavid, and S.S.Y. Wang. "Simulation of channel confluence and bifurcation using the CCHE2D model". In: *Water and Maritime Engineering* 142 (2000), pp. 97–102.

[246] A. Khosronejad, S. Kang, and F. Sotiropoulos. "Experimental and computational investigation of local scour around bridge piers". In: *Advances in Water Resources* 37 (2012), pp. 73–85. ISSN: 0309-1708. DOI: 10.1016/j.advwatres.2011.09.013.

[247] S. Kim et al. "Chemical accidents in freshwater: Development of forecasting system for drinking water resources". In: *Journal of Hazardous Materials* 432 (2022), p. 128714. ISSN: 0304-3894. DOI: 10.1016/j.jhazmat.2022.128714.

[248] K.Ya. Kondratyev and Nikolai Filatov. *Limnology and Remote Sensing*. 1st ed. Springer Praxis Books. London: Springer London, 1999. ISBN: 978-1-85233-112-2.

[249] J. Kong et al. "A high-resolution method for the depth-integrated solute transport equation based on an unstructured mesh". In: *Environmental Modelling & Software* 40 (2013), pp. 109–127. ISSN: 13648152. DOI: 10.1016/j.envsoft.2012.08.009.

[250] O.A. Kovyrkina and V.V. Ostapenko. "Comparison between the theory and the numerical experiment in the problem of dam break on a jump of the cross-sectional area of a rectangular channel". In: *Fluid Dynamics* 48.3 (2013), pp. 291–302. ISSN: 1573-8507. DOI: 10.1134/S0015462813030022.

[251] L. Krivodonova. "An efficient local time-stepping scheme for solution of nonlinear conservation laws". In: *Journal of Computational Physics* 229.22 (2010), pp. 8537–8551. ISSN: 0021-9991. DOI: 10.1016/j.jcp.2010.07.037.

[252] Sam Kubba. "Chapter 5 - Building Information Modeling". In: *Handbook of Green Building Design and Construction*. Ed. by S. Kubba. Boston: Butterworth-Heinemann, 2012, pp. 201–226. ISBN: 978-0-12-385128-4. DOI: 10.1016/B978-0-12-385128-4.00005-6.

[253] A. Kurganov and G. Petrova. "Central-Upwind Schemes for Two-Layer Shallow Water Equations". In: *SIAM Journal on Scientific Computing* 31.3 (2009), pp. 1742–1773. DOI: 10.1137/080719091.

[254] D. Kvočka, R.A. Falconer, and M. Bray. "Appropriate model use for predicting elevations and inundation extent for extreme flood events". In: *Natural Hazards* 79.3 (2015), pp. 1791–1808. ISSN: 1573-0840. DOI: 10.1007/s11069-015-1926-0.

[255] A. Lacasta et al. "Simulation of PID Control Applied to Irrigation Channels". In: *Procedia Engineering* 70 (2014), pp. 978–987. ISSN: 18777058. DOI: 10.1016/j.proeng.2014.02.109.

[256] S. N. Lane et al. "Numerical modeling of flow processes over gravelly surfaces using structured grids and a numerical porosity treatment". In: *Water Resources Research* 40.1 (2004). DOI: 10.1029/2002WR001934.

[257] B. Latorre et al. "Accurate and efficient simulation of transport in multidimensional flow". In: *International Journal for Numerical Methods in Fluids* 65.4 (2011), pp. 405–431. ISSN: 0271-2091. DOI: 10.1002/fld.2189.

[258] S.W. Law and A.J. Reynolds. "Dividing flow in open channel". In: *Journal of Hydraulic Division* 92.HY2 (1966), pp. 207–231.

[259] P. D. Lax and B. Wendroff. "Systems of conservation laws". In: *Communications on Pure and Applied Mathematics* 13 (1960), pp. 217–237.

[260] T. Lazzarin et al. "Flow under vertical sluice gates: Flow stability at large gate opening and disambiguation of partial dam-break multiple solutions". In: *Physics of Fluids* 35.2 (2023), p. 024114. ISSN: 1070-6631. DOI: 10.1063/5.0131953.

[261] S. Leakey, V. Glenis, and C.J.M. Hewett. "A novel Godunov-type scheme for free-surface flows with artificial compressibility". In: *Computer Methods in Applied Mechanics and Engineering* 393 (2022). ISSN: 00457825. DOI: 10.1016/j.cma.2022.114763.

[262] S. Leakey et al. “Investigating the Behaviour of Leaky Barriers with Flume Experiments and 3D Modelling”. In: *Advances in Hydroinformatics*. Ed. by P. Gourbesville and G. Caignaert. Singapore: Springer Nature Singapore, 2022, pp. 965–978. ISBN: 978-981-19-1600-7.

[263] S. Leakey et al. “Modelling the Impact of Leaky Barriers with a 1D Godunov-Type Scheme for the Shallow Water Equations”. In: *Water* 12.2 (2020). ISSN: 2073-4441. DOI: 10.3390/w12020371.

[264] P.G. LeFloch and A.E. Tzavaras. “Existence theory for the Riemann problem for non-conservative hyperbolic systems”. English (US). In: *Comptes Rendus de l’Academie des Sciences - Series I: Mathematics* 323.4 (1996), pp. 347–352. ISSN: 0764-4442.

[265] P.G. LeFloch and A.E. Tzavaras. “Representation of Weak Limits and Definition of Nonconservative Products”. In: *SIAM Journal on Mathematical Analysis* 30.6 (1999), pp. 1309–1342. DOI: 10.1137/S0036141098341794.

[266] J. Leibinger et al. “A path-conservative Osher-type scheme for axially symmetric compressible flows in flexible viscoelastic tubes”. In: *Applied Numerical Mathematics* 105 (2016), pp. 47–63. DOI: 10.1016/j.apnum.2016.03.008.

[267] S. Leichombam and R. Bhattacharjya. “Identification of Unknown Groundwater Pollution Sources and Determination of Optimal Well Locations Using ANN-GA Based Simulation-Optimization Model”. In: *Journal of Water Resource and Protection* 8 (2016), pp. 411–424. DOI: 10.4236/jwarp.2016.83034.

[268] R.J. LeVeque. *Finite Volume Methods for Hyperbolic Problems*. Cambridge Texts in Applied Mathematics. Cambridge University Press, 2002. DOI: 10.1017/CBO9780511791253.

[269] R.J. LeVeque. *Numerical Methods for Conservation Laws*. 2nd ed. Lectures in Mathematics. ETH Zürich. Birkhäuser Basel, 1992, p. 220. ISBN: 978-3-7643-2723-1. DOI: 10.1007/978-3-0348-8629-1.

[270] J. Lhomme. “One-dimensional, two-dimensional and macroscopic approaches to urban flood modelling”. French. PhD thesis. Université Montpellier, 2006.

[271] S. Li and C.J. Duffy. “Fully-Coupled Modeling of Shallow Water Flow and Pollutant Transport on Unstructured Grids”. In: *Procedia Environmental Sciences* 13 (2012), pp. 2098–2121. ISSN: 18780296. DOI: 10.1016/j.proenv.2012.01.200.

[272] Z. Li et al. “Estimation of river pollution source using the space-time radial basis collocation method”. In: *Advances in Water Resources* 88 (2016), pp. 68–79. ISSN: 0309-1708. DOI: 10.1016/j.advwatres.2015.11.019.

[273] D. Liang et al. “Solving the depth-integrated solute transport equation with a TVD-MacCormack scheme”. In: *Environmental Modelling & Software* 25.12 (2010), pp. 1619–1629. ISSN: 13648152. DOI: 10.1016/j.envsoft.2010.06.008.

[274] Q. Liang and F. Marche. “Numerical resolution of well-balanced shallow water equations with complex source terms”. In: *Advances in Water Resources* 32.6 (2009), pp. 873–884. ISSN: 0309-1708. DOI: 10.1016/j.advwatres.2009.02.010.

[275] Q. Liang and F. Marche. “Numerical resolution of well-balanced shallow water equations with complex source terms”. In: *Advances in Water Resources* 32.6 (2009), pp. 873–884. ISSN: 03091708. DOI: 10.1016/j.advwatres.2009.02.010.

[276] C. H. Lin, J. F. Yen, and C. T. Tsai. "Influence of Sluice Gate Contraction Coefficient on Distinguishing Condition". In: *Journal of Irrigation and Drainage Engineering* 128.4 (2002), pp. 249–252. DOI: 10.1061/(ASCE)0733-9437(2002)128:4(249).

[277] N. Lind, D. Hartford, and H. Assaf. "Hydrodynamic Models of Human Stability in a Flood". In: *JAWRA Journal of the American Water Resources Association* 40.1 (2004), pp. 89–96. DOI: 10.1111/j.1752-1688.2004.tb01012.x.

[278] L. Liu et al. "Building performance in dam-break flow - an experimental study". In: *Urban Water Journal* 15.3 (2018), pp. 251–258. DOI: 10.1080/1573062X.2018.1433862.

[279] M. Loli et al. "Flood characterization based on forensic analysis of bridge collapse using UAV reconnaissance and CFD simulations". In: *Science of The Total Environment* 822 (2022), p. 153661. ISSN: 0048-9697. DOI: 10.1016/j.scitotenv.2022.153661.

[280] P. Lonetti and R. Maletta. "Dynamic impact analysis of masonry buildings subjected to flood actions". In: *Engineering Structures* 167 (2018), pp. 445–458. ISSN: 0141-0296. DOI: 10.1016/j.engstruct.2018.03.076.

[281] B.C. Lugão, D.C. Knupp, and P.P.G.W. Rodriges. "Direct and inverse simulation applied to the identification and quantification of point pollution sources in rivers". In: *Environmental Modelling & Software* 156 (2022), p. 105488. ISSN: 1364-8152. DOI: 10.1016/j.envsoft.2022.105488.

[282] H. Luo et al. "Comparative 1D and 3D numerical investigation of open-channel junction flows and energy losses". In: *Advances in Water Resources* 117 (2018), pp. 120–139. ISSN: 0309-1708. DOI: 10.1016/j.advwatres.2018.05.012.

[283] L. Luo et al. "A new method for point pollution source identification based on remote sensing inversion and water streamlines". In: *Journal of Hydrology* 628 (2024), p. 130571. ISSN: 0022-1694. DOI: 10.1016/j.jhydrol.2023.130571.

[284] J.M.V. Samani M. Mazaheri and H.M.V. Samani. "Mathematical Model for Pollution Source Identification in Rivers". In: *Environmental Forensics* 16.4 (2015), pp. 310–321. DOI: 10.1080/15275922.2015.1059391.

[285] F. Macchione et al. "Extracting quantitative data from non-conventional information for the hydraulic reconstruction of past urban flood events. A case study". In: *Journal of Hydrology* 576 (2019), pp. 443–465. ISSN: 0022-1694. DOI: 10.1016/j.jhydrol.2019.06.031.

[286] T. Maijala, M. Huokuna, and T. Honkakunnas. *RESCDAM: Development of Rescue Actions Based on Dam-Break Flood Analysis*. Final Report Grant Agreement No Subv 99/52623. P.O. Box 140, FIN-00251 Helsinki, Finland: Finnish Environment Institute, June 2001, p. 47.

[287] A. Malekpour and B.W. Karney. "Spurious Numerical Oscillations in the Preissmann Slot Method: Origin and Suppression". In: *Journal of Hydraulic Engineering* 142.3 (2016), p. 04015060. ISSN: 0733-9429 1943-7900. DOI: 10.1061/(ASCE)hy.1943-7900.0001106.

[288] M.A Mallin, V.L Johnson, and S.H Ensign. "Comparative impacts of stormwater runoff on water quality of an urban, a suburban, and a rural stream". In: *Environmental Monitoring and Assessment* 159.1-4 (2009), pp. 475–491.

[289] A. Maranzoni and P. Mignosa. "Numerical treatment of a discontinuous top surface in 2D shallow water mixed flow modeling". In: *International Journal for Numerical Methods in Fluids* 86.4 (2018), pp. 290–311. ISSN: 02712091. DOI: 10.1002/fld.4418.

[290] A. Maranzoni and M. Tomirotti. "New formulation of the two-dimensional steep-slope shallow water equations. Part I: Theory and analysis". In: *Advances in Water Resources* 166 (2022), p. 104255. ISSN: 0309-1708. DOI: 10.1016/j.advwatres.2022.104255.

[291] A. Maranzoni and M. Tomirotti. "New formulation of the two-dimensional steep-slope shallow water equations. Part II: Numerical modeling, validation, and application". In: *Advances in Water Resources* 177 (2023), p. 104403. ISSN: 0309-1708. DOI: 10.1016/j.advwatres.2023.104403.

[292] A. Maranzoni and M. Tomirotti. "Three-Dimensional Numerical Modelling of Real-Field Dam-Break Flows: Review and Recent Advances". In: *Water* 15.17 (2023). ISSN: 2073-4441. DOI: 10.3390/w15173130.

[293] O. Mark et al. "A new methodology for modelling of health risk from urban flooding exemplified by cholera - case Dhaka, Bangladesh". In: *Journal of Flood Risk Management* 11.S1 (2018), S28–S42. DOI: 10.1111/jfr3.12182.

[294] O. Mark et al. "Potential and limitations of 1D modelling of urban flooding". In: *Journal of Hydrology* 299.3 (2004), pp. 284–299. ISSN: 0022-1694. DOI: 10.1016/j.jhydrol.2004.08.014.

[295] K. Marks and P.D. Bates. "Integration of high resolution topographic data with floodplain flow models". English. In: *Hydrological Processes* 14 (2000). Publisher: John Wiley & Sons, pp. 2109–2122. ISSN: 1099-1085.

[296] J.P. Martín-Vide et al. "Large wood debris that clogged bridges followed by a sudden release. The 2019 flash flood in Catalonia." In: *Journal of Hydrology: Regional Studies* 47 (2023), p. 101348. ISSN: 2214-5818. DOI: 10.1016/j.ejrh.2023.101348.

[297] E. Martínez-Gomariz et al. "Stability criteria for flooded vehicles: a state-of-the-art review". In: *Journal of Flood Risk Management* 11.S2 (2018), S817–S826. DOI: 10.1111/jfr3.12262.

[298] J. Mateo-Lázaro et al. "Comparative Hydrodynamic Analysis by Using Two-Dimensional Models and Application to a New Bridge". In: *Water* 12.4 (2020). ISSN: 2073-4441. DOI: 10.3390/w12040997.

[299] B. Mazzorana et al. "Determining flood hazard patterns through a combined stochastic-deterministic approach". In: *Natural Hazards* 59.1 (2011), pp. 301–316. ISSN: 1573-0840. DOI: 10.1007/s11069-011-9755-2.

[300] Bruce M. McEnroe. *Downstream Effects of Culvert and Bridge Replacement*. Tech. rep. University of Kansas. Center for Research, University of Kansas. Dept. of Civil, Environmental, and Architectural Engineering, Mar. 2006. URL: https://rosap.ntl.bts.gov/view/dot/36542.

[301] J. Mckenna. "Investigating the Limitations of Industry Standard Urban Flood Inundation Modelling Software". MA thesis. Newcastle University, Newcastle upon-Tyne, 2019.

[302] J. McKenna, V. Glenis, and C. Kilsby. "A Local Multi-Layer Approach to Modelling Interactions between Shallow Water Flows and Obstructions". In: *arXiv preprint arXiv:2304.10262* (2023).

[303] J. Mckenna, V. Glenis, and C. Kilsby. "A new Riemann solver for modelling bridges in flood flows - Development and experimental validation". In: *Applied Mathematics and Computation* 447 (2023), p. 127870. ISSN: 0096-3003. DOI: 10.1016/j.amc.2023.127870.

[304] M.A. Mejía-Morales et al. "Impact of the porosity of an urban block on the flood risk assessment: A laboratory experiment". In: *Journal of Hydrology* 602 (2021), p. 126715. ISSN: 0022-1694. DOI: 10.1016/j.jhydrol.2021.126715.

[305] B. Merz, A.H. Thieken, and M. Gocht. "Flood Risk Mapping At The Local Scale: Concepts and Challenges". In: *Flood Risk Management in Europe: Innovation in Policy and Practice*. Ed. by Selina Begum, Marcel J. F. Stive, and Jim W. Hall. Dordrecht: Springer Netherlands, 2007, pp. 231–251. ISBN: 978-1-4020-4200-3. DOI: 10.1007/978-1-4020-4200-3_13.

[306] E. Metcalf. *University of Florida and Water Resources Engineers, Inc, Storm Water Management Model, Volume I-Final Report*. EPA Report 11024 DOC 07/71 (NTIS PB-203289). Washington, DC: Environmental Protection Agency, 1971, p. 352.

[307] V. Meyer et al. "Recommendations for the user-specific enhancement of flood maps". In: *Natural Hazards and Earth System Sciences* 12.5 (2012), pp. 1701–1716. DOI: 10.5194/nhess-12-1701-2012.

[308] E. Mignot, L. Camusson, and N. Riviere. "Measuring the flow intrusion towards building areas during urban floods: Impact of the obstacles located in the streets and on the facade". In: *Journal of Hydrology* 583 (2020), p. 124607. ISSN: 0022-1694. DOI: 10.1016/j.jhydrol.2020.124607.

[309] E. Mignot and B. Dewals. "Hydraulic modelling of inland urban flooding: Recent advances". In: *Journal of Hydrology* 609 (2022). ISSN: 00221694. DOI: 10.1016/j.jhydrol.2022.127763.

[310] E. Mignot, X. Li, and B. Dewals. "Experimental modelling of urban flooding: A review". In: *Journal of Hydrology* 568 (2019), pp. 334–342. ISSN: 0022-1694. DOI: 10.1016/j.jhydrol.2018.11.001.

[311] E. Mignot, N. Riviere, and B. Dewals. "Formulations and Diffusivity Coefficients of the 2D Depth-Averaged Advection-Diffusion Models: A Literature Review". In: *Water Resources Research* 59.12 (2023), e2023WR035053. ISSN: 0043-1397. DOI: 10.1029/2023WR035053.

[312] E. Mignot et al. "Closure to 'Flow patterns in a four branches junction with supercritical flow'". In: *Journal of Hydraulic Engineering* 135 (2009), pp. 1023–1024.

[313] E. Mignot et al. "Flow patterns in a four branches junction with supercritical flow". In: *Journal of Hydraulic Engineering* 134.6 (2008), pp. 701–713.

[314] E. Mignot et al. "Hydraulic Models of the Flow Distribution in a Four Branch Open Channel Junction with Supercritical Flow". In: *Journal of Hydraulic Engineering* 137.3 (2011), pp. 289–299. DOI: 10.1061/(ASCE)HY.1943-7900.0000302.

[315] E. Mignot et al. "Impact of topographic obstacles on the discharge distribution in open-channel bifurcations". In: *Journal of Hydrology* 494 (2013), pp. 10–19. ISSN: 0022-1694. DOI: 10.1016/j.jhydrol.2013.04.023.

[316] J. E. Miller. *Basic concepts of kinematic-wave models*. Report 1302. 1984. DOI: 10.3133/pp1302. URL: https://pubs.usgs.gov/publication/pp1302.

[317] E. Milnes and P. Perrochet. "Simultaneous identification of a single pollution point-source location and contamination time under known flow field conditions". In: *Advances in Water Resources* 30.12 (2007), pp. 2439–2446. ISSN: 0309-1708. DOI: 10.1016/j.advwatres.2007.05.013.

[318] X. Ming et al. "A quantitative multi-hazard risk assessment framework for compound flooding considering hazard inter-dependencies and interactions". In: *Journal of Hydrology* 607 (2022), p. 127477. ISSN: 0022-1694. DOI: 10.1016/j.jhydrol.2022.127477.

[319] A. Mohsen and C.Y. Solomon. "Simulation and Estimation of Tsunami Loads on Bridge Superstructures". In: *Journal of Waterway, Port, Coastal, and Ocean Engineering* 141.2 (2015), p. 04014031. DOI: 10.1061/(ASCE)WW.1943-5460.0000262.

[320] G.I. Montecinos and E.F. Toro. "Reformulations for general advection-diffusion-reaction equations and locally implicit ADER schemes". In: *Journal of Computational Physics* 275 (2014), pp. 415–442. ISSN: 00219991. DOI: 10.1016/j.jcp.2014.06.018.

[321] M. Morales-Hernández, J. Murillo, and P. García-Navarro. "Diffusion-dispersion numerical discretization for solute transport in 2D transient shallow flows". In: *Environmental Fluid Mechanics* 19.5 (2018), pp. 1217–1234. ISSN: 1567-7419 1573-1510. DOI: 10.1007/s10652-018-9644-2.

[322] M. Morales-Hernández, J. Murillo, and P. García-Navarro. "The formulation of internal boundary conditions in unsteady 2-D shallow water flows: Application to flood regulation". In: *Water Resources Research* 49.1 (2013), pp. 471–487. ISSN: 00431397. DOI: 10.1002/wrcr.20062.

[323] M. Morales-Hernández et al. "High-performance computing in water resources hydrodynamics". In: *Journal of Hydroinformatics* 22.5 (Mar. 2020), pp. 1217–1235. DOI: 10.2166/hydro.2020.163.

[324] J. Morgan. *Introduction to Geometrical and Physical Optics*. New York: McGraw-Hill Book Company, Inc, 1953.

[325] M. Morris and M. Hassan. "IMPACT: Investigation of extreme flood processes and uncertainty - a European research project". In: *Proceedings of the 40th DEFRA Flood and Coastal Management Conference*. HR Wallingford Ltd. University of York, UK, July 2005.

[326] R.D. Morris. "Drinking water and cancer". In: *Environ Health Perspect* 103.Suppl 8 (Nov. 1995), pp. 225–231. DOI: 10.1289/ehp.95103s8225.

[327] D.H. Munoz and G. Constantinescu. "A fully 3-D numerical model to predict flood wave propagation and assess efficiency of flood protection measures". In: *Advances in Water Resources* 122 (2018), pp. 148–165. ISSN: 03091708. DOI: 10.1016/j.advwatres.2018.10.014.

[328] Claus-Dieter Munz. "On the construction and comparison of two-step schemes for the Euler equations". In: *Notes Numer. Fluid Mech.* 14 (1986), pp. 195–217.

[329] J Murillo et al. "Extension of an explicit finite volume method to large time steps (CFL ¿ 1): application to shallow water flows". In: *International Journal for Numerical Methods in Fluids* 50 (2006), pp. 63–102.

[330] J. Murillo and P. García-Navarro. "Improved Riemann solvers for complex transport in two-dimensional unsteady shallow flow". In: *Journal of Computational Physics* 230.19 (2011), pp. 7202–7239. ISSN: 00219991. DOI: 10.1016/j.jcp.2011.05.022.

[331] J. Murillo, P. García-Navarro, and J. Burguete. "Analysis of a second-order upwind method for the simulation of solute transport in 2D shallow water flow". In: *International Journal for Numerical Methods in Fluids* 56.6 (2008), pp. 661–686. ISSN: 02712091 10970363. DOI: 10.1002/fld.1546.

[332] J. Murillo, P. García-Navarro, and J. Burguete. "Conservative numerical simulation of multi-component transport in two-dimensional unsteady shallow water flow". In: *Journal of Computational Physics* 228.15 (2009), pp. 5539–5573. ISSN: 00219991. DOI: 10.1016/j.jcp.2009.04.039.

[333] J. Murillo et al. "A Conservative 2D Model of Inundation Flow with Solute Transport over Dry Bed". In: *International Journal for Numerical Methods in Fluids* 52 (2006), p. 33. DOI: 10.1002/d.1216.

[334] J. Murillo et al. "Coupling between shallow water and solute flow equations: analysis and management of source terms in 2D". In: *International Journal for Numerical Methods in Fluids* 49.3 (2005), pp. 267–299. ISSN: 0271-2091 1097-0363. DOI: 10.1002/fld.992.

[335] L.S. Nania, M. Gomez, and J. Dolz. "Experimental study of the dividing flow in steep street crossings". In: *Journal of Hydraulic Research* 42.4 (2004), pp. 406–412.

[336] A. Nardini and S. Pavan. "River restoration: not only for the sake of nature but also for saving money while addressing flood risk. A decision-making framework applied to the Chiese River (Po basin, Italy)". In: *Journal of Flood Risk Management* 5.2 (2012), pp. 111–133. DOI: 10.1111/j.1753-318X.2011.01132.x.

[337] J.C. Neal et al. "Distributed whole city water level measurements from the Carlisle 2005 urban flood event and comparison with hydraulic model simulations". In: *Journal of Hydrology* 368.1 (2009), pp. 42–55. ISSN: 0022-1694. DOI: 10.1016/j.jhydrol.2009.01.026.

[338] Jeffrey Neal et al. "Optimisation of the two-dimensional hydraulic model LISFOOD-FP for CPU architecture". In: *Environmental Modelling Software* 107 (2018), pp. 148–157. ISSN: 1364-8152. DOI: 10.1016/j.envsoft.2018.05.011.

[339] V. S. Neary, F. Sotiropoulos, and A. J. Odgaard. "Three-Dimensional Numerical Model of Lateral-Intake Inflows". In: *Journal of Hydraulic Engineering* 125.2 (1999), pp. 126–140. DOI: 10.1061/(ASCE)0733-9429(1999)125:2(126).

[340] H. Nishikawa. "A first-order system approach for diffusion equation. II: Second-order residual-distribution schemes". In: *Journal of Computational Physics* 227.1 (2007), pp. 315–352. ISSN: 00219991. DOI: 10.1016/j.jcp.2007.07.029.

[341] R. Noori et al. "Reliability of functional forms for calculation of longitudinal dispersion coefficient in rivers". In: *Sci Total Environ* 791 (2021), p. 148394. ISSN: 1879-1026 (Electronic) 0048-9697 (Linking). DOI: 10.1016/j.scitotenv.2021.148394.

[342] J.J. O'Sullivan et al. "Enhancing flood resilience through improved risk communications". In: *Natural Hazards and Earth System Sciences* 12.7 (2012), pp. 2271–2282. DOI: 10.5194/nhess-12-2271-2012.

[343] M. Oberguggenberger. *Multiplication of Distributions and Applications to Partial Differential Equations*. Longman Scientific & Technical, 1992.

[344] S.J. Ormerod. "A golden age of river restoration science?" In: *Aquatic Conservation: Marine and Freshwater Ecosystems* 14.6 (2004), pp. 543–549. DOI: 10.1002/aqc.663.

[345] A. Osei-Twumasi, R. A. Falconer, and B. N. Bockelmann-Evans. "Experimental Studies on Water and Solute Transport Processes in a Hydraulic Model of the Severn Estuary, UK". In: *Water Resources Management* 29.6 (2015), pp. 1731–1748. ISSN: 1573-1650. DOI: 10.1007/s11269-014-0908-4.

[346] S. Osher and F. Solomon. "Upwind difference schemes for hyperbolic systems of conservation laws". In: *Mathematics of Computation* 38.158 (1982), pp. 339–374. ISSN: 0025-5718. DOI: 10.1090/S0025-5718-1982-0645656-0.

[347] V.V. Ostapenko. "Dam-break flows at a jump in the width of a rectangular channel". In: *Journal of Applied Mechanics and Technical Physics* 53.5 (2012), pp. 679–689. ISSN: 1573-8620. DOI: 10.1134/S0021894412050070.

[348] V.V. Ostapenko. "Discontinuous Solutions of the Shallow Water Equations for Flow Over a Bottom Step". In: *Journal of Applied Mechanics and Technical Physics* 43.6 (2002), pp. 836–846. ISSN: 1573-8620. DOI: 10.1023/A:1020708419286.

[349] V.V. Ostapenko. "Discontinuous solutions of the shallow water equations in a channel with an abrupt change in the cross sectional area". In: *Journal of Applied Mathematics and Mechanics* 76.6 (2012), pp. 666–676. ISSN: 0021-8928. DOI: 10.1016/j.jappmathmech.2013.02.004.

[350] K. Oudenbroek et al. "Hydrodynamic and Debris-Damming Failure of Bridge Decks and Piers in Steady Flow". In: *Geosciences* 8.11 (2018). ISSN: 2076-3263. DOI: 10.3390/geosciences8110409.

[351] M. Ouni, A. Habbal, and M. Kallel. "A three-player Nash game for point-wise source identification in Cauchy-Stokes problems". In: *Journal of Computational and Applied Mathematics* 417 (2023), p. 114613. ISSN: 0377-0427. DOI: 10.1016/j.cam.2022.114613.

[352] L.V. Ovsyannikov. "Two-layer "Shallow water" model". In: *Journal of Applied Mechanics and Technical Physics* 20.2 (1979), pp. 127–135. ISSN: 1573-8620. DOI: 10.1007/BF00910010.

[353] I. Özgen, D. Liang, and R. Hinkelmann. "Shallow water equations with depth-dependent anisotropic porosity for subgrid-scale topography". In: *Applied Mathematical Modelling* 40.17 (2016), pp. 7447–7473. ISSN: 0307-904X. DOI: 10.1016/j.apm.2015.12.012.

[354] F. Pappenberger et al. “Influence of uncertain boundary conditions and model structure on flood inundation predictions”. In: *Advances in Water Resources* 29.10 (2006), pp. 1430–1449. ISSN: 0309-1708. DOI: 10.1016/j.advwatres.2005.11.012.

[355] A. Paquier, E. Mignot, and P.H. Bazin. “From Hydraulic Modelling to Urban Flood Risk”. In: *Procedia Engineering* 115 (2015), pp. 37–44. ISSN: 1877-7058. DOI: 10.1016/j.proeng.2015.07.352.

[356] C. Parés. “Numerical methods for nonconservative hyperbolic systems: a theoretical framework.” In: *SIAM Journal on Numerical Analysis* 44.1 (2006), pp. 300–321. DOI: 10.1137/050628052.

[357] Y. Peng, J. G. Zhou, and R. Burrows. “Modelling solute transport in shallow water with the lattice Boltzmann method”. In: *Computers and Fluids* 50.1 (2011), pp. 181–188. ISSN: 00457930 (ISSN). DOI: 10.1016/j.compfluid.2011.07.008.

[358] Y. Peng et al. “Experimental and numerical estimation of velocity and concentration distributions in partially vegetated open channels”. In: *Journal of Hydrology* 628 (2024). ISSN: 00221694 (ISSN). DOI: 10.1016/j.jhydrol.2023.130537.

[359] V. Pepe et al. “The solution of the Riemann problem in rectangular channels with constrictions and obstructions”. In: *Advances in Water Resources* 129 (2019), pp. 146–164. ISSN: 03091708. DOI: 10.1016/j.advwatres.2019.05.013.

[360] G. Petaccia et al. “Flood wave propagation in steep mountain rivers”. In: *Journal of Hydroinformatics* 15.1 (2012), pp. 120–137. ISSN: 1464-7141. DOI: 10.2166/hydro.2012.122.

[361] M. Pregnolato. “Bridge safety is not for granted - A novel approach to bridge management”. In: *Engineering Structures* 196 (2019), p. 109193. ISSN: 0141-0296. DOI: 10.1016/j.engstruct.2019.05.035.

[362] M. Pregnolato et al. “Assessing flooding impact to riverine bridges: an integrated analysis”. In: *Natural Hazards and Earth System Sciences* 22.5 (2022), pp. 1559–1576. DOI: 10.5194/nhess-22-1559-2022.

[363] A. Preissmann. “Propagation des intumescences dans les canaux et rivières”. In: *1st Congress of the French Association for Computation (AFCALTI)*. 1961, pp. 433–442.

[364] R. W. Preston. *The representation of dispersion in two-dimensional shallow-water flow*. Report TPRD/L/2783/N84. Leatherhead, England: CEGB, 1985.

[365] J. Pyo et al. “Effect of hyperspectral image-based initial conditions on improving short-term algal simulation of hydrodynamic and water quality models”. In: *Journal of Environmental Management* 294 (2021), p. 112988. ISSN: 0301-4797. DOI: 10.1016/j.jenvman.2021.112988.

[366] N Rajaratnam and K Subramanya. “Flow equation for the sluice gate”. In: *ASCE Journal of Irrigation and Drainage Division* 93.IR3 (1967), pp. 167–186. DOI: 10.1061/JRCEA4.0000503.

[367] A.S. Ramamurthy, L.B. Carballada, and D.M. Tran. “Combining open channel flow at right angled junctions”. In: *Journal of Hydraulic Engineering* 114.12 (1988), pp. 1449–1460.

[368] A.S. Ramamurthy, J. Qu, and D. Vo. "Numerical and Experimental Study of Dividing Open-Channel Flows". In: *Journal of Hydraulic Engineering* 133.10 (2007), pp. 1135–1144. DOI: 10.1061/(ASCE)0733-9429(2007)133:10(1135).

[369] A.S. Ramamurthy and M.G. Satish. "Division of flow in short open channel branches". In: *Journal of Hydraulic Engineering* 114.4 (1988), pp. 428–438.

[370] A.S. Ramamurthy, D.M. Tran, and L.B. Carballada. "Dividing flow in open channels". In: *Journal of Hydraulic Engineering* 116.3 (1990), pp. 449–455.

[371] H. Ratia, J. Murillo, and P. García-Navarro. "Numerical modelling of bridges in 2D shallow water flow simulations". In: *International Journal for Numerical Methods in Fluids* 75.4 (2014), pp. 250–272. ISSN: 02712091. DOI: 10.1002/fld.3892.

[372] R.C. Reiner Jr et al. "Highly localized sensitivity to climate forcing drives endemic cholera in a megacity". In: *Proc Natl Acad Sci USA* 109.6 (2012), pp. 2033–2036. DOI: 10.1073/pnas.1119908109.

[373] The Centre for Research on the Epidemiology of Disasters (CRED) and United Nations Officer for Disaster Risk Reduction (UNISDR). *The human cost of weather-related disasters 1995-2015*. May 2015.

[374] *Rhodamine WT, 20% Solution in Water Specification Sheet*. Thermo Fisher Scientific. 2024. URL: https://www.thermofisher.com/order/catalog/product/446971000.

[375] C.E. Rice. *Open channel junctions with supercritical flow*. Tech. rep. 34. U.S. Department of Agriculture, 1985.

[376] G.L. Richard and S.L. Gavrilyuk. "The classical hydraulic jump in a model of shear shallow-water flows". In: *Journal of Fluid Mechanics* 725 (2013), pp. 492–521. ISSN: 0022-1120 1469-7645. DOI: 10.1017/jfm.2013.174.

[377] S. Richardson. "On the no-slip boundary condition". In: *Journal of Fluid Mechanics* 59.4 (1973), pp. 707–719. ISSN: 0022-1120. DOI: 10.1017/S0022112073001801.

[378] Z. Rida et al. "Experimental investigation of mixing efficiency in particle-laden Taylor-Couette flows". In: *Experiments in Fluids* 60.4 (2019), p. 61. ISSN: 1432-1114. DOI: 10.1007/s00348-019-2710-9. URL: 10.1007/s00348-019-2710-9.

[379] N. Rivière, R. Perkins, and E. Mignot. "Flow in a four branch channel intersection-A comparative study of subcritical and supercritical regimes". In: *Proc. of the 31st IAHR Congress*. Vol. 1. Seoul, 2005.

[380] N. Rivière and R. J. Perkins. "Supercritical flow in channel intersections". In: *Proc. of the 2nd Int. Conf. on Fluvial Hydraulics*. Ed. by M. Grecco, A. Carravetta, and R. Della Morte. Napoli, Italy, 2004, pp. 1073–1077.

[381] P.L. Roe. "Approximate Riemann Solvers, Parameter Vectors, and Difference Schemes". In: *Journal of Computational Physics* 43.2 (1981), pp. 357–372. DOI: 10.1016/0021-9991(81)90128-5.

[382] E. Rollason et al. "Rethinking flood risk communication". In: *Natural Hazards* 92.3 (2018), pp. 1665–1686. ISSN: 1573-0840. DOI: 10.1007/s11069-018-3273-4.

[383] B. R. Rosenzweig et al. "The Value of Urban Flood Modeling". In: *Earth's Future* 9.1 (2021). DOI: 10.1029/2020EF001739.

[384] V. Rözer et al. “Coping with Pluvial Floods by Private Households”. In: *Water* 8.7 (2016). ISSN: 2073-4441. DOI: 10.3390/w8070304.

[385] M. Rubinato et al. “Flow exchange, energy losses and pollutant transport in a surcharging manhole linked to street profiles”. In: *Journal of Hydrology* 604 (2022), p. 127201. ISSN: 0022-1694. DOI: 10.1016/j.jhydrol.2021.127201.

[386] A. Rummel, C.F. von Carmer, and G.H. Jirka. “Combined planar measurements of flow velocity and mass concentration in shallow turbulent flow. Part 1: Development of a planar concentration analysis (PCA) system”. In: *In: Proceedings. ASCE/IAHR International Conference on Hydraulic Measurements & Experimental Methods, Estes Park, USA 2002.* 2002.

[387] V. Guinot S. Soares-Frazão J. Lhomme and Y. Zech. “Two-dimensional shallow-water model with porosity for urban flood modelling”. In: *Journal of Hydraulic Research* 46.1 (2008), pp. 45–64. DOI: 10.1080/00221686.2008.9521842.

[388] A. Salatino, F. Osborne, and E. Motta. “ResearchFlow: Understanding the Knowledge Flow Between Academia and Industry”. In: *Knowledge Engineering and Knowledge Management*. Ed. by C. M. Keet and M. Dumontier. Cham: Springer International Publishing, 2020, pp. 219–236. ISBN: 978-3-030-61244-3.

[389] S. Salehi and A.H. Azimi. “Discharge Characteristics of Weir-Orifice and Weir-Gate Structures”. In: *Journal of Irrigation and Drainage Engineering* 145.11 (2019), p. 04019025. DOI: 10.1061/(ASCE)IR.1943-4774.0001421.

[390] S. Salehi, A.H. Azimi, and H. Bonakdari. “Hydraulics of sharp-crested weir culverts with downstream ramps in free-flow, partially, and fully submerged-flow conditions”. In: *Irrigation Science* 39.2 (2021), pp. 191–207. ISSN: 1432-1319. DOI: 10.1007/s00271-020-00695-y.

[391] S. Salehi, A. Mostaani, and A.H. Azimi. “Experimental and Numerical Investigations of Flow over and under Weir-Culverts with a Downstream Ramp”. In: *Journal of Irrigation and Drainage Engineering* 147.7 (2021). ISSN: 0733-9437 1943-4774. DOI: 10.1061/(asce)ir.1943-4774.0001576.

[392] H. Salem et al. “Collapse Analysis of Utatsu Ohashi Bridge Damaged by Tohuku Tsunami using Applied Element Method”. In: *Journal of Advanced Concrete Technology* 12.10 (2014), pp. 388–402. DOI: 10.3151/jact.12.388.

[393] J.M. Samani and M. Mazaheri. “Combined Flow over Weir and under Gate”. In: *Journal of Hydraulic Engineering* 135.3 (2009), pp. 224–227. DOI: 10.1061/(ASCE)0733-9429(2009)135:3(224).

[394] R. Sämann. “A Lagrangean model for pollutant transport in urban hydrology - Application in pluvial flood events”. PhD thesis. Hannover, Germany: Gottfried Wilhelm Leibniz Universität Hannover, June 2021.

[395] R. Sämann, T. Graf, and I. Neuweiler. “Modeling of contaminant transport during an urban pluvial flood event - The importance of surface flow”. In: *Journal of Hydrology* 568 (2019), pp. 301–310. ISSN: 0022-1694. DOI: 10.1016/j.jhydrol.2018.10.002.

[396] B.F. Sanders, J.E. Schubert, and H.A. Gallegos. “Integral formulation of shallow-water equations with anisotropic porosity for urban flood modeling”. In: *Journal of Hydrology* 362.1-2 (2008), pp. 19–38. ISSN: 00221694. DOI: 10.1016/j.jhydrol.2008.08.009.

[397] J. Sang et al. "Prediction model for pollution accidents trend in drinking water source areas: Enhancing water safety and comprehensive applications". In: *Process Safety and Environmental Protection* 184 (2024), pp. 12–24. ISSN: 0957-5820. DOI: 10.1016/j.psep.2024.01.089.

[398] M. Sanz-Ramos et al. "A CUDA Fortran GPU-parallelised hydrodynamic tool for high-resolution and long-term eco-hydraulic modelling". In: *Environmental Modelling & Software* 161 (2023), p. 105628. ISSN: 1364-8152. DOI: 10.1016/j.envsoft.2023.105628.

[399] L. Sarno et al. "Some considerations on numerical schemes for treating hyperbolicity issues in two-layer models". In: *Advances in Water Resources* 100 (2017), pp. 183–198. ISSN: 0309-1708. DOI: 10.1016/j.advwatres.2016.12.014.

[400] J. T. S. Savage et al. "When does spatial resolution become spurious in probabilistic flood inundation predictions?" In: *Hydrological Processes* 30.13 (2016), pp. 2014–2032. ISSN: 0885-6087. DOI: 10.1002/hyp.10749.

[401] J.T.S. Savage et al. "Quantifying the importance of spatial resolution and other factors through global sensitivity analysis of a flood inundation model". In: *Water Resources Research* 52.11 (2016), pp. 9146–9163. ISSN: 0043-1397. DOI: 10.1002/2015WR018198.

[402] A. Savitzky and M.J.E Golay. "Smoothing and Differentiation of Data by Simplified Least Squares Procedures". In: *Analytical Chemistry* 36.8 (1964), pp. 1627–1639. DOI: 10.1021/ac60214a047.

[403] J. Schijf and J.C. Schönfled. "Theoretical considerations on the motion of salt and fresh water". In: *Proceedings Minnesota International Hydraulic Convention*. Rijkswaterstaat, Netherlands: IAHR, Sept. 1953, pp. 321–333.

[404] J.E. Schubert and B.F. Sanders. "Building treatments for urban flood inundation models and implications for predictive skill and modeling efficiency". In: *Advances in Water Resources* 41 (2012), pp. 49–64. ISSN: 0309-1708. DOI: 10.1016/j.advwatres.2012.02.012.

[405] J.E. Schubert et al. "Unstructured mesh generation and landcover-based resistance for hydrodynamic modeling of urban flooding". In: *Advances in Water Resources* 31.12 (2008), pp. 1603–1621. ISSN: 0309-1708. DOI: 10.1016/j.advwatres.2008.07.012.

[406] S. Scutt, J. Shucksmith, and I. Douterelo. "Investigating the microbiological risks associated with urban flooding in the UK". In: *Access Microbiology* 4.5, po0008 (2022). ISSN: 2516-8290. DOI: 10.1099/acmi.ac2021.po0124.

[407] E.A. Shaw et al. "Importance of partial barriers and temporal variation in flow when modelling connectivity in fragmented river systems". In: *Ecological Engineering* 91 (2016), pp. 515–528. ISSN: 0925-8574. DOI: 10.1016/j.ecoleng.2016.01.030.

[408] X. Shen et al. "Shelter construction for fish at the confluence of a river to avoid the effects of total dissolved gas supersaturation". In: *Ecological Engineering* 97 (2016), pp. 642–648. ISSN: 0925-8574. DOI: 10.1016/j.ecoleng.2016.10.055.

[409] F. Shi et al. "Alterations in microbial community during the remediation of a black-odorous stream by acclimated composite microorganisms". In: *Journal of Environmental Sciences* 118 (2022), pp. 181–193. ISSN: 1001-0742. DOI: 10.1016/j.jes.2021.12.034.

[410] C.S. Shim, N.R. Yun, and H.H. Song. "Application of 3D Bridge Information Modeling to Design and Construction of Bridges". In: *Procedia Engineering* 14 (2011), pp. 95–99. ISSN: 1877-7058. DOI: 10.1016/j.proeng.2011.07.010.

[411] P. L. Smart and I. M. S. Laidlaw. "An evaluation of some fluorescent dyes for water tracing". In: *Water Resources Research* 13.1 (2010), pp. 15–33. ISSN: 0043-1397 1944-7973. DOI: 10.1029/WR013i001p00015.

[412] G.P. Smith and C.D. Wasko. *Australian Rainfall And Runoff Revision Project 15: Two Dimensional Simulations In Urban Areas- Representation Of Buildings In 2D Numerical Flood Models*. Report P15/S2/023. Engineers Australia Water Engineering, Feb. 2012.

[413] C. Sneddon, R. Barraud, and M.A. Germaine. "Dam removals and river restoration in international perspective". In: *Water Alternatives* 10.3 (2017), p. 648.

[414] S. Soares-Frazão and Y. Zech. "Dam-break flow experiment: The isolated building test case". In: *EC Contract EVG1-CT-2001-00037 IMPACT Investigation of Extreme Flood Processes and Uncertainty, Proceedings 2nd Project Workshop*. CD-ROM. Mo-i-Rana, Norway, Sept. 2004.

[415] S. Soares-Frazão and Y. Zech. "Dam-break flow through an idealised city". In: *Journal of Hydraulic Research* 46.5 (2008), pp. 648–658. ISSN: 0022-1686. DOI: 10.3826/jhr.2008.3164.

[416] S. Soares-Frazão and Y. Zech. "Experimental study of dam-break flow against an isolated obstacle". In: *Journal of Hydraulic Research* 45.sup1 (2007), pp. 27–36. ISSN: 0022-1686. DOI: 10.1080/00221686.2007.9521830.

[417] T. Sorgente et al. "A Survey of Indicators for Mesh Quality Assessment". In: *Computer Graphics Forum* 42.2 (2023), pp. 461–483. ISSN: 0167-7055. DOI: 10.1111/cgf.14779.

[418] V. Spinewine B.and Guinot, S. Soares-Frazão, and Y. Zech. "Solution properties and approximate Riemann solvers for two-layer shallow flow models". In: *Computers & Fluids* 44.1 (2011), pp. 202–220. ISSN: 00457930. DOI: 10.1016/j.compfluid.2011.01.001.

[419] A.L. Stewart and P.J. Dellar. "Multilayer shallow water equations with complete Coriolis force. Part 3. Hyperbolicity and stability under shear". In: *Journal of Fluid Mechanics* 723 (2013), pp. 289–317. ISSN: 0022-1120 1469-7645. DOI: 10.1017/jfm.2013.121.

[420] J.J. Stoker. *Water Waves*. New York: Interscience Publishers, Wiley and Sons, 1957.

[421] T. Stoltefaut et al. "A long-term case study indicates improvements in floodplain biodiversity after river restoration". In: *Ecological Engineering* 198 (2024), p. 107143. ISSN: 0925-8574. DOI: 10.1016/j.ecoleng.2023.107143.

[422] A. Strathie et al. "How presentation format affects the interpretation of probabilistic flood risk information". In: *Journal of Flood Risk Management* 10.1 (2017), pp. 87–96. ISSN: 1753-318X. DOI: 10.1111/jfr3.12152.

[423] L. Stuyt et al. "The Environmental Impact of Flooding of The Dutch 'Delta-Metropole'". In: *Flood Risk Management in Europe: Innovation in Policy and Practice*. Ed. by Selina Begum, Marcel J. F. Stive, and Jim W. Hall. Dordrecht: Springer Netherlands, 2007, pp. 107–129. ISBN: 978-1-4020-4200-3. DOI: 10.1007/978-1-4020-4200-3_7.

[424] W.J. Syme. "Flooding in Urban Areas-2D Modelling Approaches for Buildings and Fences". In: *9th National Conference on Hydraulics in Water Engineering: Hydraulics 2008*. Engineers Australia. Darwin Convention Centre, Australia, Sept. 2008, p. 25.

[425] D. Y. Tai and R. E. Rathbun. "Photolysts of rhodamine-WT dye". In: *Chemosphere* 17.3 (1988), pp. 559–573. ISSN: 0045-6535. DOI: 10.1016/0045-6535(88)90031-8.

[426] B. Tang and T.W. Gallien. "Predicting Compound Coastal Flooding in Embayment-Backed Urban Catchments: Seawall and Storm Drain Implications". In: *Journal of Marine Science and Engineering* 11.7 (2023). ISSN: 2077-1312. DOI: 10.3390/jmse11071454.

[427] A. Taube et al. "A high-order discontinuous Galerkin method with time-accurate local time stepping for the Maxwell equations". In: *International Journal of Numerical Modelling: Electronic Networks, Devices and Fields* 22.1 (2009), pp. 77–103. DOI: 10.1002/jnm.700.

[428] E. H. Taylor. "Flow characteristics at rectangular open-channel junctions". In: *Transactions, ASCE* (1944).

[429] J. Teng et al. "Flood inundation modelling: A review of methods, recent advances and uncertainty analysis". In: *Environmental Modelling & Software* 90 (2017), pp. 201–216. ISSN: 1364-8152. DOI: 10.1016/j.envsoft.2017.01.006.

[430] G. Testa et al. "Flash flood flow experiment in a simplified urban district". In: *Journal of Hydraulic Research* 45.sup1 (2007), pp. 37–44. ISSN: 0022-1686. DOI: 10.1080/00221686.2007.9521831.

[431] The European Parliament and the Council of the European Union. *Directive 2000/60/EC of the European Parliament and of the Council*. Official Journal L 327. Oct. 2000. URL: http://data.europa.eu/eli/dir/2000/60/oj.

[432] O. Thual. "Modelling rollers for shallow water flows". In: *Journal of Fluid Mechanics* 728 (2013), pp. 1–4. ISSN: 0022-1120 1469-7645. DOI: 10.1017/jfm.2013.238.

[433] V. A. Titarev and E. F. Toro. "ADER: Arbitrary High Order Godunov Approach". In: *Journal of Scientific Computing* 17.1 (2002), pp. 609–618. ISSN: 1573-7691. DOI: 10.1023/A:1015126814947.

[434] V.A. Titarev and E.F. Toro. "ADER schemes for three-dimensional non-linear hyperbolic systems". In: *Journal of Computational Physics* 204.2 (2005), pp. 715–736. ISSN: 0021-9991. DOI: 10.1016/j.jcp.2004.10.028.

[435] E. F. Toro. "The HLLC Riemann solver". In: *Shock Waves* 29.8 (2019), pp. 1065–1082. ISSN: 0938-1287 1432-2153. DOI: 10.1007/s00193-019-00912-4.

[436] E.F Toro and V.A. Titarev. "Solution of the generalized Riemann problem for advection-reaction equations". In: *Proc. R. Soc. Lond. A* 458 (2002), pp. 271–281. DOI: 10.1098/rspa.2001.0926.

[437] E.F. Toro. *Riemann Solvers and Numerical Methods for Fluid Dynamics: A Practical Introduction*. Heidelberg: Springer, 2009, pp. 315–336.

[438] E.F. Toro. *Shock-Capturing Methods for Free-Surface Shallow Flows*. John Wiley & Sons, 2001.

[439] E.F. Toro and G.I. Montecinos. "Advection-Diffusion-Reaction Equations: Hyperbolization and High-Order ADER Discretizations". In: *SIAM Journal on Scientific Computing* 36.5 (2014), A2423–A2457. ISSN: 1064-8275 1095-7197. DOI: 10.1137/130937469.

[440] R. Touma and M. A. Saleh. "Well-balanced central schemes for pollutants transport in shallow water equations". In: *Mathematics and Computers in Simulation* 190 (2021), pp. 1275–1293. ISSN: 03784754. DOI: 10.1016/j.matcom.2021.07.021.

[441] J.M. Townson and A.H. Al-Salihi. "Models of dam-break flow in R-T space". In: *Journal of Hydraulic Engineering* 115.5 (1989), pp. 561–575. DOI: 10.1061/(ASCE)0733-9429(1989)115:5(561).

[442] Transportation Association of Canada. *Guide to Bridge Hydraulics*. London: Thomas Telford Publishing, 2004.

[443] M.E. Trueheart et al. "Simulating hydraulic interdependence between bridges along a river corridor under transient flood conditions". In: *Science of The Total Environment* 699 (2020), p. 134046. ISSN: 0048-9697. DOI: 10.1016/j.scitotenv.2019.134046.

[444] TUFLOW. *Modelling Bridge Piers in 2D Using Tuflow: Technical Memo*. Report. TUFLOW, 2013.

[445] *TUFLOW Classic/HPC User Manual*. Build 2018-03-AD. TUFLOW and BMT. Brisbane, Australia, 2018. URL: https://www.tuflow.com.

[446] S. Ueda et al. "Nuclear accident-derived 3H in river water of Fukushima Prefecture during 2011-2014". In: *Journal of Environmental Radioactivity* 146 (2015), pp. 102–109. ISSN: 0265-931X. DOI: 10.1016/j.jenvrad.2015.04.014.

[447] United Nations. *United Nations Decade on Ecosystem Restoration (2021–2030)*. General Assembly Resolution A/RES/73/284. Mar. 2019.

[448] United Nations. *United Nations Sustainable Development Goals*. 2015. URL: https://sdgs.un.org/ (visited on 02/23/2024).

[449] United Nations. *World Urbanization Prospects: The 2018 Revision*. UN. (2018). World urbanisation prospects: the 2018 revision key facts. Retrieved from https://esa.un.org/unpd/wup/Publications/Files/WUP2018-KeyFacts.pdf. 2018.

[450] R. Vacondio et al. "Simulation of the January 2014 flood on the Secchia River using a fast and high-resolution 2D parallel shallow-water numerical scheme". In: *Natural Hazards* 80.1 (2016), pp. 103–125. ISSN: 1573-0840. DOI: 10.1007/s11069-015-1959-4.

[451] A. Valiani and L. Begnudelli. "Divergence Form for Bed Slope Source Term in Shallow Water Equations". In: *Journal of Hydraulic Engineering* 132.7 (2006), pp. 652–665. DOI: 10.1061/(ASCE)0733-9429(2006)132:7(652).

[452] A. Valiani and V. Caleffi. "Dam break in rectangular channels with different upstream-downstream widths". In: *Advances in Water Resources* 132 (2019), p. 103389. ISSN: 0309-1708. DOI: 10.1016/j.advwatres.2019.103389.

[453] A. Valiani and V. Caleffi. "Momentum balance in the shallow water equations on bottom discontinuities". In: *Advances in Water Resources* 100 (2017), pp. 1–13. ISSN: 0309-1708. DOI: 10.1016/j.advwatres.2016.12.002.

[454] A. Valiani, V. Caleffi, and A. Zanni. "Case Study: Malpasset Dam-Break Simulation using a Two-Dimensional Finite Volume Method". In: *Journal of Hydraulic Engineering* 128.5 (2002), pp. 460–472. DOI: 10.1061/(ASCE)0733-9429(2002)128:5(460).

[455] Geoffrey K. Vallis. *Essentials of Atmospheric and Oceanic Dynamics*. Cambridge: Cambridge University Press, 2019. DOI: DOI:10.1017/9781107588431.

[456] D. Vanzo, A. Siviglia, and E.F. Toro. "Pollutant transport by shallow water equations on unstructured meshes: Hyperbolization of the model and numerical solution via a novel flux splitting scheme". In: *Journal of Computational Physics* 321 (2016), pp. 1–20. ISSN: 00219991. DOI: 10.1016/j.jcp.2016.05.023.

[457] G. Varra et al. "Coping with geometric discontinuities in porosity-based shallow water models". In: *Physics of Fluids* 35.10 (2023), p. 106612. ISSN: 1070-6631. DOI: 10.1063/5.0168385.

[458] G. Varra et al. "Internal boundary conditions for flood simulation with 2D Shallow water Equations using Finite Volume models: bridge piers". In: *Proceedings of the 39th IAHR World Congress*. Granada, Spain, June 2022. DOI: 10.3850/IAHR-39WC2521716X20221306.

[459] G. Varra et al. "On integral and differential porosity models for urban flooding simulation". In: *Advances in Water Resources* 136 (2020), p. 103455. ISSN: 0309-1708. DOI: 10.1016/j.advwatres.2019.103455.

[460] G. Varra et al. "Porous Shallow-Water Equations Model with Disambiguation of Multiple Solutions". In: *Environmental Sciences Proceedings* 21.1 (2022). ISSN: 2673-4931. DOI: 10.3390/environsciproc2022021055.

[461] G. Varra et al. "The exact solution to the Shallow water Equations Riemann problem at width jumps in rectangular channels". In: *Advances in Water Resources* 155 (2021), p. 103993. ISSN: 0309-1708. DOI: 10.1016/j.advwatres.2021.103993.

[462] J. Vasconcelos, S.J. Wright, and P.L. Roe. "Current Issues on Modeling Extreme Inflows in Stormwater Systems". In: *Journal of Water Management Modeling* 14 (2006). ISSN: 22926062. DOI: 10.14796/JWMM.R225-19.

[463] J.G. Vasconcelos, Wright S.J, and P.L Roe. "Improved Simulation of Flow Regime Transition in Sewers: Two-Component Pressure Approach". In: *Journal of Hydraulic Engineering* 132.6 (2006), pp. 553–562. DOI: 10.1061/(ASCE)0733-9429(2006)132:6(553). URL: 10.1061/(ASCE)0733-9429(2006)132:6(553).

[464] A.R. Vatankhah and S. Khalili. "Stage-Discharge Relationship for Weir-Orifice Structure Located at the End of Circular Open Channels". In: *Journal of Irrigation and Drainage Engineering* 146.8 (2020), p. 06020006. DOI: 10.1061/(ASCE)IR.1943-4774.0001494.

[465] M. Velickovic. "Macroscopic Modelling of Urban Flood by a Porosity Approach". Thesis. 2012. URL: http://hdl.handle.net/2078.1/114509.

[466] M. Velickovic, Y. Zech, and S. Soares-Frazão. "Steady-flow experiments in urban areas and anisotropic porosity model". In: *Journal of Hydraulic Research* 55.1 (2017), pp. 85–100. DOI: 10.1080/00221686.2016.1238013.

[467] D. Veríssimo and C. Roseta-Palma. "Rewilding with the beaver in the iberian peninsula - Economic potential for river restoration". In: *Nature-Based Solutions* 3 (2023), p. 100055. ISSN: 2772-4115. DOI: 10.1016/j.nbsj.2023.100055.

[468] H K Versteeg and W Malalasekera. *An Introduction to Computational Fluid Dynamics*. Essex, England: Pearson, 2007.

[469] L. Vezzaro, A. Ledin, and P. S. Mikkelsen. "Integrated modelling of Priority Pollutants in stormwater systems". In: *Physics and Chemistry of the Earth, Parts A/B/C* 42-44 (2012), pp. 42–51. ISSN: 1474-7065. DOI: 10.1016/j.pce.2011.07.002.

[470] D. P. Viero and A. Defina. "Extended Theory of Hydraulic Hysteresis in Open-Channel Flow". In: *Journal of Hydraulic Engineering* 143.9 (2017), p. 06017014. DOI: 10.1061/(ASCE)HY.1943-7900.0001342.

[471] P. Virtanen et al. "SciPy 1.0: Fundamental Algorithms for Scientific Computing in Python". In: *Nature Methods* 17 (2020), pp. 261–272. DOI: 10.1038/s41592-019-0686-2.

[472] C. B. Vreugdenhil. *Numerical Methods for Shallow-Water Flow*. 1st ed. Vol. 13. Water Science and Technology Library. Dordrecht, The Netherlands: Springer Dordrecht, 1994. ISBN: 978-0-7923-3164-3. DOI: 10.1007/978-94-015-8354-1.

[473] G. Wang et al. "Analysis on the formation condition of the algae-induced odorous black water agglomerate". In: *Saudi Journal of Biological Sciences* 21.6 (2014), pp. 597–604. ISSN: 1319-562X. DOI: 10.1016/j.sjbs.2014.07.002.

[474] H. Wang et al. "Influences of hydrodynamic conditions on the biomass of benthic diatoms in a natural stream". In: *Ecological Indicators* 92 (2018), pp. 51–60. ISSN: 1470-160X. DOI: 10.1016/j.ecolind.2017.05.061.

[475] J. Wang et al. "A new method for multi-point pollution source identification". In: *Atmospheric and Oceanic Science Letters* 14.6 (2021), p. 100098. ISSN: 1674-2834. DOI: 10.1016/j.aosl.2021.100098.

[476] J. Wang et al. "An effective method for point pollution source identification in rivers with performance-improved ensemble Kalman filter". In: *Journal of Hydrology* 577 (2019), p. 123991. ISSN: 0022-1694. DOI: 10.1016/j.jhydrol.2019.123991.

[477] J. Wang et al. "New approach for point pollution source identification in rivers based on the backward probability method". In: *Environmental Pollution* 241 (2018), pp. 759–774. ISSN: 0269-7491. DOI: 10.1016/j.envpol.2018.05.093.

[478] J. Wang et al. "Release process identification of non-instantaneous point source pollution in rivers via reverse flow and pollution routing". In: *Environmental Research* 213 (2022), p. 113704. ISSN: 0013-9351. DOI: 10.1016/j.envres.2022.113704.

[479] W. Wang et al. "Effects of Bridge Piers on Flood Hazards: A Case Study on the Jialing River in China". In: *Water* 11.6 (2019). ISSN: 2073-4441. DOI: 10.3390/w11061181.

[480] Y. Wang et al. "An integrated framework for high-resolution urban flood modelling considering multiple information sources and urban features". In: *Environmental Modelling & Software* 107 (2018), pp. 85–95. ISSN: 1364-8152. DOI: 10.1016/j.envsoft.2018.06.010.

[481] N. B. Webber and C. A. Greated. "An investigation of flow behaviour at the junction of rectangular channels". In: *Proceedings of the Institution of Civil Engineers* 34 (1966), pp. 312–334.

[482] L.J. Weber, E.D. Schumate, and N. Mawer. "Experiments on flow at a 90° open-channel junction". In: *Journal of Hydraulic Engineering* 127.5 (2001), pp. 340–350.

[483] O.E.J. Wing et al. "Inequitable patterns of US flood risk in the Anthropocene". In: *Nature Climate Change* 12.2 (2022), pp. 156–162. ISSN: 1758-678X 1758-6798. DOI: 10.1038/s41558-021-01265-6.

[484] H. Woo et al. "Sedimentation issues of the Four Major Rivers Restoration Project in South Korea". In: *Journal of Hydro-environment Research* 50 (2023), pp. 57–61. ISSN: 1570-6443. DOI: 10.1016/j.jher.2023.08.001.

[485] T. Wool et al. *Water Quality Analysis Simulation Program (WASP). Users Manual, Version 6*. Tech. rep. Washington, DC, USA: US Environmental Protection Agency, 2015.

[486] J. Xia et al. "New criterion for the stability of a human body in floodwaters". In: *Journal of Hydraulic Research* 52.1 (2014), pp. 93–104. DOI: 10.1080/00221686.2013.875073.

[487] T. Xu and J.J. Gómez-Hernández. "Simultaneous identification of a contaminant source and hydraulic conductivity via the restart normal-score ensemble Kalman filter". In: *Advances in Water Resources* 112 (2018), pp. 106–123. ISSN: 0309-1708. DOI: 10.1016/j.advwatres.2017.12.011.

[488] T.H. Yoon and S.K. Kang. "Finite Volume Model for Two-Dimensional Shallow Water Flows on Unstructured Grids". In: *Journal of Hydraulic Engineering* 130.7 (2004), pp. 678–688. DOI: 10.1061/(ASCE)0733-9429(2004)130:7(678).

[489] D. Yu and S. N. Lane. "Urban fluvial flood modelling using a two-dimensional diffusion-wave treatment, part 1: mesh resolution effects". In: *Hydrological Processes* 20.7 (2006), pp. 1541–1565. ISSN: 0885-6087. DOI: 10.1002/hyp.5935.

[490] M. Zandsalimy and C. Ollivier-Gooch. "A novel approach to mesh optimization to stabilize unstructured finite volume simulations". In: *Journal of Computational Physics* 453 (2022), p. 110959. ISSN: 0021-9991. DOI: 10.1016/j.jcp.2022.110959.

[491] O. Zanotti and M. Dumbser. "Efficient conservative ADER schemes based on WENO reconstruction and space-time predictor in primitive variables". In: *Computational Astrophysics and Cosmology* 3.1 (2016), p. 1. ISSN: 2197-7909. DOI: 10.1186/s40668-015-0014-x.

[492] E. Zavattero et al. "2D Surface Water Quality Model: A Forecasting Tool for Accidental Pollution in Urban River-Application to the Var River, France". In: *Advances in Hydroinformatics*. Ed. by P. Gourbesville, J. Cunge, and G. Caignaert. Singapore: Springer Singapore, 2018, pp. 285–299. ISBN: 978-981-10-7218-5.

[493] A. Zhai et al. "Hazardous chemical accident prediction for drinking water sources in Three Gorges Reservoir". In: *Journal of Cleaner Production* 296 (2021), p. 126529. ISSN: 0959-6526. DOI: 10.1016/j.jclepro.2021.126529.

[494] J. Zhang et al. “An adaptive Gaussian process-based method for efficient Bayesian experimental design in groundwater contaminant source identification problems”. In: *Water Resources Research* 52.8 (2016), 5971 – 5984. DOI: 10.1002/2016WR018598.

[495] S.P. Zhang and X.K. Xin. “Pollutant source identification model for water pollution incidents in small straight rivers based on genetic algorithm”. In: *Applied Water Science* 7.4 (2017), pp. 1955–1963. ISSN: 2190-5495. DOI: 10.1007/s13201-015-0374-z.

[496] X. Zhang and M. Huang. “Ensemble-based release estimation for accidental river pollution with known source position”. In: *Journal of Hazardous Materials* 333 (2017), pp. 99–108. ISSN: 0304-3894. DOI: 10.1016/j.jhazmat.2017.03.028.

[497] Y. Zhang, M.M. Meerschaert, and R.M. Neupauer. “Backward fractional advection dispersion model for contaminant source prediction”. In: *Water Resources Research* 52.4 (2016), pp. 2462–2473. DOI: 10.1002/2015WR018515.

[498] D.H. Zhao et al. “Finite Volume Two-Dimensional Unsteady Flow Model for River Basins”. In: *Journal of Hydraulic Engineering* 120.7 (1994), p. 20. DOI: 10.1061/(ASCE)0733-9429(1994)120:7(863).

[499] J. G. Zhou. “A lattice Boltzmann method for solute transport”. In: *International Journal for Numerical Methods in Fluids* 61.8 (2009), pp. 848–863. ISSN: 10970363 (ISSN). DOI: 10.1002/fld.1978.

[500] J. G. Zhou and P. K. Stansby. “2D shallow water flow model for the hydraulic jump”. In: *International Journal for Numerical Methods in Fluids* 29.4 (1999), pp. 375–387. ISSN: 0271-2091 1097-0363.

[501] A.P. Zischg et al. “Validation of 2D flood models with insurance claims”. In: *Journal of Hydrology* 557 (2018), pp. 350–361. DOI: 10.1016/j.jhydrol.2017.12.042.

Appendix A

Appendices

A.1 Test Case Five Adjusted Inflow

Comparison between the numerical results for Solver 2, for $q = q_{avg}$ and $q = 1.02q_{avg}$ shown in Figure A.1a. Where q is the inflow rate and q_{avg} is the average measured inflow rate over the duration of the experiment. Comparison between results for the adjusted inflow and the experimental data is provided in Table A.1b.

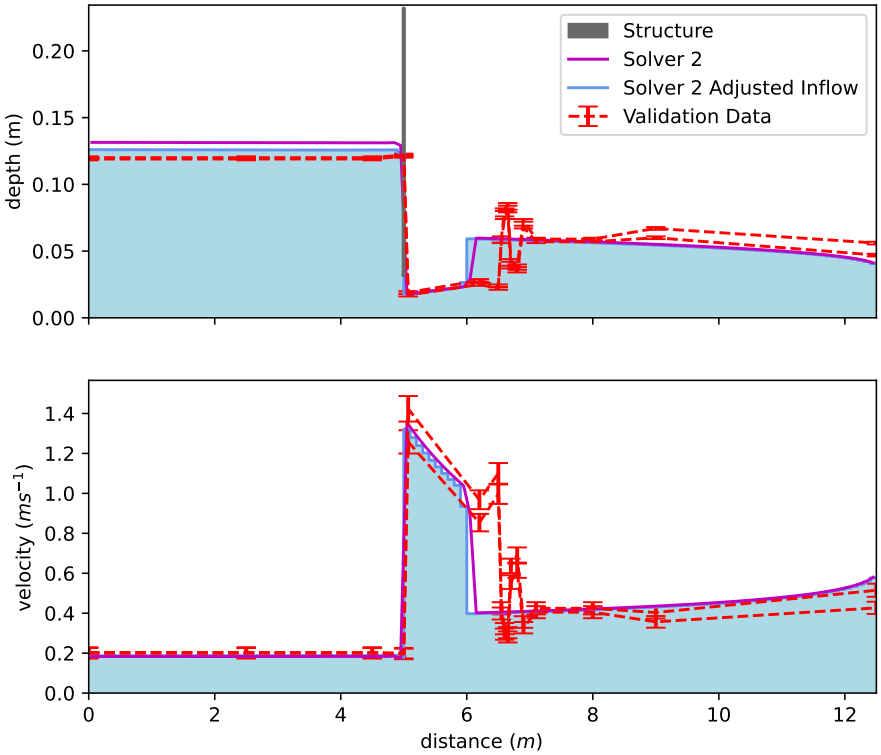

(a)

		Distance											
		0.00m	4.50m	5.07m	6.20m	6.50m	6.55m	6.60m	6.90m	7.10m	8.00m	9.00m	12.50m
Average Depth (m)		0.1195	0.1195	0.0180	0.0265	0.0230	0.0585	0.0780	0.0705	0.0580	0.0580	0.0635	0.0515
Average Velocity (m/s)		0.2013	0.2013	1.3361	0.9075	1.0457	0.4111	0.3083	0.3411	0.4147	0.4147	0.3787	0.4670
Average Discharge (m^2/s)		0.0241	0.0241	0.0241	0.0241	0.0241	0.0241	0.0241	0.0241	0.0241	0.0241	0.0241	0.0241
Depth (m)		0.1260	0.1257	0.0178	0.0591	0.0586	0.0586	0.0585	0.0581	0.0578	0.0563	0.0545	0.0407
Velocity (m/s)		0.1870	0.1875	1.3228	0.3984	0.4012	0.4017	0.4022	0.4052	0.4073	0.4177	0.4317	0.5761
Discharge (m^2/s)		0.0236	0.0236	0.0236	0.0235	0.0235	0.0235	0.0235	0.0235	0.0235	0.0235	0.0235	0.0234
Depth (m)	Absolute Error	0.0065	0.0062	-0.0002	0.0326	0.0356	0.0001	-0.0195	-0.0124	-0.0002	-0.0017	-0.0090	-0.0108
	Percentage Error	5.5%	5.1%	1.0%	122.9%	155.0%	0.1%	25.0%	17.6%	0.4%	2.9%	14.2%	21.0%
Velocity (m/s)	Absolute Error	-0.0143	-0.0137	-0.0133	-0.5091	-0.6444	-0.0094	0.0939	0.0641	-0.0074	0.0030	0.0529	0.1091
	Percentage Error	7.1%	6.8%	1.0%	56.1%	61.6%	2.3%	30.4%	18.8%	1.8%	0.7%	14.0%	23.4%
Discharge (m^2/s)	Absolute Error	-0.0005	-0.0005	-0.0005	-0.0005	-0.0005	-0.0005	-0.0005	-0.0005	-0.0005	-0.0005	-0.0005	-0.0006
	Percentage Error	2.0%	2.0%	2.0%	2.2%	2.2%	2.2%	2.2%	2.2%	2.2%	2.2%	2.2%	2.5%

Validation Data | Numerical Data | Error

(b)

Figure A.1: Comparison between numerical and experimental results for test case five following adjustment of the inflow rate within the ±2% error margin.

A.2 Test Case Six Adjusted Inflow

Comparison between the numerical results for Solver 2, for $q = q_{avg}$ and $q = 0.98q_{avg}$ shown in Figure A.2a. Where q is the inflow rate and q_{avg} is the average measured inflow rate over the duration of the experiment. Comparison between results for the adjusted inflow and the experimental data is provided in Table A.2b.

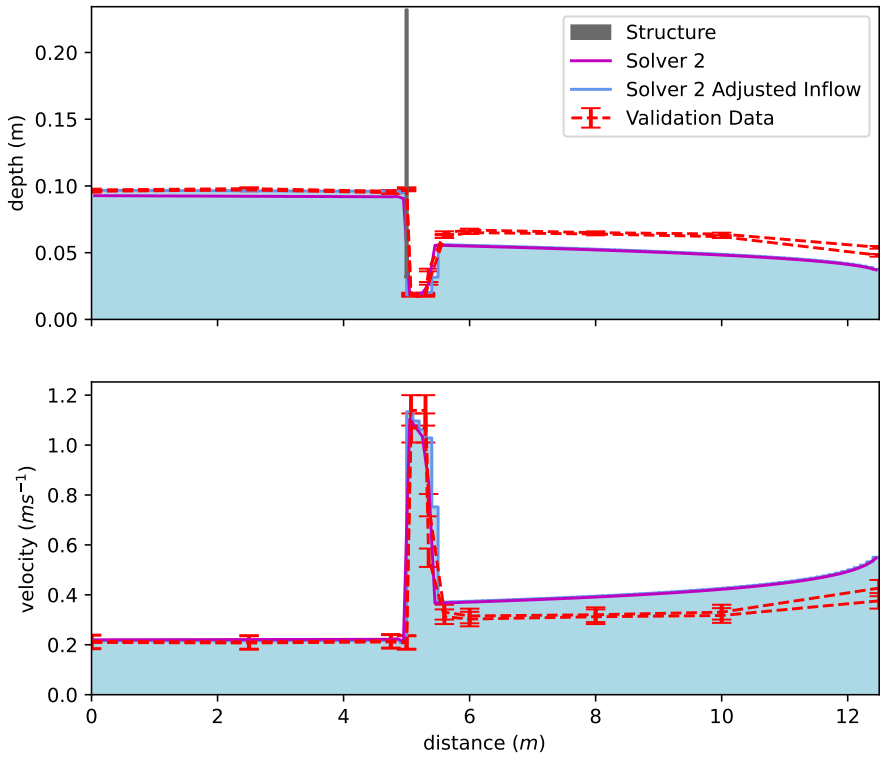

(a)

		Distance											
		0.00m	2.50m	4.75m	5.00m	5.07m	5.35m	5.60m	6.00m	8.00m	10.00m	12.50m	
Average Depth (m)		0.0965	0.0975	0.0955	0.0975	0.0185	0.0320	0.0635	0.0660	0.0645	0.0630	0.0510	Validation Data
Average Velocity (m/s)		0.2114	0.2092	0.2136	0.2092	1.1027	0.6375	0.3213	0.3091	0.3163	0.3238	0.4000	
Average Discharge (m^2/s)		0.0204	0.0204	0.0204	0.0204	0.0204	0.0204	0.0204	0.0204	0.0204	0.0204	0.0204	
Depth (m)		0.0968	0.0964	0.0960	0.0947	0.0184	0.0202	0.0560	0.0555	0.0526	0.0487	0.0376	Numerical Data
Velocity (m/s)		0.2150	0.2159	0.2167	0.2083	1.1336	1.0286	0.3710	0.3743	0.3946	0.4259	0.5507	
Discharge (m^2/s)		0.0208	0.0208	0.0208	0.0197	0.0208	0.0208	0.0208	0.0208	0.0208	0.0208	0.0207	
Depth (m)	Absolute Error	0.0003	-0.0011	0.0005	-0.0028	-0.0001	-0.0118	-0.0075	-0.0105	-0.0119	-0.0143	-0.0134	Error
	Percentage Error	0.3%	1.2%	0.5%	2.8%	0.8%	36.8%	11.8%	15.9%	18.4%	22.6%	26.4%	
Velocity (m/s)	Absolute Error	0.0036	0.0066	0.0031	-0.0009	0.0309	0.3911	0.0497	0.0652	0.0784	0.1021	0.1507	
	Percentage Error	1.7%	3.2%	1.4%	0.4%	2.8%	61.4%	15.5%	21.1%	24.8%	31.5%	37.7%	
Discharge (m^2/s)	Absolute Error	0.0004	0.0004	0.0004	-0.0007	0.0004	0.0004	0.0004	0.0004	0.0004	0.0004	0.0003	
	Percentage Error	2.0%	2.0%	2.0%	3.3%	2.0%	2.0%	1.8%	1.8%	1.8%	1.8%	1.4%	

(b)

Figure A.2: Comparison between numerical and experimental results for test case six following adjustment of the inflow rate within the ±2% error margin.

A.3 Simple Weir Internal Boundary Condition

Consider the scenario outlined in Figure A.3 whereby there is a wet left state in the third layer for the left cell and a corresponding dry state in the third layer for the right cell.

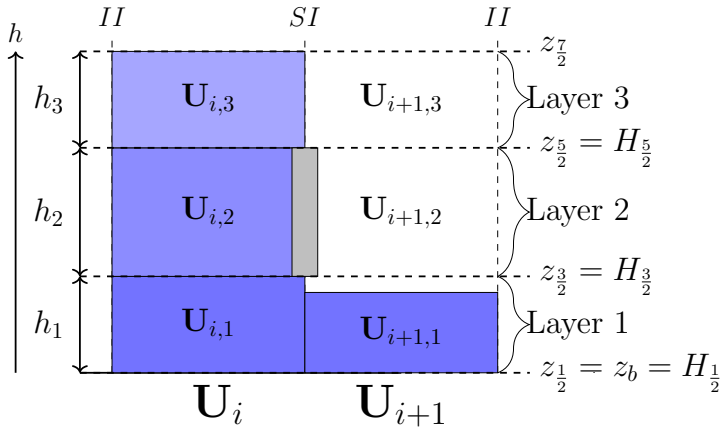

Figure A.3: An example of combined gate and weir flow across a structure interface for which a coupling condition can be implemented.

A simple approximation of the flow rate q generated by the height, $h_{i,3}$, of water flowing over the top of the gate is provided by [190]:

$$q = C\sqrt{g}(h_i, 3)^{\frac{3}{2}} \tag{A.1}$$

where C is an empirical constant which accounts the energy losses, taken as equal to 0.6 in this case. A simple weir coupling condition can be introduced, by implementing a fictitious right state, $h^{(+)}$, $u^{(+)}$, connected to the left state, $h_{i,3}$, $u_{i,3}$, by the following Riemann invariant:

$$u_L - 2a_L = u_R - 2a_R \tag{A.2}$$

where $a_k = \sqrt{g(h_k + h_{k_{(+)}})}$. If the discharge across the interface, q, is governed by (A.1) then $h^{(+)}u^{(+)} = C\sqrt{g}(h_i, 3)^{\frac{3}{2}}$ which may be substituted into (A.2):

$$u_{i,3} - 2\sqrt{g(h_{i,3} + h_{i,3_{(+)}})} = \frac{C\sqrt{g}(h_i, 3)^{\frac{3}{2}}}{h^{(+)}} - 2\sqrt{gh^{(+)}} \tag{A.3}$$

This equation can be rearranged to give:

$$\frac{C\sqrt{g}(h_{i,3})^{\frac{3}{2}}}{h^{(+)}} - u_{i,3} - 2\sqrt{g}\left(\sqrt{h^{(+)}} - \sqrt{(h_{i,3} + h_{i,3_{(+)}})}\right) = 0 \tag{A.4}$$

Let:

$$f\left(h_i, 3, h_{i,3_{(+)}}, u_{i,3}, h^{(+)}, u^{(+)}\right) = \frac{C\sqrt{g}(h_{i,3})^{\frac{3}{2}}}{h^{(+)}} - u_{i,3} - 2\sqrt{g}\left(\sqrt{h^{(+)}} - \sqrt{(h_{i,3} + h_{i,3_{(+)}})}\right) \tag{A.5}$$

$$\frac{\partial f}{\partial h^{(+)}} = -\frac{C\sqrt{g}(h_{i,3})^{\frac{3}{2}}}{(h^{(+)})^2} - \frac{\sqrt{g}}{\sqrt{h^{(+)}}} \tag{A.6}$$

A suitable numerical method such as the Newton-Raphson method can then be used to determine $h^{(+)}$, using an initial guess of $h_0 = h_L$. Once $h^{(+)}$ has been determined, $u^{(+)}$ may be evaluated as:

$$u^{(+)} = \frac{C\sqrt{g}(h_i, 3)^{\frac{3}{2}}}{h^{(+)}} \tag{A.7}$$

This coupling condition ensures that the flow across the interface for the third layer is governed by the weir equation (A.1) in the case that the corresponding right state is dry. For two wet states or two dry states, the standard solution procedure should be followed. A coupling condition for a left dry state and corresponding wet right state can be derived following the same arguments. The use of Riemann invariants to connect the neighbouring states assumes the existence of simple waves, which is the case for the outlined implementation [438]. For a more rigorous exploration of weir coupling for the shallow water equations refer to [190].

A.4 Test Case: Internal Weir Boundary Condition

Comparison between the numerical results for Solver 2 following the implementation of weir coupling as derived in A.3 is shown in Figure A.4a. Comparison between results for Solver 2 with weir coupling and the experimental data is provided in Table A.4b.

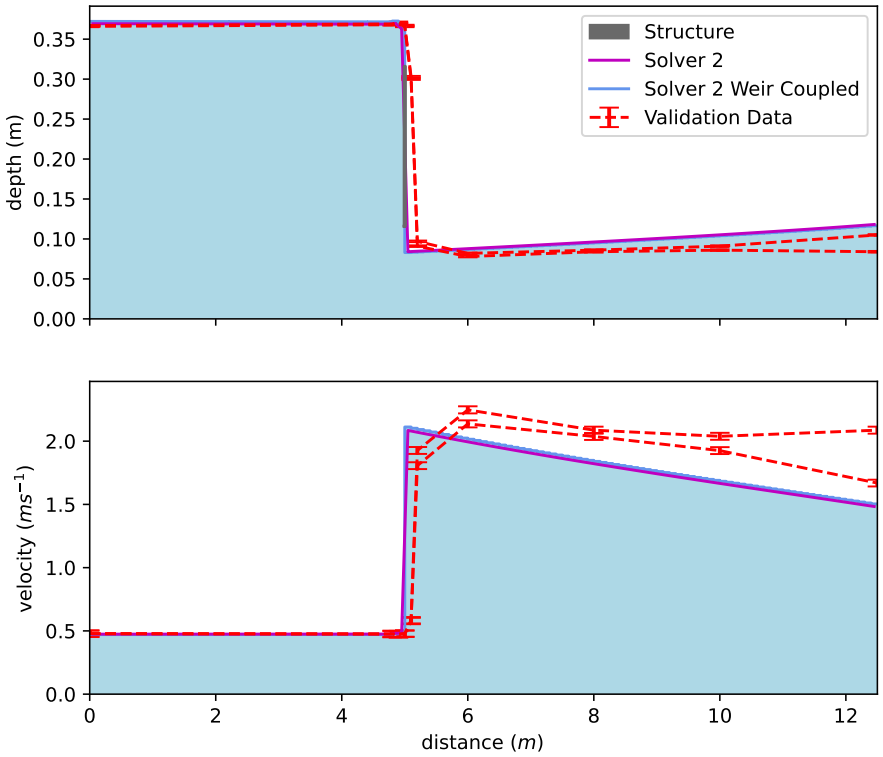

(a)

		Distance									
		0.00m	4.80m	4.90m	5.00m	5.20m	6.00m	8.00m	10.00m	12.50m	
Average Depth (m)		0.3665	0.3685	0.3700	0.3665	0.0940	0.0800	0.0850	0.0885	0.0945	Validation Data
Average Velocity (m/s)		0.4782	0.4756	0.4736	0.4782	1.8644	2.1906	2.0618	1.9802	1.8545	
Average Discharge (m^2/s)		0.1753	0.1753	0.1753	0.1753	0.1753	0.1753	0.1753	0.1753	0.1753	
Depth (m)		0.3722	0.3721	0.3695	0.3663	0.0836	0.0868	0.0950	0.1039	0.1165	Numerical Data
Velocity (m/s)		0.4708	0.4742	0.4779	0.4790	2.0969	2.0197	1.8441	1.6865	1.5039	
Discharge (m^2/s)		0.1752	0.1765	0.1766	0.1755	0.1753	0.1753	0.1752	0.1753	0.1753	
Depth (m)	Absolute Error	0.0057	0.0036	-0.0005	-0.0002	-0.0104	0.0068	0.0100	0.0154	0.0220	Error
	Percentage Error	1.6%	1.0%	0.1%	0.1%	11.1%	8.5%	11.8%	17.4%	23.3%	
Velocity (m/s)	Absolute Error	-0.0074	-0.0014	0.0043	0.0008	0.2326	-0.1709	-0.2176	-0.2938	-0.3506	
	Percentage Error	1.5%	0.3%	0.9%	0.2%	12.5%	7.8%	10.6%	14.8%	18.9%	
Discharge (m^2/s)	Absolute Error	0.0000	0.0012	0.0013	0.0002	0.0000	0.0000	0.0000	0.0000	0.0000	
	Percentage Error	0.0%	0.7%	0.8%	0.1%	0.0%	0.0%	0.0%	0.0%	0.0%	

(b)

Figure A.4: Comparison between numerical and experimental results for test case six following the introduction of weir coupling.

A.5 Test Case Nine: Internal Weir Boundary Condition

Comparison between the numerical results for Solver 2 following the implementation of weir coupling as derived in A.3 is shown in Figure A.5a. Comparison between results for Solver 2 with weir coupling and the experimental data is provided in Table A.5b.

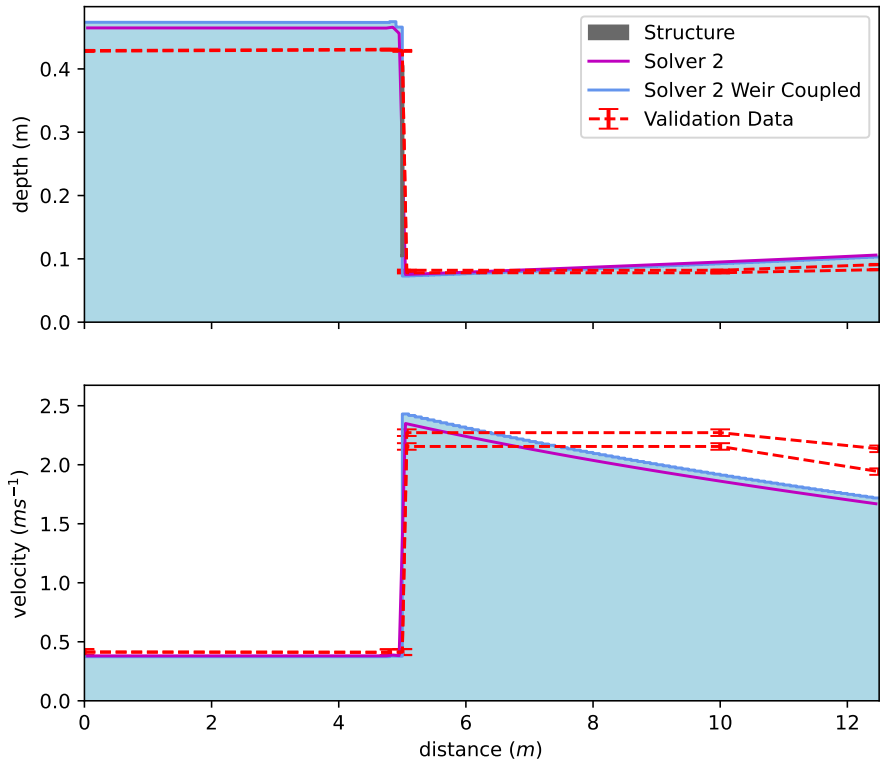

(a)

		Distance						
		0.00m	4.80m	5.00m	5.07m	10.00m	12.50m	
Average Depth (m)		0.4285	0.4305	0.4285	0.0800	0.0800	0.0870	Validation Data
Average Velocity (m/s)		0.4130	0.4110	0.4130	2.2119	2.2119	2.0339	
Average Discharge (m^2/s)		0.1770	0.1770	0.1770	0.1770	0.1770	0.1770	
Depth (m)		0.4737	0.4740	0.4660	0.0728	0.0924	0.1030	Numerical Data
Velocity (m/s)		0.3736	0.3765	0.3775	2.4303	1.9157	1.7184	
Discharge (m^2/s)		0.1769	0.1785	0.1759	0.1770	0.1770	0.1770	
Depth (m)	Absolute Error	0.0452	0.0435	0.0375	-0.0072	0.0124	0.0160	Error
	Percentage Error	10.5%	10.1%	8.8%	9.0%	15.5%	18.4%	
Velocity (m/s)	Absolute Error	-0.0394	-0.0345	-0.0354	0.2184	-0.2962	-0.3155	
	Percentage Error	9.5%	8.4%	8.6%	9.9%	13.4%	15.5%	
Discharge (m^2/s)	Absolute Error	0.0000	0.0015	-0.0010	0.0000	0.0000	0.0000	
	Percentage Error	0.0%	0.9%	0.6%	0.0%	0.0%	0.0%	

(b)

Figure A.5: Comparison between numerical and experimental results for test case six following the introduction of weir coupling.

A.6 Camera 1 Calibration

The following figures show the median measured green light intensity of each cell contained within the frame of Camera 1, for each of the calibration concentrations in Table A.1. In each case, $7s$ of footage, equal to 210 frames, was analysed. For each frame, within each calibration recording, the mean green light intensity of the pixels contained within each cell is obtained by extracting the G value from the RGB pixel data. Due to the requirement to well mix the Rhodamine WT, small variations in the free surface are present since the recordings were performed before the motion of the fluid had entirely ceased. This is beneficial since it mimics the behaviour of the fluid during the experiment, enabling the filtering of the surface reflections via time-averaging.

Calibration Number	0	1	2	3	4	5	6	7	8	9
Concentration (mg/L)	0.00	2.89	5.78	8.68	11.57	14.46	17.35	20.24	23.14	26.02

Table A.1: Calibration concentrations for the upstream calibration of Camera 1.

A.6.1 Camera 1: Calibration 0

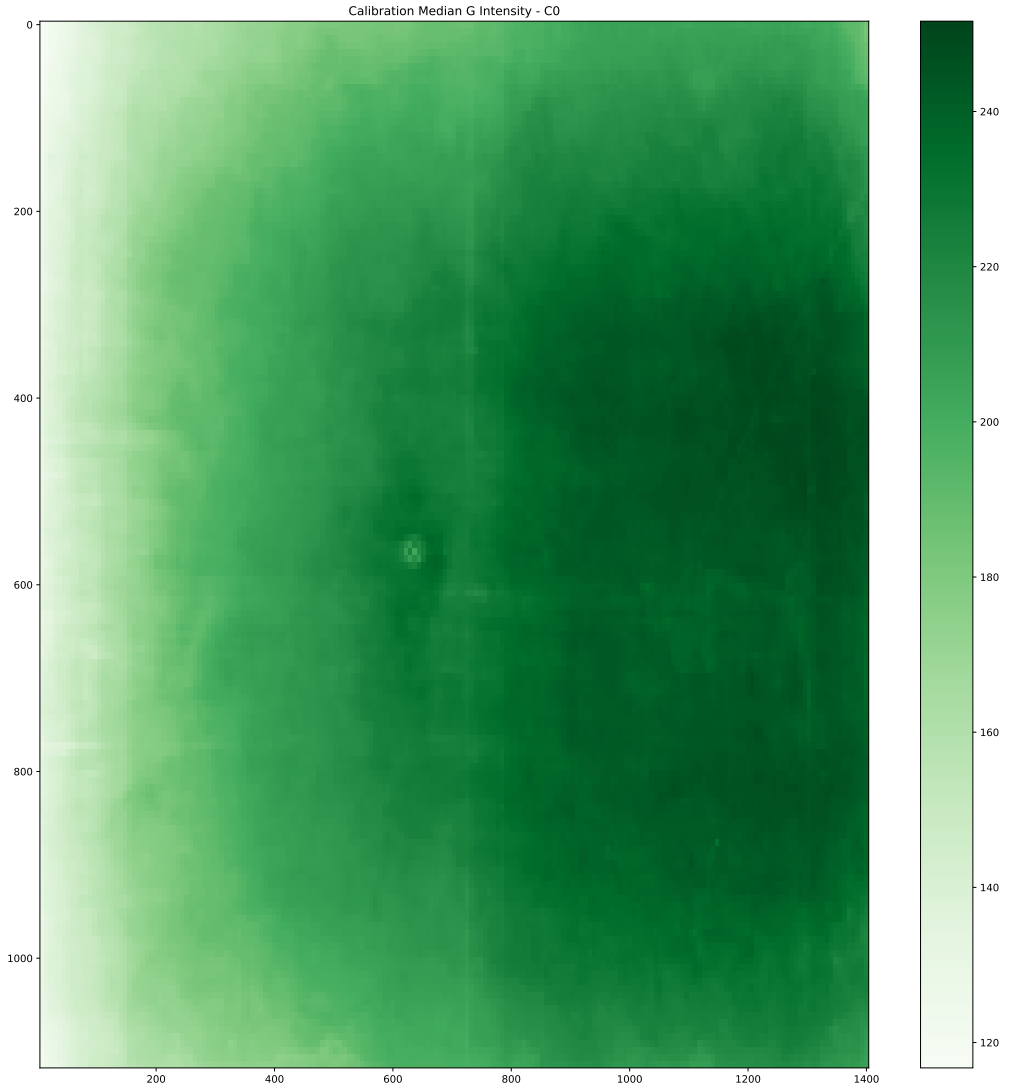

Figure A.6: Recorded median green light intensity for a $0.00mg/L$ concentration of Rhodamine WT - 20% aqueous solution.

A.6.2 Camera 1: Calibration 1

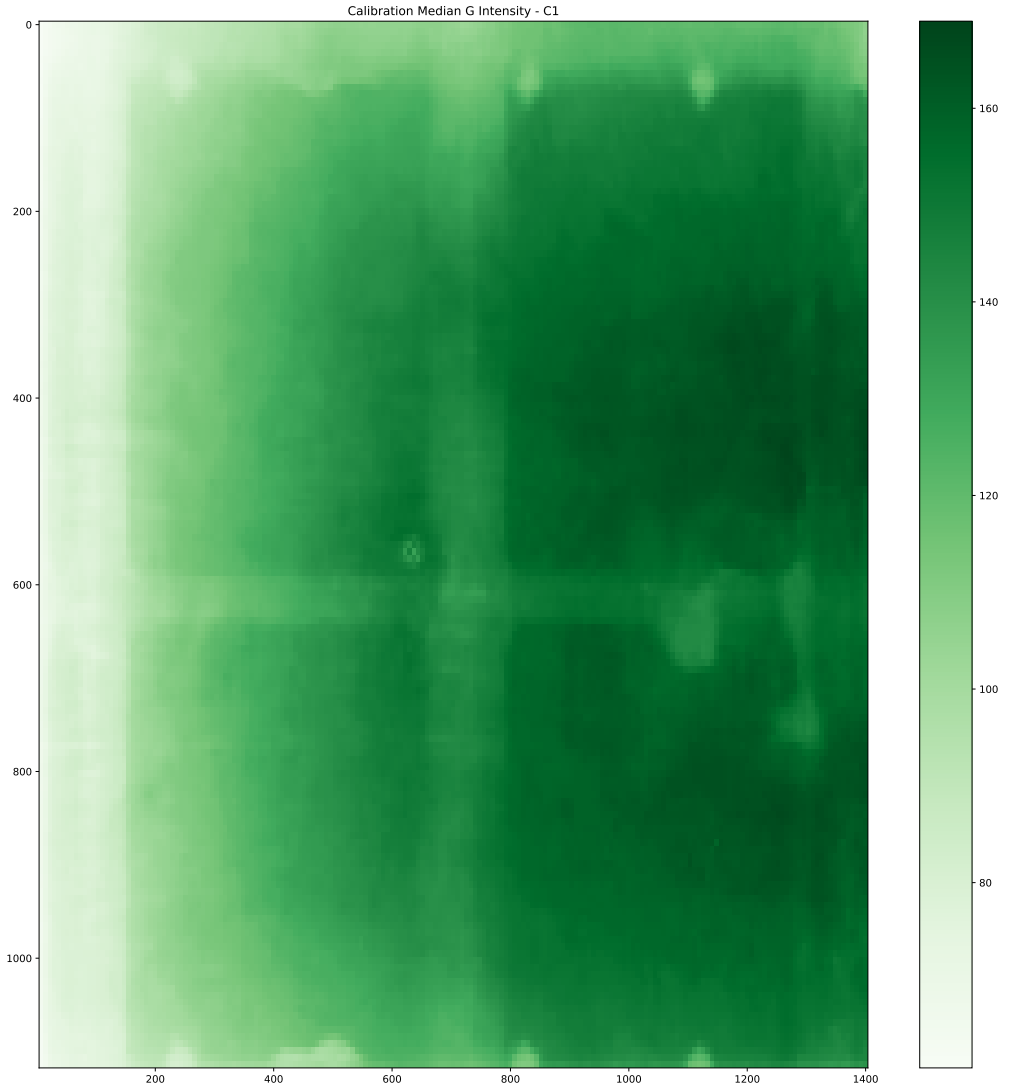

Figure A.7: Recorded median green light intensity for a $2.89 mg/L$ concentration of Rhodamine WT - 20% aqueous solution.

A.6.3 Camera 1: Calibration 2

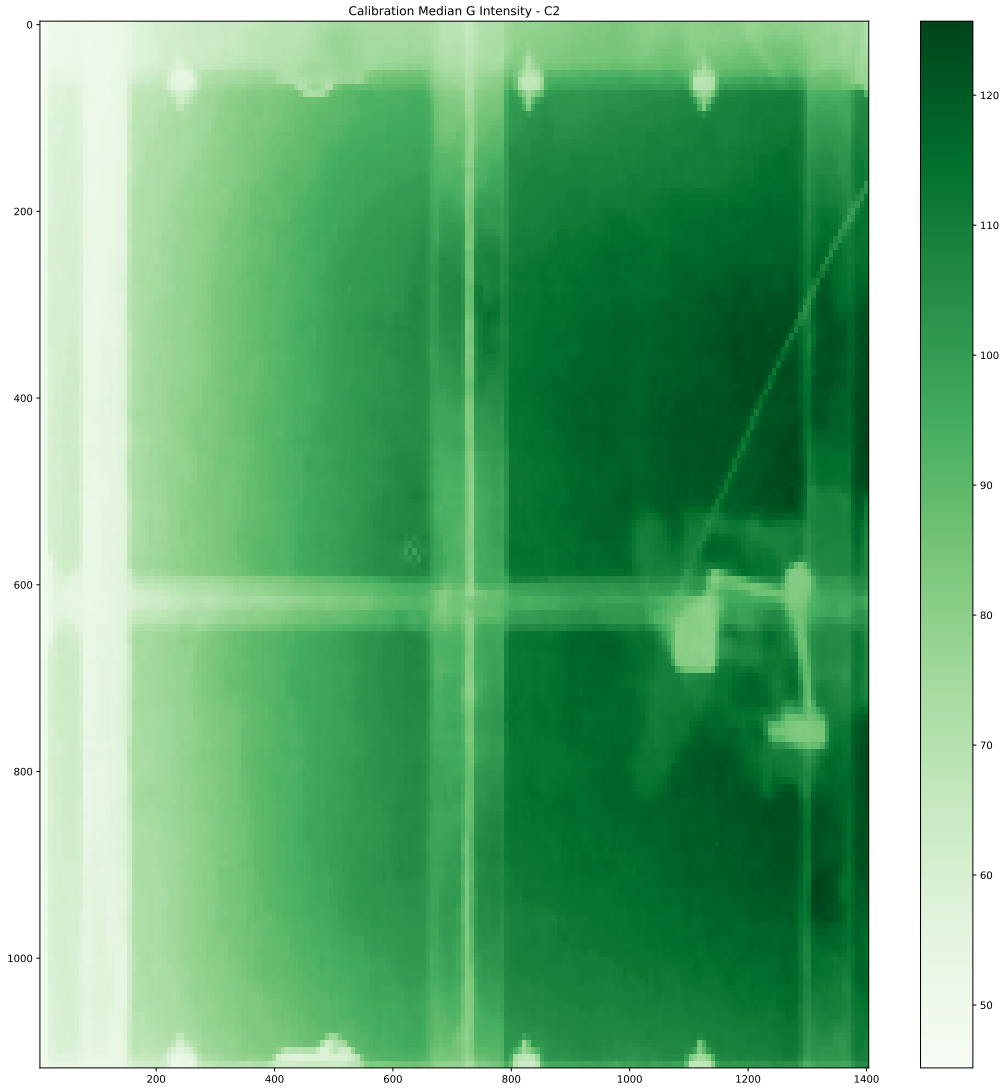

Figure A.8: Recorded median green light intensity for a $5.78 mg/L$ concentration of Rhodamine WT - 20% aqueous solution.

A.6.4 Camera 1: Calibration 3

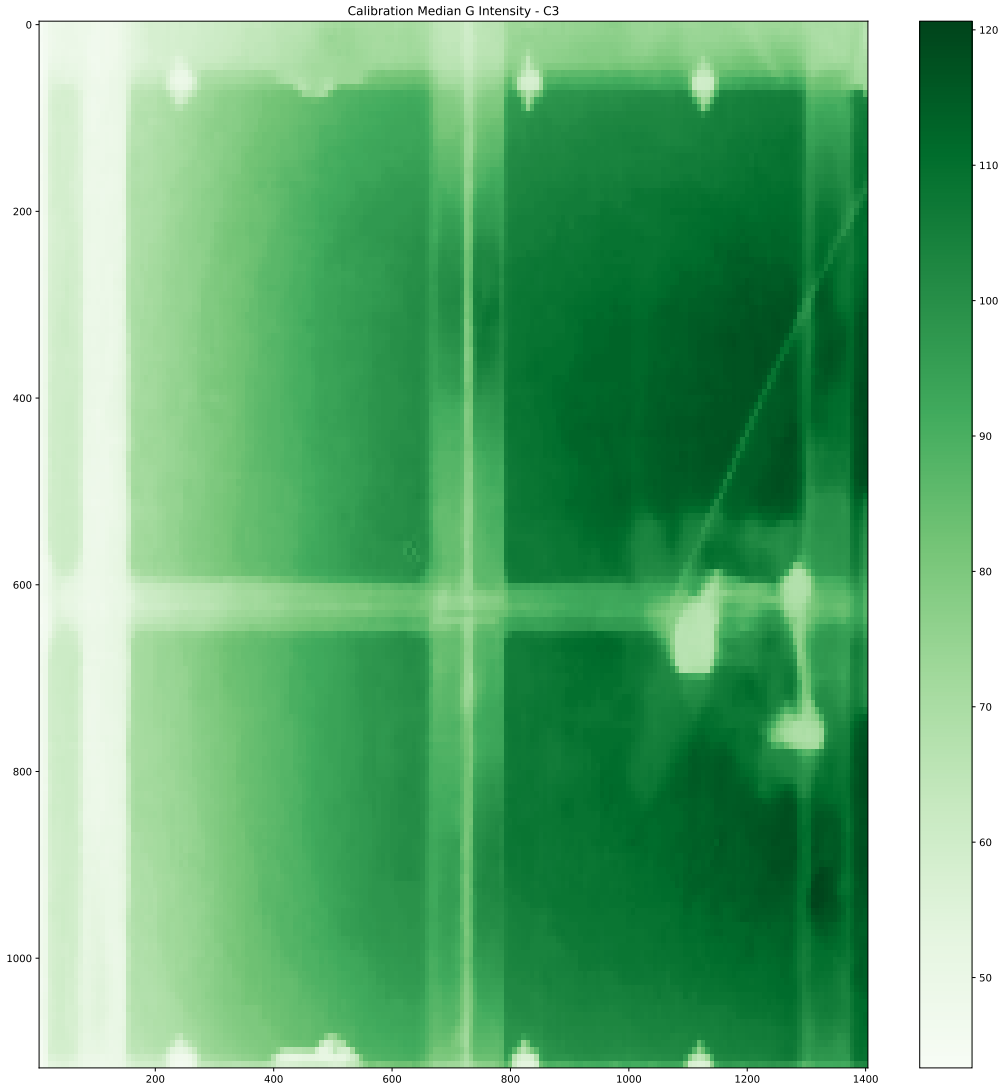

Figure A.9: Recorded median green light intensity for a $8.68 mg/L$ concentration of Rhodamine WT - 20% aqueous solution.

A.6.5 Camera 1: Calibration 4

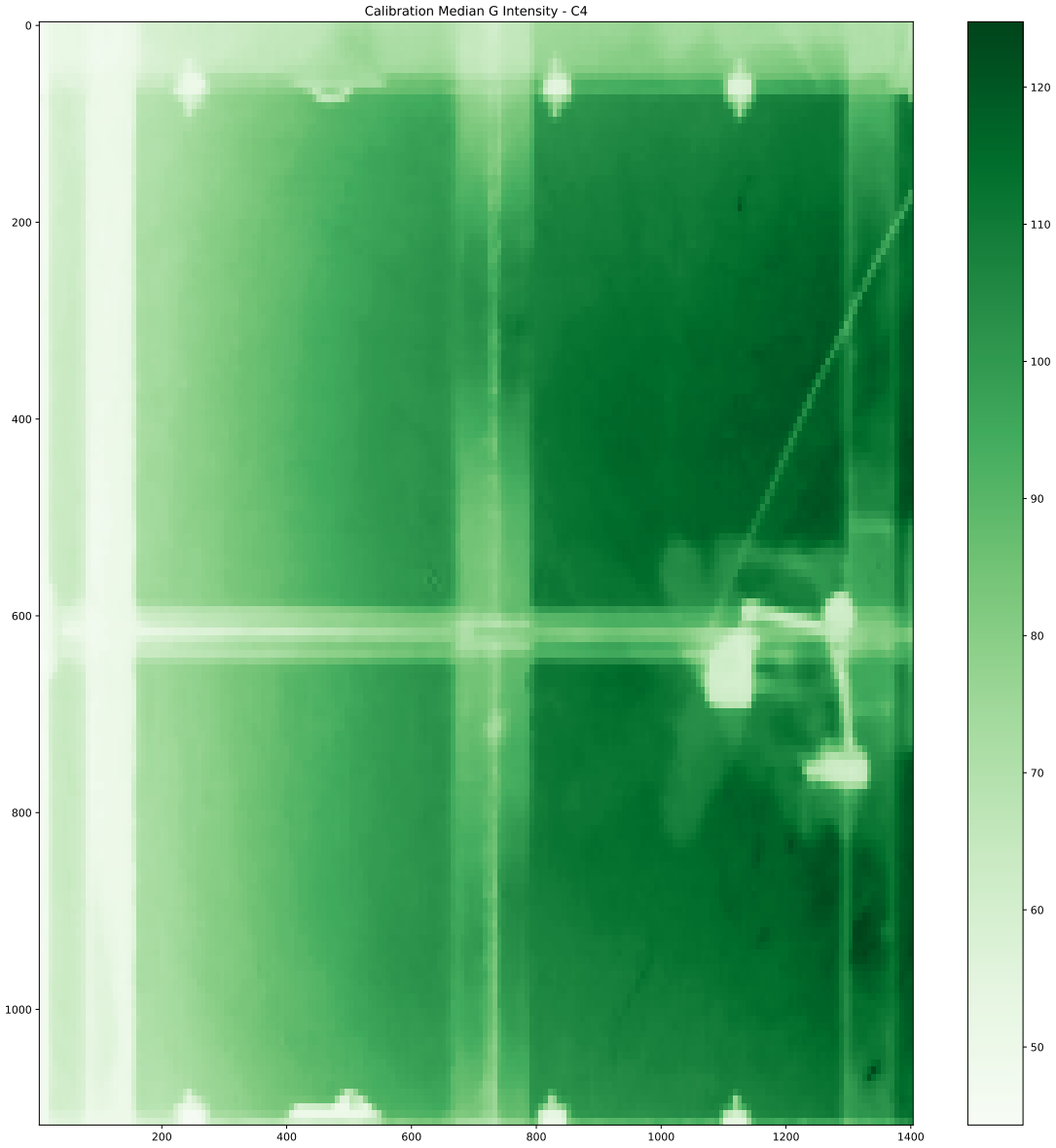

Figure A.10: Recorded median green light intensity for a 11.57mg/L concentration of Rhodamine WT - 20% aqueous solution.

A.6.6 Camera 1: Calibration 5

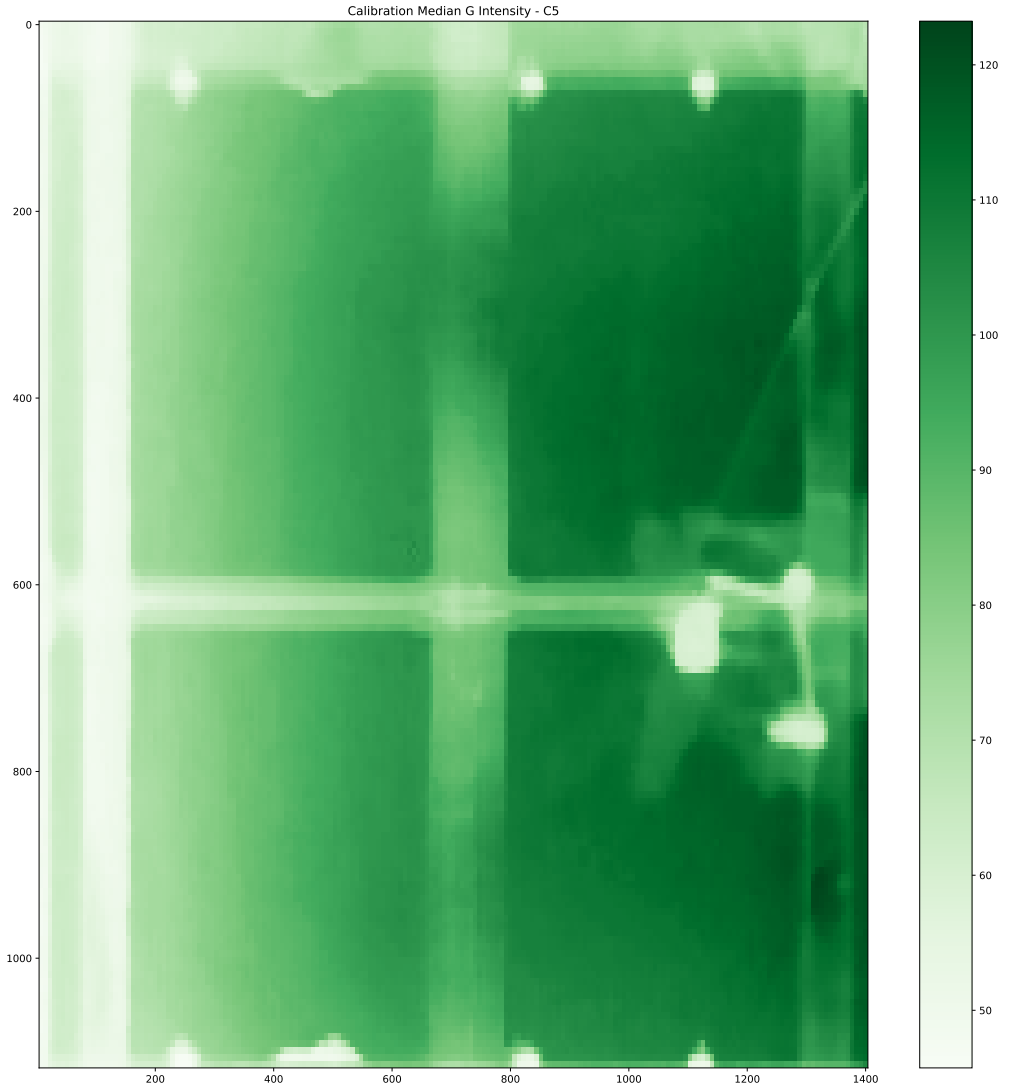

Figure A.11: Recorded median green light intensity for a $14.46 mg/L$ concentration of Rhodamine WT - 20% aqueous solution.

A.6.7 Camera 1: Calibration 6

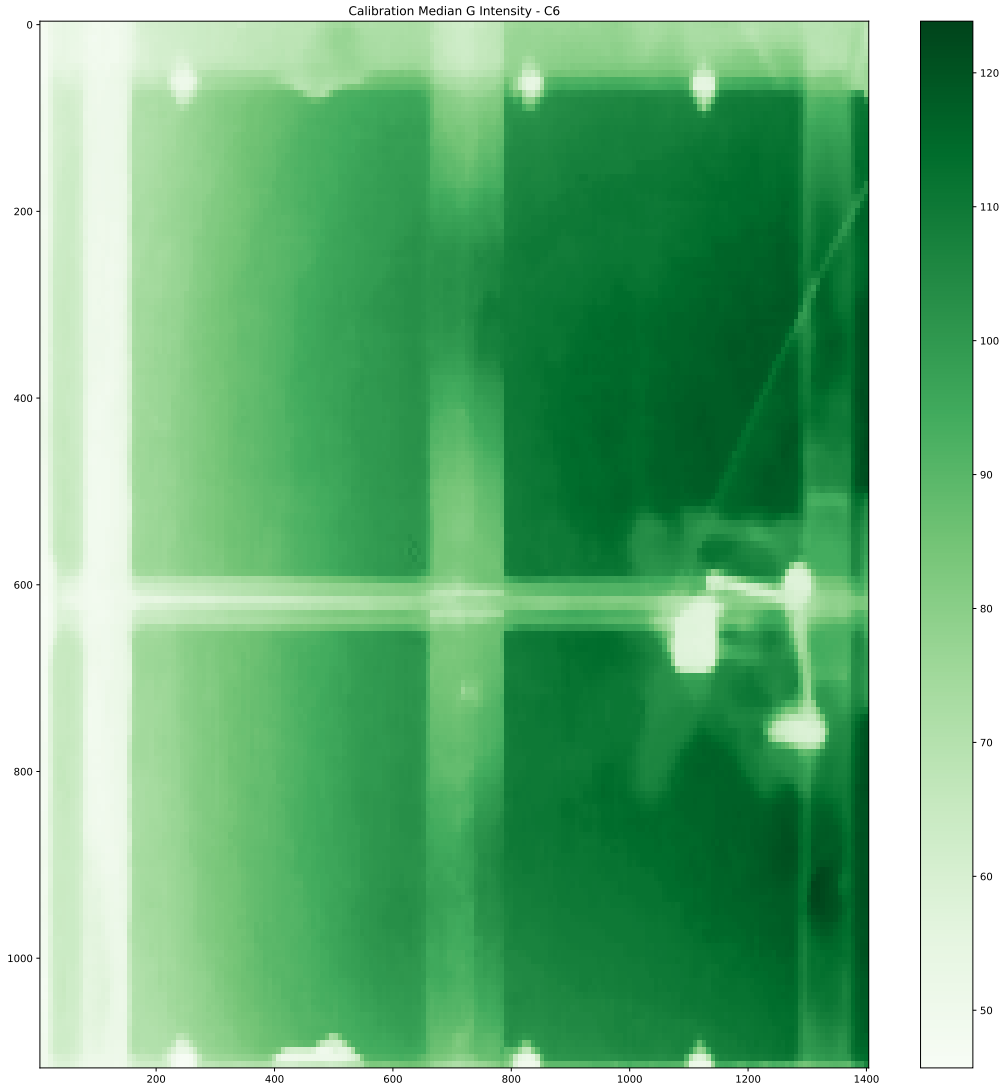

Figure A.12: Recorded median green light intensity for a 17.35mg/L concentration of Rhodamine WT - 20% aqueous solution.

A.6.8 Camera 1: Calibration 7

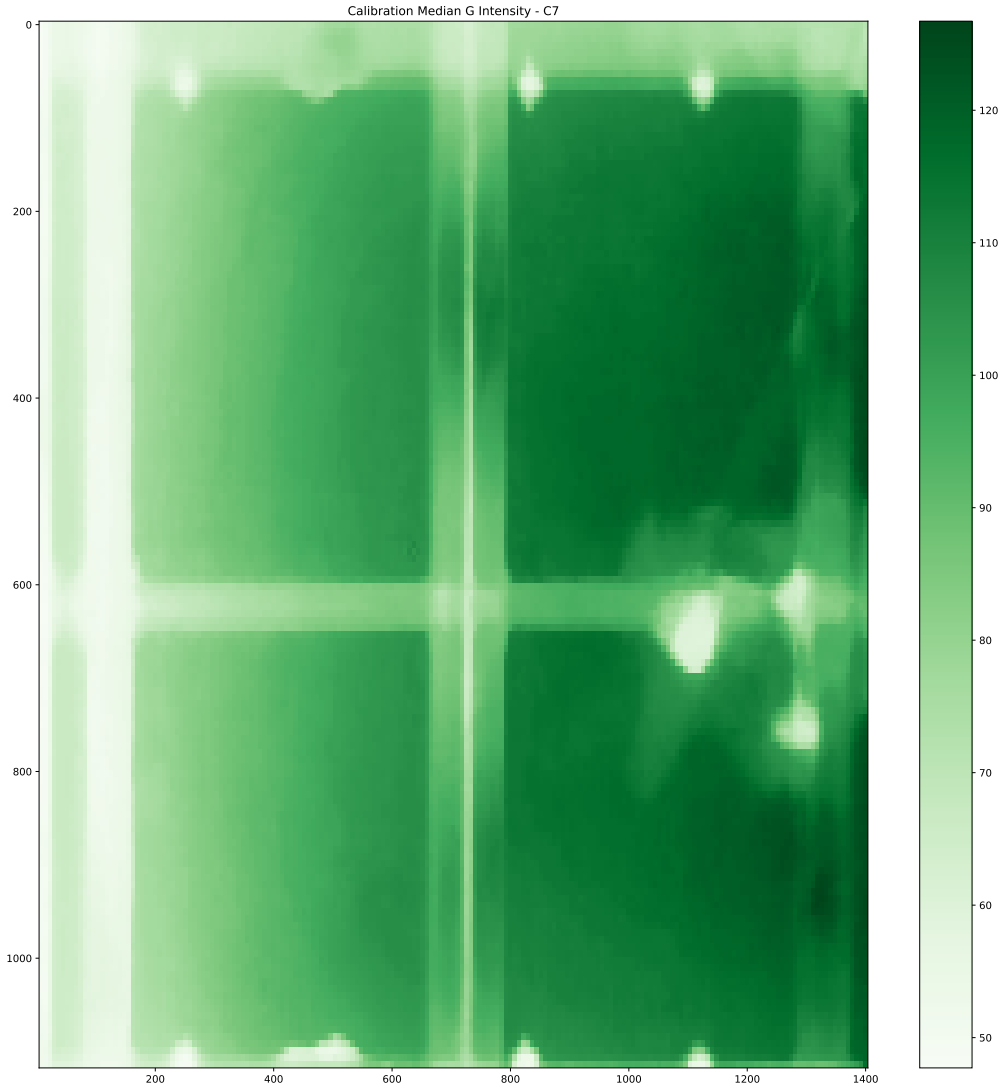

Figure A.13: Recorded median green light intensity for a $20.24 mg/L$ concentration of Rhodamine WT - 20% aqueous solution.

A.6.9 Camera 1: Calibration 8

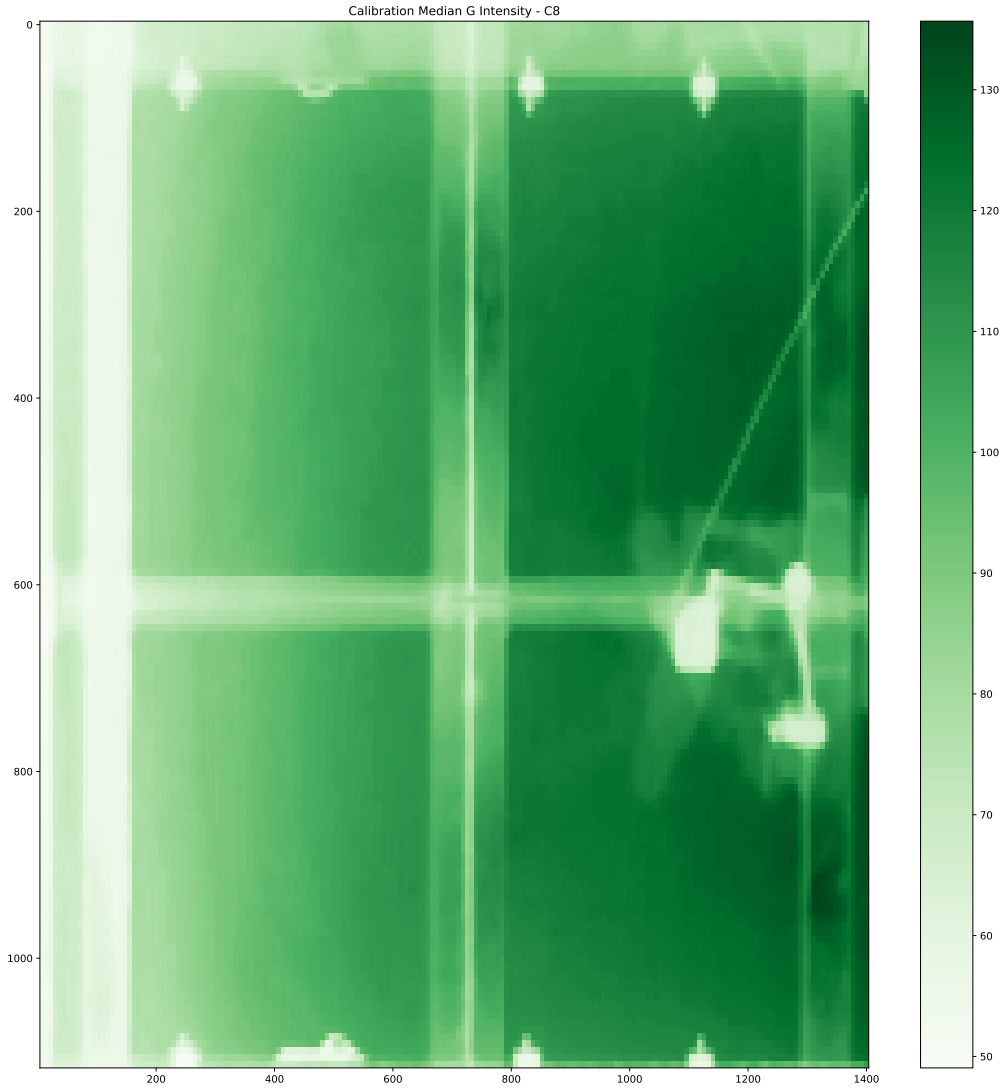

Figure A.14: Recorded median green light intensity for a $23.14 mg/L$ concentration of Rhodamine WT - 20% aqueous solution.

A.6.10 Camera 1: Calibration 9

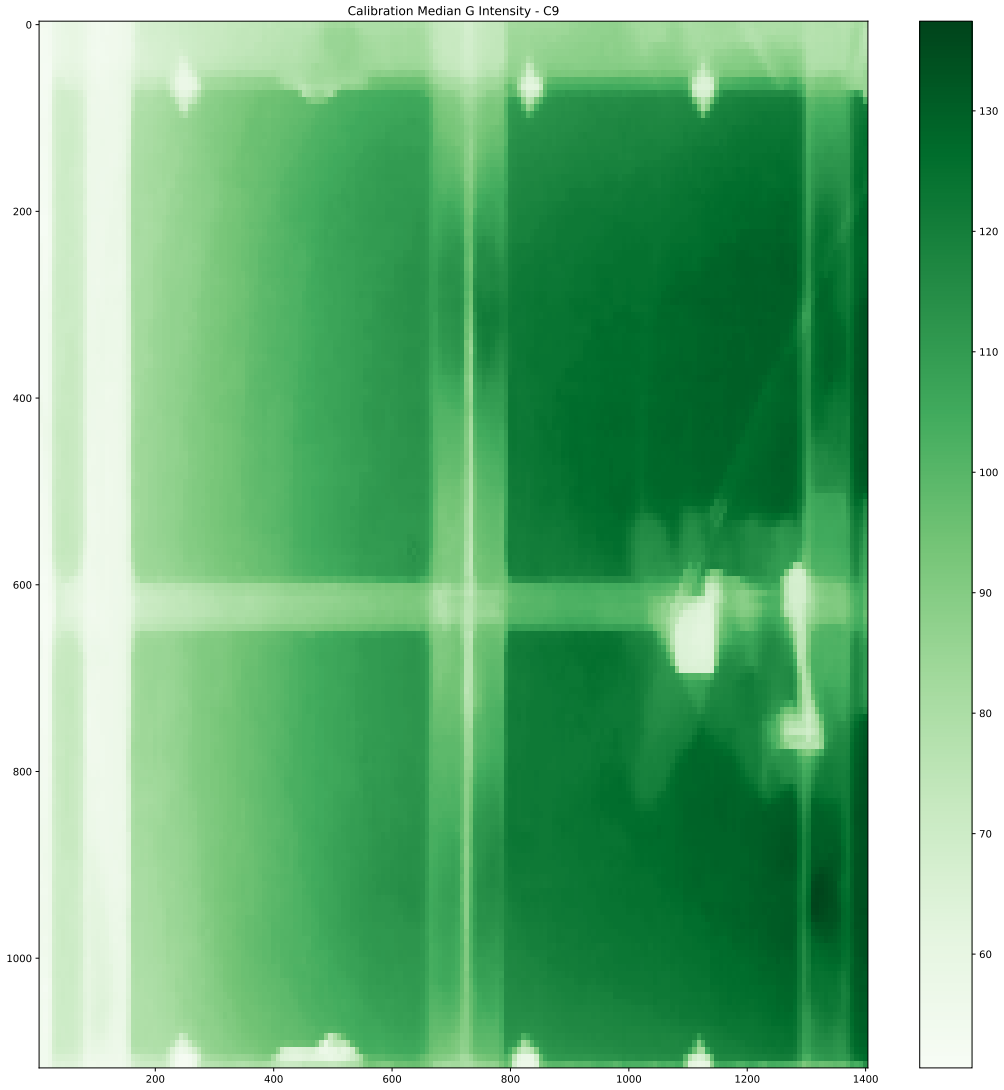

Figure A.15: Recorded median green light intensity for a $26.02 mg/L$ concentration of Rhodamine WT - 20% aqueous solution.

A.7 Camera 2 Calibration

The following figures show the median measured green light intensity of each cell contained within the frame of Camera 2, for each of the calibration concentrations in Table A.2. In each case, $7s$ of footage, equal to 210 frames, was analysed. For each frame, within each calibration recording, the mean green light intensity of the pixels contained within each cell is obtained by extracting the G value from the RGB pixel data. Due to the requirement to well mix the Rhodamine WT, small variations in the free surface are present since the recordings were initiated before the motion of the fluid had entirely ceased. This is beneficial since it mimics the behaviour of the fluid during the experiment, enabling the filtering of the surface reflections via time-averaging.

Calibration Number	0	1	2	3	4	5	6	7	8	9
Concentration (mg/L)	0.00	3.50	6.99	10.49	13.99	17.48	20.98	24.47	27.97	31.46

Table A.2: Calibration concentrations for the downstream calibration of Camera 2.

A.7.1 Camera 2: Calibration 0

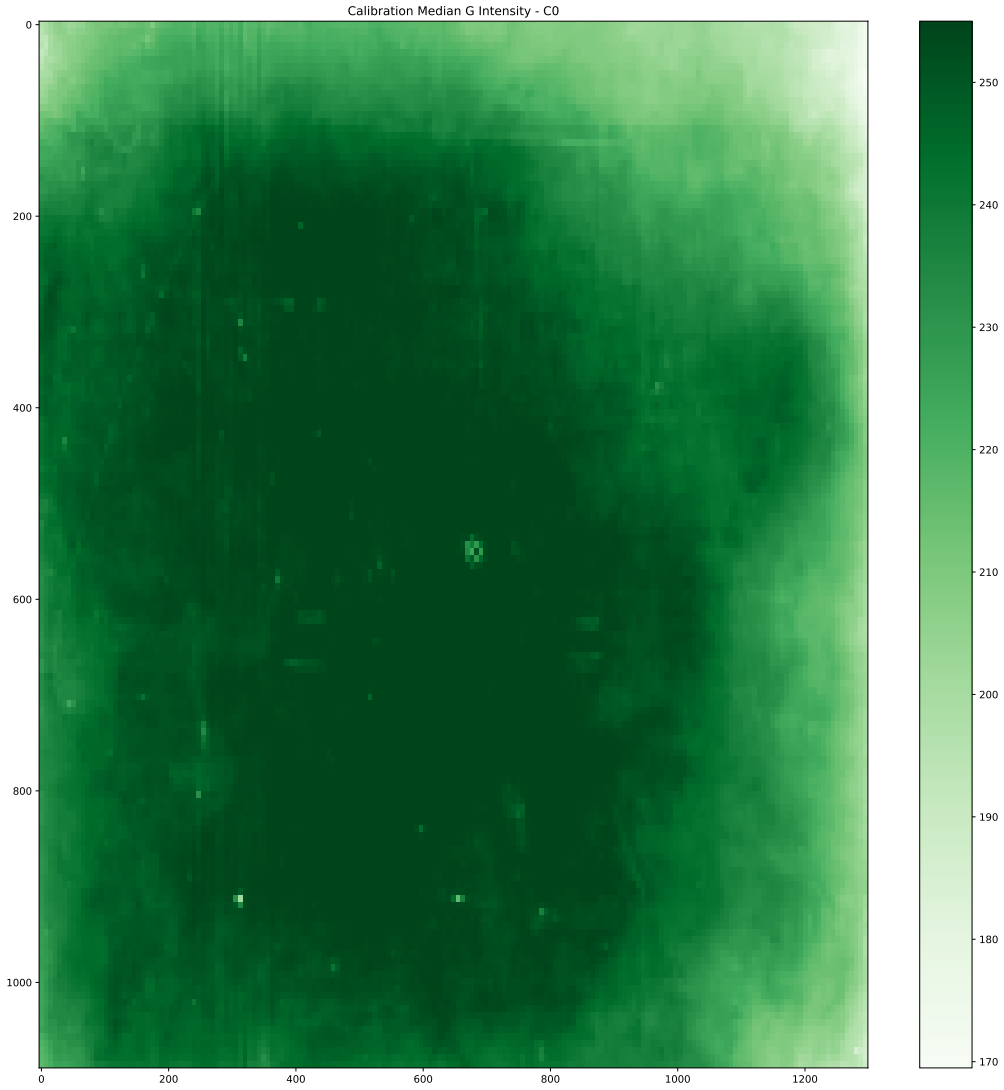

Figure A.16: Recorded median green light intensity for a $0.00mg/L$ concentration of Rhodamine WT - 20% aqueous solution.

A.7.2 Camera 2: Calibration 1

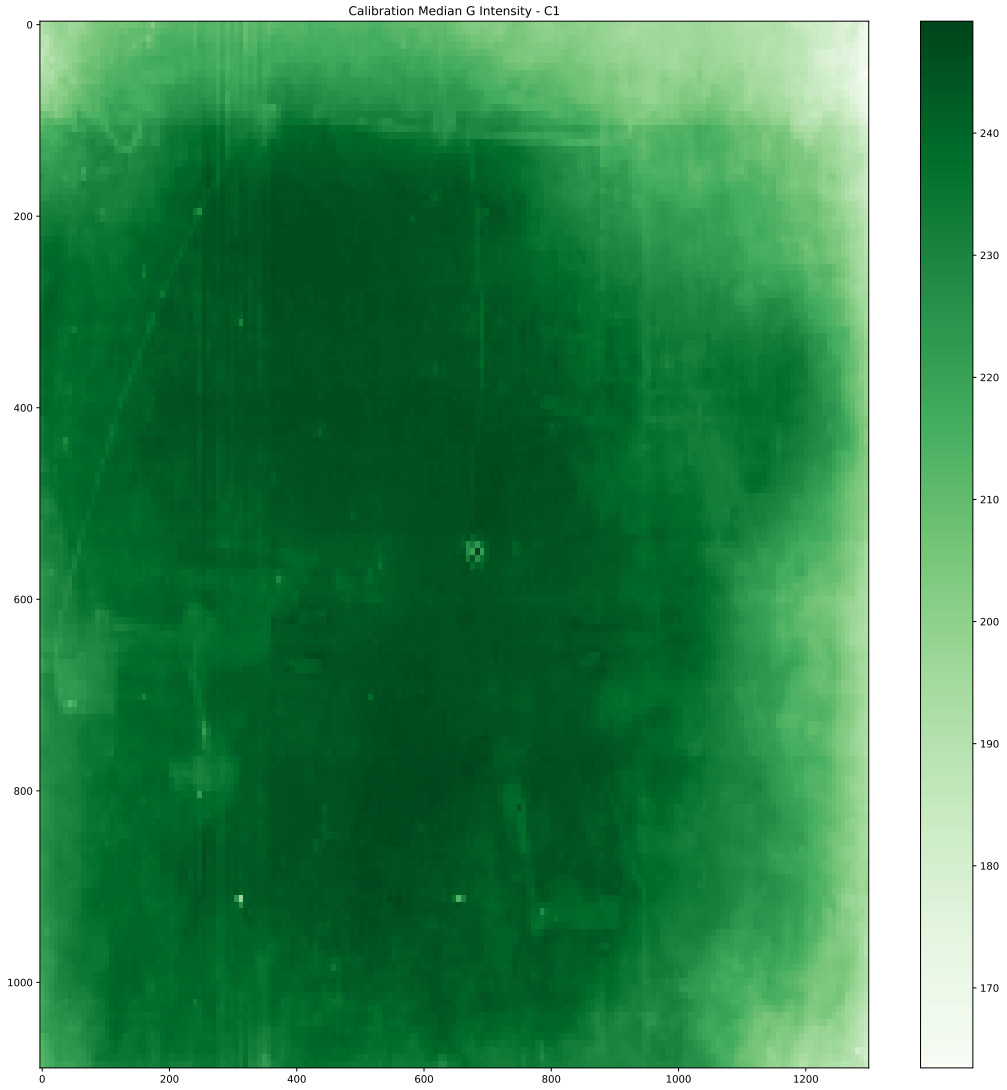

Figure A.17: Recorded median green light intensity for a $3.50 mg/L$ concentration of Rhodamine WT - 20% aqueous solution.

A.7.3 Camera 2: Calibration 2

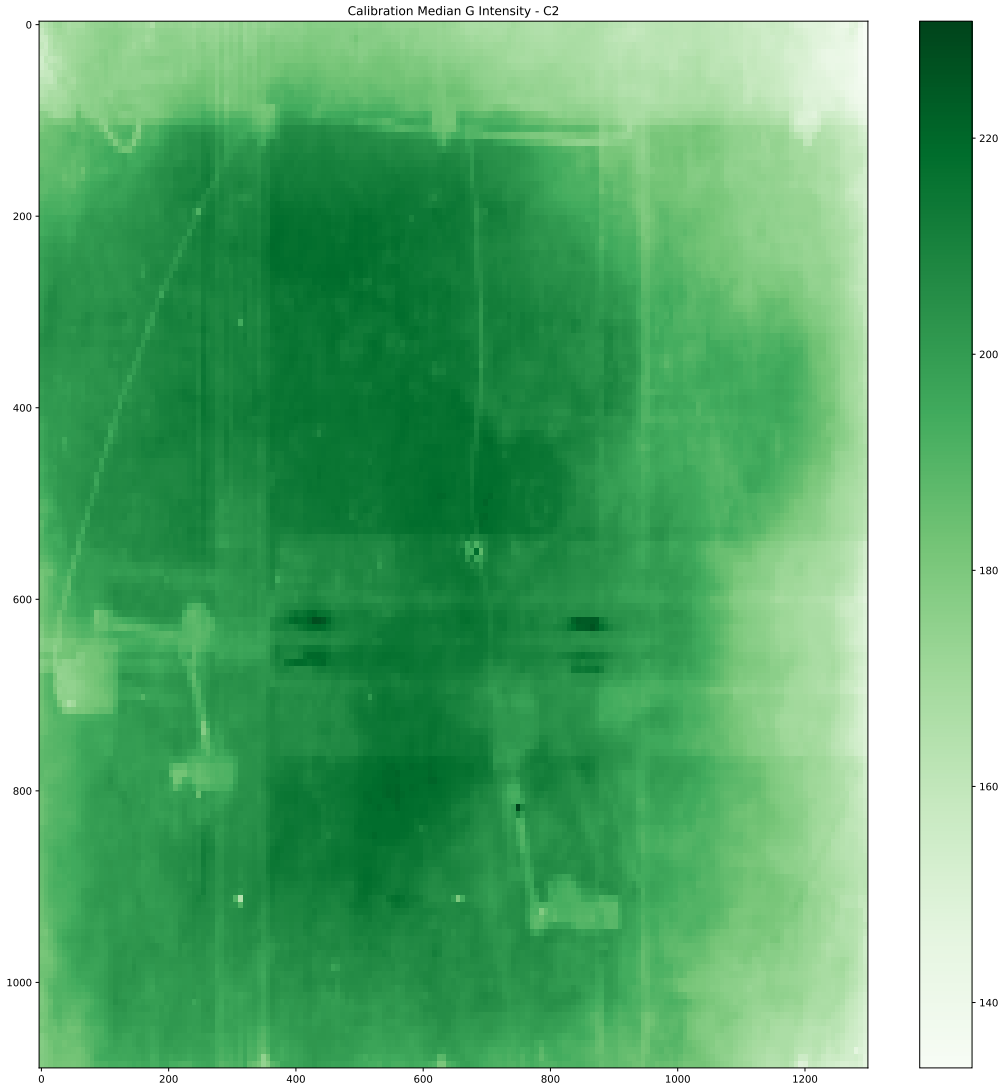

Figure A.18: Recorded median green light intensity for a $6.99 mg/L$ concentration of Rhodamine WT - 20% aqueous solution.

A.7.4 Camera 2: Calibration 3

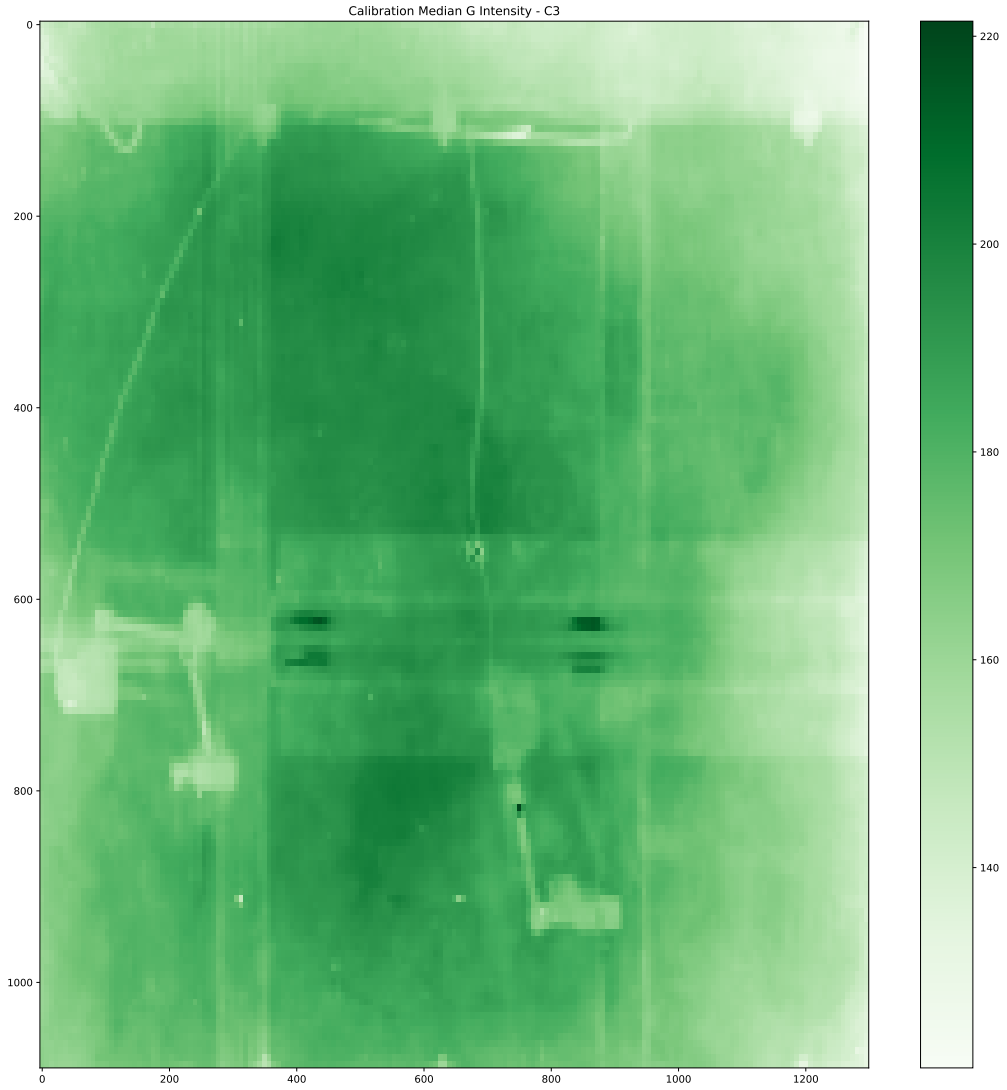

Figure A.19: Recorded median green light intensity for a $10.49 mg/L$ concentration of Rhodamine WT - 20% aqueous solution.

A.7.5 Camera 2: Calibration 4

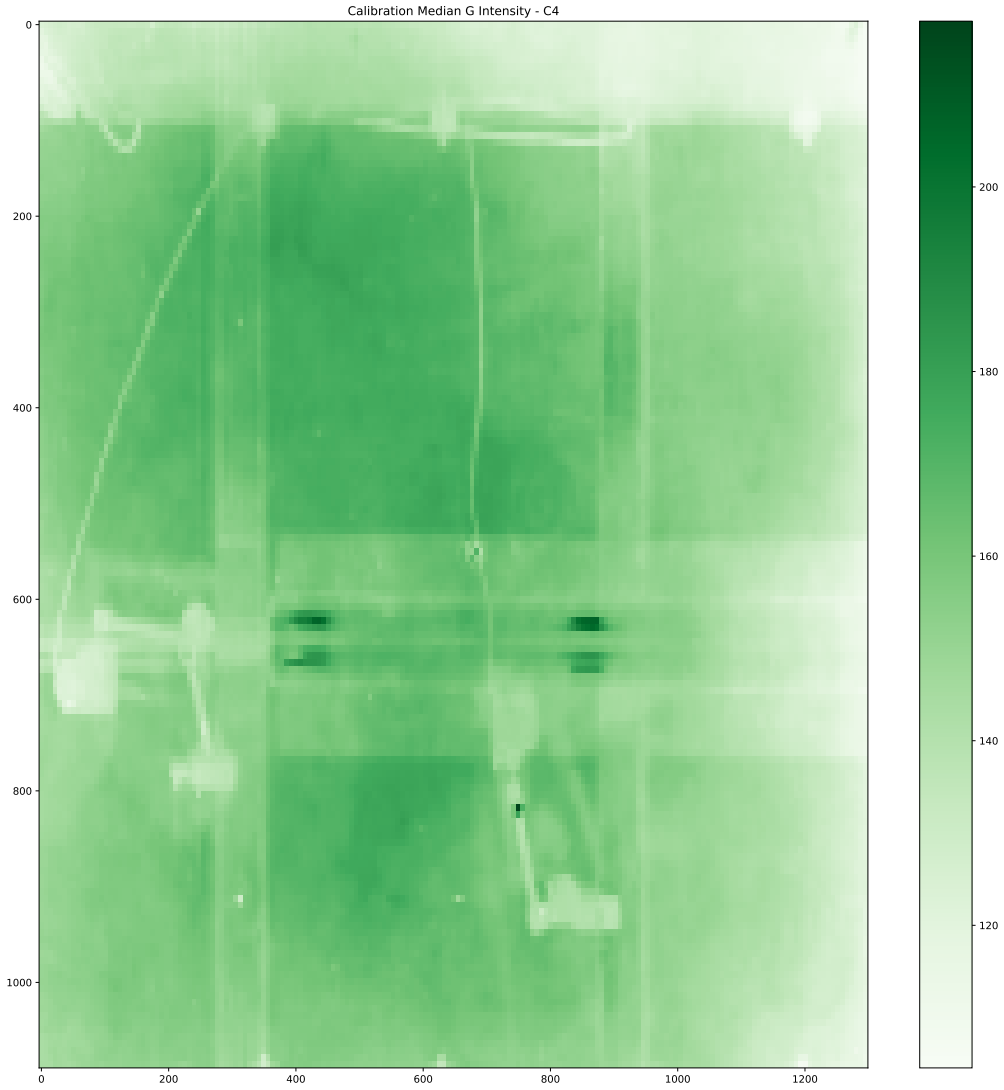

Figure A.20: Recorded median green light intensity for a $13.99 mg/L$ concentration of Rhodamine WT - 20% aqueous solution.

A.7.6 Camera 2: Calibration 5

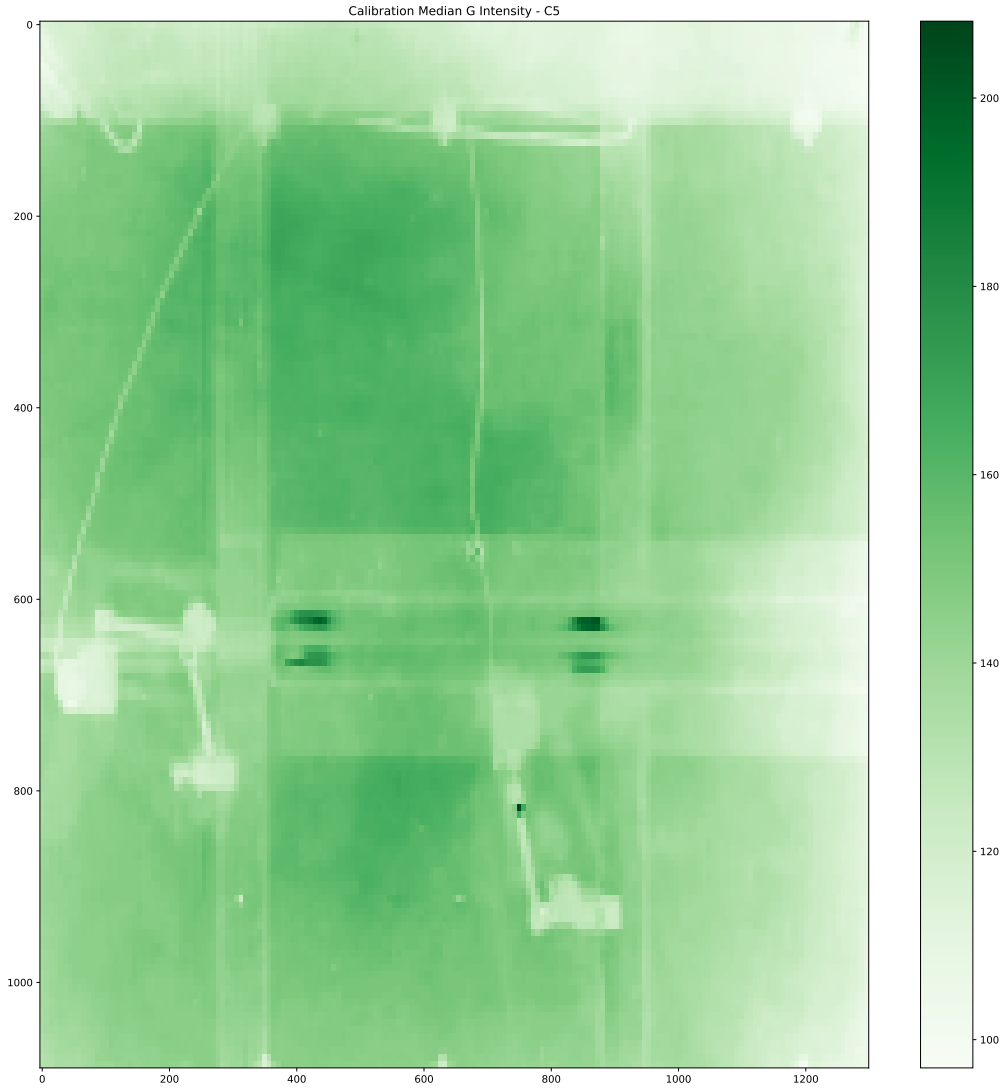

Figure A.21: Recorded median green light intensity for a $17.48 mg/L$ concentration of Rhodamine WT - 20% aqueous solution.

A.7.7 Camera 2: Calibration 6

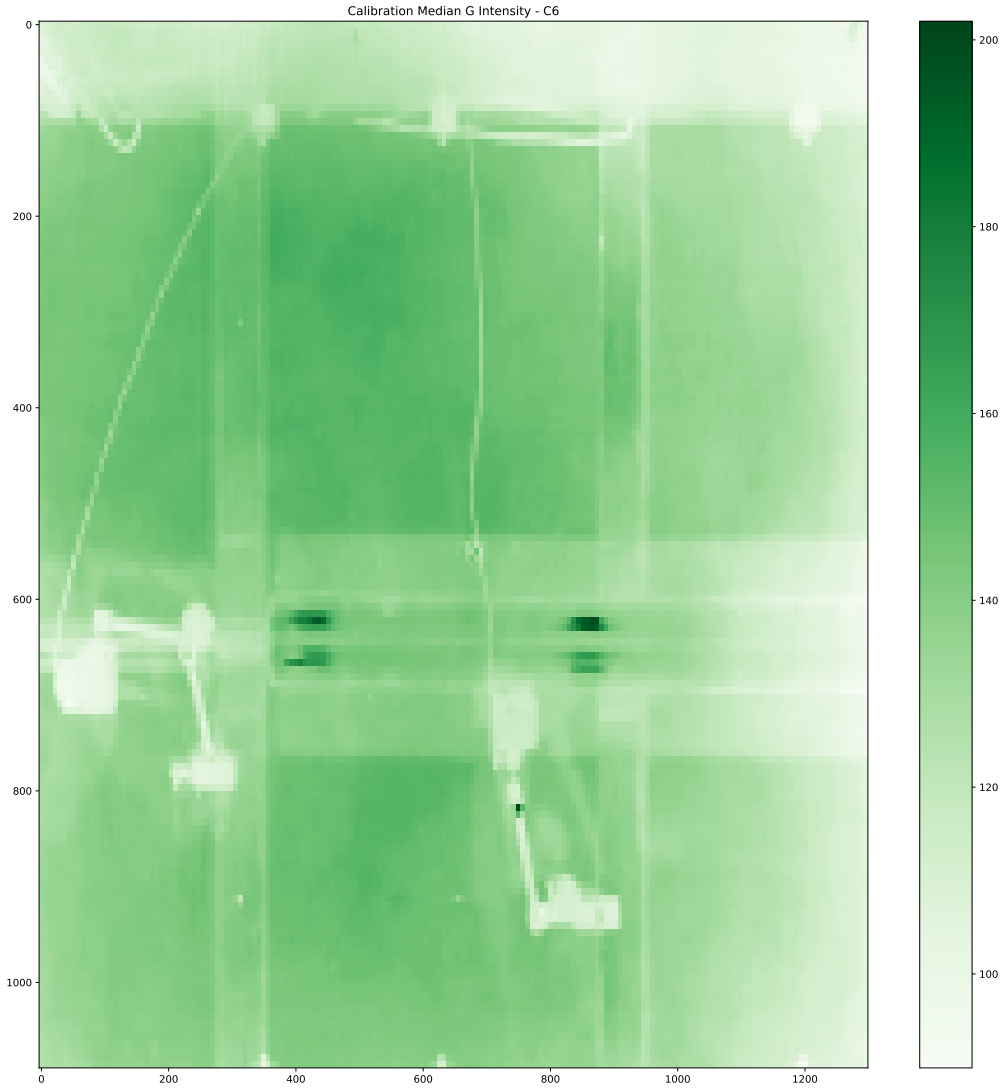

Figure A.22: Recorded median green light intensity for a $20.98 mg/L$ concentration of Rhodamine WT - 20% aqueous solution.

A.7.8 Camera 2: Calibration 7

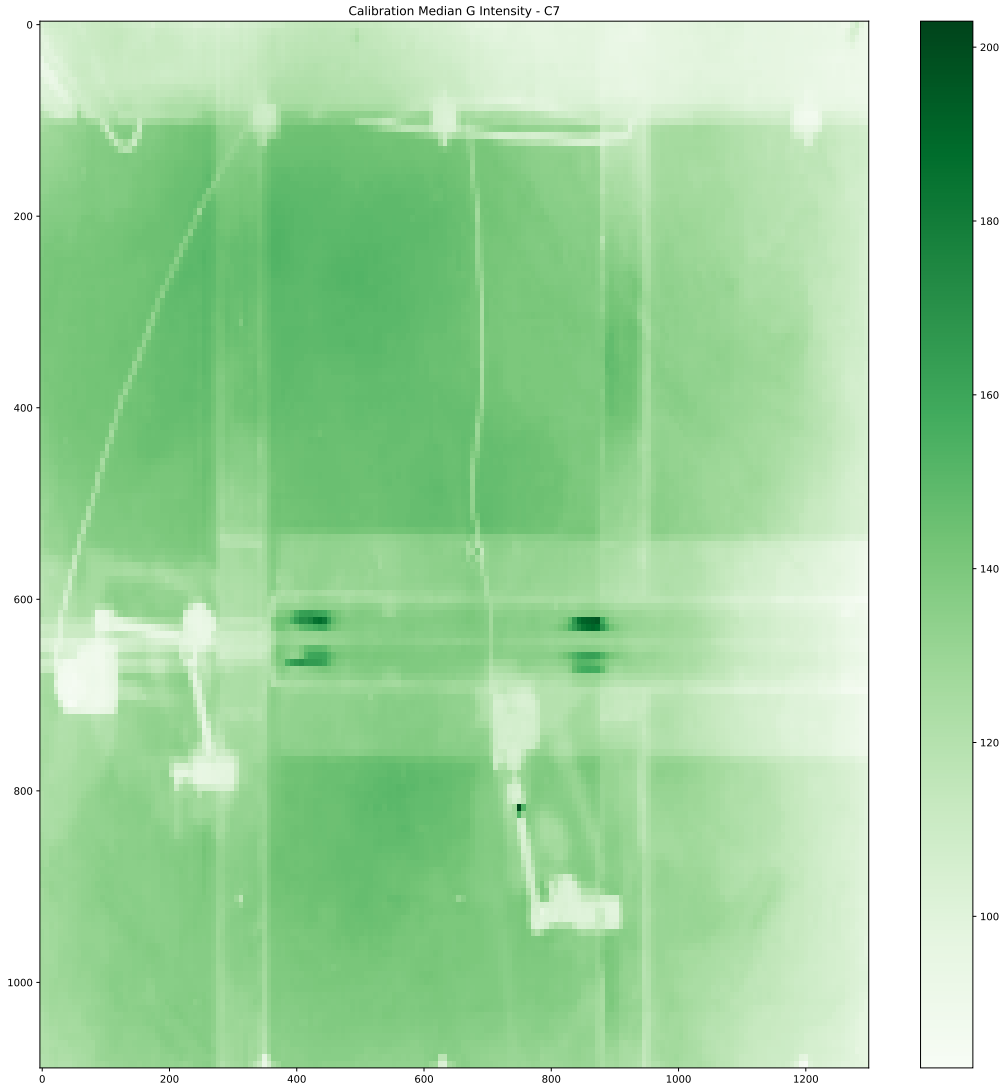

Figure A.23: Recorded median green light intensity for a $24.47 mg/L$ concentration of Rhodamine WT - 20% aqueous solution.

A.7.9 Camera 2: Calibration 8

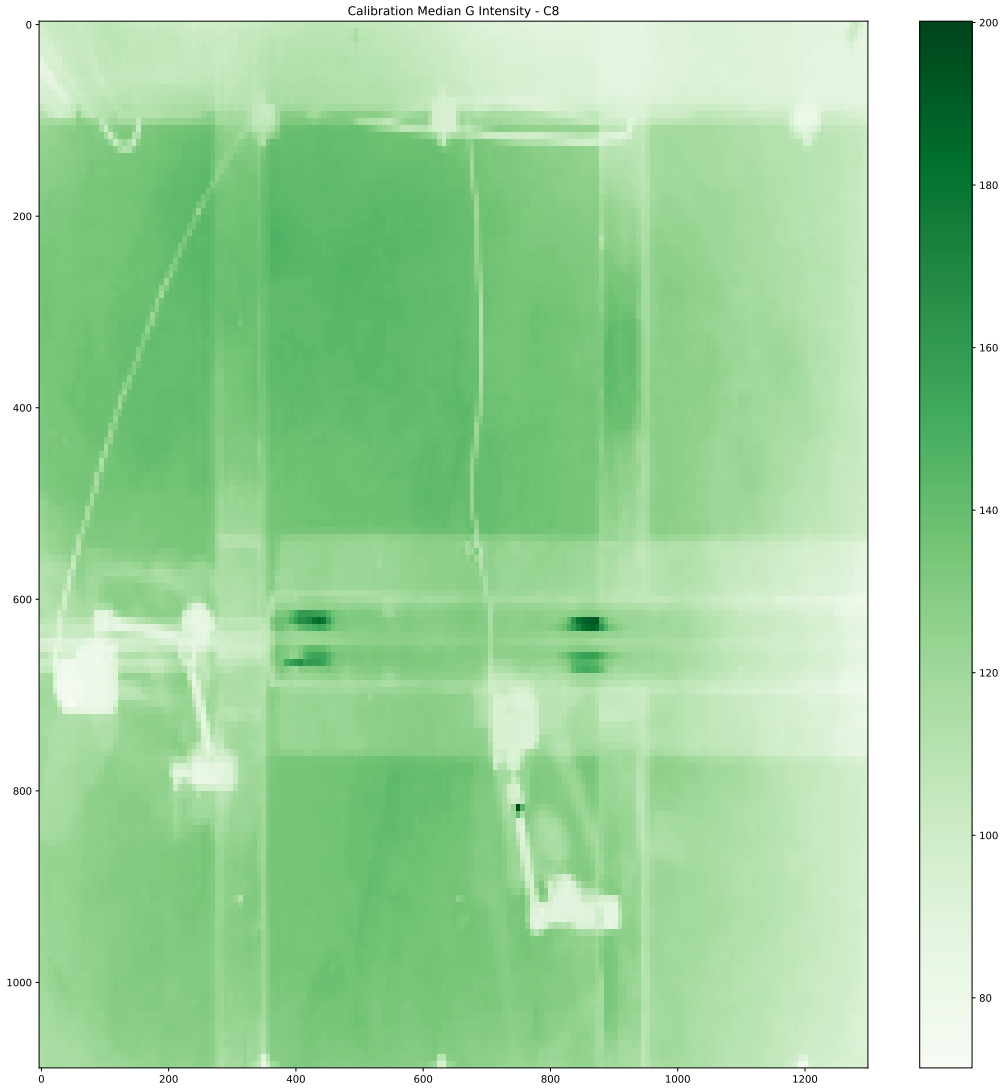

Figure A.24: Recorded median green light intensity for a $27.97 mg/L$ concentration of Rhodamine WT - 20% aqueous solution.

A.7.10 Camera 2: Calibration 9

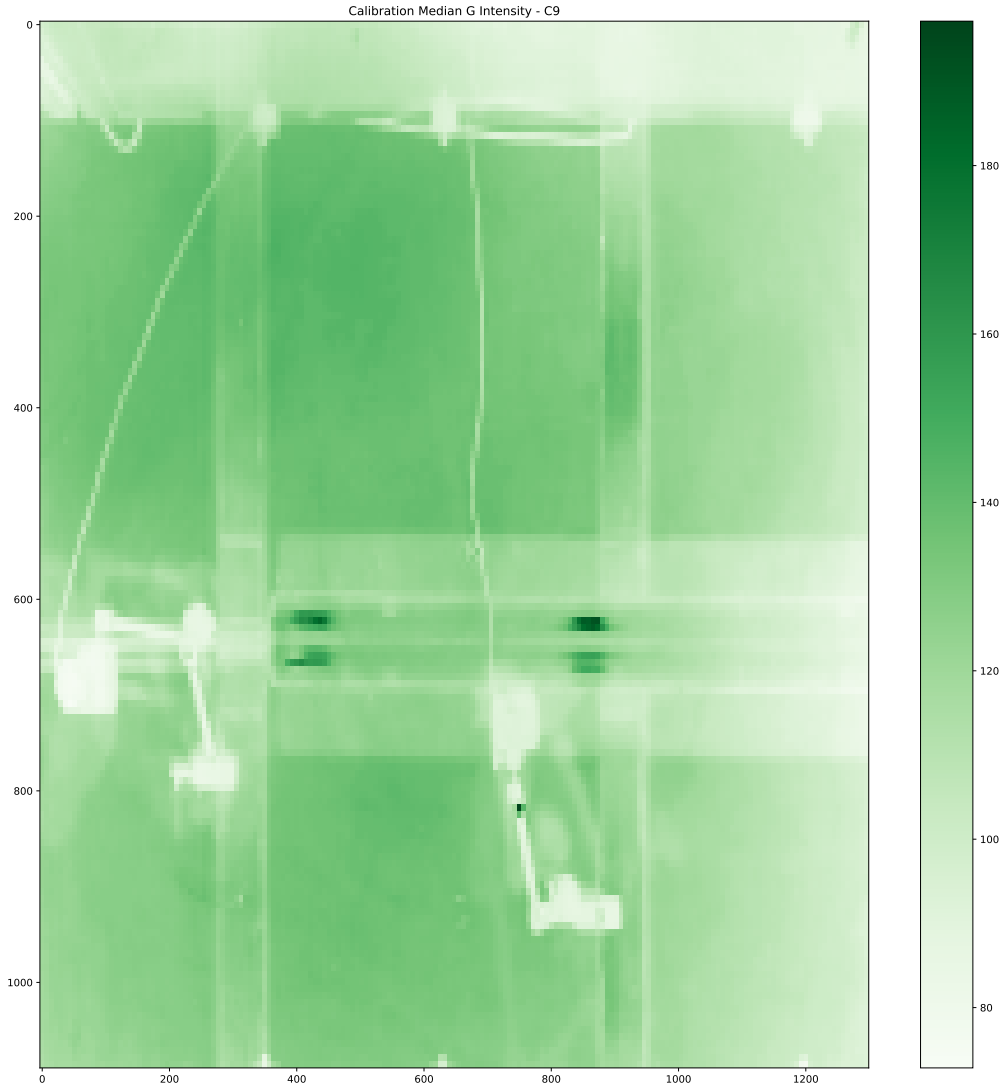

Figure A.25: Recorded median green light intensity for a $31.46 mg/L$ concentration of Rhodamine WT - 20% aqueous solution.

A.8 Cell Refinement

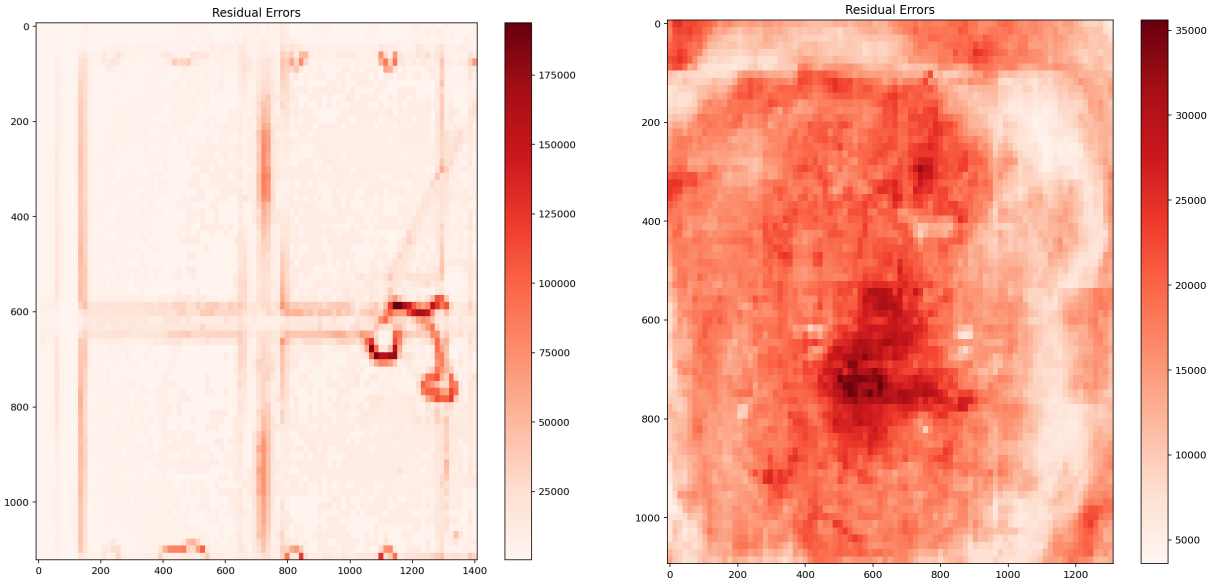

(a) Camera 1 (10mm Cells) (b) Camera 2 (10mm Cells)

Figure A.26: Spatial distribution of the residual errors for $10mm$ cells.

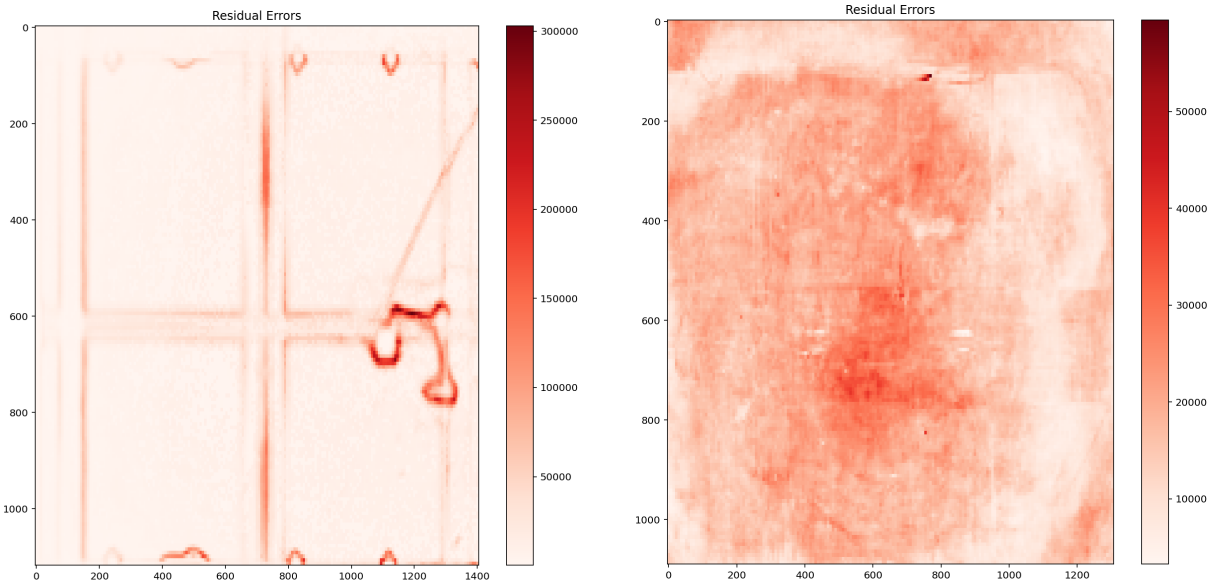

(a) Camera 1 (5mm Cells) (b) Camera 2 (5mm Cells)

Figure A.27: Spatial distribution of the residual errors for $5mm$ cells.

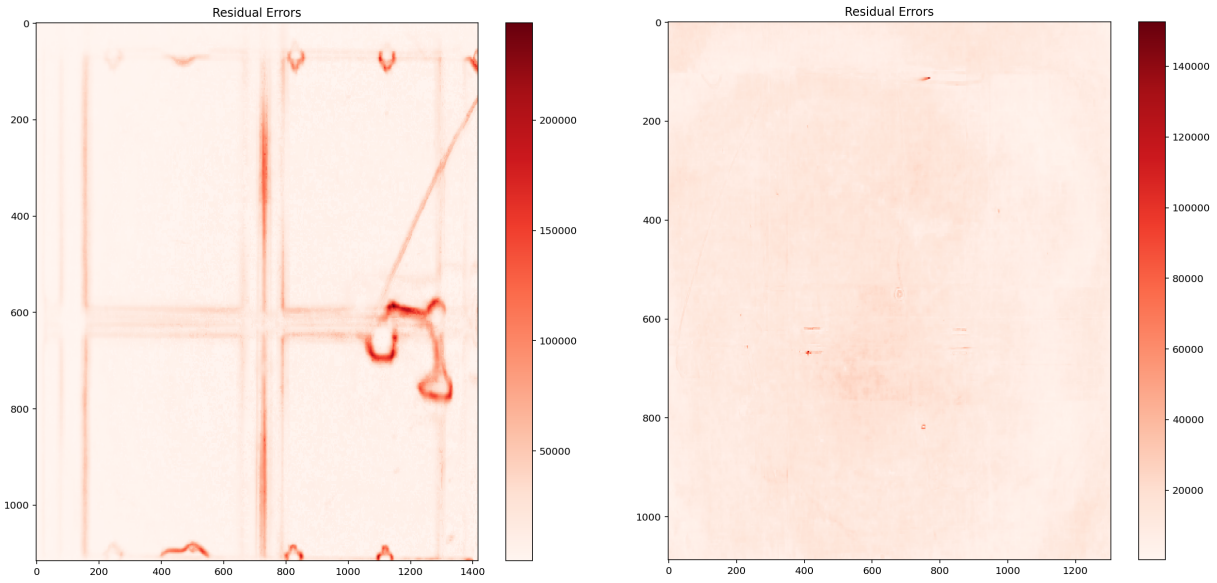

(a) Camera 1 (2mm Cells)

(b) Camera 2 (2mm Cells)

Figure A.28: Spatial distribution of the residual errors for $2mm$ cells.

A.9 Background Concentration Analysis

The determination of the background concentration for each of the camera frames is performed via analysis of $7s$ of footage, equal to 210 frames, obtained just prior to the injection of a Rhodamine WT slug for each experiment. The background concentration is determined by calculating the median green light intensity observed for each pixel over the duration of the recording. Conversion of the median green light intensity into a concentration value is performed using the transfer algorithm.

A.9.1 Experiment 1

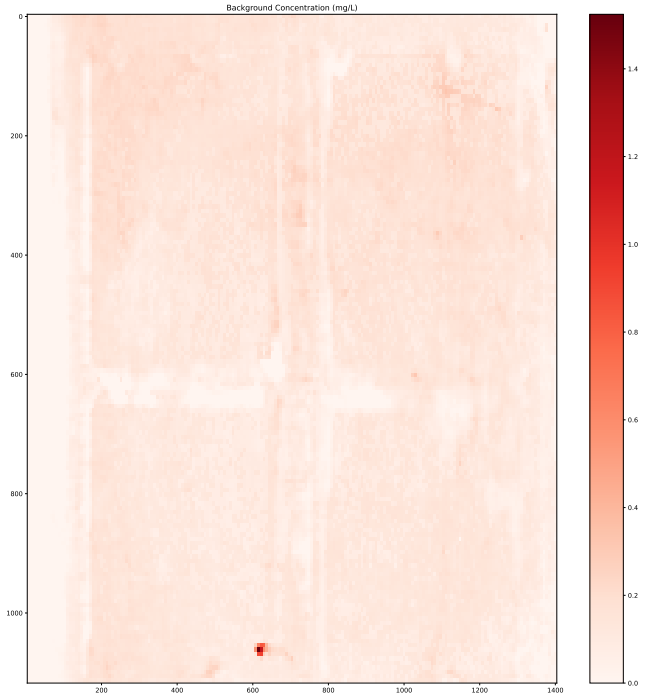

(a) Camera 1

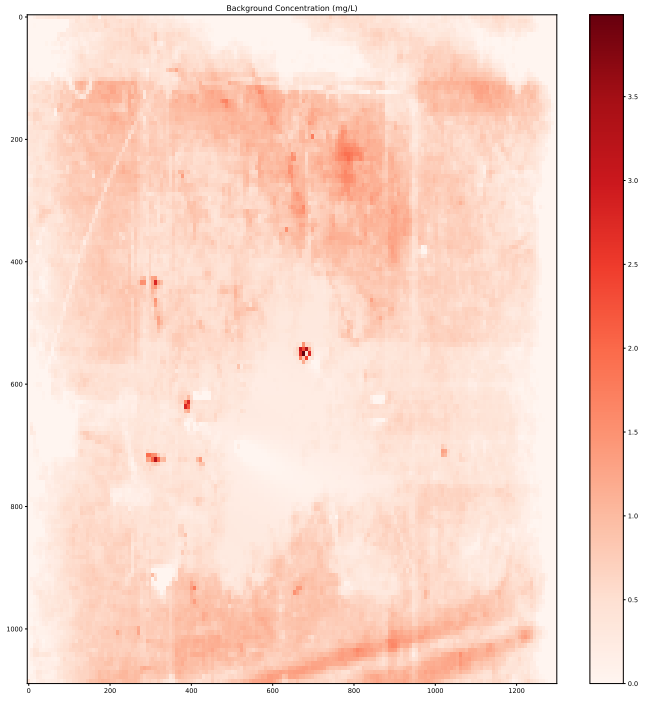

(b) Camera 2

Figure A.29: Background concentration for Experiment 1.

A.9.2 Experiment 2

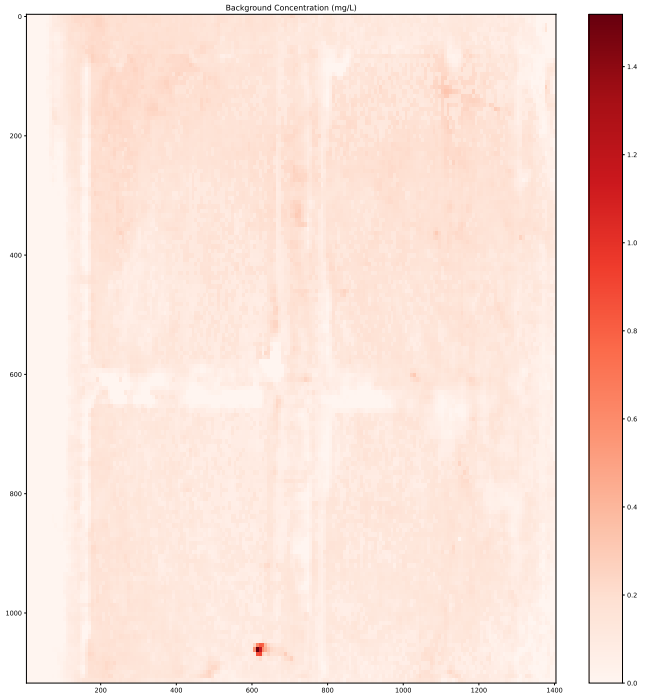

(a) Camera 1

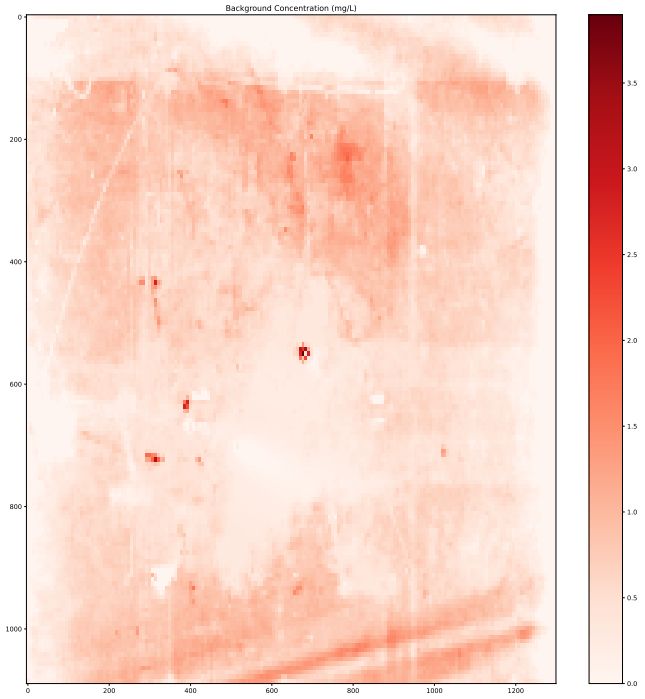

(b) Camera 2

Figure A.30: Background concentration for Experiment 2.